Mechanical modeling and numerical methods for poromechanics : Application to myocardium perfusion

Bruno Burtschell

NNT : 2016SACLX022

Thèse de Doctorat
de
l'Université Paris-Saclay
préparée à
l'Ecole polytechnique

Ecole Doctorale n^o 579
Sciences mécaniques et énergétiques, matériaux et géosciences

Spécialité Mécanique des Solides

Modélisation mécanique et méthodes numériques pour la poromécanique

Application à la perfusion du myocarde

Bruno Burtschell

Thèse présentée et soutenue à Palaiseau le 30/09/2016 devant un jury composé de :

Olivier Pironneau	UPMC	Président
Céline Grandmont	Inria	Rapporteur
Wolfgang A. Wall	Technische Universität München	Rapporteur
Emmanuel de Langre	Ecole polytechnique	Examinateur
Anne-Virginie Salsac	CNRS	Examinatrice
Dominique Chapelle	Inria	Directeur de thèse
Philippe Moireau	Inria	Directeur de thèse

Remerciements

Je tiens avant tout à remercier mes deux directeurs de thèse, Dominique Chapelle et Philippe Moireau, pour tout ce qu'ils m'ont apporté pendant ces trois années. Leur rigueur scientifique, leur persévérance et leur disponibilité m'auront permis de mener cette première expérience de recherche dans un environnement particulièrement stimulant et bienveillant. Le sang froid de Dominique lui permet d'aborder avec recul et clarté tous les problèmes qui se posent, et le dynamisme et l'enthousiasme de Philippe, ainsi que sa culture multi-scientifique, sont un moteur exceptionnel de motivation. De leur complémentarité résulte une dynamique de travail que rien ne semble pouvoir arrêter. Je leur suis très reconnaissant de m'avoir permis cette expérience à leur côté et d'avoir toujours été disponibles en gardant leurs portes ouvertes.

Je remercie très sincèrement Céline Grandmont et Wolfgang Wall pour avoir pris le temps de rapporter sur cette thèse, ainsi qu'Emmanuel de Langre, Olivier Pironneau et Anne-Virginie Salsac pour avoir accepté de faire partie de mon jury.

Enfin, je tiens à remercier chacun des membres de l'équipe MΞDISIM, avec qui j'ai toujours été heureux de partager un café, un magnan ou quelques marches dans la montée de Lozère. Il règne dans l'équipe une ambiance particulièrement agréable, studieuse et teintée d'un très bon esprit de camaraderie. J'ai évidemment une pensée particulière pour Radek et Sébastien Gilles, avec qui j'aurai eu beaucoup de plaisir à travailler sur les modèles 0D et sur le code HappyHeart. Et pour Sébastien Imperiale, toujours disponible et enthousiaste pour échanger sur des sujets tout azimuts, dans les locaux, les RER ou sur un VTT. Merci bien sûr à Alexandre et Gauthier, à Aurora, Federica et Fabrice ainsi qu'à tous les membres de l'équipe, que j'ai été très heureux de rencontrer. Merci pour ces bons moments partagés.

Contents

Chapitre 1

Introduction

Cette thèse s'inscrit dans un vaste projet de modélisation du coeur humain, entrepris depuis une douzaine d'année par l'équipe MΞDISIM d'Inria Saclay. Elle a été co-dirigée par Dominique Chapelle et Philippe Moireau, MΞDISIM.

1.1 Contexte

1.1.1 Paysage général

L'objectif de cette thèse est le développement de méthodes numériques pour la poromécanique et l'application à la perfusion du myocarde. Elle est motivée par la prise en compte dans les modèles du couplage entre le flux coronarien et le comportement mécanique du myocarde au cours d'un cycle cardiaque. Elle se situe donc à l'interface entre plusieurs disciplines et communautés scientifiques : les mathématiques appliquées et la modélisation numérique, la mécanique, la biologie, la médecine et l'informatique. La médecine est un champ d'application de plus en plus courant des mathématiques appliquées, et de nombreux efforts ont été faits, notamment au niveau européen, pour encourager la recherche biomédicale, et mettre à la disposition des médecins de nouveaux outils numériques pour mieux comprendre, soigner ou anticiper le vivant. Le but est de leur fournir des outils de description et de simulation des phénomènes physiques très complexes qui interviennent en biologie. Ces modèles, qui favorisent une première compréhension, ont ensuite vocation à être couplés aux outils d'acquisition de données et d'imagerie médicale non invasifs (scanner, IRM, échographie 3D...) pour s'adapter au mieux à chaque patient, et permettre d'assister les médecins dans leurs diagnostics et leurs stratégies opératoires ou thérapeutiques.

Dans l'Union Européenne, les maladies cardio-vasculaires sont à l'origine de 40% des décès (Nichols et al., 2014) et représentent un coût économique estimé à 196 milliards d'euros par an. Leur compréhension constitue donc un réel enjeu social et économique à l'échelle mondiale, car cette problématique concerne autant les pays développés que ceux en voie de développement (Liu, 2007; Go et al., 2014).

C'est dans cette dynamique et ce contexte que s'inscrivent depuis plus d'une dizaine d'année les travaux de l'équipe MΞDISIM, qui ont pour double objectif de mettre au point des modèles numériques de coeurs humains, et de fournir des outils mathématiques permettant de les adapter au mieux aux spécificités de chaque patient par acquisition de données. Le couplage de ces deux volets de recherche permettrait par exemple à un cardiologue de simuler plusieurs traitements ou stratégies opératoires à comparer, sur une réplique numérique du coeur de son patient, afin de sélectionner celui qui fournirait à terme les meilleurs résultats.

Deux éléments sont donc nécessaires pour permettre le développement de tels instruments.

Dans un premiers temps, il est nécessaire d'être capable de décrire précisément la physique et la mécanique cardiaque dans toutes leurs complexités, de l'échelle cellulaire à l'échelle macroscopique. Cela fait intervenir de nombreuses disciplines, de l'électrophysiologie, l'électrochimie et la biologie, à la mécanique des fluides et des solides. Dans un second temps, il s'agit de paramétrer ces modèles pour les ajuster à chaque patient par assimilation de données. Cela fait appel à un autre champ de théorie mathématique.

Cette thèse s'inscrit dans le premier de ces deux volets, sur les aspects de description, mise en équation et modélisation d'un cycle cardiaque. Le but étant de décrire au mieux les différents phénomènes constitutifs d'un cycle cardiaque, il s'agit de transcrire en équations le plus finement possible les interactions entre les différentes grandeurs physiques et mécaniques (signaux électriques, flux et pressions sanguines, déformations du milieu musculaire).

1.1.2 Le coeur humain

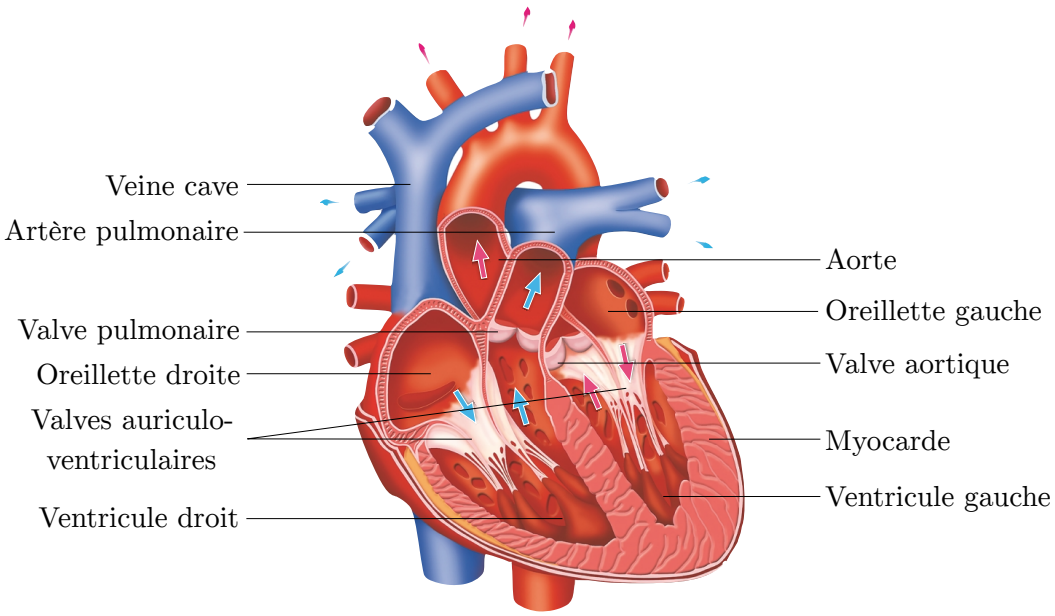

FIGURE 1.1 – **Le coeur humain.** Adapté de http ://www.howitworksdaily.com/inside-the-human-heart/.

Le fonctionnement des différents organes du corps humain (cerveau, muscles, reins, foie, etc) nécessite de l'oxygène et crée du dioxyde de carbone. Le sang achemine l'oxygène depuis les poumons vers les organes, et évacue le dioxyde de carbone depuis les organes vers les poumons. Le coeur joue le rôle central de « station de pompage », et permet ainsi la circulation sanguine au sein de l'organisme. Il assure cette fonction grâce à des cycles rythmés, de contraction et relaxation de quatre cavités cardiaques : deux oreillettes et deux ventricules. Ces cycles sont amorcés par la propagation d'une onde électrique qui active les tissus du muscle cardiaque (le myocarde), et permettent le maintien d'une circulation grâce à un jeu de valves, qui s'ouvrent ou se ferment en fonction des pressions sanguines des différents compartiments.

En fonction des phases de contraction et relaxation des différentes cavités, le cycle cardiaque peut se décomposer en quatre étapes. Celles-ci ont lieu à peu près simultanément dans les deux ventricules (droit et gauche).

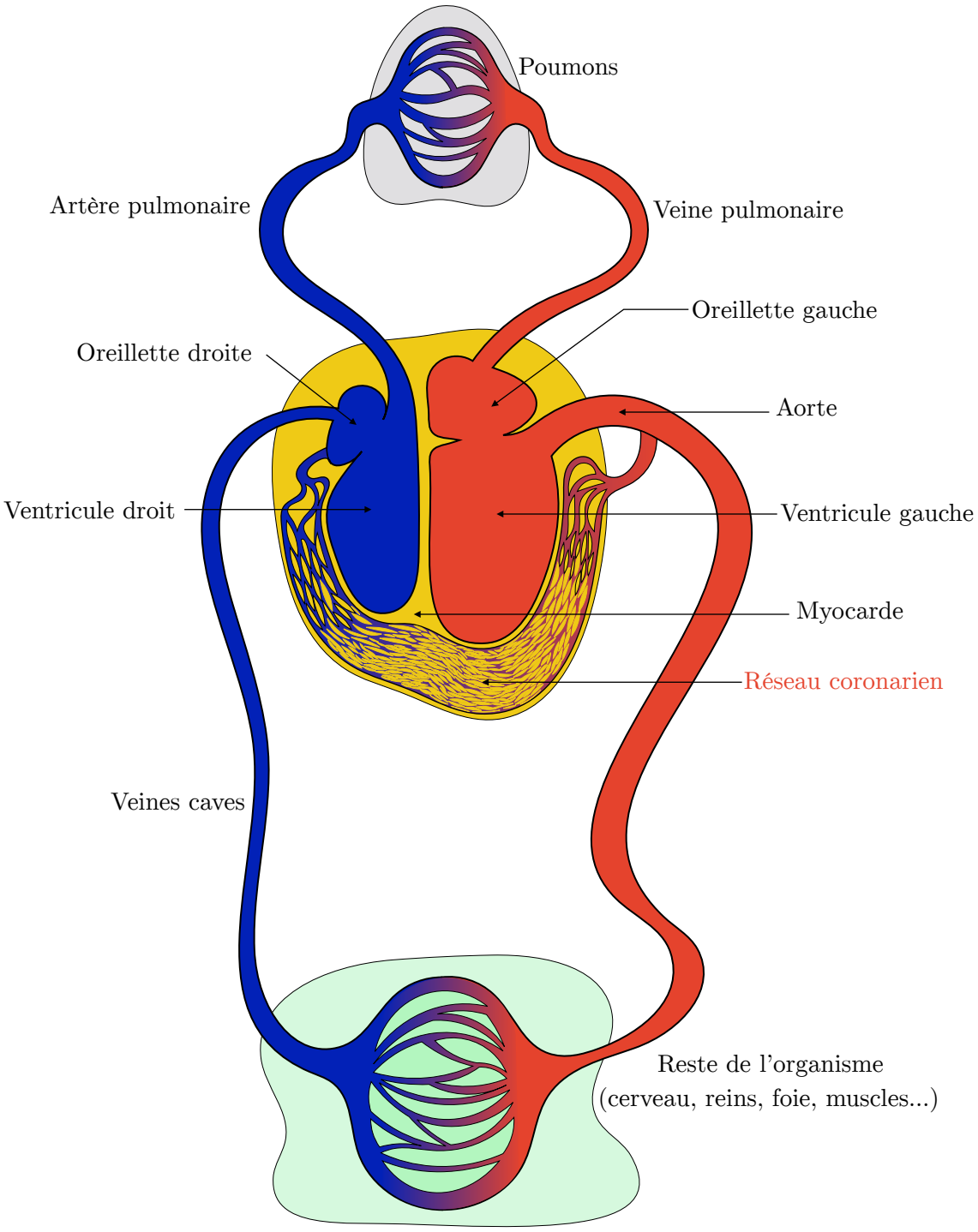

FIGURE 1.2 – **Le coeur et la circulation sanguine.**

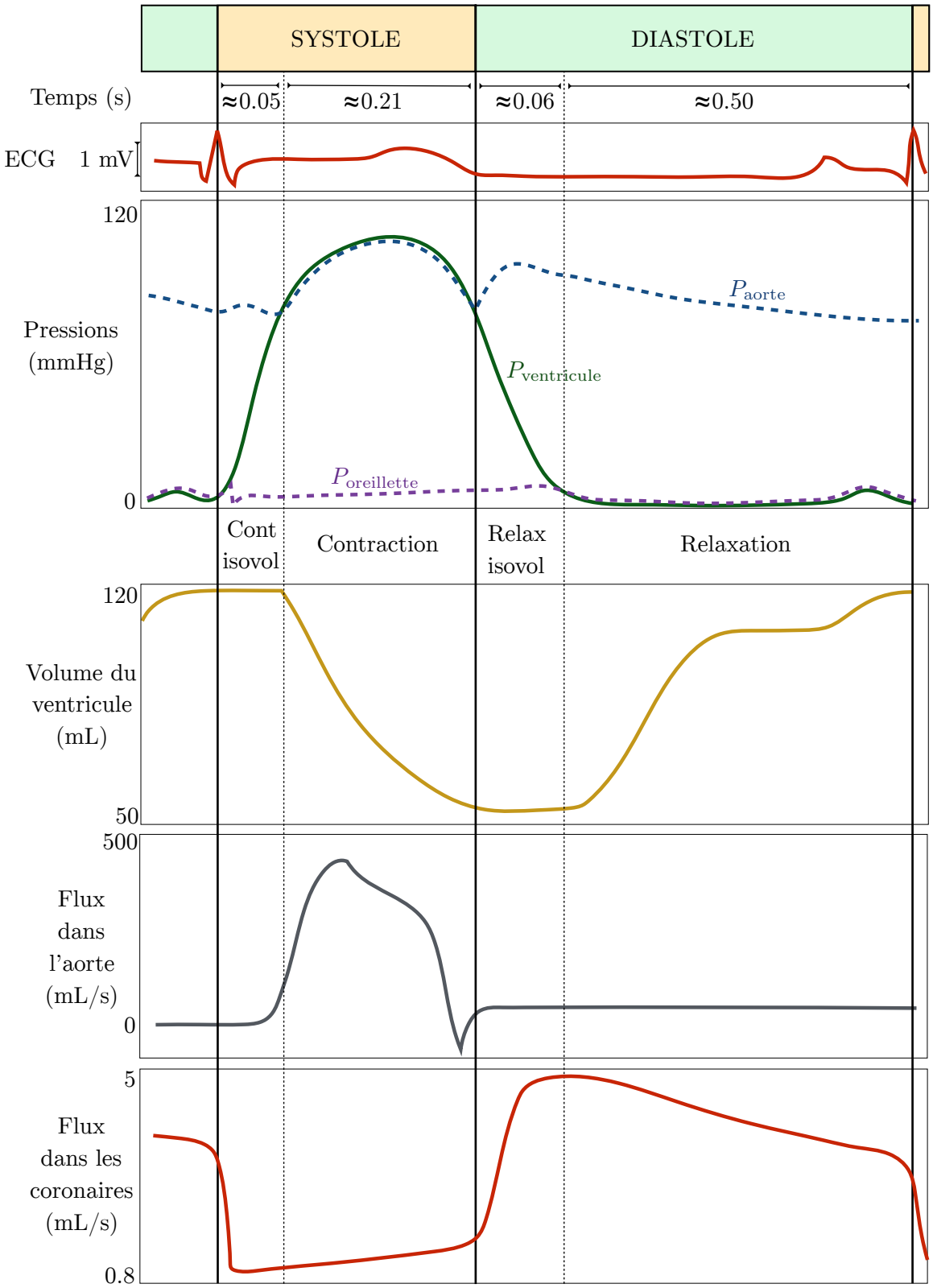

FIGURE 1.3 – **Profil type des principaux indicateurs au cours d'un cycle cardiaque (au repos) : ECG, pressions, volume de la cavité, flux dans l'aorte et dans le réseau coronarien.** Adapté de (Moireau, 2008).

- **La contraction isovolumique :** La systole commence lorsque le champ électrique atteint les tissus myocardiques du ventricule et provoque leur contraction. Le réseau coronarien qui assure la perfusion de ces tissus est alors en compression et son flux sanguin chute, c'est le « flow impediment » (voir le paragraphe 1.2.3). D'un autre coté, la pression ventriculaire augmentant, la valve auriculo-ventriculaire se ferme pour clore complètement le ventricule. La pression s'élève très rapidement jusqu'à atteindre celle de l'aorte (ou de l'artère pulmonaire), provoquant l'ouverture de la valve aortique (ou pulmonaire).

- **L'éjection :** Alors que la pression du ventricule continue de croître, le sang est éjecté dans le réseau artériel et le débit dans l'aorte atteint son maximum. Les tissus du myocarde restant en contraction, le flux sanguin dans le réseau coronarien reste bas. Ensuite, l'excitation du myocarde cesse, la pression ventriculaire retombe et la valve aortique se ferme.

- **La relaxation isovolumique :** Après le passage de l'onde électrique, c'est le début de la diastole. Les tissus du myocarde se relaxent et le flux de perfusion coronarien se rétablit. Les valves sont toutes fermées et l'oreillette est de nouveau chargée en sang. La pression ventriculaire retombe, jusqu'à atteindre celle de l'oreillette, et permettre l'ouverture de la valve auriculo-ventriculaire.

- **Le remplissage :** Dans un premier temps, le sang accumulé dans l'oreillette passe dans le ventricule dont le volume augmente sous l'effet de la relaxation du myocarde. 80% du ventricule est approvisionné en un quart de la durée de la diastole, c'est le remplissage passif. Ensuite, l'activation du noeud sinusal relance la propagation de l'onde électrique. Les tissus musculaires de l'oreillette sont les premiers touchés et leur contraction parachève le remplissage du ventricule.

1.2 La modélisation cardiaque

1.2.1 Historique

L'objectif de mettre au point un modèle numérique prenant en compte l'ensemble de ces phénomènes multi-physiques et reproduisant le comportement du coeur sur l'ensemble d'un cycle est très ambitieux. Les grandeurs physiques qui interviennent au cours d'un cycle cardiaque (déplacements, vitesses fluides et solides, champ électriques, pressions etc...) et les interactions qui les lient sont très nombreuses et complexes. La démarche de modélisation consiste à considérer dans un premier temps les plus importantes (les variables d'état du système), et à faire des hypothèses sur les interactions qui les lient, pour parvenir à un premier modèle numérique. Ensuite, l'enjeu est d'affiner ce modèle en y ajoutant de plus en plus d'éléments, pour prendre en compte davantage de variables d'état et d'interactions, et être de plus en plus fidèle à la réalité.

Parmi l'abondante littérature qui couvre ces sujets, on peut citer (Hunter, 1975) dès 1975 (mécanique du solide) et (Peskin, 1977; Peskin, 1982) en 1977 et 1982 pour décrire le flux sanguin et le rôle des valves au cours d'un cycle. Plus récemment, (Watanabe et al., 2004) couplent ce flux à un ventricule gauche hyper-élastique au sein d'un code élément finis en 3D. En 2001, (Nash and Hunter, 2001) et (Costa et al., 2001) modélisent les comportements actifs et passifs du ventricule. En 2006, un modèle 3D de myocarde hyperélastique électriquement activé est proposé dans (Sainte-Marie et al., 2006). Celui-ci est complété par (Chapelle et al., 2012) qui revisite les travaux de Huxley (prix Nobel de médecine en 1963) sur la contraction des muscles (Huxley, 1957) pour présenter une modélisation des tissus musculaires cardiaques, via une loi de comportement compatible avec une conservation de l'énergie aux niveaux continu et discret.

D'autres modèles complexes multiphysiques de cycles cardiaques 3D voient le jour (Kerckhoffs et al., 2005; Niederer and Smith, 2009). Cependant, la complexité de la résolution de formulations 3D rend difficile la calibration de modèles 3D, leur validation et leur exploitation dans le cadre d'applications cliniques. Cela motive la démarche de (Caruel et al., 2014) qui propose une stratégie de réduction dimensionnelle de modèle pour réduire les temps de calcul, typiquement la durée nécessaire pour obtenir la simulation d'un cycle cardiaque. L'idée est de simplifier la géométrie de l'organe, et de faire des hypothèses de symétrie de manière à réduire le nombre d'inconnues et la complexité des équations à résoudre. Bien sûr, cela dégrade la précision et la fidélité de la modélisation, mais cela permet en même temps une réduction drastique des coûts de calcul. Typiquement, les cavités cardiaques et leur couplage peuvent être traités en 0D en réduisant par exemple le déplacement à une inconnue scalaire en fonction du temps, et les structures en élongation telles que les échantillons musculaires peuvent être modélisés en 1D. Ce faisant, les temps de calcul passent typiquement de la journée à la minute, et ce genre de réduction peut servir par exemple à la calibration des modèles 3D plus complexes, en simulant plus rapidement davantage de cycles cardiaques à comparer aux données disponibles. Un autre objectif de leur développement est également de les utiliser pour faire du monitoring : suivi de patients dans le temps, avec assimilation régulière de données (pression en sortie de coeur, flux sanguins, ECG, déformation cardiaque obtenue par SCG...).

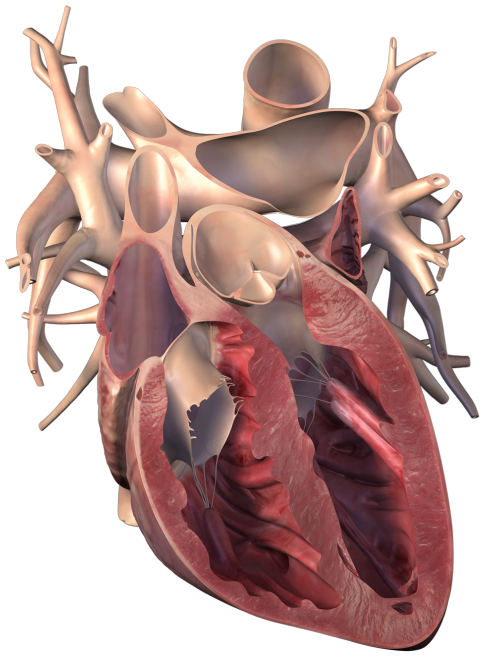

FIGURE 1.4 – **Le coeur humain, en coupe.** Tiré de 3D Science.

1.2.2 Les différents ingrédients de la modélisation cardiaque

Voici, de manière très synthétique, les différentes briques constituantes que l'on retrouve aujourd'hui dans un simulateur cardiaque (à l'échelle de l'organe) :

- **Le principe des travaux virtuels** régit la dynamique du déplacement solide $\underline{y}_s$. Elle fait intervenir le tenseur des contraintes dans le milieu solide $\underline{\underline{\Sigma}}$ comme une somme de deux contributions : une contribution passive $\underline{\underline{\Sigma}}_p$ (fonction de $\underline{y}_s$) et une contribution active $\underline{\underline{\Sigma}}_c$ modélisant la contraction des fibres musculaires.

- **Modélisation du tissu cardiaque passif.** Jusqu'à présent, le tissu cardiaque est modélisé comme un solide, cette équation fait donc localement le lien entre $\underline{\underline{\Sigma}}_p$ et les déformations $\underline{\underline{e}}(\underline{y}_s)$ engendrées par le champ de déplacement solide. Typiquement, une contribution de la loi de comportement dérive d'un potentiel hyperélastique anisotrope (prenant en compte l'organisation géométrique des fibres musculaires), l'autre transcrit les effets visqueux au sein du solide.

- **Les contraintes actives.** Un modèle de tissu musculaire relie les contraintes actives dans le ventricule $\underline{\underline{\Sigma}}_c$ au potentiel électrique V_m qui se propage dans le milieu.

- **L'électrophysiologie.** Ici on modélise la propagation, depuis le noeud sinusal, du potentiel électrique V_m dans les tissus cardiaques.

- **Les valves.** Elles séparent les différentes cavités cardiaques et les vaisseaux sortant du coeur. Leur modélisation permet de faire le lien entre la pression intra-ventriculaire P_v, la pression aortique P_{aorte} (ou pulmonaire P_{pul}) et la pression de l'oreillette P_{at}.

- **Modèles de circulation.** Le coeur en lui même est un système ouvert, il faut donc savoir quels sont les éléments (aorte, artère pulmonaire, réseau artériel et veineux) avec lesquels il interagit et échange des flux physiques (débits, pressions, etc), pour fermer le système. En effet, en plus du cycle de pompage effectué par le coeur, la propagation du sang dans l'organisme résulte des interactions entre le sang (représenté par son flux et sa pression) et la paroi des vaisseaux. Une modélisation de ces phénomènes permet par exemple d'évaluer la pression en sortie du coeur P_{aorte}. Plus généralement, les problèmes d'interactions fluide-structure dans les vaisseaux sanguins font l'objet de nombreux travaux qui prendront une importance particulière dans ce qui suit. Cependant, pour ce qui nous concerne, une modélisation exhaustive de la circulation sanguine dans l'organisme étant impossible, il s'agit en pratique de proposer des modèles simplifiés pour obtenir des liens entre les différentes pressions qui interviennent.

Comme mentionné précédemment, à ces éléments s'ajoutent les méthodes de réduction dimensionnelle de modèle. Une modélisation 3D de tous ces phénomènes et de leurs couplages étant très complexe et coûteuse, des hypothèses (simplification géométrique, invariances, symétries) permettent de réduire la dimension des problèmes sur certains aspects du modèle, voire sur le modèle complet (2D, 1D ou 0D). Par exemple, les modèles de circulations sont généralement développés en 1D, ou bien utilisent des modèles de Windkessel (dits 0D), s'appuyant sur une analogie entre circulation sanguine et réseaux électriques (l'intensité représente le flux et la tension la pression).

1.2.3 Une brique supplémentaire : la perfusion du myocarde

Dans cette logique, cette thèse est motivée par l'ajout d'une nouvelle brique : la prise en compte de la perfusion du myocarde par le réseau coronarien. Jusqu'à présent, on modélise le comportement mécanique du myocarde comme la somme de deux contributions. La contribution passive, en plus de rendre compte des effets visqueux, est modélisée comme dérivant d'un potentiel hyperélastique anisotrope (en fonction de la disposition géométrique des fibres). La contribution active repose sur des modèles de tissus cellulaires et rend compte de la contraction musculaire provoquée par la propagation de l'onde électrique.

Cependant, une fraction du sang qui s'engage dans l'aorte en sortie du coeur est directement redirigée vers le réseau coronarien (voir Figures 1.2 et 1.3) pour assurer l'oxygénation du myocarde, indispensable à son activité. La finesse de ce réseau et la multitude de ses ramifications et de ses vaisseaux garantissent l'irrigation du muscle cardiaque. Cette perfusion vient

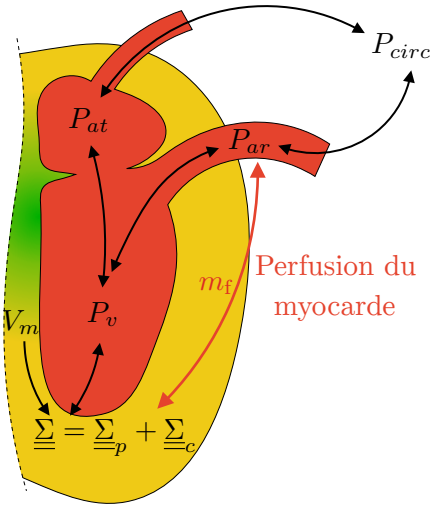

FIGURE 1.5 – **Une brique supplémentaire dans la modélisation cardiaque.** Le réseau coronarien qui part de l'aorte et irrigue le myocarde influence doublement son comportement mécanique : 1 - il assure l'oxygénation indispensable à la contraction musculaire, 2 - la fraction fluide perturbe le comportement de la matrice solide.

doublement influencer le comportement mécanique du myocarde. Premièrement, la fraction de fluide sanguin qui se mêle à la matrice solide modifie le comportement mécanique passif, et rend incomplète l'hypothèse d'un myocarde uniquement solide. Ensuite, le sang en question assure l'oxygénation des tissus, sans laquelle l'activité musculaire est impossible.

Cela nous conduit, dans la logique détaillée ci-dessus, à introduire une nouvelle variable d'état, la masse de sang par unité de volume localement au sein du myocarde m_f ; et à affiner les modèles existants en modélisant ces interactions (d'un côté avec la pression aortique, de l'autre, avec le tenseur des contraintes du myocarde) avec les variables d'état préexistantes.

Lors de la contraction du myocarde, le réseau de coronaires intimement lié aux fibres musculaires est mis en compression. Ce phénomène d'étranglement fait croître la pression dans les coronaires et chuter le flux de perfusion sanguine (voir Figure 1.3) : c'est le « flow impediment » (Westerhof et al., 2006). Propre à la circulation coronarienne, il témoigne de sa situation critique et de sa sensibilité par rapport à la qualité de l'écoulement, dont la dégradation engendre de nombreuses pathologies vasculaires et ischémies. La dynamique du flux sanguin est très complexe, (Davies et al., 2006) étudie par exemple le rôle de vagues d'aspiration remontant le flux sanguin lors du remplissage diastolique des coronaires.

L'intégration de la perfusion à la modélisation cardiaque permettra typiquement d'obtenir des informations sur le flux coronarien et de reproduire le « flow impediment », pour mieux comprendre l'origine des pathologies vasculaires, ce que les modèles existants ne sont pas encore en mesure de faire.

1.3 Du réseau coronarien à la poromécanique

1.3.1 Le réseau coronarien

Un double enjeu incite à affiner le modèle dans les tissus cardiaques en remplaçant les lois hyperélastiques par un modèle plus réaliste intégrant leur perfusion sanguine. C'est d'abord un enjeu physiologique : la prise en compte du flux sanguin qui irrigue et approvisionne en oxygène

le muscle cardiaque, au sein du réseau coronarien. Effectivement, cette oxygénation est capitale pour l'activité musculaire du myocarde, et des pathologies apparaissent dès que l'écoulement du sang est dégradé et que celle-ci est mise en défaut. Les maladies coronariennes sont à elles seules à l'origine de 20% des décès dans l'Union Européenne (Nichols et al., 2014). L'infarctus du myocarde est déclenché par l'obstruction d'une artère coronaire, ce qui lyse rapidement des cellules musculaires sur une zone plus ou moins étendue du myocarde par ischémie, en les privant d'oxygène. Les problèmes de contraction résultant menacent directement le cycle, et peuvent conduire à un arrêt cardiaque.

Ensuite, d'un point de vue théorique, le couplage d'un écoulement fluide rapide de type Navier-Stokes et d'une matrice solide hyperélastique anisotrope active en grandes déformations, au sein d'un même domaine représente un réel enjeu de modélisation.

1.3.2 Arbre coronarien et perfusion - les approches multi-échelles

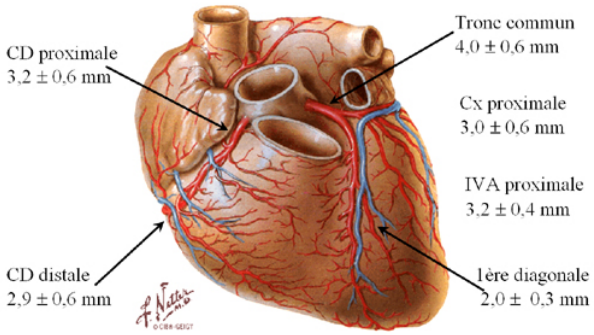

FIGURE 1.6 – **Le réseau coronarien tiré de Netter (1969).**

Lorsque l'on considère la perfusion du muscle cardiaque, la question se pose de comment modéliser le flux sanguin provenant de l'aorte et irriguant le myocarde via le réseau coronarien (Aharinejad et al., 1998). La modélisation précise des interactions entre le sang et les parois des vaisseaux qui permettent la propagation d'ondes de pressions sanguines, et les méthodes numériques associées, font l'objet de nombreux travaux (Figueroa et al., 2006; Fernández et al., 2007; Astorino et al., 2009a; Xiong et al., 2011) (voir le paragraphe1.5). Dans (Formaggia et al., 2003), les auteurs étudient la propagation de ces ondes grâce à des modèles 1D d'artères, avec notamment l'enjeu de la modélisation des bifurcations. Dans cette lignée, on pourrait vouloir modéliser l'arbre coronarien dans son ensemble, mais sa complexité, la multitude de ses ramifications et sa finesse en bout de chaîne rendent irréaliste un tel objectif. Dans (Mynard and Nithiarasu, 2008), un écoulement coronarien simplifié est intégré à un modèle 1D d'écoulement artériel non linéaire avec pression ventriculaire et valve aortique. Plus tard, (Lee and Smith, 2012) propose une approche multi-échelle, avec un même algorithme qui combine, en fonction du niveau de raffinement du réseau coronarien, des modèles 3D (vaisseaux épicardiques, les plus gros), 1D puis enfin, en bout de chaîne, poroélastiques (matrice solide et écoulement fluide sur le même domaine). De nombreux travaux s'orientent vers ce genre de compromis entre affinement et complexité de la modélisation. Cela motive les travaux qui suivent, qui proposent des méthodes numériques permettant de décrire le comportement d'un milieu poreux où cohabitent un écoulement de type Navier-Stokes incompressible et un solide représenté par un potentiel d'énergie libre hyperélastique généralisé (permettant d'inclure la partie active), en grandes déformations.

Les approches multi-échelles mentionnées posent la question des conditions de transmissions entre les différents modèles, par exemple pour des raccords 3D-1D (Formaggia et al., 2001).

Des travaux établissent des modèles 0D (de type Windkessel pression/flux sanguins, où capacitance et résistance sont à calibrer par expérimentations) à brancher sur du 3D (Quarteroni and Veneziani, 2003; Vignon-Clementel et al., 2006) ou 1D (Fernández et al., 2005), pour traiter les conditions de sorties du réseau coronarien (en bout de chaîne, là où interviendrait la poromécanique). Dans cette idée, des modèles réduits d'écoulement pourraient être branchés en entrée d'un modèle de poromécanique, pour représenter l'apport massique fluide au sein du milieu poreux. Ces termes sources pourraient être répartis en surface du domaine, ou intervenir à l'intérieur du volume (voir θ dans ce qui suit), de manière homogène ou localisée.

Les problématiques liées aux approches multi-échelles pour coupler des réseaux complexes d'écoulement à des modèles de poromécaniques sont partagées par ceux qui modélisent au sein des poumons la circulation des gaz, qui contrairement au sang sont compressibles et non visqueux (Sapoval et al., 2002; Berger, 2015; Berger et al., 2015; Baffico et al., 2010). Motivé par le même objectif, une approche mathématique et numéricienne de la propagation d'ondes dans des arbres fractals est proposée (Joly and Semin, 2011; Deheuvels, 2013).

1.3.3 La poromécanique

Discipline très active depuis quelques dizaines d'années (voir (De Boer, 2006)), elle nous vient historiquement du génie civil (Biot, 1941; Biot, 1962; Bryant et al., 1975) et des géophysiciens, avec la nécessité de comprendre comment le pétrole, le gaz ou l'eau interagissent avec la roche dans les sols. Des théories s'appuient sur les principes fondamentaux de la physique et la thermodynamique (Bowen, 1980; Coussy, 2004; Coussy, 2011; Loret and Simões, 2005; Borja, 2006) pour formaliser une approche macroscopique appelée théorie des mixtures, dans laquelle en tout point du milieu poreux, supposé saturé, coexistent deux phases fluide et solide (en proportions volumiques respectives ϕ et $1-\phi$).

Cependant, les outils développés dans un tel cadre satisfont à un cahier des charges très différent du nôtre, et font des hypothèses (petites déformations, écoulements lents...) qui les rendent non transposables au contexte cardiaque. En effet, le muscle cardiaque se déforme de 10% à 20% au cours d'un cycle, alors que le sang se déplace à des vitesses de pointe de 10 à 20 cm/s.

Un modèle de poromécanique est proposé (Chapelle et al., 2009), adapté à la description de la perfusion du myocarde, et pouvant prendre en compte des lois de comportements générales compatibles avec la modélisation de tissus vivants (Fung, 2013; Ogden and Holzapfel, 2006). L'incompressibilité des constituants fluide et solide est considérée, mais l'inertie fluide est négligée. Cette hypothèse est trop réductrice, notamment car les artères coronaires sont le lieu de grandes accélérations du sang : les vitesses mentionnées ci-dessus (qui sont les mêmes pour le solide) sont atteintes alternativement et à différents instants pour les deux constituants (Johnson et al., 2008). En négligeant ainsi les échanges d'énergies cinétiques, il serait impossible, tant au niveau continu qu'au niveau discret, de récupérer le bilan énergétique physique qui pourtant joue un rôle primordial pour garantir la stabilité (voir le paragraphe 1.5) puis la convergence.

D'autres approches, double échelle, prennent en compte l'organisation détaillée du milieu poreux au niveau microscopique et relient celle-ci au comportement macroscopique, par homogénéisation (Hornung, 2012; Cimrman and Rohan, 2010; Brown et al., 2014).

Les travaux qui suivent s'appuient sur (Chapelle and Moireau, 2014), plus adapté au développement d'outils numériques de modélisation, et qui, destiné à la modélisation cardiaque, présente l'avantage de faire un minimum d'hypothèses sur l'écoulement et la matrice solide. En effet, (Chapelle and Moireau, 2014) utilise la théorie des mixtures et repart des principes thermodynamiques pour coupler un écoulement poreux rapide à un solide hyperélastique dans un cadre général et en grandes déformations. De plus, sont établis un bilan d'énergie au niveau continu, et un

premier schéma en temps, monolithique et conservatif, qui, bien que difficile à implémenter, donne des premiers éléments d'analyse numérique.

1.4 La formulation de poromécanique

1.4.1 Formulation forte de poromécanique

Dans l'optique notamment de modéliser la perfusion, (Chapelle and Moireau, 2014) reprend les principes fondamentaux de la thermodynamique (conservations de la masse et des moments, premier et second principes de la thermodynamique) pour établir un modèle général de poromécanique compatible avec ceux-ci. Ce modèle couple un écoulement poreux et un solide hyperélastique et reste valide en grands déplacements et grandes déformations, avec une forte inertie fluide. C'est un modèle de type mixture, dans lequel une phase solide et une phase liquide (de fraction volumique notée ϕ) coexistent et interagissent en tout point. La phase solide, en formalisme lagrangien, est représentée en tout point $\underline{\xi}$ du domaine de référence Ω^0 (fixe) par son déplacement $\underline{y}_{\mathrm{s}}(\underline{\xi}, t)$. Celui-ci envoie le domaine de référence Ω^0 sur le domaine déformé Ω_t, sur lequel est décrite la phase fluide en formalisme eulérien :

$$\underline{\xi} \in \Omega^0 \mapsto \underline{\mathrm{x}} = \underline{\varphi}(\underline{\xi}, t) = \underline{\xi} + \underline{y}_{\mathrm{s}}(\underline{\xi}, t) \in \Omega_t.$$

Le tenseur de déformation est noté

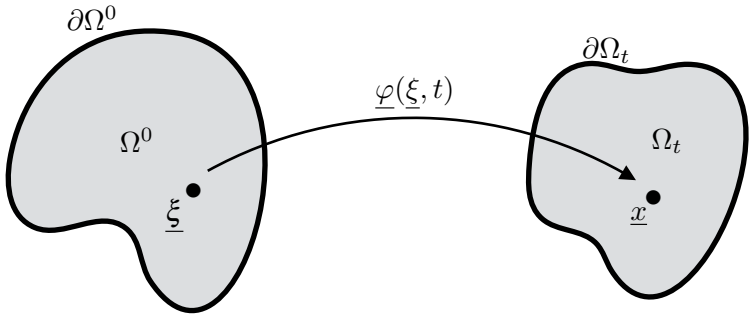

FIGURE 1.7 – **Carte de déformations du domaine.**

$$\underline{\underline{F}} = \underline{\underline{\mathbb{1}}} + \underline{\underline{\nabla}}_{\underline{\xi}} \underline{y}_{\mathrm{s}},$$

le tenseur des déformations de Cauchy-Green et le tenseur des déformations de Green-Lagrange prennent respectivement les formes suivantes,

$$\underline{\underline{C}} = \underline{\underline{F}}^T \cdot \underline{\underline{F}} \quad \text{et} \quad \underline{\underline{e}} = \tfrac{1}{2}(\underline{\underline{C}} - \underline{\underline{\mathbb{1}}});$$

et le changement de volume de la mixture globale est localement donné par le jacobien $J = \det \underline{\underline{F}}$. Notons ϕ_0 la fraction volumique fluide dans la configuration non déformée, et définissons $J_{\mathrm{s}} = J(1-\phi)$, alors le changement de volume du constituant solide est localement donné par $J_{\mathrm{s}}/(1-\phi_0)$.

L'écoulement fluide est décrit en tout point de Ω_t par sa vitesse $\underline{v}_{\mathrm{f}}$ et sa pression p. Nous supposons l'incompressibilité du fluide, de sorte que la masse de fluide par unité de volume ρ_{f} est constante. Afin de décrire les apports de masse fluide au sein de la matrice, nous introduisons enfin m, définie comme la quantité de masse ajoutée de fluide par unité de volume dans la configuration de référence :

$$m = \rho_{\mathrm{f}}(J\phi - \phi_0).$$

ρ_{s0} représente la masse de la phase solide par unité de volume dans la configuration de référence.

Pour représenter les contraintes de la mixture globale, le second tenseur des contraintes de Piola-Kirchhoff (en configuration initiale) est donné en fonction du tenseur des contraintes de Cauchy $\underline{\underline{\sigma}}$ par la relation suivante

$$\underline{\underline{\Sigma}} = J\underline{\underline{F}}^{-1} \cdot \underline{\underline{\sigma}} \cdot \underline{\underline{F}}^{-T}.$$

Sa contribution solide $\underline{\underline{\Sigma}}_s$ est donnée par

$$\underline{\underline{\Sigma}}_s = \underline{\underline{\Sigma}} - \phi J\underline{\underline{F}}^{-1} \cdot \underline{\sigma}_f \cdot \underline{\underline{F}}^{-T} = \underline{\underline{\Sigma}} - \phi\underline{\underline{\Sigma}}_{vis} + \phi pJ\underline{\underline{C}}^{-1}, \tag{1.1}$$

où $\underline{\underline{\Sigma}}_{vis} = J\underline{\underline{F}}^{-1} \cdot \underline{\underline{\sigma}}_{vis} \cdot \underline{\underline{F}}^{-T}$ représente la contribution visqueuse des contraintes du fluide supposé Newtonien, et $-pJ\underline{\underline{C}}^{-1}$ leur contribution hydrostatique. Les éventuelles hypothèses portant sur les lois de comportement et les énergies dont elles dérivent seront détaillées ultérieurement.

Nous introduisons $\underline{\underline{k}}_f$ un tenseur de perméabilité régissant les forces de friction entre les phases fluides et solides au sein de la mixture, $\underline{f}$ la force volumique distribuée sur l'ensemble, et θ le terme source de masse fluide par unité de volume et de temps dans la configuration déformée.

Pour alléger et faciliter la lecture des équations, nous userons dans tout ce document d'un abus de notation consistant à sous-entendre l'éventuelle composition par la carte de déformation du domaine $\underline{\varphi}$ ou son inverse, et à utiliser ainsi les mêmes notations pour un champ de vecteur défini sur Ω^0 et Ω_t.

La formulation forte de poromécanique de (Chapelle and Moireau, 2014) prend alors la forme suivante :

$$\begin{cases} \rho_{s0}(1-\phi_0)\partial_t \underline{v}_s - \underline{\nabla}_{\underline{\xi}} \cdot (\underline{\underline{F}} \cdot \underline{\underline{\Sigma}}_s) + pJ\underline{\underline{F}}^{-T} \cdot \underline{\nabla}_{\underline{\xi}}\phi \\ \qquad\qquad - J\phi^2 \underline{\underline{k}}_f^{-1} \cdot (\underline{v}_f - \underline{v}_s) = \rho_{s0}(1-\phi_0)\underline{f}, & \text{in } \Omega^0, \quad (1.2a) \\ \frac{1}{J}\partial_t(\rho_f J\phi\, \underline{v}_f) + \underline{\nabla}_{\underline{x}} \cdot \big(\rho_f \phi\, \underline{v}_f \otimes \rho_f(\underline{v}_f - \underline{v}_s)\big) - \theta \underline{v}_f \\ \qquad + \phi^2 \underline{\underline{k}}_f^{-1} \cdot (\underline{v}_f - \underline{v}_s) - \underline{\nabla}_{\underline{x}} \cdot (\phi\, \underline{\underline{\sigma}}_{vis}) + \phi \underline{\nabla}_{\underline{x}} p = \rho_f \phi\, \underline{f}, & \text{in } \Omega_t, \quad (1.2b) \\ \qquad \frac{1}{J}\partial_t(J\rho_f\phi) + \underline{\nabla}_{\underline{x}} \cdot \big(\rho_f \phi(\underline{v}_f - \underline{v}_s)\big) = \theta, & \text{in } \Omega_t. \quad (1.2c) \end{cases}$$

La première équation régit la dynamique de la déformation solide, la seconde l'écoulement fluide, et la dernière la conservation de la masse fluide. Le couplage entre les constituants se fait via le terme de friction volumique $\underline{\underline{k}}_f$, ainsi que sur certaines portions du bord $\partial\Omega$. En effet, pour compléter ce système, considérons les conditions au bord suivantes. Avec $\underline{t}$ la traction totale sur le bord du domaine Ω_t, et $\underline{t}_0 = J\|\underline{\underline{F}}^{-T} \cdot \underline{n}_0\|\underline{t}$ sa contrepartie sur le domaine de référence Ω^0, (voir (Chapelle and Moireau, 2014)) :

- Des conditions de Dirichlet pour chacune des phases, c'est à dire un déplacement prescrit pour le squelette et une vitesse fluide imposée

  $$\underline{y}_s = \underline{y}_s^{pr}, \quad \underline{v}_f = \underline{v}_f^{pr},$$

  sur une partie de la frontière notée Γ_D^0 dans la configuration de référence et Γ_D^t en configuration courante ;

- Des conditions de Neumann pour chacune des deux phases, avec répartition proportionelle de la traction au bord

  $$\underline{\underline{\sigma}} \cdot \underline{n} = \underline{t} \Leftrightarrow \underline{\underline{F}} \cdot \underline{\underline{\Sigma}} \cdot \underline{n}_0 = \underline{t}_0, \quad \underline{\underline{\sigma}}_f \cdot \underline{n} = \underline{t},$$

  sur Γ_N^0 (ou Γ_N^t) ;

- Des conditions de Neumann pour la mixture globale, avec un flux fluide nul et une répartition proportionnelle de l'effort surfacique tangentiel

$$\underline{\underline{\sigma}} \cdot \underline{n} = \underline{t} \Leftrightarrow \underline{\underline{F}} \cdot \underline{\underline{\Sigma}} \cdot \underline{n}_0 = \underline{t}_0, \quad \pi_\tau(\underline{\underline{\sigma}}_{\mathrm{f}} \cdot \underline{n}) = \pi_\tau(\underline{t}), \quad (\underline{v}_{\mathrm{f}} - \underline{v}_{\mathrm{s}}) \cdot \underline{n} = 0,$$

  sur $\Gamma^0_{N\mathrm{nof}}$ (ou $\Gamma^t_{N\mathrm{nof}}$), où $\pi_\tau = \underline{\underline{\mathbb{1}}} - \underline{n} \otimes \underline{n}$ est la projection sur le plan tangent ;

- Des conditions de Neumann pour la mixture dans son ensemble, avec une égalité des vitesses fluide et solide, sans glissement,

$$\underline{\underline{\sigma}} \cdot \underline{n} = \underline{t} \Leftrightarrow \underline{\underline{F}} \cdot \underline{\underline{\Sigma}} \cdot \underline{n}_0 = \underline{t}_0, \quad \underline{v}_{\mathrm{f}} = \underline{v}_{\mathrm{s}},$$

  sur $\Gamma^0_{N\mathrm{nos}}$ (ou $\Gamma^t_{N\mathrm{nos}}$).

Notons que le même type de modèle poromécanique a été récemment pris en compte dans (Vuong et al., 2015).

1.4.2 Parallèle avec l'interaction fluide-structure

Cette formulation présente de nombreuses similitudes avec le problème d'interaction fluide-structure (IFS) traité dans (Fernández et al., 2007; Astorino et al., 2009a) et motivé par exemple par la modélisation de l'aorte. Cette proximité a guidé grand nombre des développements présentés dans ce document. Notons que les principaux éléments différentiateurs sont les suivants :

- Dans le problème d'interaction fluide-structure, la résolution du problème fluide sur un domaine qui évolue en fonction des mouvements de la structure requiert un formalisme « Arbitrary Lagrangian Eulerian » (ALE). Dans notre cas, les deux constituants sont sur le même domaine dont le mouvement est simplement décrit par le déplacement solide $\underline{y}_{\mathrm{s}}$. En pratique, la vitesse ALE du problème IFS est remplacé par $\underline{v}_{\mathrm{s}}$.

- La description locale de la mixture nécessite l'introduction de $\phi(t)$ la fraction volumique de fluide, $(1 - \phi_0)$ est alors la fraction de solide.

- En plus d'interagir au niveau de la frontière $\Gamma_{N\mathrm{nos}}$ en échangeant comme en IFS vitesse et effort, les deux constituants frictionnent désormais sur l'ensemble du domaine via le terme dissipatif $\phi^2 \underline{\underline{k}}_{\mathrm{f}}^{-1} \cdot (\underline{v}_{\mathrm{f}} - \underline{v}_{\mathrm{s}})$.

- Le terme de pression hydrostatique $\underline{\nabla}_{\mathrm{x}}(\phi p)$ est séparé en deux contributions $\phi \underline{\nabla}_{\mathrm{x}} p$ et $p \underline{\nabla}_{\mathrm{x}} \phi$; la première s'intègre à l'équation solide, alors que la seconde intervient côté fluide.

- La relation d'incompressibilité du fluide en IFS est remplacé par (1.2c), dont le format en formulation faible rappelle également largement la loi de conservation géométrique qu'il faut supposer lors de la discrétisation temporelle avec ALE en IFS. On note au passage le nouveau terme source θ comme apport de masse fluide au sein du volume.

Au delà de ces éléments, la proximité entre notre problème de poromécanique et celui d'IFS rend légitime notre approche, qui consiste à s'inspirer des développements autour des méthodes de discrétisation en IFS et à les étendre à notre cadre.

1.4.3 Formulation faible en poromécanique

Pour un champ de vitesse $\underline{w}_D^0$ dans $V^0 = H^1(\Omega^0)^3$, on définit l'espace de fonction

$$V^0(\underline{w}_D^0) = \{\underline{v}^* \in V^0 \;\Big|\; \underline{v}^*|_{\Gamma_D^0} = \underline{w}_D^0\}.$$

En supposant suffisamment de régularité pour le déplacement $\underline{y}_\mathrm{s}$ qui envoie le domaine de référence Ω^0 sur la configuration déformée Ω_t, on définit

$$Q^t = L^2(\Omega_t),$$

et, pour $(\underline{w}_D, \underline{w})$ dans $(V^t)^2 = (H^1(\Omega^t)^3)^2$,

$$\begin{aligned} V^t(\underline{w}_D) &= \{\underline{v}^* \in V^t \;\Big|\; \underline{v}^*|_{\Gamma_D^t} = \underline{w}_D\}, \\ V^t(\underline{w}_D, \underline{w}) &= \{\underline{v}^* \in V^t \;\Big|\; \underline{v}^*|_{\Gamma_D^t} = \underline{w}_D,\ \underline{v}^*|_{\Gamma_{N\mathrm{nos}}^t} = \underline{w}|_{\Gamma_{N\mathrm{nos}}^t},\ (\underline{v}^* - \underline{w}) \cdot \underline{n} = 0 \text{ on } \Gamma_{N\mathrm{nof}}^t\}. \end{aligned}$$

Après multiplication de (1.2) par des fonctions test et intégration en espace, on recherche $(\underline{v}_\mathrm{f}, \underline{v}_\mathrm{s}, \underline{y}_\mathrm{s}, m)$ dans $V^t(\underline{v}_\mathrm{f}^{\mathrm{pr}}, \underline{v}_\mathrm{s}) \times V(\underline{\dot{y}}_\mathrm{s}^{\mathrm{pr}}) \times V(\underline{y}_\mathrm{s}^{\mathrm{pr}}) \times Q^t$ tel que pour tout $(\underline{v}_\mathrm{f}^*, \underline{v}_\mathrm{s}^*, q^*)$ dans $V^t(0,0) \times V(0) \times Q^t$, (61) dans (Chapelle and Moireau, 2014), $\underline{v}_\mathrm{s} = \partial_t \underline{y}_\mathrm{s}$ et

$$\left\{ \begin{aligned} &\int_{\Omega^0} \rho_{\mathrm{s}0}(1-\phi_0) \frac{\mathrm{d}\underline{v}_\mathrm{s}}{\mathrm{dt}} \cdot \underline{v}_\mathrm{s}^* \, d\Omega + \int_{\Omega^0} \underline{\underline{\Sigma}}_s : d_{\underline{y}}\underline{\underline{e}} \cdot \underline{v}_\mathrm{s}^* \, d\Omega - \int_{\Omega_t} (\underline{v}_\mathrm{f} - \underline{v}_\mathrm{s}) \cdot \phi^2 \underline{\underline{k}}_\mathrm{f}^{-1} \cdot \underline{v}_\mathrm{s}^* \, d\Omega \\ &\qquad + \int_{\Omega_t} p \underline{\nabla}_{\underline{\mathrm{x}}} \phi \cdot \underline{v}_\mathrm{s}^* \, d\Omega = \int_{\Omega^0} \rho_{s0}(1-\phi_0) \underline{f} \cdot \underline{v}_\mathrm{s}^* \, d\Omega + \int_{\Gamma_N^0} (1-\phi) \underline{t}_0 \cdot \underline{v}_\mathrm{s}^* \, dS \\ &\qquad + \int_{\Gamma_{N\mathrm{nof}}^0 \bigcup \Gamma_{N\mathrm{nos}}^0} \underline{t}_0 \cdot \underline{v}_\mathrm{s}^* \, dS - \int_{\Gamma_{N\mathrm{nof}}^t} \phi(\pi_\tau \underline{t}) \cdot \underline{v}_\mathrm{s}^* \, dS - \mathcal{R}_\mathrm{f}^c(\underline{v}_\mathrm{s}^*) \quad (1.3a) \\ &\mathcal{P}_i^\mathrm{f}(\underline{v}_\mathrm{f}^*) + \int_{\Omega_t} (\underline{v}_\mathrm{f} - \underline{v}_\mathrm{s}) \cdot \phi^2 \underline{\underline{k}}_\mathrm{f}^{-1} \cdot \underline{v}_\mathrm{f}^* \, d\Omega + \int_{\Omega_t} \Big(-\frac{p}{\rho_\mathrm{f}} \underline{\nabla}_{\underline{\mathrm{x}}} \cdot (\rho_\mathrm{f} \phi \underline{v}_\mathrm{f}^*) + \phi \, \underline{\underline{\sigma}}_{\mathrm{vis}} : \underline{\underline{\varepsilon}}(\underline{v}_\mathrm{f}^*) \Big) \, d\Omega \\ &\qquad = \int_{\Omega_t} \rho_\mathrm{f} \phi \, \underline{f} \cdot \underline{v}_\mathrm{f}^* \, d\Omega + \int_{\Gamma_N^t \bigcup \Gamma_{N\mathrm{nof}}^t} \phi \, \underline{t} \cdot \underline{v}_\mathrm{f}^* \, dS \quad (1.3b) \\ &\int_{\Omega^0} \frac{\mathrm{d}m}{\mathrm{dt}} q^* \, d\Omega + \int_{\Omega_t} \underline{\nabla}_{\underline{\mathrm{x}}} \cdot (\rho_\mathrm{f} \phi \, (\underline{v}_\mathrm{f} - \underline{v}_\mathrm{s})) \, q^* \, d\Omega = \int_{\Omega_t} \theta q^* \, d\Omega \quad (1.3c) \end{aligned} \right.$$

avec la puissance virtuelle de l'inertie fluide

$$\mathcal{P}_i^\mathrm{f}(\underline{v}^*) = \int_{\Omega^0} \frac{\mathrm{d}}{\mathrm{dt}} \big(J \rho_\mathrm{f} \phi \, \underline{v}_\mathrm{f} \big) \cdot \underline{v}^* \, d\Omega + \int_{\Omega_t} \underline{\nabla}_{\underline{\mathrm{x}}} \cdot (\rho_\mathrm{f} \phi \underline{v}_\mathrm{f} \otimes (\underline{v}_\mathrm{f} - \underline{v}_\mathrm{s})) \cdot \underline{v}^* \, d\Omega - \int_{\Omega_t} \theta \underline{v}_\mathrm{f} \cdot \underline{v}^* \, d\Omega,$$

et le résidu continu, représentant la contribution des efforts sur $\Gamma_{N\mathrm{nos}}$ et des efforts de pression sur $\Gamma_{N\mathrm{nof}}$ que le fluide supporte,

$$\begin{aligned} \mathcal{R}_\mathrm{f}^c(\underline{v}_\mathrm{s}^*) = \mathcal{P}_i^\mathrm{f}(\underline{v}_\mathrm{s}^*) &+ \int_{\Omega_t} (\underline{v}_\mathrm{f} - \underline{v}_\mathrm{s}) \cdot \phi^2 \underline{\underline{k}}_\mathrm{f}^{-1} \cdot \underline{v}_\mathrm{s}^* \, d\Omega + \int_{\Omega_t} \Big(-\frac{p}{\rho_\mathrm{f}} \underline{\nabla}_{\underline{\mathrm{x}}} \cdot (\rho_\mathrm{f} \phi \underline{v}_\mathrm{s}^*) + \phi \, \underline{\underline{\sigma}}_{\mathrm{vis}} : \underline{\underline{\varepsilon}}(\underline{v}_\mathrm{s}^*) \Big) \, d\Omega \\ &- \int_{\Omega_t} \rho_\mathrm{f} \phi \, \underline{f} \cdot \underline{v}_\mathrm{s}^* \, d\Omega - \int_{\Gamma_N^t} \phi \, \underline{t} \cdot \underline{v}_\mathrm{s}^* \, dS - \int_{\Gamma_{N\mathrm{nof}}^t} \phi(\pi_\tau \underline{t}) \cdot \underline{v}_\mathrm{s}^* \, dS. \quad (1.4) \end{aligned}$$

Notons que la substitution de (1.4) dans la conservation des moments pour le constituant solide (1.3a) permet d'écrire la conservation des moments pour la mixture globale, (63) dans (Chapelle and Moireau, 2014)

$$\begin{cases} \displaystyle\int_{\Omega^0} \rho_{\mathrm{s}0}(1-\phi_0)\frac{\mathrm{d}\underline{v}_{\mathrm{s}}}{\mathrm{dt}} \cdot \underline{v}_{\mathrm{s}}^* \, d\Omega + \mathcal{P}_i^{\mathrm{f}}(\underline{v}_{\mathrm{s}}^*) + \int_{\Omega^0} \underline{\underline{\Sigma}} : d_{\underline{y}}\underline{\underline{e}} \cdot \underline{v}_{\mathrm{s}}^* \, d\Omega \\ \qquad\qquad = \displaystyle\int_{\Omega^0} (\rho_0 + m)\underline{f} \cdot \underline{v}_{\mathrm{s}}^* \, d\Omega + \int_{\Gamma_N^0 \bigcup \Gamma_{N\mathrm{nof}}^0 \bigcup \Gamma_{N\mathrm{nos}}^0} \underline{t}_0 \cdot \underline{v}_{\mathrm{s}}^* \, dS \quad (1.5a) \\ (1.3b) \\ (1.3c) \end{cases}$$

1.5 Analyse et méthodes numériques

Comme nous venons de le voir au paragraphe 1.4.2, d'importantes similitudes existent entre notre formulation de poromécanique et celles rencontrées en interaction fluide-structure (IFS) lors de la modélisation d'écoulement et de propagation d'ondes dans des vaisseaux sanguins. Ainsi, donnons quelques éléments pour situer les efforts qui ont été faits pour développer des méthodes numériques de modélisation d'IFS, notamment autour du coeur humain. Le sujet se présente généralement comme le couplage d'un écoulement Navier-Stokes avec une structure élastique. Citons par exemple les travaux concernant la modélisation de l'aorte (Moireau et al., 2012), ou des valves aortiques régulant le flux sanguin en sortie du coeur (Astorino et al., 2009b).

Les méthodes énergétiques. Soulignons l'importance particulière que nous accordons aux propriétés de conservation d'énergie discrète (ou stabilité énergétique). Le principe consiste à exhiber une grandeur discrète contrôlant la solution numérique et faisant office d'énergie discrète (généralement inspirée de l'énergie continue au sens de la physique), puis à s'assurer qu'elle satisfasse un équivalent discret du bilan d'énergie. Il est établi que ce genre de propriété garantit au moins la stabilité des solutions numériques, et la convergence dans un cadre linéaire (Dautray and Lions, 1988; Le Tallec and Hauret, 2002; Le Tallec et al., 2005). Dans ce qui suit, les analyses théoriques et numériques de nos schémas seront en grande partie guidées par la recherche et l'exploitation de majorations énergétiques discrètes. Cette propriété est d'autant plus intéressante que la dissipation numérique est faible. Cela justifie l'intérêt que l'on portera à la méthode proposée par (Gonzalez, 2000; Le Tallec and Hauret, 2002) qui permet de conserver exactement l'énergie discrète en élasticité non linéaire.

1.5.1 Discrétisation en temps

Méthodes monolithiques ou partitionnées - couplage fort ou faible. Il s'agit de résoudre simultanément un problème de fluide visqueux et incompressible et un problème d'élasticité, qui interagissent au niveau d'une interface surfacique. Avant toute chose, remarquons l'utilisation récurrente de formulations de type « Arbitrary Lagrangian Eulerian » (ALE) (Bathe and Rugonyi, 2001; Heil, 2004), pour déplacer le domaine fluide en accord avec les mouvements de la structure. Pour imposer le couplage, la plupart des algorithmes se fondent alors sur une stratégie appelée *Dirichlet-Neumann* : la condition à l'interface est vue côté fluide comme une vitesse imposée, alors que côté solide l'action du fluide se traduit par l'application d'une force. Une première catégorie de méthodes pour implémenter la résolution de tels problèmes consiste à utiliser un unique « solver », qui résout simultanément les deux problèmes : ce sont les méthodes *directes*, ou *monolithiques*. Les exemples sont très nombreux (Bathe and Rugonyi, 2001; Heil, 2004) et par construction, une résolution monolithique garantit que la

contrepartie discrète de la condition d'interface soit respectée, on parle de *couplage fort*, cela permet généralement de garantir au niveau discret une conservation d'énergie et une stabilité. Cependant, ces méthodes présentent plusieurs inconvénients. En effet, elles ne permettent pas à deux environnements distincts (fluides et solides) de fusionner leurs propres outils de calcul pour résoudre un problème d'interaction. En outre, elles nécessitent le développement et la mise à jour d'un logiciel qui leur soit propre, ce qui ne leur permet pas de bénéficier des outils de calculs dernier cri développés indépendamment par les communautés de mécanique du solide et du fluide. Enfin, la matrice du problème à inverser étant la concaténation des deux sous-problèmes, ces méthodes sont très coûteuses en temps de calcul. Avec les méthodes *partitionnées*, les problèmes fluides et solides peuvent être résolus dans des codes différents. Cela permet de faire évoluer la procédure en même temps que chacun d'entre eux, et garantit d'avoir pour chacun des sous problèmes des méthodes de résolutions optimales et adaptées au mieux à leurs spécificités mathématiques. Parmi ces techniques, certaines permettent un couplage *fort*, alors que pour d'autres le couplage est *faible* : l'équivalent discret de la condition de couplage interfacique n'est alors pas exactement imposée à chaque pas de temps, c'est généralement le cas en partitionné. Notons qu'avec un couplage faible, en particulier entre deux codes de calcul, des itérations peuvent permettre d'imposer avec précision la condition de couplage discrète. Cela augmente considérablement les coûts de calcul et a motivé la mise au point de différentes stratégies, par exemple de type point-fixe (Le Tallec and Mouro, 2001), Aitken (Mok and Wall, 2001; Mok et al., 2001), Newton (Fernández and Moubachir, 2005) ou pseudo-Newton (on utilise un approché du Jacobien) (Gerbeau and Vidrascu, 2003). Pour de nombreux problèmes, la résolution, la stabilité et la consistance peuvent être obtenues sans imposer un couplage fort, par exemple en aéroélasticité (Farhat et al., 2006).

Un schéma semi-implicite avec projection. Cependant, dans de nombreux cas, un couplage faible conduit à des instabilités numériques. C'est le cas notamment dans les écoulements sanguins, à cause d'effets de masse ajoutée, lorsque la densité d'un fluide incompressible se rapproche de celle de la paroi solide. Cela motive la mise au point dans (Fernández et al., 2007) d'un schéma partitionné adapté à un tel contexte et fournissant des résultats numériques satisfaisant et stables. Ce schéma s'appuie sur deux idées. La première consiste à résoudre le Navier-Stokes en deux temps, pour ne coupler implicitement au problème solide que la contribution en pression du fluide. Elle est suggérée par (Causin et al., 2005), qui montre qu'un couplage explicite des termes de masse ajoutée introduit des instabilités. Par contre, les termes restant du Navier-Stokes (dissipation, convection et non-linéarités géométriques) sont alors couplés explicitement au solide. Cela permet une réduction considérable du coût du couplage, sans compromettre la stabilité. La seconde idée consiste à profiter de la méthode de projection de Chorin-Temam (Chorin, 1968; Chorin, 1969; Temam, 1968; Guermond et al., 2006) pour effectuer ce découpage implicite-explicite : pour passer d'un pas de temps à celui d'après, on commence par approcher la solution fluide en résolvant la partie ALE-advection-viscosité du Navier-Stokes sans se soucier de la relation d'incompressibilité. Ensuite, la solution fluide (vitesse et pression) est obtenue par projection sur l'espace satisfaisant la relation d'incompressibilité. Dans ce contexte d'interaction avec une structure, cela permet un très intéressant compromis entre temps de calcul et stabilité numérique : un couplage faible sur la partie non linéaire et coûteuse du Navier-Stokes (ALE-advection-viscosité), mais fort sur la partie pression contenant les effets de masse ajoutée, pour garantir la stabilité. Cet algorithme, relativement facile à implémenter, donne dans de nombreuses situations une stabilité numérique et de très bons résultats, bien que l'énergie discrète ne soit pas parfaitement conservée. Il présente néanmoins deux inconvénients : la stabilité énergétique théorique est obtenue pour un schéma de type saute-mouton (dissipatif) côté solide ; et est soumise à une condition de type CFL faisant intervenir le rapport des

densités fluide et solide (voir Théoreme 1 (Fernández et al., 2007)), donc demeure liée aux effets de masse ajoutée. Ces deux limitations motivent (Astorino et al., 2009a), qui propose de traiter la condition de couplage entre la structure et le fluide côté explicite par un terme de Robin-Robin dérivé de la méthode de Nitsche (Hansbo et al., 2004; Becker et al., 2003; Burman and Fernández, 2007; Burman and Fernández, 2009). Cette modification permet d'élargir les résultats de stabilité à des plages de paramètres encore plus larges, en s'affranchissant des effets de masse ajoutée, et à une discrétisation solide conservative de type Newmark, bien plus répandue et compatible avec des solides non linéaires.

1.5.2 Discrétisation en espace - stabilité et convergence

La discrétisation spatiale. Le choix des espaces d'approximation des variables primitives est déterminant pour la stabilité numérique lors de la résolution d'un Navier-Stokes par élément finis. L'analyse mathématique du problème de Stokes montre que les espaces éléments finis choisis pour la vitesse et la pression fluide doivent généralement satisfaire une condition de compatibilité, connue sous le nom de *condition inf-sup* et référencée dans la littérature comme la condition de Ladyzhenskaya (Ladyzhenskaya and Silverman, 1969), Babuska (Babuška, 1973), et Brezzi (Brezzi, 1974) (LBB). Numériquement, la violation de cette condition conduit généralement à de fortes oscillations spatiales noeud-à-noeud du champ de pression. Des méthodes de stabilisation permettent d'éviter ces phénomènes non physiques sans avoir à imposer la condition inf-sup. Des techniques de projection s'appuient par exemple sur l'équation de Poisson pour la pression (Guermond and Quartapelle, 1998; Badia and Codina, 2007). Les travaux qui suivent n'explorent pas ces pistes, mais cherchent plutôt à déterminer la forme prise par ce type de condition dans notre contexte, puis à établir des méthodes de discrétisation garantissant à la fois la stabilité et une relative simplicité d'implémentation.

Existence et unicité de solutions - convergence totale. Les méthodes fondées sur des arguments de conservation d'énergie permettent d'obtenir la convergence totale (du schéma discrétisé en temps et en espace vers la solution continue) d'un problème IFS linéaire (fluide de Stokes, sur un domaine fixe) (Le Tallec and Mani, 2000). Dans (Du et al., 2003), les auteurs obtiennent l'existence et l'unicité de vitesse fluide et déplacement solide sur des problèmes d'IFS couplant un fluide lineaire visqueux et incompressible à une structure élastique, ainsi que l'existence d'une pression. Dans (Grandmont and Maday, 2000), les auteurs obtiennent l'existence pour un fluide non linéaire et en ALE. Une analyse d'erreur du schéma semi-implicite en projection (Fernández et al., 2007) permet d'étudier sa convergence totale (Astorino and Grandmont, 2010).

1.6 Organisation et contributions de la thèse

En dehors de cette introduction, cette thèse est organisée en trois chapitres, relativement indépendants, dont les principales contributions sont les suivantes.

1.6.1 Chapitre 2 – Intégrer la perfusion du myocarde à des simulations de cycles cardiaques en modèle réduit

Ce projet a débuté avec l'encadrement du Projet de Recherche en Laboratoire de Magali Bardon, étudiante à Polytechnique, auquel j'ai participé avec Dominique Chapelle, Philippe Moireau et Radomir Chabiniok. Il comporte les contributions suivantes :

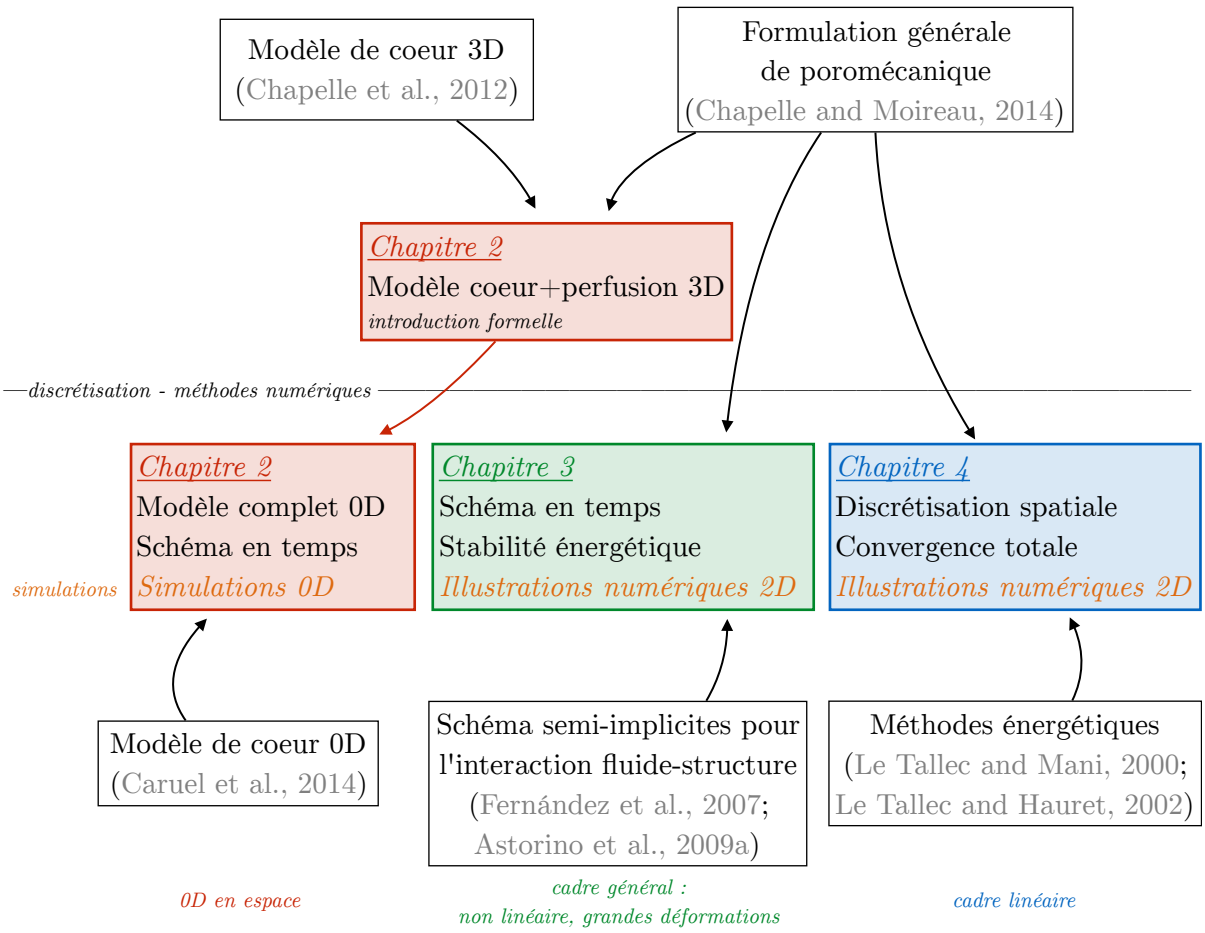

Organisation, contributions et éléments bibliographiques principaux.

- Intégration formelle (en 3D), dans un modèle de coeur complet existant, d'un compartiment poreux (Chapelle and Moireau, 2014) à la place du solide hyperélastique pour modéliser un myocarde hébergeant un écoulement coronarien couplé à la circulation sanguine.
- Proposition d'une réduction dimensionnelle de modèle de la formulation de poromécanique de (Chapelle and Moireau, 2014) pour intégrer la perfusion coronarienne au modèle 0D existant (Caruel et al., 2014).
- Proposition d'une discrétisation temporelle du schéma de poromécanique 0D, satisfaisant un bilan énergétique au niveau discret.
- Obtention de résultats numériques de cycles cardiaques avec perfusion : en plus des indicateurs auparavant reproduits (volume, pression et débit dans l'aorte), nous simulons la pression et la masse de sang dans les coronaires. On retrouve notamment le flow impediment dans les coronaires au moment de la systole.
- Simulations de phénomènes physiologiques spontanés (la vasodilatation et l'effet inotrope) et pathologiques (la sténose), dont l'importance est cruciale en terme d'applications cliniques.

Les objectifs de ce projet étaient multiples :

- Proposer dans un cadre simplifié une première mise en oeuvre du couplage entre l'écoulement coronarien et le comportement du myocarde.
- Compléter le modèle 0D (Caruel et al., 2014) pour y intégrer le réseau coronarien, afin d'accéder à la masse et la pression de perfusion.
- Ce type de modèle réduit s'avère être un excellent compromis entre précision et temps de calcul. Ils peuvent être utilisés pour la calibration de modèles plus complexes en 3D. L'objectif à terme est également d'utiliser ce modèle pour faire du monitoring sur du matériel de calcul ordinaire (téléphone portable par exemple) : suivi de patient dans le temps avec acquisition régulière de données.
- La simplicité de mise en oeuvre et la rapidité de calcul de ce modèle permet de simuler rapidement une grande variété de phénomènes physiologiques. Nous proposons ici quelques résultats pour illustrer le vaste potentiel de ces travaux en terme d'applications cliniques.
- D'un point de vue pédagogique, ce projet a permis de faire toucher du doigt à une élève de master des problématiques de recherches, entre défi scientifique et contraintes opérationnelles.
- Enfin, il a également constitué pour moi une première expérience d'encadrement. Les principales difficultés associées à ce travail, au delà de la gestion même du projet, furent liées au nombre de disciplines scientifiques à l'intersection desquelles il se situait : théorie mathématique de la réduction dimensionnelle de modèle, équations de poromécanique, modélisation cardiaque, analyse numérique et schéma discret, implémentation. Dans un tel contexte, il s'agissait de donner à Magali suffisamment d'éléments pour qu'elle puisse être en mesure de comprendre et produire, mais pas trop pour ne pas la perdre dans l'information et la complexité des problèmes traités.

Une difficulté réside également dans la calibration des modèles, en interaction avec des cardiologues et par comparaison avec des données réelles, pour reproduire le plus fidèlement les phénomènes physiologiques.

1.6.2 Chapitre 3 – Proposer un schéma en temps qui respecte un bilan d'énergie discret

Ce chapitre prend la forme d'un article rédigé avec Dominique Chapelle et Philippe Moireau et accepté pour publication dans la revue *Computers & Structures* :

Effective and energy-preserving time discretization for a general nonlinear poromechanical formulation.

S'inspirant des schémas d'IFS semi-implicite en projection (Fernández et al., 2007; Astorino et al., 2009a), et de la démarche d'analyse numérique de (Le Tallec and Hauret, 2002) reposant sur des arguments énergétiques, nous présentons les contributions suivantes :

- Etablissement d'un schéma en temps semi-implicite en projection adapté au problème de poromécanique (1.3) non linéaire.
- Preuve théorique de la stabilité énergétique inconditionnelle de ce schéma de couplage au niveau continu en espace en non linéaire.
- Validation numérique des bilans d'énergie discrets et présentation de résultats de simulations sur des cas test classiques présents dans la littérature, dans l'environnement de calcul éléments finis FreeFem++ (Hecht, 2012).

Les objectifs étant

- De proposer un schéma en temps efficace, réaliste et opérationnel pour l'implémentation du problème de poromécanique.
- De garantir mathématiquement sa stabilité énergétique et ainsi sa légitimité.
- De l'implémenter pour le valider sur des cas pratiques.

En pratique, toutes ces étapes ont en premier lieu été effectuées dans un contexte d'IFS, avant d'être adaptées à la poromécanique. Les principales difficultés eurent trait à la mise au point du schéma en temps respectant le bilan d'énergie discret, puis à l'implémentation avec FreeFem++ de ce schéma numérique complexe. En effet, lors d'une itération en temps, chaque sous-problème (non linéaire) de l'étape implicite est résolu par un algorithme de Newton, et un troisième Newton est nécessaire pour les coupler. Dans un premier temps, de nombreuses tentatives consistaient à utiliser des couplage de type Aitken, ou bien à simplifier les problèmes par linéarisation.

1.6.3 Chapitre 4 – Etudier les problèmes liés à la discrétisation spatiale et proposer un schéma stable

Une étude théorique et numérique des aspects de discrétisation spatiale nous permet de présenter les contributions qui suivent.

- Linéarisation de la formulation de poromécanique (1.3) et de sa discrétisation spatio-temporelle.
- Etablissement sous condition de la convergence totale de la solution discrète vers la solution continue de ce problème.

- Mise en évidence avec FreeFem++ de l'apparition de perturbations numériques dans des cas tests pratiques, et illustration de leur stabilisation lorsque les conditions établies sont respectées, par observation et étude de convergence spatiale. Un solveur monolithique est utilisé.
- Proposition d'une méthode numérique opérationnelle, compromis entre convergence et complexité d'implémentation.
- Illustration de la pertinence de cette méthode pour régulariser des cas pathologiques, sur des cas pratiques avec FreeFem++, d'abord dans le cadre linéaire, puis extension au cadre non linéaire.

L'objectif de cette section est de déterminer des conditions suffisantes à la convergence totale, pour proposer une méthode de discrétisation spatiale du problème de poromécanique à la fois stable et opérationnelle, puis d'illustrer sa pertinence.

Une fois de plus, toutes ces étapes ont été dans un premier temps effectuées dans un cadre d'IFS. Avec les questions liées à l'analyse mathématique, la difficulté principale eut trait à la mise au point d'outils permettant l'obtention de courbes de convergence.

1.6.4 Annexe A – Analyse de stabilité du schéma en temps semi-implicite en interaction fluide-structure non linéaire

Cette première annexe consiste à présenter dans un cadre non linéaire l'analyse de stabilité énergétique du schéma semi-implicite pour l'interaction fluide-structure (Astorino et al., 2009a). Chronologiquement dans ma thèse, ce fut la première étape vers son analogue en poromécanique qu'est le Chapitre 3. Il est intéressant de noter que le schéma semi-implicite en projection (Fernández et al., 2007) a directement inspiré le schéma en Robin (Astorino et al., 2009a). La raison d'être du second est l'introduction à l'interface fluide-solide d'une dissipation qui permet d'établir un résultat de stabilité énergétique (établi en en configuration linéaire dans (Astorino et al., 2009a)). Cependant dans la pratique, le premier est largement utilisé, il plus simple à mettre en oeuvre, et a démontré d'excellentes propriétés numériques. Afin de faciliter le passage de l'un à l'autre dans les travaux théoriques et l'implémentation (pour écrire un code commun), nous avons permuté les étapes explicite et implicite du schéma en Robin pour proposer une écriture explicite-implicite cohérente avec le schéma initial (Fernández et al., 2007).

1.6.5 Annexe B – Convergence totale d'un schéma monolithique pour l'interaction fluide-structure en linéaire

Cette seconde annexe présente la preuve de convergence totale sous conditions d'un schéma monolithique avec un couplage en Robin pour l'interaction fluide-structure en linéaire. Là encore, j'ai commencé par ce travail en interaction fluide-structure, avant de l'étendre au cadre plus complexe de la poromécanique. Cette preuve est donc l'équivalent en IFS du Chapitre 4. Une analyse de convergence existe en IFS pour le schéma semi-implicite en projection (Astorino and Grandmont, 2010) qui a inspiré le Chapitre 3. Cependant, le but de cette annexe ayant été de constituer une première étape vers la prise en compte des difficultés associées à la poromécanique, nous nous inspirons de (Le Tallec and Mani, 2000), et étudions un schéma moins complexe, monolithique avec un couplage en Robin.

Chapter 2

Cardiac model with perfusion and model reduction

The heart is supplied with a flow of about 1,3 mL/s at rest, which represents 5% of the left ventricle output. This flow is considerably reduced in systole as stresses squeeze the subendocardial vessels, this is the so-called "flow impediment".

At rest, most of the tissues in the body remove approximately 40% of the oxygen contained by the blood through the capillary bed. When activity increases and more oxygen is needed, it can be taken directly from the capillaries. However, the situation is much less comfortable in the coronary arteries, where the myocardium removes 80-90% of the arterial oxygen even at rest! Therefore, as soon as the heart has higher oxygen demand, perfusion must increase; and the heart function is regulated very sensitively according to the metabolic state of the body.

Understanding and reproducing in models the processes that allow this regulation requires an ability to account for the interactions between the coronary circulation and the myocardium contraction. For example, an increasing heart contractility can strengthen contraction and increase the output flow, but in the same time it will reinforce the flow impediment and obstruct the perfusion circulation necessary for cardiac activity. This motivated the work that follows, in which we model the coronary network as a porous flow within the myocardium.

Dimensional reduction has proven to be very cost-effective in calculation and to reproduce realistic cardiac cycles outputs (Caruel et al., 2014), therefore it was natural to explore first the relevance of integrating the coronary circulation in a reduced geometry. Much easier to use, this type of model allows to reproduce quickly very interesting physiological phenomena. It could also be used for patient monitoring or for calibration of a more complex 3D cardiac model.

In this chapter, we propose to integrate our poromechanical formulation to model the perfusion of myocardium by the coronaries. First, a complete model is derived in 3D. Then, we perform a dimensional reduction and propose an algorithm that enables us to run numerical illustrations to provide preliminary validations for this model. This improvement enables us to model the perfusion throughout the cardiac cycle, in particular observing flow impediment during systole, and to reproduce physiological processes like vasodilatation, stenosis and inotropy.

2.1 3D cardiac model with perfused myocardium

The multi-scale cardiac model proposed in (Sainte-Marie et al., 2006) and (Chapelle et al., 2012) uses a hyperelastic potential for the description of the myocardium passive behavior. The purpose of this chapter is to modify this hypothesis and to integrate for the myocardium behavior a poromechanical formulation, in order to take into account the blood perfusion permitted by the coronary network.

The cardiac tissue will be described by the general poromechanical model proposed in (Chapelle and Moireau, 2014) and described in Section 1.4, to which we add an active stress contribution.

In this first section, we present the cardiac model of (Chapelle et al., 2012) in 3D, integrating a poromechanical formulation (Chapelle and Moireau, 2014) for the passive part of the myocardium.

2.1.1 Active behavior and overall constitutive law

Let us give some elements on the active behavior of the solid matrix. The sarcomeres are the contractile units of muscle fibers at the micro-scale. Their shortening, and the resulting macroscopic contraction, is the consequence of the creation of *cross-bridges* (when myosin molecules of *thick filaments* periodically attach to surrounding thinner actin-made filaments) in the presence of adenosine tri-phosphate (ATP). Previous works on muscles modeling (Chapelle et al., 2012) have described the active stiffness k_c and the tension generated in the tissue per unit area of fiber cross-section (in the reference configuration) τ_c by the dynamical system

$$\begin{cases} \dot{k}_c = -(|u| + \alpha|\dot{e}_c|)k_c + n_0 k_0 |u|_+ \\ \dot{\tau}_c = -(|u| + \alpha|\dot{e}_c|)\tau_c + n_0 \sigma_0 |u|_+ + k_c \dot{e}_c, \end{cases}$$

where u denotes a variable reaction rate summarizing chemical activation ($|u|_+$ its positive values), e_c is the sarcomere extension, σ_0 is the maximum active stress, $\alpha|\dot{e}_c|$ accounts for bridges destruction upon rapid length changes, $n_0(e_c)$ is a length dependence function and k_0 a stiffness within the sarcomere.

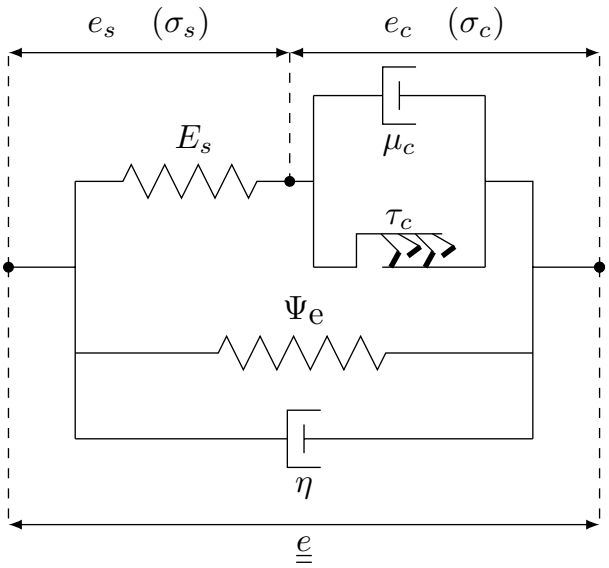

Figure 2.1 – **Hill-Maxwell rheological model.** Incorporation of the contractile unit into the solid constituent of the myocardium tissue.

The forthcoming work (Caruel et al., 2016) uses a Hill-Maxwell rheological model (for strains e and stresses σ) to incorporate the above contractile modeling into the overall behavior of the solid constituent of the myocardium tissue, see Figure 2.1. The contractile element is placed in parallel with a linear damping element of viscous parameter μ_c, so that the tension in a fiber reads

$$\tau_{fib} = \tau_c + \mu_c \dot{e}_c.$$

This association is placed in series with a linear elastic element of Young's modulus E_s, satisfying $\sigma_s = E_s e_s$. This whole branch is assumed to produce stresses $\sigma_{1\mathrm{D}} \underline{\tau}_1 \otimes \underline{\tau}_1$ along the fiber direction and $\lambda\sigma_{1\mathrm{D}}$ along directions transverse to $\underline{\tau}_1$, and is placed in parallel with the passive behavior of the myocardium solid tissue (a viscous branch and a hyperelastic potential).

Then, we adopt the non-linear rheology model proposed in (Caruel et al., 2016) ; strains and stresses of the first branch satisfy the following relations (extensions of the usual series-type rheological identities)

$$\begin{cases} \sigma_{1\mathrm{D}} = \dfrac{\tau_{fib}}{1+e_{fib}} \\ \tau_{fib} = \tau_c + \mu_c \dot{e}_c = E_s e_s = E_s(e_{fib} - e_c), \end{cases}$$

where the total (local) extension of a fiber $e_{fib} = e_s + e_c$ can be directly computed from the 3D Green-Lagrange strain tensor

$$1 + e_{fib} = \sqrt{1 + 2\underline{\tau}_1 \cdot \underline{\underline{e}} \cdot \underline{\tau}_1}.$$

We assume here that the active stress $\sigma_{1\mathrm{D}}$ along $\underline{\tau}_1$ also produces stresses along directions transverse to the fiber, with a factor λ. Then, according to (Chapelle and Moireau, 2014), and integrating the active contribution, we consider a total second Piola-Kirchhoff stress tensor for the mixture of the following form

$$\underline{\underline{\Sigma}} = \phi \underline{\underline{\Sigma}}_{\mathrm{vis}} + \frac{\partial \Psi(\underline{\underline{e}}, m)}{\partial \underline{\underline{e}}}\Big|_m + \frac{\partial \Psi^{\mathrm{damp}}(\underline{\underline{e}}, \dot{\underline{\underline{e}}})}{\partial \dot{\underline{\underline{e}}}} + \lambda\sigma_{1\mathrm{D}} \underline{\underline{\mathbb{1}}} + (1-\lambda)\sigma_{1\mathrm{D}} \underline{\tau}_1 \otimes \underline{\tau}_1,$$

with $\Psi(\underline{\underline{e}}, m)$ the Helmholtz free energy of the mixture, and $\Psi^{\mathrm{damp}} = \frac{\eta}{2} \operatorname{tr}(\dot{\underline{\underline{e}}})^2$ a viscous pseudo-potential. Assumed to be incompressible, the fluid cannot store any energy, and therefore we have $\Psi(\underline{\underline{e}}, m) = \Psi_{\mathrm{s}}(\underline{\underline{e}}, J_{\mathrm{s}})$ with Ψ_{s} the solid free energy, and $\underline{\underline{\Sigma}}$ rewrites (see (Chapelle and Moireau, 2014))

$$\underline{\underline{\Sigma}} = \phi \underline{\underline{\Sigma}}_{\mathrm{vis}} + \frac{\partial \Psi_{\mathrm{s}}(\underline{\underline{e}}, J_{\mathrm{s}})}{\partial \underline{\underline{e}}}\Big|_{J_{\mathrm{s}}} - pJ\underline{\underline{C}}^{-1} + \frac{\partial \Psi^{\mathrm{damp}}(\underline{\underline{e}}, \dot{\underline{\underline{e}}})}{\partial \dot{\underline{\underline{e}}}} + \lambda\sigma_{1\mathrm{D}} \underline{\underline{\mathbb{1}}} + (1-\lambda)\sigma_{1\mathrm{D}} \underline{\tau}_1 \otimes \underline{\tau}_1, \tag{2.1}$$

with a pressure

$$p = -\frac{\partial \Psi_{\mathrm{s}}(\underline{\underline{e}}, J_{\mathrm{s}})}{\partial J_{\mathrm{s}}}\Big|_{\underline{\underline{e}}} = \rho_{\mathrm{f}} \frac{\partial \Psi(\underline{\underline{e}}, m)}{\partial m}\Big|_{\underline{\underline{e}}}. \tag{2.2}$$

We assume that the free energy functional can be constructed in the following manner

$$\Psi_{\mathrm{s}}(\underline{\underline{e}}, J_{\mathrm{s}}) = \Psi_{\mathrm{e}}(\underline{\underline{e}}) + \Psi_{\mathrm{bulk}}(J_{\mathrm{s}}), \tag{2.3}$$

where Ψ_{bulk} describes how the energy depends on the solid phase volume changes, typically

$$\Psi_{\mathrm{bulk}}(J_{\mathrm{s}}) = \kappa_{\mathrm{s}} \left[\frac{J_{\mathrm{s}}}{1-\phi_0} - 1 - \log\left(\frac{J_{\mathrm{s}}}{1-\phi_0} \right) \right], \tag{2.4}$$

and $\Psi_{\mathrm{e}}(J_1, J_2, J_3, J_4)$ is a transverse-isotropic (with the fiber as privileged direction given by $\underline{\tau_1}$) hyperelastic potential representing the constitutive behavior of the skeleton, function of the classical reduced invariants of the Cauchy-Green strain tensor

$$J_1 = I_1 I_3^{-1/3},\ J_2 = I_2 I_3^{-2/3},\ J_3 = I_3^{1/2},\ J_4 = I_4 I_3^{-1/3},$$

where the standard invariants I_i are

$$I_1 = \operatorname{tr} \underline{\underline{C}},\ I_2 = \frac{1}{2}\left((\operatorname{tr} \underline{\underline{C}})^2 - \operatorname{tr}(\underline{\underline{C}}^2) \right),\ I_3 = \det \underline{\underline{C}},\ I_4 = \underline{\tau}_1 \cdot \underline{\underline{C}} \cdot \underline{\tau}_1.$$

The hyperelastic part of the skeleton passive stress is derived from the chain rule

$$\frac{\partial \Psi_{\mathrm{e}}}{\partial \underline{\underline{e}}} = 2 \sum_i \left(\frac{\partial \Psi_{\mathrm{e}}}{\partial J_i} \right) \left(\frac{\partial J_i}{\partial \underline{\underline{C}}} \right), \tag{2.5}$$

where the invariant derivatives are

$$\begin{cases} \dfrac{\partial J_1}{\partial \underline{\underline{C}}} = I_3^{-1/3} \left(\underline{\underline{I}} - \dfrac{1}{3} I_1 \underline{\underline{C}}^{-1} \right) \\ \dfrac{\partial J_2}{\partial \underline{\underline{C}}} = I_3^{-2/3} \left(I_1 \underline{\underline{I}} - \underline{\underline{C}} - \dfrac{2}{3} I_2 \underline{\underline{C}}^{-1} \right) \\ \dfrac{\partial J_3}{\partial \underline{\underline{C}}} = \dfrac{1}{2} I_3^{\frac{1}{2}} \, \underline{\underline{C}}^{-1} \\ \dfrac{\partial J_4}{\partial \underline{\underline{C}}} = I_3^{-1/3} \left(\underline{\tau}_1 \otimes \underline{\tau}_1 - \dfrac{1}{3} I_4 \underline{\underline{C}}^{-1} \right). \end{cases}$$

2.1.2 Poromechanical formulation for the myocardium modeling

The strong form (1.2) of the poromechanical model rewrites (see (58) in (Chapelle and Moireau, 2014))

$$\begin{cases} (\rho_0 + m)\underline{\gamma} - \underline{\nabla}_{\underline{\xi}} \cdot (\underline{\underline{F}} \cdot \underline{\underline{\Sigma}}) = (\rho_0 + m)\underline{f}, & \text{in } \Omega^0, \quad (2.6a) \\ \rho_{\mathrm{f}} \underline{\gamma}_{\mathrm{f}} + \phi \underline{\underline{k}}_{\mathrm{f}}^{-1} \cdot (\underline{v}_{\mathrm{f}} - \underline{v}_{\mathrm{s}}) + \underline{\nabla}_{\underline{\mathrm{x}}} p - \dfrac{1}{\phi} \underline{\nabla}_{\underline{\mathrm{x}}} \cdot (\phi \, \underline{\underline{\sigma}}_{\mathrm{vis}}) = \rho_{\mathrm{f}} \, \underline{f}, & \text{in } \Omega_t, \quad (2.6b) \\ \dfrac{1}{J} \dfrac{\mathrm{d}m}{\mathrm{d}t} + \underline{\nabla}_{\underline{\mathrm{x}}} \cdot (\rho_{\mathrm{f}} \phi (\underline{v}_{\mathrm{f}} - \underline{v}_{\mathrm{s}})) = \theta, & \text{in } \Omega_t \quad (2.6c) \end{cases}$$

with

$$\underline{\gamma} = \frac{\rho_{\mathrm{s}}(1-\phi)\partial_t \underline{v}_{\mathrm{s}} + \rho_{\mathrm{f}} \phi \partial_t \underline{v}_{\mathrm{f}}}{\rho_0 + m} \quad \text{and} \quad \rho_0 + m = \rho_{\mathrm{s}}(1-\phi) + \rho_{\mathrm{f}} \phi, \tag{2.7}$$

and the notations introduced in Section 1.4.1.

We complement the above equations with the boundary conditions introduced in Section 1.4.1, where we assume $\Gamma_{N\mathrm{nof}} = \varnothing$ (see Figure 2.2). Then, we multiply System (2.6) by

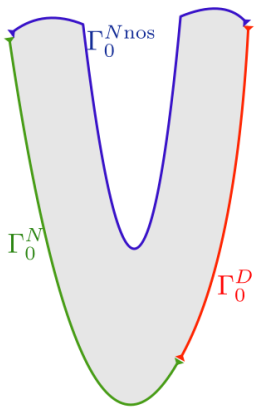

Figure 2.2 – **Boundary conditions of the poromechanical formulation.**

test functions $(\underline{v}_{\mathrm{s}}^*, \underline{v}_{\mathrm{f}}^*, q^*)$ and we integrate space-wise to get (see (63) in (Chapelle and Moireau,

2014))

$$
\begin{cases}
\underbrace{\displaystyle\int_{\Omega^0} \rho_{\mathrm{s}0}(1-\phi_0)\frac{\mathrm{d}\underline{v}_{\mathrm{s}}}{\mathrm{dt}}\cdot\underline{v}_{\mathrm{s}}^*\,d\Omega}_{\mathcal{P}_a^{\mathrm{s}}(\underline{v}_{\mathrm{s}}^*)} + \mathcal{P}_a^{\mathrm{f}}(\underline{v}_{\mathrm{s}}^*) + \underbrace{\displaystyle\int_{\Omega^0} \underline{\underline{\Sigma}} : d_{\underline{y}}\underline{\underline{e}}\cdot\underline{v}_{\mathrm{s}}^*\,d\Omega}_{\mathcal{P}_i(\underline{v}_{\mathrm{s}}^*)} \\
\qquad = \displaystyle\int_{\Omega^0}(\rho_0+m)\underline{f}\cdot\underline{v}_{\mathrm{s}}^*\,d\Omega + \underbrace{\displaystyle\int_{\Gamma^0_{N\mathrm{nos}}\cup\Gamma^0_N}\underline{t}_0\cdot\underline{v}_{\mathrm{s}}^*\,dS}_{\mathcal{P}_e(\underline{v}_{\mathrm{s}}^*)} \qquad (2.8a) \\
\mathcal{P}_a^{\mathrm{f}}(\underline{v}_{\mathrm{f}}^*) + \underbrace{\displaystyle\int_{\Omega_t}(\underline{v}_{\mathrm{f}}-\underline{v}_{\mathrm{s}})\cdot\phi^2\underline{\underline{k}}_{\mathrm{f}}^{-1}\cdot\underline{v}_{\mathrm{f}}^*\,d\Omega + \int_{\Omega_t}\Big(-\frac{p}{\rho_{\mathrm{f}}}\underline{\nabla}_{\underline{\mathrm{x}}}\cdot(\rho_{\mathrm{f}}\phi\underline{v}_{\mathrm{f}}^*) + \phi\,\underline{\underline{\sigma}}_{\mathrm{vis}} : \underline{\underline{\varepsilon}}(\underline{v}_{\mathrm{f}}^*)\Big)\,d\Omega}_{\mathcal{P}_i^{\mathrm{f}}(\underline{v}_{\mathrm{f}}^*)} \\
\qquad = \displaystyle\int_{\Omega_t}\rho_{\mathrm{f}}\phi\,\underline{f}\cdot\underline{v}_{\mathrm{f}}^*\,d\Omega + \underbrace{\displaystyle\int_{\Gamma_N^t}\phi\,\underline{t}\cdot\underline{v}_{\mathrm{f}}^*\,dS}_{\mathcal{P}_e^{\mathrm{f}}(\underline{v}_{\mathrm{f}}^*)} \qquad (2.8b) \\
\displaystyle\int_{\Omega^0}\frac{\mathrm{d}m}{\mathrm{dt}}q^*\,d\Omega + \int_{\Omega_t}\underline{\nabla}_{\underline{\mathrm{x}}}\cdot(\rho_{\mathrm{f}}\phi\,(\underline{v}_{\mathrm{f}}-\underline{v}_{\mathrm{s}}))\,q^*\,d\Omega = \int_{\Omega_t}\theta q^*\,d\Omega \qquad (2.8c)
\end{cases}
$$

with

$$
\mathcal{P}_a^{\mathrm{f}}(\underline{v}^*) = \int_{\Omega^0}\frac{\mathrm{d}}{\mathrm{dt}}\big(J\rho_{\mathrm{f}}\phi\,\underline{v}_{\mathrm{f}}\big)\cdot\underline{v}^*\,d\Omega + \int_{\Omega_t}\underline{\nabla}_{\underline{\mathrm{x}}}\cdot(\rho_{\mathrm{f}}\phi\underline{v}_{\mathrm{f}}\otimes(\underline{v}_{\mathrm{f}}-\underline{v}_{\mathrm{s}}))\cdot\underline{v}^*\,d\Omega - \int_{\Omega_t}\theta\underline{v}_{\mathrm{f}}\cdot\underline{v}^*\,d\Omega
$$

and

$$
d_{\underline{y}}\underline{\underline{e}}\cdot\underline{y}^* = \frac{1}{2}(\underline{\underline{F}}^T\cdot\nabla\underline{y}^* + (\nabla\underline{y}^*)^T\cdot\underline{\underline{F}}).
$$

2.1.3 Cardiac system

We will assume that there is no distributed force, $\underline{f}=0$. On the endocardium surface $\Gamma_{N\mathrm{nos}}$, $\underline{t}_0$ will be typically $-P_v\,\underline{\underline{F}}^{-T}\underline{n}_e$, with P_v the intraventricular blood pressure exerting forces on the endocardium surfaces $\Gamma_{N\mathrm{nos}}$ of outward unit normal $\underline{n}_e$, so that $\mathcal{P}_e$ becomes

$$
\mathcal{P}_e(\underline{v}_{\mathrm{s}}^*) = \int_{\Gamma_N^0}\underline{t}_0\cdot\underline{v}_{\mathrm{s}}^*\,dS - \int_{\Gamma^0_{N\mathrm{nos}}}P_v\underline{v}_{\mathrm{s}}^*\cdot\underline{\underline{F}}^{-T}\cdot\underline{n}_e\,dS.
$$

According to (Sainte-Marie et al., 2006), we model the opening and closure of the valves by the following relation that links P_v to the cardiac outflow $-\dot{V}=Q$ (with V the ventricular cavity volume),

$$
-\dot{V} = Q = q(P_v, P_{ar}, P_{at}),
$$

with P_{ar} and P_{at} the aorta (or pulmonary) and atrium pressures and q a regularized version of the ideal behavior

$$
\begin{cases}
Q\le 0 & \text{if } P_v = P_{at} \text{ (filling)},\\
Q = 0 & \text{if } P_{at}\le P_v\le P_{ar} \text{ (isovolumic phases)},\\
Q\ge 0 & \text{if } P_v\ge P_{ar} \text{ (ejection)},
\end{cases}
$$

approximated by

$$
\begin{cases}
Q = K_{at}(P_v-P_{at}), & \text{if } P_v\le P_{at},\\
Q = K_p(P_v-P_{at}), & \text{if } P_{at}\le P_v\le P_{ar},\\
Q = K_{ar}(P_v-P_{ar}) + K_p(P_{ar}-P_{at}), & \text{if } P_v\ge P_{ar},
\end{cases}
$$

where (K_{at}, K_p, K_{ar}) are constants satisfying $K_p \leq \min(K_{at}, K_{ar})$.

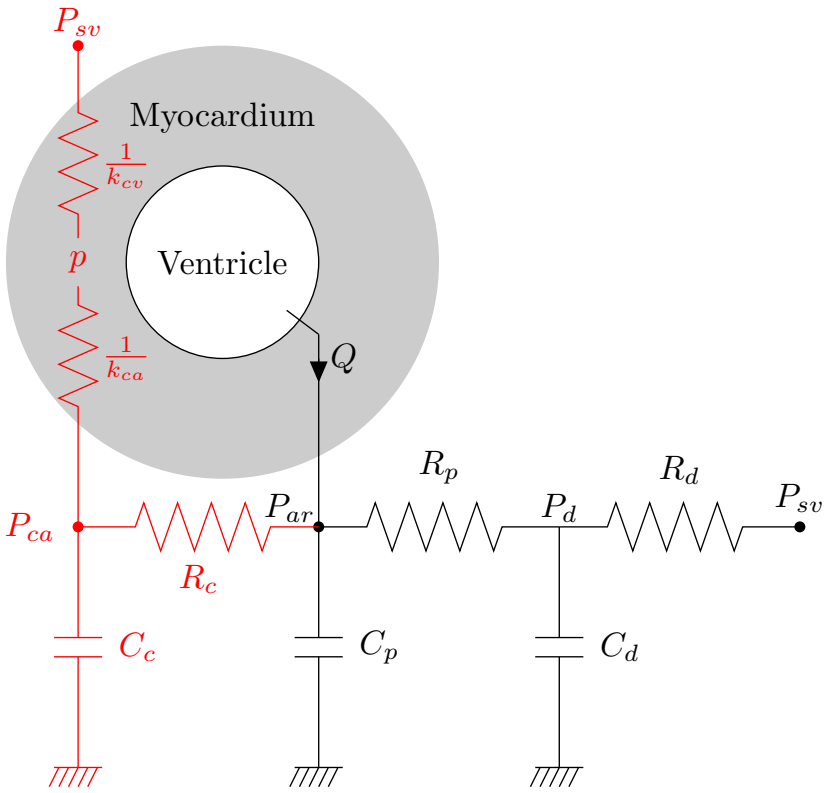

Figure 2.3 – **Rheological model of the circulatory system plugged into the aorta.** The new branch in red models the coronaries.

In future works, the porous compartment will be coupled with 3D models of the largest coronary vessels, but for now it will be assumed to be only fed by the distributed source term θ according to (see also (Chapelle et al., 2009))

$$\theta = \rho_{\mathrm{f}} k_{ca}(P_{ca} - p) - \rho_{\mathrm{f}} k_{cv}(p - P_{sv}),$$

where k_{ca} (resp. k_{cv}) is constant and characterizes the small coronary arteries (resp. veins) conductance, P_{sv} the small veins pressure, and the coronary artery pressure P_{ca} is linked to the global circulation within the following model.

Indeed, the system is closed by a two-stage Windkessel model that represents the external circulation, and a Windkessel that links the aorta to the porous compartment, representing the big coronary arteries circulation

$$\begin{cases} C_c \dot{P}_{ca} + (P_{ca} - P_{ar})/R_c + (P_{ca} - p) k_{ca} V_{myo} = 0, \\ C_p \dot{P}_{ar} + (P_{ar} - P_d)/R_p + (P_{ar} - P_{ca})/R_c = Q, \\ C_d \dot{P}_d + (P_d - P_{ar})/R_p = (P_{vs} - P_d)/R_d, \end{cases}$$

with C_p, R_p, C_d, R_d and C_c, R_c the capacitances and resistances of the proximal, distal and coronary circulations Windkessel, P_d is the distal pressure, V_{myo} the myocardium reference volume and P_{vs} represents the venous system pressure, see Figure 2.3.

All together, these elements give the following 3D cardiac system of equations

$$
\begin{cases}
\mathcal{P}_a^{\mathrm{s}}(\underline{v}^*) + \mathcal{P}_a^{\mathrm{f}}(\underline{v}^*) + \mathcal{P}_i(\underline{v}^*) = \mathcal{P}_e(\underline{v}^*) \quad \forall \underline{v}^* \in \mathcal{V} & \text{(2.9a)}\\
\mathcal{P}_a^{\mathrm{f}}(\underline{v}_{\mathrm{f}}^*) + \mathcal{P}_i^{\mathrm{f}}(\underline{v}_{\mathrm{f}}^*) = \mathcal{P}_e^{\mathrm{f}}(\underline{v}_{\mathrm{f}}^*) \quad \forall \underline{v}_{\mathrm{f}}^* \in \mathcal{V} & \text{(2.9b)}\\
\dfrac{1}{J}\dfrac{\mathrm{d}m}{\mathrm{d}t} + \underline{\nabla}_{\underline{x}} \cdot (\rho_{\mathrm{f}}\phi(\underline{v}_{\mathrm{f}} - \underline{v}_{\mathrm{s}})) = \rho_{\mathrm{f}} k_{ca}(P_{ca} - p) - \rho_{\mathrm{f}} k_{cv}(p - P_{sv}) & \text{(2.9c)}\\
\quad p = -\dfrac{\partial \Psi_{\mathrm{bulk}}}{\partial J_{\mathrm{s}}} & \text{(2.9d)}\\
\quad \underline{\underline{\Sigma}} = \phi \underline{\underline{\Sigma}}_{\mathrm{vis}} + \dfrac{\partial \Psi_{\mathrm{e}}}{\partial \underline{\underline{e}}} + \dfrac{\partial \Psi^{\mathrm{damp}}}{\partial \dot{\underline{\underline{e}}}} - pJ\underline{\underline{C}}^{-1} + \lambda\sigma_{1\mathrm{D}}\underline{\underline{\mathbb{1}}} + (1-\lambda)\sigma_{1\mathrm{D}}\underline{\tau}_1 \otimes \underline{\tau}_1 & \text{(2.9e)}\\
\quad \sigma_{1\mathrm{D}} = \tau_{fib}/(1 + e_{fib}) & \text{(2.9f)}\\
\quad e_{fib} = \sqrt{1 + 2\underline{\tau}_1 \cdot \underline{\underline{e}} \cdot \underline{\tau}_1} - 1 & \text{(2.9g)}\\
\tau_{fib} = \tau_c + \mu_c \dot{e}_c = E_s(e_{fib} - e_c) & \text{(2.9h)}\\
\dot{k}_c = -(|u| + \alpha|\dot{e}_c|)k_c + n_0 k_0 |u|_+ & \text{(2.9i)}\\
\dot{\tau}_c = -(|u| + \alpha|\dot{e}_c|)\tau_c + n_0\sigma_0|u|_+ + k_c\dot{e}_c & \text{(2.9j)}\\
-\dot{V} = Q = q(P_v, P_{ar}, P_{at}) & \text{(2.9k)}\\
C_c\dot{P}_{ca} + (P_{ca} - P_{ar})/R_c + (P_{ca} - p)k_{ca}V_{myo} = 0 & \text{(2.9l)}\\
C_p\dot{P}_{ar} + (P_{ar} - P_d)/R_p + (P_{ar} - P_{ca})/R_c = Q & \text{(2.9m)}\\
C_d\dot{P}_d + (P_d - P_{ar})/R_p = (P_{vs} - P_d)/R_d. & \text{(2.9n)}
\end{cases}
$$

2.2 Dimensional reduction of the cardiac model with poromechanics

2.2.1 0D cardiac model

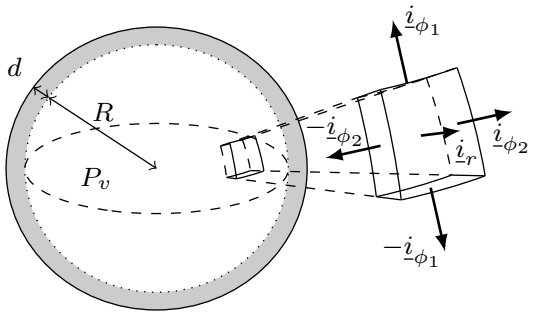

Figure 2.4 – **Spherical model of a ventricle**

As proposed in (Caruel et al., 2014), let us perform a dimensional reduction of the above cardiac model. A ventricle is represented by a sphere of radius R_0 and thickness d_0 in the reference configuration Ω^0. We assume that this spherical symmetry is shared by the constitutive properties, and we apply an internal pressure. As a consequence, for symmetry reasons, the deformed configuration is described by a sphere of radius R and thickness d. We define $(\underline{i}_r, \underline{i}_{\phi_1}, \underline{i}_{\phi_2})$ a local basis on Ω^0, with $\underline{i}_r$ radial, $\underline{i}_{\phi_1} = \underline{\tau}_1$ and $(\underline{i}_{\phi_1}, \underline{i}_{\phi_2})$ orthoradial, see Figure 2.4. In our framework, the displacement with respect to the reference configuration writes $\underline{y} = y\underline{i}_r = (R - R_0)\underline{i}_r$ and

the Cauchy-Green deformation tensor reduces to

$$\underline{\underline{C}} = \begin{pmatrix} C_{rr} & 0 & 0 \\ 0 & C & 0 \\ 0 & 0 & C \end{pmatrix}.$$

Circumferential lengths are scaled by $\sqrt{C} = 1 + y/R_0$ between the reference and deformed configurations. Passing by, we note that, unlike in (Caruel et al., 2014), no incompressibility is assumed due to perfusion, in particular, and therefore $J = \det \underline{\underline{C}}^{1/2}$ has no reason to be 1. In addition, the relative thinness of the wall compared to the sphere radius combined to the equality $\underline{v}_\mathrm{f} = \underline{v}_\mathrm{s}$ on the endocardium surface justifies in this framework the assumption $\underline{v}_\mathrm{f} = \underline{v}_\mathrm{s}$ on the whole domain, and the introduction of $\underline{v}$ to denote velocities (then, $\Gamma^0_N = \emptyset$). Therefore, (2.7) becomes $\underline{\gamma} = \partial_t \underline{v}$, (2.6b) is replaced by $\underline{v}_\mathrm{f} = \underline{v}_\mathrm{s}$, and multiplying (2.6a) by test functions $\underline{v}^*$ and integrating space-wise yields (assuming $\underline{f} = \underline{0}$)

$$\int_{\Omega^0} (\rho_0 + m) \frac{\mathrm{d}\underline{v}}{\mathrm{dt}} \cdot \underline{v}^* \, d\Omega + \int_{\Omega^0} \underline{\underline{\Sigma}} : d_{\underline{y}}\underline{\underline{e}} \cdot \underline{v}^* \, d\Omega = \int_{\Gamma^0_{N\mathrm{nos}}} \underline{t}_0 \cdot \underline{v}^* \, dS \tag{2.10}$$

Considering a radial virtual velocity $\underline{v}^* = v^* \underline{i}_r$ with the assumed kinematic symmetry, we find that

$$(d_{\underline{y}}\underline{\underline{e}} \cdot \underline{v}^*)_{\phi_1\phi_1} = (d_{\underline{y}}\underline{\underline{e}} \cdot \underline{v}^*)_{\phi_2\phi_2} = (1 + y/R_0)(v^*/R_0).$$

We neglect fluid viscous effects $\underline{\underline{\Sigma}}_\mathrm{vis}$. Thanks to the smallness of d/R, classical arguments of shell theory enable us to neglect radial stress Σ_{rr} compared to the orthoradial components (Chapelle and Bathe, 2010), and to explicitly infer p from $\Sigma_{rr} = 0$ in (2.1),

$$p = \frac{C_{rr}}{J} \left[\left(\frac{\partial \Psi_\mathrm{e}}{\partial \underline{\underline{e}}} \right)_{rr} + \left(\frac{\partial \Psi^\mathrm{damp}}{\partial \dot{\underline{\underline{e}}}} \right)_{rr} + \lambda \sigma_\mathrm{1D} \right] = \frac{J}{C^2} \left[\left(\underline{\underline{\Sigma}}_p \right)_{rr} + \lambda \sigma_\mathrm{1D} \right], \tag{2.11}$$

where we define the 3D passive stress as

$$\underline{\underline{\Sigma}}_p = \frac{\partial \Psi_\mathrm{e}}{\partial \underline{\underline{e}}}(\underline{\underline{e}}) + \frac{\partial \Psi^\mathrm{damp}}{\partial \dot{\underline{\underline{e}}}}(\underline{\underline{e}}, \dot{\underline{\underline{e}}}). \tag{2.12}$$

Therefore, we have

$$\underline{\underline{\Sigma}} : \mathrm{d}_{\underline{y}}\underline{\underline{e}} \cdot \underline{v}^* = \left(1 + \frac{y}{R_0} \right) \frac{v^*}{R_0} \Sigma_\mathrm{sph},$$

with

$$\Sigma_\mathrm{sph} = \Sigma_{\phi_1\phi_1} + \Sigma_{\phi_2\phi_2} = \left(\underline{\underline{\Sigma}}_p \right)_{\phi_1\phi_1} + \left(\underline{\underline{\Sigma}}_p \right)_{\phi_2\phi_2} - 2J^2 C^{-3} \left(\underline{\underline{\Sigma}}_p \right)_{rr} + \sigma_\mathrm{1D}(1 + \lambda - 2\lambda J^2 C^{-3}),$$

and J that can be obtained thanks to the following combination of (2.2), (2.3) and (2.11)

$$-\frac{\partial \Psi_\mathrm{bulk}}{\partial J_\mathrm{s}} = \frac{J}{C^2} \left[\left(\underline{\underline{\Sigma}}_p \right)_{rr} + \lambda \sigma_\mathrm{1D} \right].$$

Note that the passive stress $\underline{\underline{\Sigma}}_p$ is calculated with the chain rule (2.5), and that the invariants and their derivatives reduce to

$$\begin{cases} I_1 = C_{rr} + 2C = J^2 C^{-2} + 2C \\ I_2 = C^2 + 2CC_{rr} = C^2 + 2J^2 C^{-1} \\ I_3 = C_{rr} C^2 = J^2 \\ I_4 = C \end{cases}$$

and

$$\begin{cases} \dfrac{\partial J_1}{\partial \underline{\underline{C}}} = J^{-2/3}\left(\underline{\underline{\mathbb{1}}} - \dfrac{1}{3}(J^2C^{-2}+2C)\underline{\underline{C}}^{-1}\right) \\ \dfrac{\partial J_2}{\partial \underline{\underline{C}}} = J^{-4/3}\left((J^2C^{-2}+2C)\underline{\underline{\mathbb{1}}} - \underline{\underline{C}} - \dfrac{2}{3}(C^2+2J^2C^{-1})\underline{\underline{C}}^{-1}\right) \\ \dfrac{\partial J_3}{\partial \underline{\underline{C}}} = \dfrac{1}{2}J\underline{\underline{C}}^{-1} \\ \dfrac{\partial J_4}{\partial \underline{\underline{C}}} = J^{-2/3}\left(\underline{\tau}_1 \otimes \underline{\tau}_1 - \dfrac{1}{3}J^{-2/3}C\underline{\underline{C}}^{-1}\right) \end{cases}$$

while the viscosity within the skeleton gives

$$\frac{\partial \Psi^{\text{damp}}}{\partial \underline{\underline{\dot{e}}}} = \frac{\eta}{2}\underline{\underline{\dot{C}}}.$$

With this, the derivation of Σ_{sph} gives

$$\Sigma_{\text{sph}} = 4J^{-\frac{2}{3}}(1-J^2C^{-3})\left(\frac{\partial \Psi_{\text{e}}}{\partial J_1} + J^{-\frac{2}{3}}C\frac{\partial \Psi_{\text{e}}}{\partial J_2}\right) + 2J^{-\frac{2}{3}}\frac{\partial \Psi_{\text{e}}}{\partial J_4} + \sigma_{1\text{D}}(1+\lambda-2\lambda J^2C^{-3}) + \eta\left(\dot{C} - 2J^3C^{-6}(\dot{J}C - J\dot{C})\right)$$

with $\sigma_{1\text{D}}$ given by (2.9f).

Now, using that $d/d_0 = \sqrt{C_{rr}} = J(1+\frac{y}{R_0})^{-2}$, the virtual work of pressure force writes

$$\begin{aligned} \int_{\Gamma^0_{N\text{nos}}} \underline{t}_0 \cdot (v^*\underline{i}_r)\, dS &= 4\pi P_v \left(R - \frac{d}{2}\right)^2 \left(1 + J\frac{d_0}{R_0}\left(1+\frac{y}{R_0}\right)^{-3}\right) v^* \\ &= 4\pi P_v \left(R_0 + y - \sqrt{C_{rr}}\frac{d_0}{2}\right)^2 \left(1 + J\frac{d_0}{R_0}\left(1+\frac{y}{R_0}\right)^{-3}\right) v^* \\ &= 4\pi P_v R_0^2 \left(1 + \frac{y}{R_0} - \frac{Jd_0}{2R_0}\left(1+\frac{y}{R_0}\right)^{-2}\right)^2 \left(1 + J\frac{d_0}{R_0}\left(1+\frac{y}{R_0}\right)^{-3}\right) v^* \end{aligned} \tag{2.13}$$

Integrating over the sphere of radius R_0 and thickness d_0, we finally get the second order ordinary differential equation (ODE) satisfied by the mixture displacement $\underline{y}$,

$$\begin{cases} d_0(\rho_0 + m)\dfrac{\mathrm{d}^2 y}{\mathrm{d}t^2} + \dfrac{d_0}{R_0}\left(1+\dfrac{y}{R_0}\right)\Sigma_{\text{sph}} \\ \qquad\qquad = P_v\left(1 + \dfrac{y}{R_0} - \dfrac{Jd_0}{2R_0}\left(1+\dfrac{y}{R_0}\right)^{-2}\right)^2 \left(1 + J\dfrac{d_0}{R_0}\left(1+\dfrac{y}{R_0}\right)^{-3}\right) \\ \qquad \dfrac{\mathrm{d}m}{\mathrm{d}t} = J\theta \end{cases}$$

where

$$\begin{cases} \Sigma_{\text{sph}} = \left(\underline{\underline{\Sigma}}_p\right)_{\phi_1\phi_1} + \left(\underline{\underline{\Sigma}}_p\right)_{\phi_2\phi_2} - 2\dfrac{J^2}{C^3}\left(\underline{\underline{\Sigma}}_p\right)_{rr} + \sigma_{1\text{D}}(1+\lambda-2\lambda J^2C^{-3}) & \text{(2.15a)} \\ \text{and } J \text{ such that } \ -\dfrac{\partial \Psi_{\text{bulk}}}{\partial J_{\text{s}}} = \dfrac{J}{C^2}\left[\left(\underline{\underline{\Sigma}}_p\right)_{rr} + \lambda\sigma_{1\text{D}}\right]. & \text{(2.15b)} \end{cases}$$

Let us notice that unlike in (Caruel et al., 2014), y has to be completed by J, given by (2.15b), to fully characterize the 3D displacement field $\underline{y}$. Our set of dynamic variables for the mixture mechanics is (y, v, m). Finally, the intraventricular volume writes in this context

$$V = \frac{4\pi}{3}\left(R - \frac{d}{2}\right)^3 = \frac{4\pi}{3}\left(R_0 + y - \sqrt{C_{rr}}\frac{d_0}{2}\right)^3 = \frac{4\pi}{3}\left(R_0 + y - \frac{Jd_0}{2}\left(1 + \frac{y}{R_0}\right)^{-2}\right)^3,$$

so that its variations and the valve law (2.9k) become

$$\begin{aligned}\dot{V} &= 4\pi R_0^2\left(1 + \frac{y}{R_0} - \frac{Jd_0}{2R_0}\left(1 + \frac{y}{R_0}\right)^{-2}\right)^2\left[\dot{y} - \frac{\dot{J}d_0}{2}\left(1 + \frac{y}{R_0}\right)^{-2} + \frac{Jd_0}{R_0}\dot{y}\left(1 + \frac{y}{R_0}\right)^{-3}\right] \\ &= -f(P_v, P_{ar}, P_{at}).\end{aligned}$$

With these elements, the cardiac model with poromechanics (2.9) reduces to the following system on $(y, J, m, e_c, k_c, \tau_c, P_{ca}, P_{ar}, P_d)$

$$\begin{cases}
d_0(\rho_0 + m)\dfrac{\mathrm{d}^2 y}{\mathrm{d}t^2} + \dfrac{d_0}{R_0}\left(1 + \dfrac{y}{R_0}\right)\Sigma_{\mathrm{sph}} \\
\qquad = P_v\left(1 + \dfrac{y}{R_0} - \dfrac{Jd_0}{2R_0}\left(1 + \dfrac{y}{R_0}\right)^{-2}\right)^2\left(1 + J\dfrac{d_0}{R_0}\left(1 + \dfrac{y}{R_0}\right)^{-3}\right) & \text{(2.16a)} \\
\dfrac{1}{J}\dfrac{\mathrm{d}m}{\mathrm{d}t} = \theta = \rho_{\mathrm{f}} k_{ca}(P_{ca} - p) - \rho_{\mathrm{f}} k_{cv}(p - P_{sv}) & \text{(2.16b)} \\
\qquad p = \dfrac{J}{C^2}\left[\left(\underline{\underline{\Sigma}}_p\right)_{rr} + \lambda\sigma_{1\mathrm{D}}\right] & \text{(2.16c)} \\
\qquad -\dfrac{\partial \Psi_{\mathrm{bulk}}}{\partial J_{\mathrm{s}}} = \dfrac{J}{C^2}\left[\left(\underline{\underline{\Sigma}}_p\right)_{rr} + \lambda\sigma_{1\mathrm{D}}\right] & \text{(2.16d)} \\
\qquad \Sigma_{\mathrm{sph}} = \left(\underline{\underline{\Sigma}}_p\right)_{\phi_1\phi_1} + \left(\underline{\underline{\Sigma}}_p\right)_{\phi_2\phi_2} - 2pJC^{-1} + \sigma_{1\mathrm{D}}(1 + \lambda) & \text{(2.16e)} \\
\qquad \sigma_{1\mathrm{D}} = \tau_{fib}/(1 + e_{fib}) & \text{(2.16f)} \\
\tau_{fib} = \tau_c + \mu_c\dot{e}_c = E_s(e_{fib} - e_c) & \text{(2.16g)} \\
\dot{k}_c = -(|u| + \alpha|\dot{e}_c|)k_c + n_0 k_0 |u|_+ & \text{(2.16h)} \\
\dot{\tau}_c = -(|u| + \alpha|\dot{e}_c|)\tau_c + n_0\sigma_0|u|_+ + k_c\dot{e}_c & \text{(2.16i)} \\
-\dot{V} = f(P_v, P_{ar}, P_{at}) & \text{(2.16j)} \\
C_c\dot{P}_{ca} + (P_{ca} - P_{ar})/R_c + (P_{ca} - p)k_{ca}V_{myo} = 0 & \text{(2.16k)} \\
C_p\dot{P}_{ar} + (P_{ar} - P_d)/R_p + (P_{ar} - P_{ca})/R_c = Q & \text{(2.16l)} \\
C_d\dot{P}_d + (P_d - P_{ar})/R_p = (P_{vs} - P_d)/R_d. & \text{(2.16m)}
\end{cases}$$

Remark 1
The following expressions of p and Σ_{sph} can be inferred in function of the derivatives of Ψ_{e}:

$$\begin{aligned}p &= \frac{4J^{1/3}}{3C^2}\left(1 - \frac{C^3}{J^2}\right)\left[\frac{\partial \Psi_{\mathrm{e}}}{\partial J_1} + \frac{C}{J^{2/3}}\frac{\partial \Psi_{\mathrm{e}}}{\partial J_2}\right] + \frac{\partial \Psi_{\mathrm{e}}}{\partial J_3} - \frac{2C}{3J^{7/3}}\frac{\partial \Psi_{\mathrm{e}}}{\partial J_4} + \eta\frac{J^2}{C^5}(C\dot{J} - J\dot{C}) + \frac{J}{C^2}\lambda\sigma_{1\mathrm{D}} \\
\Sigma_{\mathrm{sph}} &= 4J^{-\frac{2}{3}}(1 - J^2C^{-3})\left(\frac{\partial \Psi_{\mathrm{e}}}{\partial J_1} + J^{-\frac{2}{3}}C\frac{\partial \Psi_{\mathrm{e}}}{\partial J_2}\right) + 2J^{-\frac{2}{3}}\frac{\partial \Psi_{\mathrm{e}}}{\partial J_4} \\
&\qquad + \sigma_{1\mathrm{D}}\left(1 + \lambda - 2\lambda J^2C^{-3}\right) + \eta\left(\dot{C} - 2J^3C^{-6}(\dot{J}C - J\dot{C})\right)\end{aligned}$$

Remark 2 (Solid incompressibility)
The limit $\kappa \to \infty$ in (2.4) and (2.2) gives the following relation for J, that replaces (2.16d) in the above system,

$$J = 1 + \frac{m}{\rho_{\mathrm{f}}}. \tag{2.17}$$

2.2.2 Energy balance at the continuous level in the reduced formulation

We recall that

$$\underline{\underline{e}} = \tfrac{1}{2}(\underline{\underline{C}} - \underline{\underline{\mathbb{1}}}) \text{ and } \underline{\underline{C}}(y, J) = \begin{pmatrix} \frac{J^2}{C(y)^2} & 0 & 0 \\ 0 & C(y) & 0 \\ 0 & 0 & C(y) \end{pmatrix}, \text{ with } C(y) = \frac{2y}{R_0} + \frac{y^2}{R_0^2} + 1.$$

In order to establish an energy conservation at the continuous level, we remove the loadings $f = 0$ and $P_v = 0$, the active contribution $\sigma_{1\mathrm{D}} = 0$ and the solid damping $\eta = 0$. Our objective is to derive an energy balance in which we propose to keep a fluid source θ. Substituting (2.16e), the multiplication of (2.16a) by $v = \mathrm{d}y/\mathrm{d}t$ gives

$$(\rho_0 + m) v \frac{\mathrm{d}v}{\mathrm{d}t} + \left(1 + \frac{y}{R_0}\right) \frac{1}{R_0} \frac{\mathrm{d}y}{\mathrm{d}t} \left[\left(\frac{\partial \Psi_{\mathrm{e}}}{\partial \underline{\underline{e}}} \right)_{\phi_1 \phi_1} + \left(\frac{\partial \Psi_{\mathrm{e}}}{\partial \underline{\underline{e}}} \right)_{\phi_2 \phi_2} - 2pJC^{-1} \right] = 0. \tag{2.18}$$

The first term gives

$$(\rho_0 + m) \frac{\mathrm{d}v}{\mathrm{d}t} v = \frac{\mathrm{d}}{\mathrm{d}t} \left(\frac{1}{2} (\rho_0 + m) v^2 \right) - \frac{1}{2} \frac{\mathrm{d}m}{\mathrm{d}t} v^2 = \frac{\mathrm{d}E_c}{\mathrm{d}t} - \frac{1}{2} J \theta v^2,$$

with $E_c = \frac{1}{2}(\rho_0 + m)v^2$ the kinetic energy per unit volume of the mixture, and $\frac{1}{2}J\theta v^2$ its increment brought by the source term θ.

About the second term, we introduce $e = (\underline{\underline{e}})_{\phi_1\phi_1} = (\underline{\underline{e}})_{\phi_2\phi_2} = \frac{1}{2}(C - 1)$ that depends only on y in order to write

$$\left(1 + \frac{y}{R_0}\right) \frac{1}{R_0} \frac{\mathrm{d}y}{\mathrm{d}t} = \frac{\mathrm{d}}{\mathrm{d}t} \left(\frac{y}{R_0} + \frac{y^2}{2R_0^2} \right) = \frac{\mathrm{d}e}{\mathrm{d}t},$$

and the following expression for the derivative of the free energy

$$\begin{aligned} \frac{\mathrm{d}\Psi}{\mathrm{d}t} =& \frac{\partial \Psi_{\mathrm{e}}}{\partial \underline{\underline{e}}} \frac{\mathrm{d}\underline{\underline{e}}}{\mathrm{d}t} + \frac{\partial \Psi_{\mathrm{bulk}}}{\partial J_{\mathrm{s}}} \left(\frac{\mathrm{d}J}{\mathrm{d}t} - \frac{1}{\rho_{\mathrm{f}}} \frac{\mathrm{d}m}{\mathrm{d}t} \right) \\ =& \left(\frac{\partial \Psi_{\mathrm{e}}}{\partial \underline{\underline{e}}} \right)_{rr} \frac{\mathrm{d}e_{rr}}{\mathrm{d}t} + \left(\frac{\partial \Psi_{\mathrm{e}}}{\partial \underline{\underline{e}}} \right)_{\phi_1\phi_1} \frac{\mathrm{d}e}{\mathrm{d}t} + \left(\frac{\partial \Psi_{\mathrm{e}}}{\partial \underline{\underline{e}}} \right)_{\phi_2\phi_2} \frac{\mathrm{d}e}{\mathrm{d}t} + \frac{\partial \Psi_{\mathrm{bulk}}}{\partial J_{\mathrm{s}}} \left(\frac{\mathrm{d}J}{\mathrm{d}t} - \frac{1}{\rho_{\mathrm{f}}} \frac{\mathrm{d}m}{\mathrm{d}t} \right), \end{aligned}$$

where $e_{rr} = (\underline{\underline{e}})_{rr} = \frac{1}{2}\left(\frac{J^2}{C^2} - 1\right)$ and

$$\frac{\mathrm{d}e_{rr}}{\mathrm{d}t} = \frac{J}{C^2} \frac{\mathrm{d}J}{\mathrm{d}t} - \frac{J^2}{C^3} \frac{\mathrm{d}C}{\mathrm{d}t} = \frac{J}{C^2} \frac{\mathrm{d}J}{\mathrm{d}t} - 2 \frac{J^2}{C^3} \frac{\mathrm{d}e}{\mathrm{d}t}.$$

With this, and using (2.16c) we write

$$\frac{\mathrm{d}\Psi}{\mathrm{d}t} = \left[\left(\frac{\partial \Psi_{\mathrm{e}}}{\partial \underline{\underline{e}}} \right)_{\phi_1\phi_1} + \left(\frac{\partial \Psi_{\mathrm{e}}}{\partial \underline{\underline{e}}} \right)_{\phi_2\phi_2} - 2pJC^{-1} \right] \frac{\mathrm{d}e}{\mathrm{d}t} + p \frac{\mathrm{d}J}{\mathrm{d}t} + \frac{\partial \Psi_{\mathrm{bulk}}}{\partial J_{\mathrm{s}}} \left(\frac{\mathrm{d}J}{\mathrm{d}t} - \frac{1}{\rho_{\mathrm{f}}} \frac{\mathrm{d}m}{\mathrm{d}t} \right).$$

We now use (2.16b) and (2.16d) to rewrite the above equation as

$$\frac{\mathrm{d}\Psi}{\mathrm{dt}} = \left[\left(\frac{\partial \Psi_{\mathrm{e}}}{\partial \underline{\underline{e}}} \right)_{\phi_1\phi_1} + \left(\frac{\partial \Psi_{\mathrm{e}}}{\partial \underline{\underline{e}}} \right)_{\phi_2\phi_2} - 2pJC^{-1} \right] \frac{\mathrm{d}e}{\mathrm{dt}} + \frac{pJ\theta}{\rho_{\mathrm{f}}}.$$

Remark 3
In the incompressible solid limit the establishment of this expression rely on $\frac{\mathrm{d}J}{\mathrm{dt}} = \frac{1}{\rho_{\mathrm{f}}}\frac{\mathrm{d}m}{\mathrm{dt}} = \frac{J\theta}{\rho_{\mathrm{f}}}$.

Finally, (2.18) gives the following energy balance

$$\frac{\mathrm{d}(E_c + \Psi)}{\mathrm{dt}} = J\theta \left(\frac{1}{2}v^2 + \frac{p}{\rho_{\mathrm{f}}} \right),$$

where the right hand side stands for the internal and kinetic energy input due to the fluid source θ.

2.2.3 Energy compatible time scheme

We propose here an energy-compatible time scheme. Instead of the scheme introduced in (Gonzalez, 2000) and proposed in the heart model of (Chapelle et al., 2012) and the poromechanical model of (Chapelle and Moireau, 2014), we draw our inspiration from (Le Tallec and Hauret, 2002) and use a mid-point Newmark scheme. We lose the exact energy conservation property, but mid-point schemes are easier to handle and allow us to get a second-order energy conservation. We propose the following time discretization of (2.14)

$$\begin{cases} (\rho_0 + m^{n+\frac{1}{2}}) d_0 \dfrac{v^{n+1} - v^n}{\Delta t} + \left(1 + \dfrac{y^{n+\frac{1}{2}}}{R_0}\right) \dfrac{d_0}{R_0} \Sigma_{\mathrm{sph}}^{n+\frac{1}{2}\sharp} = (\rho_0 + m^{n+\frac{1}{2}}) d_0 f^{n+\frac{1}{2}} \\ + P_v^{n+\frac{1}{2}} \left(1 + \dfrac{y^{n+\frac{1}{2}}}{R_0} - \dfrac{J^{n+\frac{1}{2}\sharp} d_0}{2R_0} \left(1 + \dfrac{y^{n+\frac{1}{2}}}{R_0}\right)^{-2}\right)^2 \left(1 + J^{n+\frac{1}{2}\sharp} \dfrac{d_0}{R_0} \left(1 + \dfrac{y^{n+\frac{1}{2}}}{R_0}\right)^{-3}\right) & \text{(2.19a)} \\ \dfrac{y^{n+1} - y^n}{\Delta t} = v^{n+\frac{1}{2}}, & \text{(2.19b)} \\ \dfrac{m^{n+1} - m^n}{\Delta t} = J^{n+\frac{1}{2}\sharp} \theta^{n+\frac{1}{2}}, & \text{(2.19c)} \end{cases}$$

with, substituting (2.16c) into (2.16e), $\Sigma_{\mathrm{sph}}^{n+\frac{1}{2}\sharp}$ and $J^{n+\frac{1}{2}\sharp}$ defined by the following two relations (we recall that $J_{\mathrm{s}} = J - \frac{m}{\rho_{\mathrm{f}}} - \phi_0$)

$$\begin{cases} \Sigma_{\mathrm{sph}}^{n+\frac{1}{2}\sharp} = \left(\dfrac{\partial \Psi_{\mathrm{e}}}{\partial \underline{\underline{e}}} \right)_{\phi_1\phi_1} (y^{n+\frac{1}{2}}, J^{n+\frac{1}{2}\sharp}) + \left(\dfrac{\partial \Psi_{\mathrm{e}}}{\partial \underline{\underline{e}}} \right)_{\phi_2\phi_2} (y^{n+\frac{1}{2}}, J^{n+\frac{1}{2}\sharp}) \\ \qquad -2(J^{n+\frac{1}{2}\sharp})^2 C(y^{n+\frac{1}{2}})^{-3} \left(\dfrac{\partial \Psi_{\mathrm{e}}}{\partial \underline{\underline{e}}} \right)_{rr} (y^{n+\frac{1}{2}}, J^{n+\frac{1}{2}\sharp}) \\ \qquad +\sigma_{\mathrm{1D}}^{n+\frac{1}{2}} \left(1 + \lambda - 2\lambda (J^{n+\frac{1}{2}\sharp})^2 C(\underline{y}^{n+\frac{1}{2}})^{-3}\right), & \text{(2.20a)} \\ -\dfrac{\partial \Psi_{\mathrm{bulk}}}{\partial J_{\mathrm{s}}} (J^{n+\frac{1}{2}\sharp} - \dfrac{m^{n+\frac{1}{2}}}{\rho_{\mathrm{f}}} - \phi_0) = J^{n+\frac{1}{2}\sharp} C(y^{n+\frac{1}{2}})^{-2} \left(\dfrac{\partial \Psi_{\mathrm{e}}}{\partial \underline{\underline{e}}} \right)_{rr} (y^{n+\frac{1}{2}}, J^{n+\frac{1}{2}\sharp}) \\ \qquad +\lambda J^{n+\frac{1}{2}\sharp} C(y^{n+\frac{1}{2}})^{-2} \sigma_{\mathrm{1D}}^{n+\frac{1}{2}}. & \text{(2.20b)} \end{cases}$$

Remark 4 (Solid incompressibility)
In the solid incompressibility limit, the use of $J^{n+\frac{1}{2}}$ is justified by the following relation that replaces (2.20b):

$$J^{n+\frac{1}{2}} = 1 + \frac{m^{n+\frac{1}{2}}}{\rho_{\mathrm{f}}}. \tag{2.21}$$

In order to establish the compatibility of the scheme (2.19a) with the energy balance derived in Section 2.2.2, we remove the loadings $f = 0$ and $P_v = 0$, the active contribution $\sigma_{1\mathrm{D}} = 0$ and the solid damping $\eta = 0$. We look for a bound of our discrete energy in function of the fluid source term θ that we keep. Moreover, we perform the analysis in the specific case of an incompressible solid constituent, hence using (2.21), where the notation $J^{n+\frac{1}{2}}$ instead of $J^{n+\frac{1}{2}\sharp}$ is justified by the explicit affine relation that now links the variables J and m. We multiply (2.19a) by $v^{n+\frac{1}{2}}$. Using (2.19c), the first term gives

$$\begin{aligned}
(\rho_0 + m^{n+\frac{1}{2}})\left(\frac{v^{n+1}-v^n}{\Delta t}\right)\left(\frac{v^{n+1}+v^n}{2}\right) &= (\rho_0 + m^{n+\frac{1}{2}})\frac{(v^{n+1})^2-(v^n)^2}{2\Delta t} \\
= (\rho_0 + m^{n+1})\frac{(v^{n+1})^2}{2\Delta t} - (\rho_0 + m^n)\frac{(v^n)^2}{2\Delta t} &+ \frac{m^n - m^{n+1}}{2}\frac{(v^{n+1})^2}{2\Delta t} - \frac{m^{n+1}-m^n}{2}\frac{(v^n)^2}{2\Delta t} \\
&= \frac{E_c^{n+1}-E_c^n}{\Delta t} - \frac{1}{2}J^{n+\frac{1}{2}}\theta^{n+\frac{1}{2}}\frac{(v^n)^2+(v^{n+1})^2}{2},
\end{aligned} \tag{2.22}$$

with $E_c^n = \frac{1}{2}(\rho_0 + m_{\mathrm{f}}^n)v^n$ the discrete kinetic energy.

To make the following derivations simpler, we express $\underline{\underline{e}}$ and $\underline{\underline{C}}$ in function of J instead of the variable state m, according to the relation (2.21). About the second term, we write that thanks to (2.19b),

$$\left(1 + \frac{y^{n+\frac{1}{2}}}{R_0}\right)\frac{y^{n+1}-y^n}{R_0\Delta t} = \frac{1}{\Delta t}\left[\left(\frac{y^{n+1}}{R_0} + \frac{(y^{n+1})^2}{2R_0^2}\right) - \left(\frac{y^n}{R_0} + \frac{(y^n)^2}{2R_0^2}\right)\right] = \frac{e^{n+1}-e^n}{\Delta t}, \tag{2.23}$$

with $e^n = (\underline{\underline{e}}(y^n, J^n))_{\phi_1\phi_1} = (\underline{\underline{e}}(y^n, J^n))_{\phi_2\phi_2}$ that depends only on y^n. With $\underline{\underline{e}}^n = \underline{\underline{e}}(y^n, J^n)$ and $\underline{\underline{e}}^{n+\frac{1}{2}\sharp} = \underline{\underline{e}}(y^{n+\frac{1}{2}}, J^{n+\frac{1}{2}})$, we have the following Taylor expansions:

$$\begin{aligned}
\Psi_{\mathrm{e}}^{n+1} = \Psi_{\mathrm{e}}(\underline{\underline{e}}^{n+1}) &= \Psi_{\mathrm{e}}(\underline{\underline{e}}^{n+\frac{1}{2}\sharp}) + (\underline{\underline{e}}^{n+1} - \underline{\underline{e}}^{n+\frac{1}{2}\sharp}) : \frac{\partial \Psi_{\mathrm{e}}}{\partial \underline{\underline{e}}}(\underline{\underline{e}}^{n+\frac{1}{2}\sharp}) \\
&\quad + \frac{1}{2}(\underline{\underline{e}}^{n+1} - \underline{\underline{e}}^{n+\frac{1}{2}\sharp})^2 : \frac{\partial^2 \Psi_{\mathrm{e}}}{\partial \underline{\underline{e}}^2}(\underline{\underline{e}}^{n+\frac{1}{2}\sharp}) + O((\underline{\underline{e}}^{n+1} - \underline{\underline{e}}^{n+\frac{1}{2}\sharp})^3), \\
\Psi_{\mathrm{e}}^{n} = \Psi_{\mathrm{e}}(\underline{\underline{e}}^{n}) &= \Psi_{\mathrm{e}}(\underline{\underline{e}}^{n+\frac{1}{2}\sharp}) - (\underline{\underline{e}}^{n+\frac{1}{2}\sharp} - \underline{\underline{e}}^{n}) : \frac{\partial \Psi_{\mathrm{e}}}{\partial \underline{\underline{e}}}(\underline{\underline{e}}^{n+\frac{1}{2}\sharp}) \\
&\quad + \frac{1}{2}(\underline{\underline{e}}^{n+\frac{1}{2}\sharp} - \underline{\underline{e}}^{n})^2 : \frac{\partial^2 \Psi_{\mathrm{e}}}{\partial \underline{\underline{e}}^2}(\underline{\underline{e}}^{n+\frac{1}{2}\sharp}) + O((\underline{\underline{e}}^{n+\frac{1}{2}\sharp} - \underline{\underline{e}}^{n})^3),
\end{aligned}$$

and

$$\begin{aligned}
\underline{\underline{e}}^{n+1} - \underline{\underline{e}}^{n+\frac{1}{2}\sharp} &= d_y\underline{\underline{e}}(y^{n+\frac{1}{2}}, J^{n+\frac{1}{2}}) \cdot \frac{y^{n+1}-y^n}{2} + d_J\underline{\underline{e}}(y^{n+\frac{1}{2}}, J^{n+\frac{1}{2}}) \cdot \frac{J^{n+1}-J^n}{2} \\
&\quad + O(((J^{n+1}-J^n),(y^{n+1}-y^n))^2), \\
\underline{\underline{e}}^{n+\frac{1}{2}\sharp} - \underline{\underline{e}}^{n} &= d_y\underline{\underline{e}}(y^{n+\frac{1}{2}}, J^{n+\frac{1}{2}}) \cdot \frac{y^{n+1}-y^n}{2} + d_J\underline{\underline{e}}(y^{n+\frac{1}{2}}, J^{n+\frac{1}{2}}) \cdot \frac{J^{n+1}-J^n}{2} \\
&\quad + O(((J^{n+1}-J^n),(y^{n+1}-y^n))^2).
\end{aligned}$$

Assuming that $d_y \underline{\underline{e}}$ and $d_J \underline{\underline{e}}$ are bounded, by subtraction,

$$\Psi_{\mathrm{e}}^{n+1} - \Psi_{\mathrm{e}}^{n} = (\underline{\underline{e}}^{n+1} - \underline{\underline{e}}^{n}) : \frac{\partial \Psi_{\mathrm{e}}}{\partial \underline{\underline{e}}}(\underline{\underline{e}}^{n+\frac{1}{2}\sharp}) + O(((y^{n+1} - y^n), (J^{n+1} - J^n))^3).$$

From now on we assume that $O(y^{n+1} - y^n) = O(J^{n+1} - J^n) = O(\Delta t)$, then

$$\begin{aligned}\frac{\Psi_{\mathrm{e}}^{n+1} - \Psi_{\mathrm{e}}^{n}}{\Delta t} = \frac{e_{rr}^{n+1} - e_{rr}^{n}}{\Delta t} \left(\frac{\partial \Psi_{\mathrm{e}}}{\partial \underline{\underline{e}}} \right)_{rr} (\underline{\underline{e}}^{n+\frac{1}{2}\sharp}) \\ + \frac{e^{n+1} - e^{n}}{\Delta t} \left[\left(\frac{\partial \Psi_{\mathrm{e}}}{\partial \underline{\underline{e}}} \right)_{\phi_1 \phi_1} (\underline{\underline{e}}^{n+\frac{1}{2}\sharp}) + \left(\frac{\partial \Psi_{\mathrm{e}}}{\partial \underline{\underline{e}}} \right)_{\phi_2 \phi_2} (\underline{\underline{e}}^{n+\frac{1}{2}\sharp}) \right] + O(\Delta t^2), \quad (2.24)\end{aligned}$$

with $e_{rr}^n = (\underline{\underline{e}}^n)_{rr}$ so that

$$e_{rr}^{n+1} - e_{rr}^{n} = \frac{1}{2} \left(\frac{(J^{n+1})^2}{C(y^{n+1})^2} - \frac{(J^n)^2}{C(y^n)^2} \right).$$

Again, Taylor expansions give

$$\begin{aligned}\frac{(J^{n+1})^2}{C(y^{n+1})^2} = \frac{(J^{n+\frac{1}{2}})^2}{C(y^{n+\frac{1}{2}})^2} \cdot \left(1 + \frac{J^{n+1} - J^n}{J^{n+\frac{1}{2}}} + \left(\frac{J^{n+1} - J^n}{2J^{n+\frac{1}{2}}} \right)^2 \right) \cdot \left[1 + \frac{C'(y^{n+\frac{1}{2}})}{C(y^{n+\frac{1}{2}})} (y^{n+1} - y^n) \right. \\ \left. + \left(\frac{C''(y^{n+\frac{1}{2}})}{C(y^{n+\frac{1}{2}})} + \frac{C'(y^{n+\frac{1}{2}})^2}{C(y^{n+\frac{1}{2}})^2} \right) \frac{(y^{n+1} - y^n)^2}{4} + O(\Delta t^3) \right]^{-1} \\ = \frac{(J^{n+\frac{1}{2}})^2}{C(y^{n+\frac{1}{2}})^2} \left[1 + \frac{J^{n+1} - J^n}{J^{n+\frac{1}{2}}} - \frac{C'(y^{n+\frac{1}{2}})}{C(y^{n+\frac{1}{2}})} (y^{n+1} - y^n) + \left(\frac{J^{n+1} - J^n}{2J^{n+\frac{1}{2}}} \right)^2 \right. \\ - \frac{C'(y^{n+\frac{1}{2}})}{J^{n+\frac{1}{2}} C(y^{n+\frac{1}{2}})} (y^{n+1} - y^n)(J^{n+1} - J^n) \\ \left. - \left(\frac{C''(y^{n+\frac{1}{2}})}{C(y^{n+\frac{1}{2}})} + \frac{C'(y^{n+\frac{1}{2}})^2}{C(y^{n+\frac{1}{2}})^2} \right) \frac{(y^{n+1} - y^n)^2}{4} + O(\Delta t^3) \right],\end{aligned}$$

and similarly

$$\begin{aligned}\frac{(J^n)^2}{C(y^n)^2} = \frac{(J^{n+\frac{1}{2}})^2}{C(y^{n+\frac{1}{2}})^2} \left[1 - \frac{J^{n+1} - J^n}{J^{n+\frac{1}{2}}} + \frac{C'(y^{n+\frac{1}{2}})}{C(y^{n+\frac{1}{2}})} (y^{n+1} - y^n) + \left(\frac{J^{n+1} - J^n}{2J^{n+\frac{1}{2}}} \right)^2 \right. \\ - \frac{C'(y^{n+\frac{1}{2}})}{J^{n+\frac{1}{2}} C(y^{n+\frac{1}{2}})} (y^{n+1} - y^n)(J^{n+1} - J^n) \\ \left. - \left(\frac{C''(y^{n+\frac{1}{2}})}{C(y^{n+\frac{1}{2}})} + \frac{C'(y^{n+\frac{1}{2}})^2}{C(y^{n+\frac{1}{2}})^2} \right) \frac{(y^{n+1} - y^n)^2}{4} + O(\Delta t^3) \right],\end{aligned}$$

Using that $C'(y^{n+\frac{1}{2}}) = 2e'(y^{n+\frac{1}{2}})$ and that

$$e'(y^{n+\frac{1}{2}})(y^{n+1} - y^n) = e^{n+1} - e^n + O(\Delta t^3),$$

this enables us to write

$$e_{rr}^{n+1} - e_{rr}^{n} = \frac{(J^{n+\frac{1}{2}})^2}{C(y^{n+\frac{1}{2}})^2} \left(\frac{J^{n+1} - J^n}{J^{n+\frac{1}{2}}} - 2\frac{e^{n+1} - e^n}{C(y^{n+\frac{1}{2}})} + O(\Delta t^3) \right).$$

Finally, (2.24) rewrites

$$\frac{\Psi_{\mathrm{e}}^{n+1}-\Psi_{\mathrm{e}}^{n}}{\Delta t} = \frac{e^{n+1}-e^{n}}{\Delta t}\left[\left(\frac{\partial \Psi_{\mathrm{e}}}{\partial \underline{\underline{e}}}\right)_{\phi_1\phi_1}(\underline{\underline{e}}^{n+\frac{1}{2}\sharp}) + \left(\frac{\partial \Psi_{\mathrm{e}}}{\partial \underline{\underline{e}}}\right)_{\phi_2\phi_2}(\underline{\underline{e}}^{n+\frac{1}{2}\sharp}) - 2\frac{(J^{n+\frac{1}{2}})^2}{C(y^{n+\frac{1}{2}})^3}\left(\frac{\partial \Psi_{\mathrm{e}}}{\partial \underline{\underline{e}}}\right)_{rr}(\underline{\underline{e}}^{n+\frac{1}{2}\sharp})\right] + \frac{J^{n+\frac{1}{2}}}{C(y^{n+\frac{1}{2}})^2}\frac{J^{n+1}-J^{n}}{\Delta t}\left(\frac{\partial \Psi_{\mathrm{e}}}{\partial \underline{\underline{e}}}\right)_{rr}(\underline{\underline{e}}^{n+\frac{1}{2}\sharp}) + O(\Delta t^2).$$

Using (2.23) and (2.20a), the second term of the multiplication of (2.19a) by $v^{n+\frac{1}{2}}$ rewrites

$$\frac{\Psi_{\mathrm{e}}^{n+1}-\Psi_{\mathrm{e}}^{n}}{\Delta t} - \frac{J^{n+\frac{1}{2}}}{C(y^{n+\frac{1}{2}})^2}\frac{J^{n+1}-J^{n}}{\Delta t}\left(\frac{\partial \Psi_{\mathrm{e}}}{\partial \underline{\underline{e}}}\right)_{rr}(\underline{\underline{e}}^{n+\frac{1}{2}\sharp}) + O(\Delta t^2)$$

and, using also (2.22), (2.19c) and (2.21), we end up with the following discrete energy balance, for $\mathcal{E}^n = E_c^n + \Psi_{\mathrm{e}}^n$ – we recall that the incompressible solid does not store any energy in Ψ_{bulk} –

$$\frac{\mathcal{E}^{n+1}-\mathcal{E}^{n}}{\Delta t} = J^{n+\frac{1}{2}}\theta^{n+\frac{1}{2}}\left[\frac{(v^n)^2+(v^{n+1})^2}{4} + \frac{p^{n+\frac{1}{2}\sharp}}{\rho_{\mathrm{f}}}\right] + O(\Delta t^2),$$

with the discrete pressure

$$p^{n+\frac{1}{2}\sharp} = \frac{J^{n+\frac{1}{2}}}{C(y^{n+\frac{1}{2}})^2}\left(\frac{\partial \Psi_{\mathrm{e}}}{\partial \underline{\underline{e}}}\right)_{rr}(\underline{\underline{e}}^{n+\frac{1}{2}\sharp}).$$

This second-order energy conservation is consistent with (Le Tallec and Hauret, 2002) and justifies our mid-point discretizations.

2.3 Numerical simulations

The cost-effectiveness of the 0D model and its relative simplicity of use makes it a very interesting tool when trying to simulate various physiological situations. As a matter of fact, calibration of complex dynamical models and initial state estimation requires the possibility to run many tests with different sets of parameters. In addition to the wide clinical application potential of the illustrations of this section, the results presented will also be very useful to calibrate and estimate initial states in more complex 3D models.

We perform simulations of contraction and myocardial perfusion, first of a healthy heart. Then, we introduce stenosis of a large coronary artery and assess typical physiological indicators used in cardiology. Finally, we modify the properties of the porous medium to mimic diseases affecting the microcirculation, and we simulate the inotropic effect.

This work was made in collaboration with Radomir Chabiniok.

2.3.1 Healthy heart simulation

We assume the incompressibility of the solid constituent, and the hyperelastic potential Ψ_{e} is in the form

$$\Psi_{\mathrm{e}} = C_0\exp(C_1(J_1-3)^2) + C_2\exp(C_3(J_4-1)^2) + C_4(J_3-1-\ln J_3).$$

We use the time scheme of Section 2.2.3, and parameters of Table 2.6, that were calibrated to reproduce a realistic simulation of a healthy heart at rest. We plot the cavity flux, the perfusion mass m, the perfusion, cavity and coronary artery pressures and the coronary artery and venous fluxes

$$Q_{ca} = V_{myo}\, k_{ca}(P_{ca} - p) \quad \text{and} \quad Q_{cv} = V_{myo}\, k_{cv}(p - P_{sv}).$$

Calibration is performed according to the following criteria:

- the volume fraction of perfusion blood within the myocardium is 12 to 15% (Spaan, 1985),
- clinical data show that the myocardial perfusion flux is typically 1mL/100g/s (and our myocardium reference volume is 130mL),
- ejection fraction and aortic pressure and flux had been previously calibrated in the model with respect to measured clinical data.

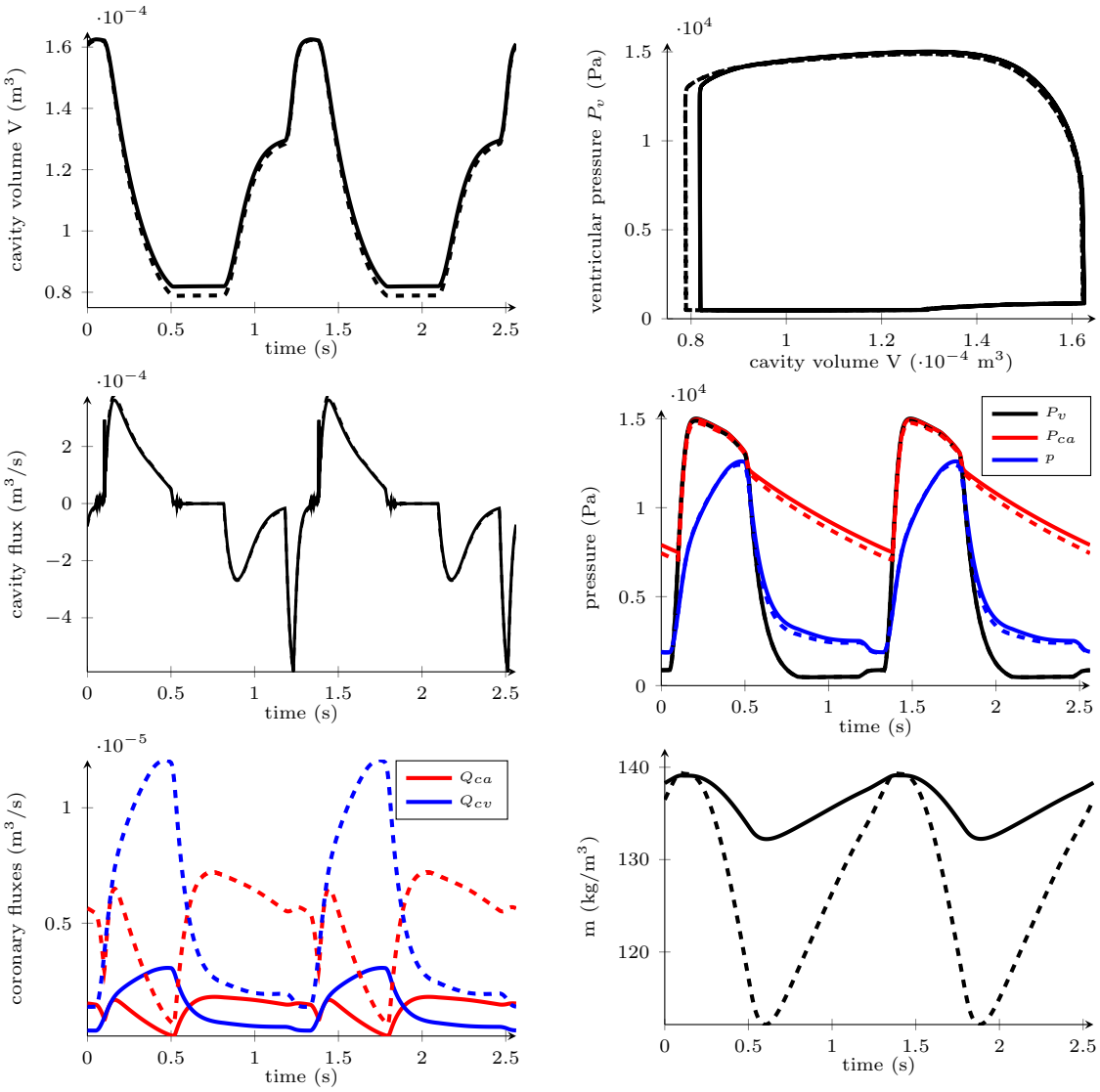

Figure 2.5 – **Cardiac cycle obtained with the 0D-model. Healthy case.** In solid line, $F_{\text{micro}} = 1$, in dashed line are the results with vasodilatation $F^{\text{vd}}_{\text{micro}} = 4$.

Δt	C_0, C_2	C_1, C_3	C_4	ρ_0, ρ_f	R_0	d	λ
1e-3	500	0.6	26000	1000	0.02	0.014	0.44
k_{ca}, k_{cv}	R_p	C_p	R_d	C_d	R_c	C_c	P_{sv}
2e-6	1.7e7	2.35e-10	1.55e8	1.1e-8	1.7e7	8.5e-11	500
σ_0	k_0	α	η	μ_c	K_{at}	K_p	K_{ar}
55e3	2.95e5	1.5	70	70	9e-6	5e-10	1.3e-5

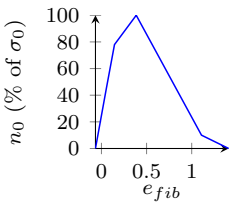

Figure 2.6 – **Parameter table and Starling effect function n_0.** All units are SI.

In Figure 2.5, the perfusion mass and pressure show the systolic flow impediment (Westerhof et al., 2006; Kajiya et al., 2007): blood is drained out of the myocardium during the contraction (systole), and coronary circulation is reestablished during the relaxation (diastole).

Vasodilatation is a regulation process by which the organism adapts the amount of blood perfusion to the physiological state (e.g. increased activity of heart). A decrease of vascular resistance by vasodilatation of small arteries, arterioles, venules and small veins allows increasing blood flow. In the case of the myocardial perfusion, this corresponds in our model to an augmentation of k_{ca} (arterial vasodilatation) and k_{cv} (venous vasodilatation). In order to reproduce this phenomenon, we consider that the two micro-vascular coronary conductances k_{ca} and k_{cv} are multiplied by a factor that can cover the interval $[F_{\text{micro}}\,,\, F^{\text{vd}}_{\text{micro}}]$, with $F_{\text{micro}} = 1$ for our healthy heart at rest, meaning that the conductances k_{ca} and k_{cv} are calibrated to the conditions at rest, and we assume $F^{\text{vd}}_{\text{micro}} = 4F_{\text{micro}}$ for maximal vasodilation in a healthy heart (Chilian et al., 1989).

Figure 2.5 reproduces the heart perfusion at baseline and at maximum vasodilatation, and illustrates that the healthy heart can increase the perfusion flow by approximately factor 4 –the so-called Coronary Flow Reserve (CFR) (Gould et al., 1990) defined by the ratio of the mean coronary flow at baseline to the one at maximum vasodilatation, see Table 2.1.

We introduce the notation $|\varphi|$ for the mean in time of a physical quantity φ.

2.3.2 Macro vascular stenosis

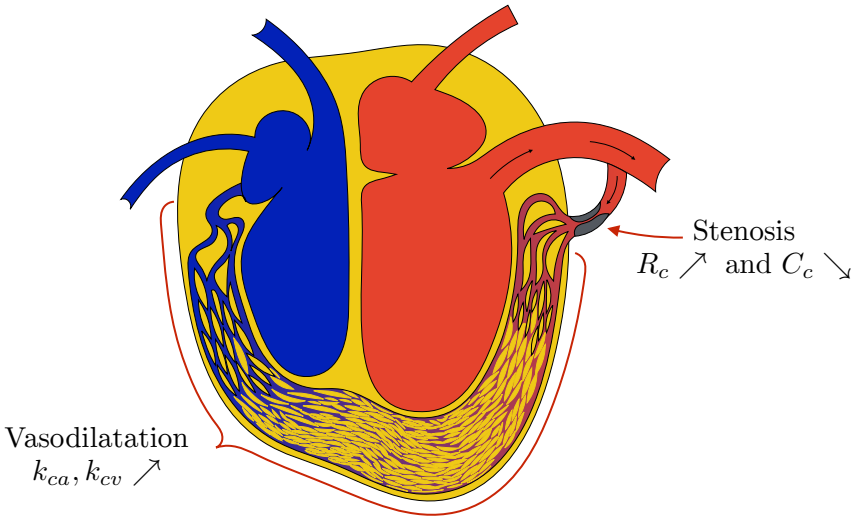

Figure 2.7 – **Coronary vasodilatation and stenosis.** To model coronary vasodilatation, k_{ca} and k_{cv} are multiplied by factor $F^{\text{vd}}_{\text{micro}} > 1$. To reproduce a macro-vascular coronary stenosis, R_c (and C_c^{-1}) are multiplied by factor F_{sten} that goes to up to 100 in our model.

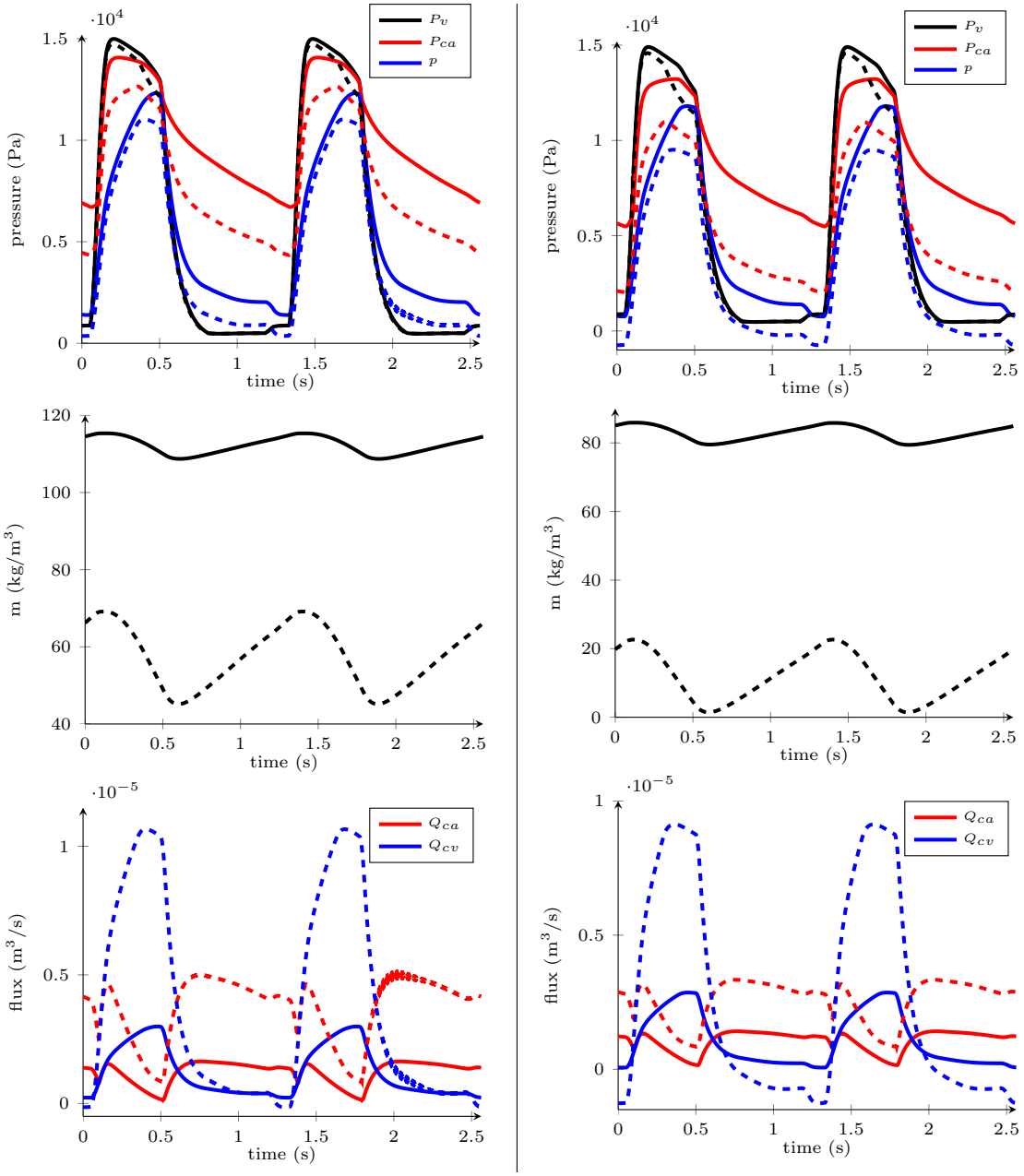

Figure 2.8 – **Stenosis simulations. On the left,** $F_{\text{sten}} = 40$**, on the right** $F_{\text{sten}} = 100$**.** In solid line, $F_{\text{micro}} = 1$, in dotted line are the results with vasodilatation $F^{\text{vd}}_{\text{micro}} = 4$.

A stenosis is an abnormal narrowing of blood vessel in coronaries, typically due to deposits in endothelial parts and atherosclerosis (Mann et al., 2014). In the coronary network it leads to ischemic heart disease. In the case of the coronaries, we distinguish two types of stenosis: a macro-vascular stenosis (typically due to atherosclerosis) that affects large coronary arteries, and micro-vascular diseases when smaller coronary vessels down to arterioles and capillary bed are concerned. The first ones can be treated interventionally by percutaneous coronary angioplasty (PTCA, e.g. by implanting stent), or surgically by coronary artery bypass grafting (CABG), while these procedures would have a limited effect if the microvascular component is predominant.

With our modeling, the microvascular stenosis corresponds in the model to $F_{\text{micro}} < 1$. In

order to reproduce macro-vascular coronary stenosis, we introduce a factor F_{sten} that multiplies the resistance of large coronary arteries R_c –and C_c^{-1} to keep the $R_c - C_c$ time constant –, see Figure 2.3. In our calibrated model, a healthy heart corresponds to $F_{\text{sten}} = 1$, whereas clinical observation of significant stenosis show that the vessel effective radius can be divided by 10, which, roughly speaking, would correspond to $F_{\text{sten}} = 100$.

To better assess the severity of stenosis than by a simple geometrical measurement (Fischer et al., 2002), currently gold standard functional measurements rely on the ratio of its downstream to upstream mean pressures assessed at maximum vasodilatation (with the use of vasodilators): the so-called Fractional Flow Reserve (FFR) (Pijls et al., 1993). Typically, FFR < 0.8 characterizes ischemia, and FFR < 0.75 suggests intervention (e.g. stenting) (Bech et al., 2001; Pijls et al., 2007). In our case, it is of high clinical interest to calculate by post-processing this ratio, that reads FFR $= |P_{ca}|/|P_{ar}|$.

Table 2.1 summarizes our results. We can see for example that in our most severe stenosis case, the patient's vessels would have to dilate even at rest to keep a viable myocardium perfusion flux (around 1.3mL/s). Although this vasodilatation at rest is automatically regulated, it decreases the potential of further dilatation at exercise (stress, etc...): the CFR is divided by factor two compared to a healthy case. While FFR $= 0.76$ for $F_{\text{sten}} = 40$ signifies a borderline stenosis, FFR $= 0.56$ for $F_{\text{sten}} = 100$ could suggest an intervention.

$F_{\text{micro}}, F_{\text{micro}}^{\text{vd}}$	F_{sten}	Δm (kg/m^3)	$\lvert Q_a \rvert$ (mL/s)	FFR	CFR
1	1	6.8	1.33		
4	1	27	5.16	1	3.9
1	40	6.6	1.22		
4	40	24	3.74	0.76	2.8
1	100	6.4	1.07		
4	100	21	2.58	0.56	1.9

Table 2.1 – **Numerical results corresponding to Figure 2.8 and 2.5.** We compute the increase of blood mass per cycle and the mean flow, for a virtual heathy patient and then in the presence of stenosis. We also derive the indicator FFR and CFR, and see that a serious stenosis can divide by factor 2 the CFR.

2.3.3 Micro and macro vascular diseases

Until now, we have considered that $F_{\text{micro}}^{\text{vd}} = 4$, which corresponds to a healthy micro-circulation in the coronaries. In the case of a micro-vascular stenosis, $F_{\text{micro}} < 1$ and it actually corresponds to a imaginary state, because even at rest the heart vessels are dilated to maintain a viable coronary flux (about 1.33 mL/s in our case); but the important consequence is that $F_{\text{micro}}^{\text{vd}}$ decreases and with it the CFR that measures the heart potential of vasodilation.

In figure 2.9, we plot the mean arterial flow in the coronaries (and the CFR), and the FFR for different values of $(F_{\text{micro}}^{\text{vd}}, F_{\text{sten}})$. Each curve corresponds to a micro-vascular state F_{micro} (with or without vasodilatation), and in abscises is the macro-vascular stenosis F_{sten} simulated. For example, for a given micro-circulation state $F_{\text{micro}}^{\text{vd}}$, moving along a curve to the left can be interpreted as "virtual stenting". This illustrates the limit of the single FFR indicator when evaluating the relevance of stenting: for example, if the micro-vascular circulation is affected, stenting can bring FFR to 1, but doesn't always sufficiently improve the CFR.

To overcome the limit of simple functional index as FFR, the model of perfusion offers other quantities such as $|m|$, see Figure 2.9, indirectly accessible by non-invasive imaging (e.g.

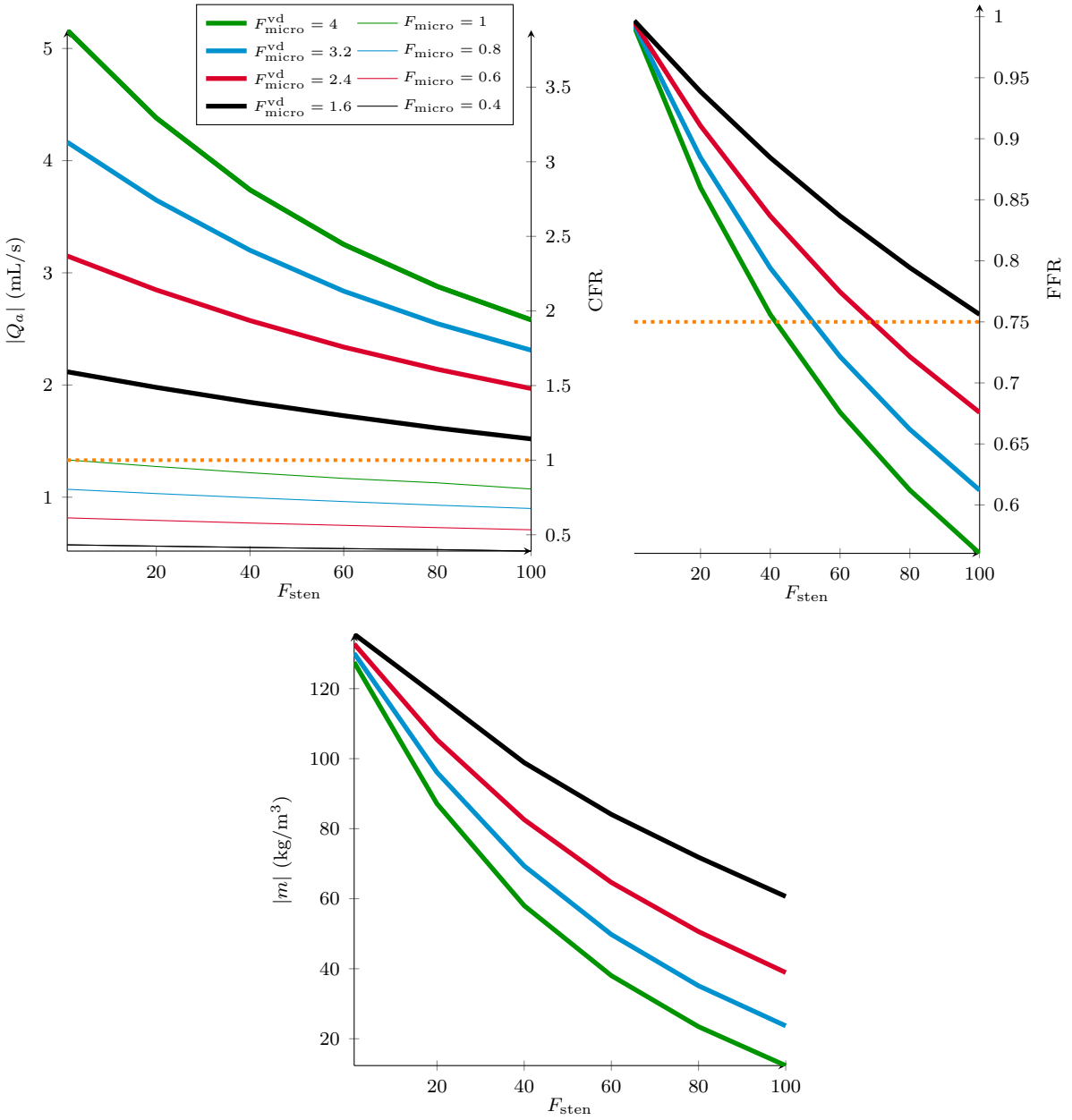

Figure 2.9 – **Main indicators for micro/macro vascular diseases.** In function of F_{sten}, we plot the mean arterial coronary flow (and CFR, on the left), the FFR (on the right) and the mean fluid mass $|m|$ (on the bottom), at maximal vasodilatation in thick lines, and at –eventually virtual –"baseline" in thin lines. Each color corresponds to a microvascular state. In orange are the flow necessary for cardiac activity at rest (assumed here to be 1.33 mL/s) –i.e. CFR = 1 – on the left, and the limit case FFR = 0.75 on the right.

perfusion MRI or PET) (Morton et al., 2012).

2.3.4 Inotropic effect

Inotropy is a regulation process that intervenes to increase the cardiac output when needed. It can be spontaneous in physiological situations (e.g. during exercise) or in pathophysiology

to compensate decreased cardiac output in heart failure. Drugs with inotropic effect can be considered in the therapy of some type of heart failure. Increasing stresses in the myocardium will effectively strengthen the cardiac output flow. However, it is known from physiology that the negative counterpart is that it also reinforces the flow impediment and disturbs the coronary circulation, essential to the myocardium contraction activity. Since our model of porous myocardium accounts for these interactions, it could be well-suited in targeting personalized therapy.

Therefore, in this last section we perform the study the so called inotropic effect, increasing the heart contractility.

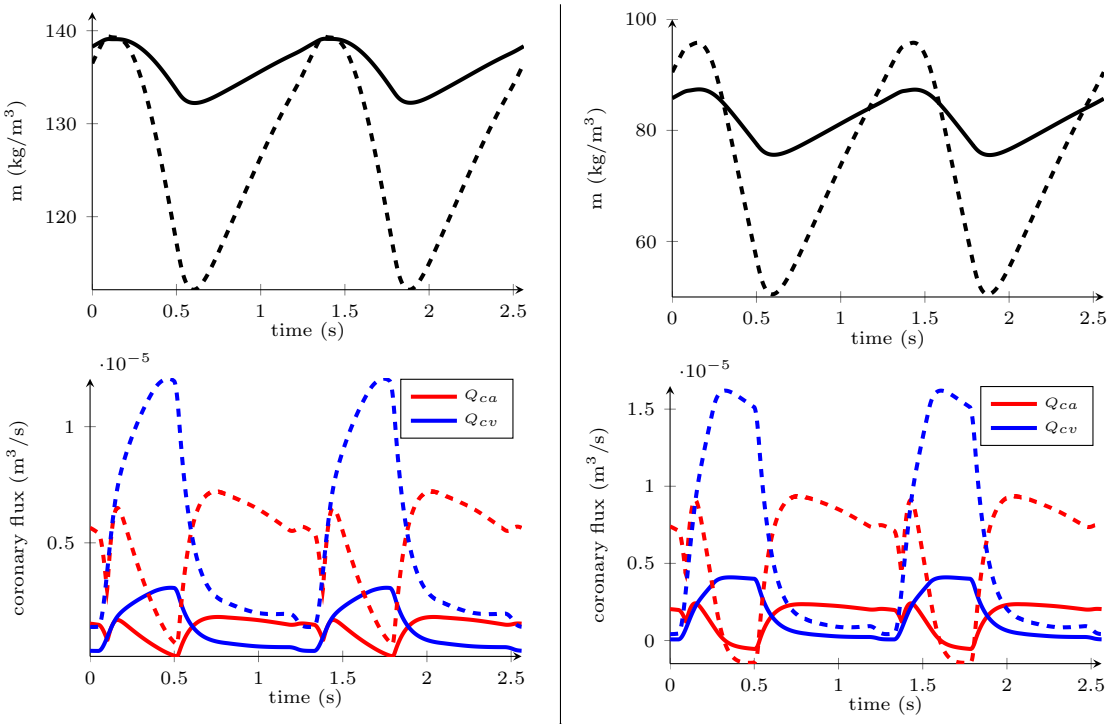

Figure 2.10 – **Baseline (on the left) versus inotropic heart (i.e. contractility σ_0 increased by factor 1.5, on the right).** We compare the mean fluid mass $|m|$ (on the top) and the coronary fluxes (on the bottom). In solid line, $F_{\text{micro}} = 1$, in dashed line are the results with vasodilatation $F^{\text{vd}}_{\text{micro}} = 4$.

Comparison made on Figure 2.10 illustrates the flow impediment strengthening, and shows that the mean fluid mass $|m|$ decreases. Indeed, stronger stresses drain more blood out of the myocardium.

We finally re-run the whole set of simulations of Section 2.3.3, see Figure 2.11, to cross-compare the effect of contractility and micro/macro vascular stenosis onto our set of indicators. This illustrates how the inotropic effect can compensate some microvascular diseases, strengthening the perfusion flow. For example, for $F^{\text{vd}}_{\text{micro}} = 3.2$, a contractility increased by factor 1.5 almost re-establishes the output flow corresponding to $F^{\text{vd}}_{\text{micro}} = 4$. In the meantime, a higher flow and a better circulation reduce the mean fluid mass $|m|$.

Nevertheless, the flow increase permitted by stronger muscular activity is accompanied by a boost in oxygen and nutriment demand within the myocardium. For further interpretation, and in order to evaluate the efficiency of this process, we would need to counterbalance the gain in output flow according to the rise in perfusion demand.

Our results show that the model gives promising qualitative reproductions of complex and

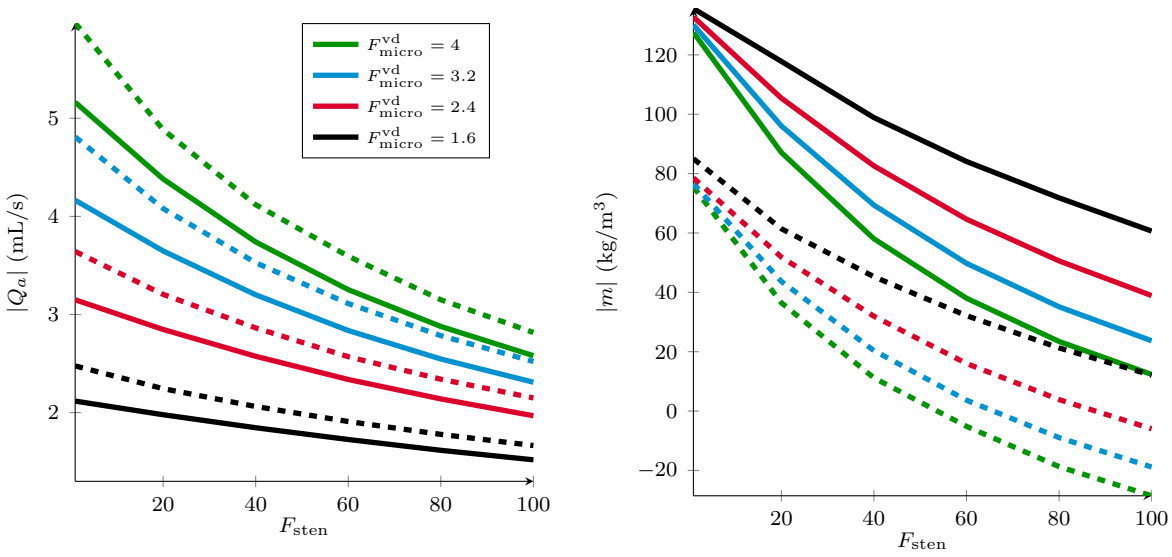

Figure 2.11 – **Main indicators for micro/macro vascular diseases, study of the inotropic effect.** In function of F_{sten}, we plot the mean arterial coronary flow (and CFR, on the left) and the mean fluid mass $|m|$ (on the right), at maximal vasodilatation. Each color corresponds to a microvascular state, solid lines represent a normal heart, whereas dashed lines reproduce an inotropic heart.

coupled physiological phenomena, and this paves the way for future quantitative study using clinical or experimental data.

2.4 Conclusion

To conclude, adapting (Chapelle et al., 2012), we have derived here a complete 3D cardiac model that now takes into account the myocardium perfusion and links the coronary circulation to the previous circulation model.

Drawing our inspiration from (Caruel et al., 2014), we then performed a dimensional reduction to write a 0D perfused heart model. It allowed us to model new physical quantities (the perfusion mass and pressure) and to reproduce phenomena such as the flow impediment that occur in systole, and the vasodilatation that enables cardiac activity adaptation. We ended up illustrating the relevance of such improvements, reproducing coronary vascular diseases that represent a wide majority of heart diseases, and that we could not explain with previous models. The porous model accounts for the mechanical interactions between the coronary circulation and the myocardium activity, and allows to illustrate qualitatively the inotropic effect.

As in (Caruel et al., 2014), this approach was motivated by the calculation efficiency of 0D simulations, which have proven again to be very effective, reproducing quickly and faithfully complex physiological phenomena. Indeed, a cardiac cycle is computed in about one minute, and we can consider using this model for physiological monitoring over a period of time. Nevertheless, here the limiting factor in cost-efficiency was the first guess of the initial state. Indeed, the heart cycle does not contain an equilibrium state, and the initial state cannot be calculated as the solution of a static problem, as it is often made in dynamical resolution. Therefore, the computation of numerous cycles (here about 50) is necessary in order to reach the actual periodic cycle. Progress could be made in this direction. Again, the final periodic cycle that we reach will be essential in future work for the calibration of more complex 3D models.

Further perspectives could also include quantitative studies of these physiological processes and others (e.g. chronotropy), and investigation of the dependance of the muscle cells activity on the nutriments and oxygen supply permitted by blood.

Chapter 3

Effective and energy-preserving time discretization for a general nonlinear poromechanical formulation

This chapter is in the verbatim form of a paper accepted for publication in *Computers & Structures*.

Effective and energy-preserving time discretization for a general nonlinear poromechanical formulation

B. Burtschell, D. Chapelle*, P. Moireau
Inria and Paris-Saclay University, France

Abstract

We consider a general nonlinear poromechanical model, formulated based on fundamental thermodynamics principle, suitable for representing the coupling of rapid internal fluid flows with large deformations of the solid, and compatible with a wide class of constitutive behavior. The objective of the present work is to propose for this model a time discretization scheme of the partitioned type, to allow the use of existing time schemes – and possibly separate solvers – for each component of the model, i.e. for the fluid and the solid. To that purpose, we adapt and extend an earlier proposed approach devised for fluid-structure interaction in an Arbitrary Lagrangian-Eulerian framework. We then establish an energy estimate for the resulting time scheme, in a form that is consistent with the underlying energy principle in the poromechanical formulation, up to some numerical dissipation effects and some perturbations that we have carefully identified and assessed. In addition, we provide some numerical illustrations of our numerical strategy with test problems that present typical features of large strains and rapid fluid flows, and also a case of singular transition related to total drainage. An example of challenging application envisioned for this model and associated numerical coupling scheme concerns the perfusion of the heart.

1 Introduction

Recently, novel challenging applications such as cardiac modeling have required the introduction of general formulations coupling porous flows and hyperelastic formulations, and compatible with large displacements, finite strains and strong inertial effects both in the solid and in the fluid. In this context, a general poromechanics formulation was proposed in [10] based on fundamental thermodynamics principles, see also [41] where the same type of model was subsequently considered. As inertia effects and large displacements are considered, the final formulation is very similar to the coupling of hyperelastic dynamics for the skeleton – i.e., the solid constituent – with a conservative form of the so-called Arbitrary Lagrangian–Eulerian (ALE) formulation of the compressible Navier–Stokes equations [15, 33] set on the same domain, hence, with a domain velocity given by the skeleton physical velocity. The compressible analogy comes from the product of the fluid volume fraction with the fluid density that, together, play the role of a varying fluid density. Finally, when compared with standard fluid-structure interaction (FSI) problems, we have the additional distributed coupling term representing the interaction between the two phases [6, 13, 14]. From this analogy, [10] introduced a time scheme with an energy balance at the time-discrete level inspired from the work [32] initially devoted to classical fluid-structure interaction problems. The proposed time scheme combined in a monolithic formulation a mid-point energy-conserving extension of the mid-point Newmark scheme and a second-order Crank–Nicolson scheme for the fluid– with an additional specific treatment

*Corresponding author: dominique.chapelle@inria.fr

of the Darcy term discretization in order to respect the energy balance in the fluid–skeleton interaction. This scheme was proved in [10] to be second-order accurate and unconditionally stable, similarly to its initial fluid-structure counterpart in [32].

However, this scheme has some drawbacks when considering its practical use in simulation software – in industrial codes in particular – as it implies the use of a Newton-Raphson solution procedure on a monolithic fluid+solid formulation. Therefore, we propose in the present article an alternative time discretization inspired from state-of-the-art partitioned FSI time-schemes [18, 19, 27]. Partitioned solvers aim at solving the interaction problem by coupling independent solvers for the fluid and the solid [2, 3, 21, 28, 29, 35]. Therefore, they are much more modular than monolithic approaches and allow the use of existing *legacy software* [30]. However, the computational efficiency of partitioned approaches compared with a monolithic approach must be assessed [4, 8, 27, 28]. Hence, the question of monolithic versus partitioned approaches has already been raised in other specific poromechanics formulations, typically with Darcy flows [34].

As we aim at relying on a classical Newmark scheme for the solid with an energy-conserving extension for general hyperelastic laws [22, 25], we set out in this article to propose our time-scheme based on the recent partitioned FSI scheme of [1]. This scheme combines a Newmark scheme for the solid [22] with an effective Chorin-Temam projection scheme in the fluid [11, 23, 39]. The fluid viscous sub-step, taking into account the convective–viscous effects and the geometrical non-linearities, is treated explicitly. Moreover, at each time step the projection sub-step is implicitly coupled with the structure with Robin coupling conditions derived from Nitsche's interface method [7, 36]. The specificity of this coupling strategy is twofold. First, it allows to prove stability independently of the added-mass effect typically present in blood flow simulations, which in particular is known to compromise the stability of explicit coupling – time-marching – schemes, see [8]. Note that this added-mass effect has also been evidenced in poroelastic models with an impact that directly correlates with fluid fraction [5]. Secondly, the coupling strategy of [1] is, to our best knowledge, the only time scheme that allows for non-linear conservative time-stepping within a 3D general solid, as opposed to the more direct Dirichlet-Neumann semi-implicit coupling [19]. From this starting point, we propose in the present article a partitioned scheme adapted to the poromechanics formulation of [10], with an adequate treatment of the additional fluid fraction variable, and a specific treatment of the distributed coupling conditions. The resulting scheme is proved to satisfy a discrete energy estimate, hence, to be unconditionally stable. Compared with [1] from which we draw the inspiration of our time scheme, our major contributions lie in

- extending this time scheme to our more complex case of a two-phase poromechanical problem;
- establishing the discrete energy estimate with the total free energy of the mixture, in a general *nonlinear* framework.

Furthermore, as our proposed method has the same algorithmic complexity as that of [1], we can similarly expect very significant gains in computational efficiency compared to a monolithic approach, as already assessed numerically in [19], in particular.

The paper is organized as follows. In Section 2, we recall the formulation of the general poromechanical model of [10] that we consider, with the associated energy balance. Next, in Section 3 we introduce our proposed partitioned time discretization scheme, and we provide a detailed stability analysis of this time scheme by establishing a discrete energy estimate. One ingredient of this analysis is an adapted form of the so-called "geometric conservation law" [16, 17, 38, 40], which in our case is shown to be satisfied by construction, up to perturbations

induced by spatial discretization that we analyse in details. In Section 4, we provide some implementation considerations, and several numerical illustrations for representative test problems proposed in the recent literature [9]. In addition, we present a test case in which we precisely monitor the energy balance and quantitatively assess the various sources of perturbations induced by spatial discretization. Finally, we give some concluding remarks in Section 5.

2 Poromechanical formulation

2.1 Basic definitions

We consider the general poromechanical model proposed in [10]. This is a two-phase mixture type model, in which a fluid phase and a solid phase are assumed to coexist and interact at each point, ϕ denoting the volume fraction of the fluid phase – also called the porosity.

The solid phase is primarily described by the displacement field $\underline{y}_{\rm s}(\underline{\xi},t)$ defined at every point $\underline{\xi}$ in the (fixed) reference domain Ω^0, and at any time t in the time window considered. We will use the corresponding velocity field

$$\underline{v}_{\rm s} = \frac{{\rm d}\underline{y}_{\rm s}}{{\rm dt}} = \partial_t \underline{y}_{\rm s}(\underline{\xi},t).$$

The displacement field maps the reference domain Ω^0 to the deformed domain Ω_t, viz.

$$\underline{\xi} \in \Omega^0 \mapsto \underline{\rm x} = \underline{\xi} + \underline{y}_{\rm s}(\underline{\xi},t),$$

and the associated deformation gradient tensor is

$$\underline{\underline{F}} = \underline{\underline{\mathbb{1}}} + \underline{\underline{\nabla}}_{\underline{\xi}}\, \underline{y}_{\rm s},$$

with determinant $J = \det \underline{\underline{F}}$. We point out that J represents the local change of volume of the *global mixture*, whereas the change of volume of the solid phase itself is given by $J(1-\phi)/(1-\phi_0)$, with ϕ_0 the fluid volume fraction in the undeformed configuration, and we define $J_{\rm s} = J(1-\phi)$. We recall the definitions of the right Cauchy-Green deformation tensor and of the Green-Lagrange strain tensor, i.e., respectively,

$$\underline{\underline{C}} = \underline{\underline{F}}^T \cdot \underline{\underline{F}}, \quad \underline{\underline{e}} = \tfrac{1}{2}(\underline{\underline{C}} - \underline{\underline{\mathbb{1}}}).$$

The mass per unit volume of the solid phase in the reference configuration is denoted by $\rho_{\rm s0}$.

The internal fluid flow is represented by the velocity $\underline{v}_{\rm f}$ and pressure p, both fields being naturally defined in the deformed domain Ω_t. The fluid is assumed to be incompressible, hence, the fluid mass per unit volume $\rho_{\rm f}$ is constant. The quantity m is defined as the added fluid mass per unit volume of the reference configuration, i.e.

$$m = \rho_{\rm f}(J\phi - \phi_0).$$

The fluid is assumed to be Newtonian, with the usual decomposition of the fluid Cauchy stress tensor into viscous and hydrostatic contributions, i.e.

$$\underline{\underline{\sigma}}_{\rm f} = \underline{\underline{\sigma}}_{\rm vis}(\underline{v}_{\rm f}) - p\underline{\underline{\mathbb{1}}}.$$

Recalling the classical transformation rule from the Cauchy stress tensor to the second Piola-Kirchhoff stress tensor

$$\underline{\underline{\Sigma}} = J\underline{\underline{F}}^{-1} \cdot \underline{\underline{\sigma}} \cdot \underline{\underline{F}}^{-T},$$

here written for the global stress tensors of the mixture, we will denote by $\underline{\underline{\Sigma}}_s$ the contribution of the solid in the second Piola-Kirchhoff stress tensor $\underline{\underline{\Sigma}}$, i.e.

$$\underline{\underline{\Sigma}}_s = \underline{\underline{\Sigma}} - \phi J \underline{\underline{F}}^{-1} \cdot \underline{\underline{\sigma}}_{\mathrm{f}} \cdot \underline{\underline{F}}^{-T} = \underline{\underline{\Sigma}} - \phi \underline{\underline{\Sigma}}_{\mathrm{vis}} + \phi p J \underline{\underline{C}}^{-1}, \tag{1}$$

with $\underline{\underline{\Sigma}}_{\mathrm{vis}} = J \underline{\underline{F}}^{-1} \cdot \underline{\underline{\sigma}}_{\mathrm{vis}} \cdot \underline{\underline{F}}^{-T}$, see Section 2.4 below for more detailed specifications of the constitutive laws.

2.2 Strong formulation

The strong form of the poromechanical model reads [10]

$$\begin{cases} \rho_{\mathrm{s}0}(1-\phi_0)\dfrac{\mathrm{d}\underline{v}_{\mathrm{s}}}{\mathrm{dt}} - \underline{\nabla}_{\underline{\xi}} \cdot (\underline{\underline{F}} \cdot \underline{\underline{\Sigma}}_s) + pJ\underline{\underline{F}}^{-T} \cdot \underline{\nabla}_{\underline{\xi}}\phi \\ \qquad\qquad -J\phi^2 \underline{\underline{k}}_{\mathrm{f}}^{-1} \cdot (\underline{v}_{\mathrm{f}} - \underline{v}_{\mathrm{s}}) = \rho_{\mathrm{s}0}(1-\phi_0)\underline{f}, \qquad \text{in } \Omega^0, \qquad (2a) \\ \dfrac{1}{J}\dfrac{\mathrm{d}}{\mathrm{dt}}(\rho_{\mathrm{f}} J\phi\, \underline{v}_{\mathrm{f}}) + \underline{\nabla}_{\underline{x}} \cdot \big(\rho_{\mathrm{f}}\phi\, \underline{v}_{\mathrm{f}} \otimes \rho_{\mathrm{f}}(\underline{v}_{\mathrm{f}} - \underline{v}_{\mathrm{s}})\big) - \theta \underline{v}_{\mathrm{f}} \\ \qquad +\phi^2 \underline{\underline{k}}_{\mathrm{f}}^{-1} \cdot (\underline{v}_{\mathrm{f}} - \underline{v}_{\mathrm{s}}) - \underline{\nabla}_{\underline{x}} \cdot (\phi\, \underline{\underline{\sigma}}_{\mathrm{vis}}) + \phi \underline{\nabla}_{\underline{x}} p = \rho_{\mathrm{f}}\phi\, \underline{f}, \qquad \text{in } \Omega_t, \qquad (2b) \\ \dfrac{1}{J}\dfrac{\mathrm{d}}{\mathrm{dt}}(J\rho_{\mathrm{f}}\phi) + \underline{\nabla}_{\underline{x}} \cdot \big(\rho_{\mathrm{f}}\phi(\underline{v}_{\mathrm{f}} - \underline{v}_{\mathrm{s}})\big) = \theta, \qquad \text{in } \Omega_t \qquad (2c) \end{cases}$$

where $\underline{\underline{k}}_{\mathrm{f}}$ denotes the so-called permeability tensor that governs the friction forces between the solid and fluid phases (we will also use its inverse $\underline{\underline{D}}_{\mathrm{f}}$), $\underline{f}$ the applied distributed force per unit mass, and θ the fluid mass input per unit volume in the deformed configuration that may be used in some problems to model some specific inflow ($\theta > 0$) or outflow ($\theta < 0$) conditions. This is a coupled system, albeit in essence the first equation governs the solid deformation, the second the fluid flow, and the third the fluid mass conservation. Note in passing the slight abuse of notation – that we will repeatedly use throughout the paper – by which we employ the same notation for fields defined over the domains Ω^0 and Ω_t – e.g., for the velocity fields – which means that composition by the deformation mapping or its inverse is implicitly used.

Remark 1 (Comparison with fluid-structure interaction)
From a formal standpoint the above system bears some interesting resemblance with a fluid-structure interaction problem written in the Arbitrary Lagrangian-Eulerian (ALE) formalism, see e.g. [1]. The main differences here are that the fluid and the solid interact everywhere – and not only on boundaries – via the distributed friction term $J\phi^2 \underline{\underline{k}}_{\mathrm{f}}^{-1} \cdot (\underline{v}_{\mathrm{f}} - \underline{v}_{\mathrm{s}})$ and the porosity gradient term $pJ\underline{\underline{F}}^{-T} \cdot \underline{\nabla}_{\underline{\xi}}\phi$, the ALE domain velocity is substituted with the *physical* solid velocity, and the fluid mass conservation is made more complex due to the combination of fluid and solid at every point (with fluid volume fraction ϕ). Nevertheless, the similarities will allow us to draw some inspiration from a previously-proposed time scheme to design our discrete problem, i.e. [1].

Of course, the above equations must be complemented with adequate boundary conditions. Denoting by $\underline{t}$ the total traction on the boundary of the domain Ω_t, and by $\underline{t}_0 = J\|\underline{\underline{F}}^{-T} \cdot \underline{n}_0\|\underline{t}$ the transported counterpart on the boundary of the reference domain Ω^0, as in [10] we will consider:

- Dirichlet boundary conditions for both phases, i.e. prescribed skeleton displacements and fluid velocities
$$\underline{y}_{\mathrm{s}} = \underline{y}_{\mathrm{s}}^{\mathrm{pr}}, \quad \underline{v}_{\mathrm{f}} = \underline{v}_{\mathrm{f}}^{\mathrm{pr}},$$
on the subpart of the boundary that we denote by Γ_D^0 in the reference configuration and Γ_D^t in the current configuration;

- Neumann boundary conditions – namely, prescribed forces – for both phases together, with proportional repartition[1] of boundary traction

$$\underline{\underline{\sigma}} \cdot \underline{n} = \underline{t} \Leftrightarrow \underline{\underline{F}} \cdot \underline{\underline{\Sigma}} \cdot \underline{n}_0 = \underline{t}_0, \quad \underline{\underline{\sigma}}_{\mathrm{f}} \cdot \underline{n} = \underline{t},$$

on Γ_N^0 (or Γ_N^t);

- Neumann boundary condition for the global mixture, but vanishing fluid flux and proportional repartition of *tangential* boundary traction

$$\underline{\underline{\sigma}} \cdot \underline{n} = \underline{t} \Leftrightarrow \underline{\underline{F}} \cdot \underline{\underline{\Sigma}} \cdot \underline{n}_0 = \underline{t}_0, \quad \pi_\tau(\underline{\underline{\sigma}}_{\mathrm{f}} \cdot \underline{n}) = \pi_\tau(\underline{t}), \quad (\underline{v}_{\mathrm{f}} - \underline{v}_{\mathrm{s}}) \cdot \underline{n} = 0,$$

on $\Gamma_{N\mathrm{nof}}^0$ (or $\Gamma_{N\mathrm{nof}}^t$), where $\pi_\tau = \underline{\underline{\mathbb{1}}} - \underline{n} \otimes \underline{n}$ denotes the projection onto the tangential plane;

- Neumann boundary condition for the global mixture with fluid velocity coinciding with the solid velocity (no sliding)

$$\underline{\underline{\sigma}} \cdot \underline{n} = \underline{t} \Leftrightarrow \underline{\underline{F}} \cdot \underline{\underline{\Sigma}} \cdot \underline{n}_0 = \underline{t}_0, \quad \underline{v}_{\mathrm{f}} = \underline{v}_{\mathrm{s}},$$

on $\Gamma_{N\mathrm{nos}}^0$ (or $\Gamma_{N\mathrm{nos}}^t$).

2.3 Weak formulation

We consider test functions $(\underline{v}_{\mathrm{s}}^*, \underline{v}_{\mathrm{f}}^*, q^*)$ associated with the main unknowns $(\underline{y}_{\mathrm{s}}, \underline{v}_{\mathrm{f}}, m)$ and satisfying similar Dirichlet boundary conditions, albeit in a homogeneous form, i.e.

$$\underline{v}_{\mathrm{s}}^*|_{\Gamma_D^0} = \underline{v}_{\mathrm{f}}^*|_{\Gamma_D^0} = 0, \quad \big((\underline{v}_{\mathrm{f}}^* - \underline{v}_{\mathrm{s}}^*) \cdot \underline{n}\big)|_{\Gamma_{N\mathrm{nof}}^0} = 0, \quad (\underline{v}_{\mathrm{f}}^* - \underline{v}_{\mathrm{s}}^*)|_{\Gamma_{N\mathrm{nos}}^0} = 0.$$

Multiplying System (2) by these test functions and integrating space-wise yields [10]

$$\begin{cases} \displaystyle\int_{\Omega^0} \rho_{\mathrm{s}0}(1-\phi_0)\frac{\mathrm{d}\underline{v}_{\mathrm{s}}}{\mathrm{dt}} \cdot \underline{v}_{\mathrm{s}}^*\, d\Omega + \int_{\Omega^0} \underline{\underline{\Sigma}}_s : d_{\underline{y}}\underline{\underline{e}} \cdot \underline{v}_{\mathrm{s}}^*\, d\Omega - \int_{\Omega_t} (\underline{v}_{\mathrm{f}} - \underline{v}_{\mathrm{s}}) \cdot \phi^2 \underline{\underline{k}}_{\mathrm{f}}^{-1} \cdot \underline{v}_{\mathrm{s}}^*\, d\Omega \\ \qquad + \displaystyle\int_{\Omega_t} p \underline{\nabla}_{\underline{\mathrm{x}}}\phi \cdot \underline{v}_{\mathrm{s}}^*\, d\Omega = \int_{\Omega^0} \rho_{s0}(1-\phi_0)\underline{f} \cdot \underline{v}_{\mathrm{s}}^*\, d\Omega + \int_{\Gamma_N^0} (1-\phi)\underline{t}_0 \cdot \underline{v}_{\mathrm{s}}^*\, dS \\ \qquad\qquad + \displaystyle\int_{\Gamma_{N\mathrm{nof}}^0 \bigcup \Gamma_{N\mathrm{nos}}^0} \underline{t}_0 \cdot \underline{v}_{\mathrm{s}}^*\, dS - \int_{\Gamma_{N\mathrm{nof}}^t} \phi(\pi_\tau \underline{t}) \cdot \underline{v}_{\mathrm{s}}^*\, dS - \mathcal{R}_{\mathrm{f}}^c(\underline{v}_{\mathrm{s}}^*) \quad \text{(3a)} \\ \\ \mathcal{P}_i^{\mathrm{f}}(\underline{v}_{\mathrm{f}}^*) + \displaystyle\int_{\Omega_t} (\underline{v}_{\mathrm{f}} - \underline{v}_{\mathrm{s}}) \cdot \phi^2 \underline{\underline{k}}_{\mathrm{f}}^{-1} \cdot \underline{v}_{\mathrm{f}}^*\, d\Omega + \int_{\Omega_t} \Big(-\frac{p}{\rho_{\mathrm{f}}} \underline{\nabla}_{\underline{\mathrm{x}}} \cdot (\rho_{\mathrm{f}}\phi \underline{v}_{\mathrm{f}}^*) + \phi\, \underline{\underline{\sigma}}_{\mathrm{vis}} : \underline{\underline{\varepsilon}}(\underline{v}_{\mathrm{f}}^*) \Big)\, d\Omega \\ \qquad\qquad = \displaystyle\int_{\Omega_t} \rho_{\mathrm{f}}\phi\, \underline{f} \cdot \underline{v}_{\mathrm{f}}^*\, d\Omega + \int_{\Gamma_N^t \bigcup \Gamma_{N\mathrm{nof}}^t} \phi\, \underline{t} \cdot \underline{v}_{\mathrm{f}}^*\, dS \quad \text{(3b)} \\ \\ \displaystyle\int_{\Omega^0} \frac{\mathrm{d}m}{\mathrm{dt}} q^*\, d\Omega + \int_{\Omega_t} \underline{\nabla}_{\underline{\mathrm{x}}} \cdot (\rho_{\mathrm{f}}\phi\, (\underline{v}_{\mathrm{f}} - \underline{v}_{\mathrm{s}}))\, q^*\, d\Omega = \int_{\Omega_t} \theta q^*\, d\Omega \quad \text{(3c)} \end{cases}$$

with

$$\mathcal{P}_i^{\mathrm{f}}(\underline{v}^*) = \int_{\Omega^0} \frac{\mathrm{d}}{\mathrm{dt}}\big(J\rho_{\mathrm{f}}\phi\, \underline{v}_{\mathrm{f}}\big) \cdot \underline{v}^*\, d\Omega + \int_{\Omega_t} \underline{\nabla}_{\underline{\mathrm{x}}} \cdot (\rho_{\mathrm{f}}\phi \underline{v}_{\mathrm{f}} \otimes (\underline{v}_{\mathrm{f}} - \underline{v}_{\mathrm{s}})) \cdot \underline{v}^*\, d\Omega - \int_{\Omega_t} \theta \underline{v}_{\mathrm{f}} \cdot \underline{v}^*\, d\Omega,$$

[1] proportionality is meant here according to the respective volume fractions of the two phases

and the residual representing the fluid reaction forces

$$\mathcal{R}_{\mathrm{f}}^{c}(\underline{v}_{\mathrm{s}}^{*}) = \mathcal{P}_{i}^{\mathrm{f}}(\underline{v}_{\mathrm{s}}^{*}) + \int_{\Omega_t} (\underline{v}_{\mathrm{f}} - \underline{v}_{\mathrm{s}}) \cdot \phi^2 \underline{\underline{k}}_{\mathrm{f}}^{-1} \cdot \underline{v}_{\mathrm{s}}^{*} \, d\Omega + \int_{\Omega_t} \Big(-\frac{p}{\rho_{\mathrm{f}}} \underline{\nabla}_{\underline{\mathrm{x}}} \cdot (\rho_{\mathrm{f}} \phi \underline{v}_{\mathrm{s}}^{*}) + \phi \, \underline{\underline{\sigma}}_{\mathrm{vis}} : \underline{\underline{\varepsilon}}(\underline{v}_{\mathrm{s}}^{*}) \Big) \, d\Omega$$
$$- \int_{\Omega_t} \rho_{\mathrm{f}} \phi \, \underline{f} \cdot \underline{v}_{\mathrm{s}}^{*} \, d\Omega - \int_{\Gamma_N^t} \phi \, \underline{t} \cdot \underline{v}_{\mathrm{s}}^{*} \, dS - \int_{\Gamma_{N\mathrm{nof}}^t} \phi(\pi_\tau \underline{t}) \cdot \underline{v}_{\mathrm{s}}^{*} \, dS.$$

This weak formulation characterizes the main unknowns $(\underline{y}_{\mathrm{s}}, \underline{v}_{\mathrm{f}}, m)$, from which all other quantities can be computed. In particular, we have $\phi = \frac{m/\rho_{\mathrm{f}} + \phi_0}{J(\underline{y}_{\mathrm{s}})}$, and the pressure p will be given by a constitutive equation, see next section. Note that – as is usual in computational mechanics, especially in a nonlinear framework – we do not dwell on the mathematical definition of the functional spaces, typically considered to be Sobolev spaces of the form $W^{1,s}$ with s sufficiently large for all integrals in (3) to be well-defined, see e.g. [12, 31] and references therein for more details.

In order to transform (3a) into a more compact form, we define the following pseudo-residual based on the above-introduced residual

$$\begin{aligned}
\bar{\mathcal{R}}_{\mathrm{f}}^{c}(\underline{v}_{\mathrm{s}}^{*}) &= \mathcal{R}_{\mathrm{f}}^{c}(\underline{v}_{\mathrm{s}}^{*}) - \int_{\Omega_t} (\underline{v}_{\mathrm{f}} - \underline{v}_{\mathrm{s}}) \cdot \phi^2 \underline{\underline{k}}_{\mathrm{f}}^{-1} \cdot \underline{v}_{\mathrm{s}}^{*} \, d\Omega + \int_{\Omega_t} p \underline{\nabla}_{\underline{\mathrm{x}}} \phi \cdot \underline{v}_{\mathrm{s}}^{*} \, d\Omega \\
&= \mathcal{P}_{i}^{\mathrm{f}}(\underline{v}_{\mathrm{s}}^{*}) + \int_{\Omega_t} \Big(-p\phi \underline{\nabla}_{\underline{\mathrm{x}}} \cdot \underline{v}_{\mathrm{s}}^{*} + \phi \, \underline{\underline{\sigma}}_{\mathrm{vis}} : \underline{\underline{\varepsilon}}(\underline{v}_{\mathrm{s}}^{*}) \Big) \, d\Omega - \int_{\Omega_t} \rho_{\mathrm{f}} \phi \, \underline{f} \cdot \underline{v}_{\mathrm{s}}^{*} \, d\Omega \\
&- \int_{\Gamma_N^t} \phi \, \underline{t} \cdot \underline{v}_{\mathrm{s}}^{*} \, dS - \int_{\Gamma_{N\mathrm{nof}}^t} \phi(\pi_\tau \underline{t}) \cdot \underline{v}_{\mathrm{s}}^{*} \, dS,
\end{aligned}$$

where we have used the identity $\underline{\nabla}_{\underline{\mathrm{x}}} \cdot (\phi \underline{v}_{\mathrm{s}}^{*}) = \phi \underline{\nabla}_{\underline{\mathrm{x}}} \cdot \underline{v}_{\mathrm{s}}^{*} + \underline{\nabla}_{\underline{\mathrm{x}}} \phi \cdot \underline{v}_{\mathrm{s}}^{*}$. We infer the following alternative form for (3a)

$$\int_{\Omega^0} \rho_{\mathrm{s}0}(1-\phi_0) \frac{\mathrm{d}\underline{v}_{\mathrm{s}}}{\mathrm{dt}} \cdot \underline{v}_{\mathrm{s}}^{*} \, d\Omega + \int_{\Omega^0} \underline{\underline{\Sigma}}_{s} : d_{\underline{y}} \underline{\underline{e}} \cdot \underline{v}_{\mathrm{s}}^{*} \, d\Omega = \int_{\Omega^0} \rho_{s0}(1-\phi_0) \underline{f} \cdot \underline{v}_{\mathrm{s}}^{*} \, d\Omega$$
$$+ \int_{\Gamma_N^0} (1-\phi) \underline{t}_0 \cdot \underline{v}_{\mathrm{s}}^{*} \, dS + \int_{\Gamma_{N\mathrm{nof}}^0 \bigcup \Gamma_{N\mathrm{nos}}^0} \underline{t}_0 \cdot \underline{v}_{\mathrm{s}}^{*} \, dS - \int_{\Gamma_{N\mathrm{nof}}^t} \phi(\pi_\tau \underline{t}) \cdot \underline{v}_{\mathrm{s}}^{*} \, dS - \bar{\mathcal{R}}_{\mathrm{f}}^{c}(\underline{v}_{\mathrm{s}}^{*}).$$

2.4 Constitutive laws and energy balance

We consider a total stress tensor given by [10]

$$\underline{\underline{\Sigma}} = \phi \underline{\underline{\Sigma}}_{\mathrm{vis}} + \frac{\partial \Psi(\underline{\underline{e}}, m)}{\partial \underline{\underline{e}}}\Big|_m + \frac{\partial \Psi^{\mathrm{damp}}(\underline{\underline{e}}, \dot{\underline{\underline{e}}})}{\partial \dot{\underline{\underline{e}}}}\Big|_{\underline{\underline{e}}},$$

with $\Psi(\underline{\underline{e}}, m)$ the Helmholtz free energy of the mixture, and $\Psi^{\mathrm{damp}}(\underline{\underline{e}}, \dot{\underline{\underline{e}}})$ a viscous pseudo-potential. Due to fluid incompressibility, $\Psi(\underline{\underline{e}}, m) = \Psi_{\mathrm{s}}(\underline{\underline{e}}, J_{\mathrm{s}})$ with Ψ_{s} the solid free energy – meaning that the fluid cannot store any energy – hence, we have

$$\underline{\underline{\Sigma}} = \phi \underline{\underline{\Sigma}}_{\mathrm{vis}} + \frac{\partial \Psi_{\mathrm{s}}(\underline{\underline{e}}, J_{\mathrm{s}})}{\partial \underline{\underline{e}}}\Big|_{J_{\mathrm{s}}} + \frac{\partial \Psi^{\mathrm{damp}}(\underline{\underline{e}}, \dot{\underline{\underline{e}}})}{\partial \dot{\underline{\underline{e}}}}\Big|_{\underline{\underline{e}}} - pJ\underline{\underline{C}}^{-1},$$

see [10]. Recalling (1), this gives for the solid contribution

$$\begin{aligned}
\underline{\underline{\Sigma}}_{\mathrm{s}} &= \frac{\partial \Psi(\underline{\underline{e}}, m)}{\partial \underline{\underline{e}}}\Big|_m + \frac{\partial \Psi^{\mathrm{damp}}(\underline{\underline{e}}, \dot{\underline{\underline{e}}})}{\partial \dot{\underline{\underline{e}}}}\Big|_{\underline{\underline{e}}} + \phi p J \underline{\underline{C}}^{-1} \\
&= \frac{\partial \Psi_{\mathrm{s}}(\underline{\underline{e}}, J_{\mathrm{s}})}{\partial \underline{\underline{e}}}\Big|_{J_{\mathrm{s}}} + \frac{\partial \Psi^{\mathrm{damp}}(\underline{\underline{e}}, \dot{\underline{\underline{e}}})}{\partial \dot{\underline{\underline{e}}}}\Big|_{\underline{\underline{e}}} - (1-\phi) p J \underline{\underline{C}}^{-1}.
\end{aligned} \tag{4}$$

In addition, we have

$$p = \rho_{\rm f} \frac{\partial \Psi(\underline{\underline{e}}, m)}{\partial m}\Big|_{\underline{\underline{e}}} = -\frac{\partial \Psi_{\rm s}(\underline{\underline{e}}, J_{\rm s})}{\partial J_{\rm s}}\Big|_{\underline{\underline{e}}}.$$

Defining the total kinetic energy of the system

$$\mathcal{K} = \frac{1}{2}\int_{\Omega^0} \rho_{\rm s0}(1-\phi_0)\underline{v}_{\rm s}^2 \, d\Omega + \frac{1}{2}\int_{\Omega_t} \rho_{\rm f}\phi \, \underline{v}_{\rm f}^2 \, d\Omega,$$

and the total Helmholtz free energy

$$\mathcal{W} = \int_{\Omega^0} \Psi(\underline{\underline{e}}, m) \, d\Omega,$$

we can now recall the following energy balance result, see [10, Theorem 7]

$$\frac{d\mathcal{K}}{dt} + \frac{d\mathcal{W}}{dt} = -\int_{\Omega^0} \frac{\partial \Psi^{\rm damp}}{\partial \dot{\underline{\underline{e}}}} : \dot{\underline{\underline{e}}} \, d\Omega - \int_{\Omega_t} \phi \, \underline{\underline{\sigma}}_{\rm vis} : \underline{\underline{\varepsilon}}(\underline{v}_{\rm f}) \, d\Omega - \int_{\Omega_t} (\underline{v}_{\rm f} - \underline{v}_{\rm s}) \cdot \phi^2 \underline{\underline{k}}_{\rm f}^{-1} \cdot (\underline{v}_{\rm f} - \underline{v}_{\rm s}) \, d\Omega + \mathcal{P}_{ext}^{total} + \mathcal{J}_{\mathcal{K}b} + \mathcal{J}_{\mathcal{K}\theta} + \mathcal{J}_{\mathcal{W}b} + \mathcal{J}_{\mathcal{G}\theta}, \quad (5)$$

the operator $\underline{\underline{\varepsilon}}$ denoting the usual symmetrized gradient, and with

$$\mathcal{P}_{ext}^{total} = \int_{\Omega^0} \rho_{s0}(1-\phi_0)\underline{f} \cdot \underline{v}_{\rm s} \, d\Omega + \int_{\Omega_t} \rho_{\rm f}\phi \, \underline{f} \cdot \underline{v}_{\rm f} \, d\Omega + \int_{\partial\Omega_t} \underline{t} \cdot \big((1-\phi)\underline{v}_{\rm s} + \phi \underline{v}_{\rm f}\big) \, dS$$

the total power of external forces,

$$\mathcal{J}_{\mathcal{K}b} = -\frac{1}{2}\int_{\partial\Omega_t} \rho_{\rm f}\phi \underline{v}_{\rm f}^2 (\underline{v}_{\rm f} - \underline{v}_{\rm s}) \cdot \underline{n} \, dS, \qquad \mathcal{J}_{\mathcal{K}\theta} = \frac{1}{2}\int_{\Omega_t} \underline{v}_{\rm f}^2 \theta \, d\Omega,$$

the incoming rates of fluid kinetic energy due to the boundary flow and source term, respectively, and

$$\mathcal{J}_{\mathcal{W}b} = -\int_{\partial\Omega_t} \rho_{\rm f}\phi\psi_m (\underline{v}_{\rm f} - \underline{v}_{\rm s}) \cdot \underline{n} \, dS, \qquad \mathcal{J}_{\mathcal{G}\theta} = \int_{\Omega_t} g_m \theta \, d\Omega,$$

similar incoming rates of Helmholtz and Gibbs free energies. The physical interpretation of (5) is that total energy variations correspond to dissipation losses – in the fluid and solid phases separately, and in their interaction – and external source terms.

3 Effective and energy-preserving time discretization

In the sequel we use the standard mid-point notation

$$g^{n+\frac{1}{2}} = \frac{g^n + g^{n+1}}{2},$$

except when otherwise specified for some specific quantities that we then denote by $g^{n+\frac{1}{2}\sharp}$, to then emphasize that a discretization rule other than simple mid-point is being considered.

For any field $\underline{w}_D^0$ in $V^0 = H^1(\Omega^0)^3$, we define

$$V^0(\underline{w}_D^0) = \{\underline{v}^* \in V^0 \;\Big|\; \underline{v}^*|_{\Gamma_D^0} = \underline{w}_D^0\}.$$

Assuming a sufficiently regular mapping between the reference domain Ω^0 and the deformed configuration of time step n denoted by $\Omega_{\rm f}^n$, we define

$$Q^n = L^2(\Omega_{\rm f}^n),$$

and for any $(\underline{w}_D, \underline{w})$ in $(V^n)^2 = (H^1(\Omega_{\rm f}^n)^3)^2$,

$$V^n(\underline{w}_D) = \{\underline{v}^* \in V^n \;\Big|\; \underline{v}^*|_{\Gamma_D^n} = \underline{w}_D\},$$
$$V^n(\underline{w}_D, \underline{w}) = \{\underline{v}^* \in V^n \;\Big|\; \underline{v}^*|_{\Gamma_D^n} = \underline{w}_D,\ \underline{v}^*|_{\Gamma_{N\rm nos}^n} = \underline{w}|_{\Gamma_{N\rm nos}^n},\ (\underline{v}^* - \underline{w}) \cdot \underline{n} = 0 \text{ on } \Gamma_{N\rm nof}^n\}.$$

As in the continuous framework, we will use the same notation for functions defined in Ω^0 and $\Omega_{\rm f}^n$.

All the solution spaces considered here are implicitly assumed from now on to be discrete in space, typically using a finite element type strategy, but we do not dwell on space discretization in this paper. Nevertheless, we will denote by h the typical maximum diameter of all the finite elements in the mesh.

3.1 Time-discrete partitioned coupling method

We now define our proposed partitioned method, drawing some inspiration from the method previously proposed in [1] for fluid-structure interaction, see above Remark 1.

Given the solutions $(\underline{y}_{\rm s}^n, \underline{v}_{\rm s}^n)$ and $(\underline{v}_{\rm f}^n, m^n)$ up to time step n, perform the following steps:

- **Step 0.** Mesh and porosity updates: $\Omega_{\rm f}^{n+1} = (I_{\Omega^0} + \underline{y}_{\rm s}^n)\Omega^0$ and $\phi^n = \frac{m^n/\rho_{\rm f} + \phi_0}{J(\underline{y}_{\rm s}^n)}$.

- **Step 1.** Explicit step: find $\tilde{\underline{v}}_{\rm f}^{n+1} \in V^{n+1}(\underline{v}_{\rm f}^{\rm pr}(t^{n+1}))$ such that $\forall \tilde{\underline{v}}_{\rm f}^* \in V^{n+1}(0)$

$$\begin{aligned}
&\int_{\Omega_{\rm f}^{n+1}} \frac{\rho_{\rm f}}{\Delta t}\phi^n \tilde{\underline{v}}_{\rm f}^{n+1} \cdot \tilde{\underline{v}}_{\rm f}^*\, d\Omega - \int_{\Omega_{\rm f}^n} \frac{\rho_{\rm f}}{\Delta t}\phi^{n-1} \underline{v}_{\rm f}^n \cdot \tilde{\underline{v}}_{\rm f}^*\, d\Omega \\
&\quad + \int_{\Omega_{\rm f}^n} \underline{\nabla}_{\underline{\rm x}} \cdot \left(\rho_{\rm f}\phi^{n-1} \tilde{\underline{v}}_{\rm f}^{n+1} \otimes (\underline{v}_{\rm f}^n - \underline{v}_{\rm s}^{n-\frac{1}{2}})\right) \cdot \tilde{\underline{v}}_{\rm f}^*\, d\Omega + 2\mu \int_{\Omega_{\rm f}^{n+1}} \phi^n \underline{\underline{\varepsilon}}(\tilde{\underline{v}}_{\rm f}^{n+1}) : \underline{\underline{\varepsilon}}(\tilde{\underline{v}}_{\rm f}^*)\, d\Omega \\
&\quad + \frac{\gamma\mu}{h} \int_{\Gamma_{N\rm nos}^{n+1}} \phi^n (\tilde{\underline{v}}_{\rm f}^{n+1} - \underline{v}_{\rm s}^{n-\frac{1}{2}}) \cdot \tilde{\underline{v}}_{\rm f}^*\, dS + \frac{\gamma\mu}{h} \int_{\Gamma_{N\rm nof}^{n+1}} \phi^n \left[(\tilde{\underline{v}}_{\rm f}^{n+1} - \underline{v}_{\rm s}^{n-\frac{1}{2}}) \cdot \underline{n}\right] \tilde{\underline{v}}_{\rm f}^* \cdot \underline{n}\, dS \\
&\qquad\qquad = 2\mu \int_{\Gamma_{N\rm nos}^{n+1} \cup \Gamma_{N\rm nof}^{n+1}} \phi^n \underline{\underline{\varepsilon}}(\tilde{\underline{v}}_{\rm f}^{n+1}) \cdot \underline{n} \cdot \tilde{\underline{v}}_{\rm f}^*\, dS + \int_{\Omega_{\rm f}^{n+1}} \theta^n \tilde{\underline{v}}_{\rm f}^{n+1} \cdot \tilde{\underline{v}}_{\rm f}^*\, d\Omega, \quad (6)
\end{aligned}$$

  where γ denotes a stabilization parameter, see Remark 2 below.

- **Step 2.** Implicit step (implicit coupling of two sub-steps, fluid and solid)

  - **Step 2a.** Fluid projection sub-step (where $p^{n+1} \hat{=} \rho_{\rm f} \dfrac{\partial \Psi}{\partial m}\Big|^{n+\frac{1}{2}\sharp}$, see below)

    Find $(\underline{v}_{\rm f}^{n+1}, m^{n+1}) \in V^{n+1}(\underline{v}_{\rm f}^{\rm pr}(t^{n+1}), \underline{v}_{\rm s}^{n+\frac{1}{2}}) \times Q^{n+1}$ such that $\forall (\underline{v}_{\rm f}^*, q^*) \in V^{n+1}(0,0) \times Q^{n+1}$

$$\begin{cases}
\displaystyle\int_{\Omega^0} \frac{m^{n+1} - m^n}{\Delta t} q^*\, d\Omega + \int_{\Omega_{\rm f}^{n+1}} \underline{\nabla}_{\underline{\rm x}} \cdot (\rho_{\rm f}\phi^n\, (\underline{v}_{\rm f}^{n+1} - \underline{v}_{\rm s}^{n+\frac{1}{2}}))q^*\, d\Omega = \int_{\Omega_{\rm f}^{n+1}} q^* \theta^n\, d\Omega & \text{(7a)} \\
\displaystyle\int_{\Omega_{\rm f}^{n+1}} \frac{\rho_{\rm f}}{\Delta t}\phi^n\, (\underline{v}_{\rm f}^{n+1} - \tilde{\underline{v}}_{\rm f}^{n+1}) \cdot \underline{v}_{\rm f}^*\, d\Omega - \int_{\Omega_{\rm f}^{n+1}} p^{n+1} (\underline{\nabla}_{\underline{\rm x}} \phi^n) \cdot \underline{v}_{\rm f}^*\, d\Omega & \\
\quad \displaystyle - \int_{\Omega_{\rm f}^{n+1}} \phi^n p^{n+1} \underline{\nabla}_{\underline{\rm x}} \cdot \underline{v}_{\rm f}^*\, d\Omega + \int_{\Omega_{\rm f}^{n+1}} (\underline{v}_{\rm f}^{n+1} - \underline{v}_{\rm s}^{n+\frac{1}{2}}) \cdot |\phi^n|^2\, \underline{\underline{D}}_{\rm f} \cdot \underline{v}_{\rm f}^*\, d\Omega & \text{(7b)} \\
\qquad\qquad \displaystyle = \int_{\Omega_{\rm f}^{n+1}} \rho_{\rm f}\phi^n \underline{f}^{n+1} \cdot \underline{v}_{\rm f}^*\, d\Omega + \int_{\Gamma_N^{n+1} \cup \Gamma_{N\rm nof}^{n+1}} \phi^n \underline{t}^{n+1} \cdot \underline{v}_{\rm f}^*\, dS &
\end{cases}$$

– **Step 2b.** Solid step (Newmark mid-point scheme)
Find $(\underline{y}_{\mathrm{s}}^{n+1}, \underline{v}_{\mathrm{s}}^{n+1}) \in V^0(\underline{y}_{\mathrm{s}}^{\mathrm{pr}}(t^{n+1})) \times V^0(\underline{\dot{y}}_{\mathrm{s}}^{\mathrm{pr}}(t^{n+1}))$ such that $\forall \underline{v}_{\mathrm{s}}^* \in V^0(0)$

$$
\begin{cases}
\dfrac{\underline{y}_{\mathrm{s}}^{n+1} - \underline{y}_{\mathrm{s}}^{n}}{\Delta t} = \dfrac{\underline{v}_{\mathrm{s}}^{n+1} + \underline{v}_{\mathrm{s}}^{n}}{2} & \text{(8a)} \\
\displaystyle\int_{\Omega^0} \frac{\rho_{\mathrm{s}0}}{\Delta t}(1-\phi_0)(\underline{v}_{\mathrm{s}}^{n+1} - \underline{v}_{\mathrm{s}}^{n}) \cdot \underline{v}_{\mathrm{s}}^* \, d\Omega \\
\qquad + \displaystyle\int_{\Omega^0} \left(\frac{\partial \Psi}{\partial \underline{\underline{e}}}\Big|^{n+\frac{1}{2}\sharp} + \frac{\partial \Psi^{\mathrm{damp}}}{\partial \underline{\underline{\dot{e}}}}\Big|^{n+\frac{1}{2}\sharp} \right) : d_{\underline{y}} \underline{\underline{e}}^{n+\frac{1}{2}\sharp} \cdot \underline{v}_{\mathrm{s}}^* \, d\Omega \\
\qquad\quad + \displaystyle\int_{\Omega_{\mathrm{f}}^{n+1}} \phi^n p^{n+1} \underline{\nabla}_{\underline{\mathrm{x}}} \cdot \underline{v}_{\mathrm{s}}^* \, d\Omega + \frac{\gamma\mu}{h} \int_{\Gamma_{N\mathrm{nos}}^{n+1}} \phi^n (\underline{v}_{\mathrm{s}}^{n+\frac{1}{2}} - \underline{v}_{\mathrm{s}}^{n-\frac{1}{2}}) \cdot \underline{v}_{\mathrm{s}}^* \, dS \\
\qquad\qquad + \dfrac{\gamma\mu}{h} \displaystyle\int_{\Gamma_{N\mathrm{nof}}^{n+1}} \phi^n \left[(\underline{v}_{\mathrm{s}}^{n+\frac{1}{2}} - \underline{v}_{\mathrm{s}}^{n-\frac{1}{2}}) \cdot \underline{n} \right] \underline{v}_{\mathrm{s}}^* \cdot \underline{n} \, dS & \text{(8b)} \\
\qquad = \displaystyle\int_{\Omega^0} \rho_{\mathrm{s}0}(1-\phi_0) \underline{f}^{n+1} \cdot \underline{v}_{\mathrm{s}}^* \, d\Omega + \int_{\Gamma_N^0} (1-\phi^n) \underline{t}_0^{n+1} \cdot \underline{v}_{\mathrm{s}}^* \, dS \\
\qquad + \displaystyle\int_{\Gamma_{N\mathrm{nos}}^0 \cup \Gamma_{N\mathrm{nof}}^0} \underline{t}_0^{n+1} \cdot \underline{v}_{\mathrm{s}}^* \, dS - \int_{\Gamma_{N\mathrm{nof}}^{n+1}} \phi(\pi_\tau \underline{t}^{n+1}) \cdot \underline{v}_{\mathrm{s}}^* \, dS - \bar{\mathcal{R}}_{\mathrm{f}}^d(\underline{v}_{\mathrm{s}}^*)
\end{cases}
$$

Here, $\bar{\mathcal{R}}_{\mathrm{f}}^d$ denotes the discrete version of $\bar{\mathcal{R}}_{\mathrm{f}}^c$, such that for any $\underline{v}^*$ in V^{n+1}

$$
\begin{aligned}
\bar{\mathcal{R}}_{\mathrm{f}}^d(\underline{v}^*) = & \int_{\Omega_{\mathrm{f}}^{n+1}} \frac{\rho_{\mathrm{f}}}{\Delta t} \phi^n \, \underline{v}_{\mathrm{f}}^{n+1} \cdot \underline{v}^* \, d\Omega - \int_{\Omega_{\mathrm{f}}^n} \frac{\rho_{\mathrm{f}}}{\Delta t} \phi^{n-1} \underline{v}_{\mathrm{f}}^n \cdot \underline{v}^* \, d\Omega \\
& + \int_{\Omega_{\mathrm{f}}^n} \underline{\nabla}_{\underline{\mathrm{x}}} \cdot \left(\rho_{\mathrm{f}} \phi^{n-1} \tilde{\underline{v}}_{\mathrm{f}}^{n+1} \otimes (\underline{v}_{\mathrm{f}}^n - \underline{v}_{\mathrm{s}}^{n-\frac{1}{2}}) \right) \cdot \underline{v}^* \, d\Omega - \int_{\Omega_{\mathrm{f}}^{n+1}} \theta^n \tilde{\underline{v}}_{\mathrm{f}}^{n+1} \cdot \underline{v}^* \, d\Omega \\
& \quad - \int_{\Omega_{\mathrm{f}}^{n+1}} \phi^n p^{n+1} \underline{\nabla}_{\underline{\mathrm{x}}} \cdot \underline{v}^* \, d\Omega + 2\mu \int_{\Omega_{\mathrm{f}}^{n+1}} \phi^n \underline{\underline{\varepsilon}}(\tilde{\underline{v}}_{\mathrm{f}}^{n+1}) : \underline{\underline{\varepsilon}}(\underline{v}^*) \, d\Omega \\
& \quad - \int_{\Omega_{\mathrm{f}}^{n+1}} \rho_{\mathrm{f}} \phi^n \underline{f}^{n+1} \cdot \underline{v}^* \, d\Omega - \int_{\Gamma_N^{n+1}} \phi^n \underline{t}^{n+1} \cdot \underline{v}^* \, dS - \int_{\Gamma_{N\mathrm{nof}}^{n+1}} \phi^n (\pi_\tau \underline{t}^{n+1}) \cdot \underline{v}^* \, dS,
\end{aligned}
$$

the strain-related quantities are discretized as follows

$$
\underline{\underline{e}}^{n+\frac{1}{2}\sharp} = \underline{\underline{e}}(\underline{y}_{\mathrm{s}}^{n+\frac{1}{2}}), \quad \underline{\underline{\dot{e}}}^{n+\frac{1}{2}\sharp} = \frac{\underline{\underline{e}}^{n+1} - \underline{\underline{e}}^{n}}{\Delta t},
$$

$$
d_{\underline{y}} \underline{\underline{e}}^{n+\frac{1}{2}\sharp} \cdot \underline{v}^* = \frac{1}{2} \left(\underline{\underline{F}}(\underline{y}_{\mathrm{s}}^{n+\frac{1}{2}})^T \cdot \underline{\underline{\nabla}}_{\underline{\xi}} \underline{v}^* + \underline{\underline{\nabla}}_{\underline{\xi}}^T \underline{v}^* \cdot \underline{\underline{F}}(\underline{y}_{\mathrm{s}}^{n+\frac{1}{2}}) \right),
$$

and the discrete solid stress tensor contribution is obtained using (4), with the following discretization choices for $\dfrac{\partial \Psi}{\partial \underline{\underline{e}}}\Big|^{n+\frac{1}{2}\sharp}$ (see [22]) and p^{n+1}

$$
\begin{cases}
\dfrac{\partial \Psi}{\partial \underline{\underline{e}}}\Big|^{n+\frac{1}{2}\sharp} \hat{=} \dfrac{\partial \Psi}{\partial \underline{\underline{e}}}(\underline{\underline{e}}^{n+\frac{1}{2}\sharp}, m^{n+1}) \\
\quad + \left(\dfrac{\Psi(\underline{\underline{e}}^{n+1}, m^{n+1}) - \Psi(\underline{\underline{e}}^{n}, m^{n+1})}{\Delta t} - \dfrac{\partial \Psi}{\partial \underline{\underline{e}}}(\underline{\underline{e}}^{n+\frac{1}{2}\sharp}, m^{n+1}) : \underline{\underline{\dot{e}}}^{n+\frac{1}{2}} \right) \dfrac{\underline{\underline{\dot{e}}}^{n+\frac{1}{2}}}{\underline{\underline{\dot{e}}}^{n+\frac{1}{2}} : \underline{\underline{\dot{e}}}^{n+\frac{1}{2}}} & \text{(9a)} \\
\dfrac{p^{n+1}}{\rho_{\mathrm{f}}} \hat{=} \dfrac{\partial \Psi}{\partial m}\Big|^{n+\frac{1}{2}\sharp} \hat{=} \dfrac{\Psi(\underline{\underline{e}}^{n}, m^{n+1}) - \Psi(\underline{\underline{e}}^{n}, m^{n})}{m^{n+1} - m^{n}}. & \text{(9b)}
\end{cases}
$$

In the sequel, we will choose $\Psi^{\rm damp} = \frac{\eta_{\rm d}}{2}\,{\rm tr}(\underline{\underline{\dot{e}}})^2$, with the discretization

$$\int_{\Omega^0} \frac{\partial \Psi^{\rm damp}}{\partial \underline{\underline{\dot{e}}}}\Big|^{n+\frac{1}{2}\sharp} : d_{\underline{y}}\underline{\underline{e}}^{n+\frac{1}{2}\sharp} \cdot \underline{v}_{\rm s}^*\, d\Omega = \int_{\Omega^0} \eta_{\rm d}\, d_{\underline{y}}\underline{\underline{e}}^{n+\frac{1}{2}\sharp} \cdot \underline{v}_{\rm s}^{n+\frac{1}{2}} : d_{\underline{y}}\underline{\underline{e}}^{n+\frac{1}{2}\sharp} \cdot \underline{v}_{\rm s}^*\, d\Omega.$$

Remark 2 (Splitting and Robin boundary conditions rationale)
In essence, Step 1 takes care of the advection-diffusion part of the fluid problem, with an explicit treatment of the advection term (linear problem), and no coupling with the solid part other than via the Robin-type boundary conditions on the "fluid-proof" boundaries, namely, $\Gamma^0_{N{\rm nof}} \bigcup \Gamma^0_{N{\rm nos}}$. Then, Step 2 corrects the velocity computed in Step 1 by taking into account the coupling of the solid component with the pressure part of the fluid problem, including for the distributed friction term. Eventually, the fluid inertia term $\displaystyle\int_{\Omega^0} \frac{\rm d}{{\rm d}t}\big(J\rho_{\rm f}\phi\,\underline{v}_{\rm f}\big)\cdot\underline{v}^*\,d\Omega$ of the continuous problem is decomposed in the discrete problem into two contributions that appear in Steps 1 and 2a, i.e., respectively,

$$\int_{\Omega_{\rm f}^{n+1}} \frac{\rho_{\rm f}}{\Delta t}\phi^n \tilde{\underline{v}}_{\rm f}^{n+1}\cdot\underline{v}^*\,d\Omega - \int_{\Omega_{\rm f}^{n}} \frac{\rho_{\rm f}}{\Delta t}\phi^{n-1}\underline{v}_{\rm f}^{n}\cdot\underline{v}^*\,d\Omega \quad\text{and}\quad \int_{\Omega_{\rm f}^{n+1}} \rho_{\rm f}\phi^n\,\frac{\underline{v}_{\rm f}^{n+1}-\tilde{\underline{v}}_{\rm f}^{n+1}}{\Delta t}\cdot\underline{v}^*\,d\Omega.$$

As for Robin boundary conditions, they are introduced in Steps 1 and 2b – with the associated stabilization parameter γ – to take care of Dirichlet boundary conditions that relate the fluid and solid velocities, while ensuring stability in the coupling, as will be demonstrated in the below stability analysis. This combination of splitting strategy with Robin boundary conditions is similar to that proposed in [1] for fluid-structure interaction, albeit here extended to a more complex problem.

3.2 Stability analysis

Our objective in this section is to establish the stability of our proposed scheme, namely, a discrete energy balance similar to (5) up to some numerical dissipation terms. We will then naturally assume that there exists a solution $(\underline{y}_{\rm s}^n, \underline{v}_{\rm s}^n, \underline{v}_{\rm f}^n, m^n)$ to the discrete equations (6)–(8) up to time step n, and that this solution is *admissible*, which we characterize by

$$J(\underline{y}_{\rm s}^n) > 0, \quad 0 < \phi^n = \frac{m^n/\rho_{\rm f} + \phi_0}{J(\underline{y}_{\rm s}^n)} < 1,$$

everywhere, with obvious physical interpretations for these conditions. In fact, in the stability analysis, for technical reasons we will make a stronger assumption on the jacobian $J(\underline{y}_{\rm s}^n)$, i.e.

$$\frac{\max_{\xi\in\Omega^0} J(\underline{y}_{\rm s}^n)}{\min_{\xi\in\Omega^0} J(\underline{y}_{\rm s}^n)} < M, \tag{10}$$

with M independent of n. This is in order to be able to invoke the following inverse inequality.

Lemma 1
Assuming that (10) *holds, there exists a constant* C_{ie} *such that*

$$\|\sqrt{\phi^n}\,\underline{\underline{\varepsilon}}(\underline{v}^*)\cdot\underline{n}\|^2_{L^2(\Gamma^{n+1}_{N{\rm nos}})} \le \frac{C_{ie}}{h}\|\sqrt{\phi^n}\,\underline{\underline{\varepsilon}}(\underline{v}^*)\|^2_{L^2(\Omega_{\rm f}^{n+1})}, \quad \forall \underline{v}^* \in H^1(\Omega_{\rm f}^n)^3. \tag{11}$$

This inverse inequality is obtained by a standard scaling argument when noting that

$$\|\sqrt{\phi^n}\,\underline{\underline{\varepsilon}}(\underline{v}^*)\cdot\underline{n}\|^2_{L^2(\Gamma^{n+1}_{N{\rm nos}})} = \|\phi^n(\underline{\underline{\varepsilon}}(\underline{v}^*)\cdot\underline{n})^2\|_{L^1(\Gamma^{n+1}_{N{\rm nos}})} = \Big\|\frac{m^n/\rho_{\rm f}+\phi_0}{J(\underline{y}_{\rm s}^n)}(\underline{\underline{\varepsilon}}(\underline{v}^*)\cdot\underline{n})^2\Big\|_{L^1(\Gamma^{n+1}_{N{\rm nos}})},$$

where $(m^n/\rho_\mathrm{f} + \phi_0)\underline{\underline{\varepsilon}}(\underline{v}^*)^2$ is a polynomial – hence, in a finite dimensional space – due to the spatial discretization of m^n and $\underline{v}^*$. By contrast, $1/J(\underline{y}_\mathrm{s}^n)$ is not a polynomial in general, which leads to Condition (10).

Remark 3 (Inverse inequality and condition (10))
First of all, it should be noted that the inverse inequality (11) is rather "conservative" in itself, due to the fact that only the mesh elements adjacent to the boundary $\Gamma_{N\mathrm{nos}}^{n+1}$ are concerned in the left-hand side, hence, in the starting point of the scaling argument. Moreover, in the course of the scaling argument, Condition (10) could clearly be relaxed in the form

$$\frac{\max_{\xi\in K} J(\underline{y}_\mathrm{s}^n)}{\min_{\xi\in K} J(\underline{y}_\mathrm{s}^n)} < M,$$

for every finite element K in the mesh. A particular case arises when considering linear finite elements for the solid displacements, in which case the Jacobian is constant within each element.

For the sake of simplicity in the stability analysis, we will assume that $\underline{t} = 0$ on $\Gamma_{N\mathrm{nos}}$, $\Gamma_{N\mathrm{nof}} = \varnothing$, $\underline{f} = \underline{0}$, $\theta = 0$, $\underline{y}_\mathrm{s}^\mathrm{pr} = \underline{0}$ and $\underline{v}_\mathrm{f}^\mathrm{pr} = \underline{0}$. We then have the following result.

Proposition 2
Assuming that (10) *holds and that* $\gamma > C_{ie}$*, the time scheme* (6)–(8) *satisfies*

$$\begin{aligned}
\frac{\mathcal{E}^{n+1}-\mathcal{E}^n}{\Delta t} + \frac{\gamma\mu}{2h}\|\underline{v}_\mathrm{s}^{n+\frac12}\|^2_{\phi^n,\Gamma_{N\mathrm{nos}}^{n+1}} - \frac{\gamma\mu}{2h}\|\underline{v}_\mathrm{s}^{n-\frac12}\|^2_{\phi^n,\Gamma_{N\mathrm{nos}}^{n+1}} \\
\le \left(\underline{t}^{n+1},\underline{v}_\mathrm{f}^{n+1}\right)_{\phi^n,\Gamma_N^{n+1}} + \left(\underline{t}_0^{n+1},\underline{v}_\mathrm{s}^{n+\frac12}\right)_{1-\phi^n,\Gamma_N^0} - \int_{\Omega^0} \frac{\partial\Psi^{damp}}{\partial\underline{\underline{\dot e}}}\Big|^{n+\frac12\sharp} : d_{\underline{y}}\underline{\underline{e}}^{n+\frac12\sharp}\cdot\underline{v}_\mathrm{s}^{n+\frac12}\,d\Omega \\
- \int_{\Omega_\mathrm{f}^{n+1}} (\underline{v}_\mathrm{f}^{n+1}-\underline{v}_\mathrm{s}^{n+\frac12})\cdot|\phi^n|^2\,\underline{\underline{D}}_\mathrm{f}\cdot(\underline{v}_\mathrm{f}^{n+1}-\underline{v}_\mathrm{s}^{n+\frac12})\,d\Omega - \mathcal{T}_1 \\
- \frac{\rho_\mathrm{f}}{2\Delta t}\left\|\tilde{\underline{v}}_\mathrm{f}^{n+1}-\underline{v}_\mathrm{f}^n\right\|^2_{\phi^{n-1},\Omega_\mathrm{f}^n} - \frac{\rho_\mathrm{f}}{2\Delta t}\left\|\underline{v}_\mathrm{f}^{n+1}-\tilde{\underline{v}}_\mathrm{f}^{n+1}\right\|^2_{\phi^n,\Omega_\mathrm{f}^{n+1}} \\
- C\mu\left\|\underline{\underline{\varepsilon}}(\tilde{\underline{v}}_\mathrm{f}^{n+1})\right\|^2_{\phi^n,\Omega_\mathrm{f}^{n+1}} - C\frac{\mu}{L}\|\tilde{\underline{v}}_\mathrm{f}^{n+1}-\underline{v}_\mathrm{s}^{n+\frac12}\|^2_{\phi^n,\Gamma_{N\mathrm{nos}}^{n+1}}, \quad (12)
\end{aligned}$$

with C *a positive dimensionless constant,* L *homogeneous to a length,* $\mathcal{E}^n$ *the total discrete energy at step* n*, i.e.*

$$\mathcal{E}^n = \mathcal{K}_\mathrm{f}^n + \mathcal{K}_\mathrm{s}^n + \mathcal{W}^n = \frac{\rho_\mathrm{f}}{2}\|\underline{v}_\mathrm{f}^n\|^2_{\phi^{n-1},\Omega_\mathrm{f}^n} + \frac{\rho_{\mathrm{s}0}}{2}\|\underline{v}_\mathrm{s}^n\|^2_{1-\phi_0,\Omega^0} + \int_{\Omega^0}\Psi(\underline{\underline{e}}^n, m^n)\,d\Omega,$$

and $\mathcal{T}_1$ *the discrete flux of outgoing fluid kinetic energy that crosses the domain borders*

$$\mathcal{T}_1 = \frac12\int_{\partial\Omega_\mathrm{f}^n\setminus\Gamma_{N\mathrm{nos}}^n} \rho_\mathrm{f}\phi^{n-1}|\tilde{\underline{v}}_\mathrm{f}^{n+1}|^2(\underline{v}_\mathrm{f}^n-\underline{v}_\mathrm{s}^{n-\frac12})\cdot\underline{n}\,dS.$$

Proof. Respectively evaluating the equations (6), (7b) and (8) with the test functions

$$\tilde{\underline{v}}_\mathrm{f}^* = \tilde{\underline{v}}_\mathrm{f}^{n+1}, \quad \underline{v}_\mathrm{f}^* = \underline{v}_\mathrm{f}^{n+1} - \underline{v}_\mathrm{s}^{n+\frac12}, \quad \text{and} \quad \underline{v}_\mathrm{s}^* = \underline{v}_\mathrm{s}^{n+\frac12},$$

we get, defining

$$\mathcal{R}_p(\underline{v}^*) = \int_{\Omega_\mathrm{f}^{n+1}} \rho_\mathrm{f}\phi^n\,\frac{\underline{v}_\mathrm{f}^{n+1}-\tilde{\underline{v}}_\mathrm{f}^{n+1}}{\Delta t}\cdot\underline{v}^*\,d\Omega - \int_{\Omega_\mathrm{f}^{n+1}}\phi^n p^{n+1}\underline{\nabla}_{\underline{\mathrm{x}}}\cdot\underline{v}^*\,d\Omega - \int_{\Gamma_N^{n+1}}\phi^n\underline{t}^{n+1}\cdot\underline{v}^*\,dS$$

and using the weighted L^2-scalar product notation $(g,h)_{\psi,\Omega} = \int_\Omega \psi\, gh\, d\Omega$,

$$\frac{\rho_{\mathrm{f}}}{\Delta t}\left(\tilde{\underline{v}}_{\mathrm{f}}^{n+1},\tilde{\underline{v}}_{\mathrm{f}}^{n+1}\right)_{\phi^n,\Omega_{\mathrm{f}}^{n+1}} - \frac{\rho_{\mathrm{f}}}{\Delta t}\left(\underline{v}_{\mathrm{f}}^{n},\tilde{\underline{v}}_{\mathrm{f}}^{n+1}\right)_{\phi^{n-1},\Omega_{\mathrm{f}}^{n}} + \int_{\Omega_{\mathrm{f}}^n} \underline{\nabla}_{\underline{\mathrm{x}}}\cdot\left(\rho_{\mathrm{f}}\phi^{n-1}\tilde{\underline{v}}_{\mathrm{f}}^{n+1}\otimes(\underline{v}_{\mathrm{f}}^{n}-\underline{v}_{\mathrm{s}}^{n-\frac{1}{2}})\right)\cdot\tilde{\underline{v}}_{\mathrm{f}}^{n+1}\,d\Omega + 2\mu\|\underline{\underline{\varepsilon}}(\tilde{\underline{v}}_{\mathrm{f}}^{n+1})\|_{\phi^n,\Omega_{\mathrm{f}}^{n+1}} + \frac{\gamma\mu}{h}\left(\tilde{\underline{v}}_{\mathrm{f}}^{n+1}-\underline{v}_{\mathrm{s}}^{n-\frac{1}{2}},\tilde{\underline{v}}_{\mathrm{f}}^{n+1}\right)_{\phi^n,\Gamma_{N\mathrm{nos}}^{n+1}} = 2\mu\left(\underline{\underline{\varepsilon}}(\tilde{\underline{v}}_{\mathrm{f}}^{n+1})\cdot\underline{n},\tilde{\underline{v}}_{\mathrm{f}}^{n+1}\right)_{\phi^n,\Gamma_{N\mathrm{nos}}^{n+1}}, \quad (13a)$$

$$\frac{\rho_{\mathrm{f}}}{\Delta t}\left(\underline{v}_{\mathrm{f}}^{n+1}-\tilde{\underline{v}}_{\mathrm{f}}^{n+1},\underline{v}_{\mathrm{f}}^{n+1}\right)_{\phi^n,\Omega_{\mathrm{f}}^{n+1}} - \int_{\Omega_{\mathrm{f}}^{n+1}} p^{n+1}(\underline{\nabla}_{\underline{\mathrm{x}}}\phi^n)\cdot(\underline{v}_{\mathrm{f}}^{n+1}-\underline{v}_{\mathrm{s}}^{n+\frac{1}{2}})\,d\Omega - \int_{\Omega_{\mathrm{f}}^{n+1}} \phi^n p^{n+1}\underline{\nabla}_{\underline{\mathrm{x}}}\cdot\underline{v}_{\mathrm{f}}^{n+1}\,d\Omega + \int_{\Omega_{\mathrm{f}}^{n+1}} (\underline{v}_{\mathrm{f}}^{n+1}-\underline{v}_{\mathrm{s}}^{n+\frac{1}{2}})\cdot|\phi^n|^2\,\underline{\underline{D}}_{\mathrm{f}}\cdot(\underline{v}_{\mathrm{f}}^{n+1}-\underline{v}_{\mathrm{s}}^{n+\frac{1}{2}})\,d\Omega = \left(\underline{t}^{n+1},\underline{v}_{\mathrm{f}}^{n+1}\right)_{\phi^n,\Gamma_N^{n+1}} + \mathcal{R}_p(\underline{v}_{\mathrm{s}}^{n+\frac{1}{2}}), \quad (13b)$$

$$\frac{\rho_{\mathrm{s}0}}{2\Delta t}\|\underline{v}_{\mathrm{s}}^{n+1}\|^2_{1-\phi_0,\Omega^0} - \frac{\rho_{\mathrm{s}0}}{2\Delta t}\|\underline{v}_{\mathrm{s}}^{n}\|^2_{1-\phi_0,\Omega^0} + \int_{\Omega^0}\left(\frac{\partial\Psi}{\partial\underline{\underline{e}}}\Big|^{n+\frac{1}{2}\sharp} + \frac{\partial\Psi^{\mathrm{damp}}}{\partial\dot{\underline{\underline{e}}}}\Big|^{n+\frac{1}{2}\sharp}\right) : d_{\underline{y}}\underline{\underline{e}}^{n+\frac{1}{2}\sharp}\cdot\underline{v}_{\mathrm{s}}^{n+\frac{1}{2}}\,d\Omega + \int_{\Omega_{\mathrm{f}}^{n+1}}\phi^n p^{n+1}\underline{\nabla}_{\underline{\mathrm{x}}}\cdot\underline{v}_{\mathrm{s}}^{n+\frac{1}{2}}\,d\Omega + \frac{\gamma\mu}{h}\left(\underline{v}_{\mathrm{s}}^{n+\frac{1}{2}}-\underline{v}_{\mathrm{s}}^{n-\frac{1}{2}},\underline{v}_{\mathrm{s}}^{n+\frac{1}{2}}\right)_{\phi^n,\Gamma_{N\mathrm{nos}}^{n+1}} = \left(\underline{t}_0^{n+1}\cdot\underline{v}_{\mathrm{s}}^{n+\frac{1}{2}}\right)_{1-\phi^n,\Gamma_N^0} - \bar{\mathcal{R}}_{\mathrm{f}}^{d}(\underline{v}_{\mathrm{s}}^{n+\frac{1}{2}}). \quad (13c)$$

For the first two terms of (13a), we use $2(a,b) = a^2+b^2-(a-b)^2$ to obtain

$$\frac{\rho_{\mathrm{f}}}{\Delta t}\left(\tilde{\underline{v}}_{\mathrm{f}}^{n+1},\tilde{\underline{v}}_{\mathrm{f}}^{n+1}\right)_{\phi^n,\Omega_{\mathrm{f}}^{n+1}} - \frac{\rho_{\mathrm{f}}}{\Delta t}\left(\underline{v}_{\mathrm{f}}^{n},\tilde{\underline{v}}_{\mathrm{f}}^{n+1}\right)_{\phi^{n-1},\Omega_{\mathrm{f}}^{n}} = \frac{\rho_{\mathrm{f}}}{\Delta t}\left(\|\tilde{\underline{v}}_{\mathrm{f}}^{n+1}\|^2_{\phi^n,\Omega_{\mathrm{f}}^{n+1}} - \frac{1}{2}\|\tilde{\underline{v}}_{\mathrm{f}}^{n+1}\|^2_{\phi^{n-1},\Omega_{\mathrm{f}}^{n}} - \frac{1}{2}\|\underline{v}_{\mathrm{f}}^{n}\|^2_{\phi^{n-1},\Omega_{\mathrm{f}}^{n}} + \frac{1}{2}\|\tilde{\underline{v}}_{\mathrm{f}}^{n+1}-\underline{v}_{\mathrm{f}}^{n}\|^2_{\phi^{n-1},\Omega_{\mathrm{f}}^{n}}\right). \quad (14)$$

Then, the next term in (13a) can be rewritten as in the proof of [10, Theorem 7]

$$\int_{\Omega_{\mathrm{f}}^n}\underline{\nabla}_{\underline{\mathrm{x}}}\cdot(\rho_{\mathrm{f}}\phi^{n-1}\tilde{\underline{v}}_{\mathrm{f}}^{n+1}\otimes(\underline{v}_{\mathrm{f}}^{n}-\underline{v}_{\mathrm{s}}^{n-\frac{1}{2}}))\cdot\tilde{\underline{v}}_{\mathrm{f}}^{n+1}\,d\Omega = \int_{\Omega_{\mathrm{f}}^n}\frac{1}{2}|\tilde{\underline{v}}_{\mathrm{f}}^{n+1}|^2\underline{\nabla}_{\underline{\mathrm{x}}}\cdot(\rho_{\mathrm{f}}\phi^{n-1}(\underline{v}_{\mathrm{f}}^{n}-\underline{v}_{\mathrm{s}}^{n-\frac{1}{2}}))\,d\Omega + \mathcal{T}_1. \quad (15)$$

Now, recalling $\phi^n = \frac{m^n/\rho_{\mathrm{f}}+\phi_0}{J(\underline{y}_{\mathrm{s}}^n)}$ we evaluate (7a) at time step $n-1$ with $q^* = |\tilde{\underline{v}}_{\mathrm{f}}^{n+1}|^2$ – assuming this is allowed by the spatial discretization, see Section 3.3. This gives

$$\frac{1}{2}\int_{\Omega_{\mathrm{f}}^n}|\tilde{\underline{v}}_{\mathrm{f}}^{n+1}|^2\underline{\nabla}_{\underline{\mathrm{x}}}\cdot(\rho_{\mathrm{f}}\phi^{n-1}\,(\underline{v}_{\mathrm{f}}^{n}-\underline{v}_{\mathrm{s}}^{n-\frac{1}{2}}))\,d\Omega = -\frac{1}{2}\int_{\Omega^0}\frac{m^n-m^{n-1}}{\Delta t}|\tilde{\underline{v}}_{\mathrm{f}}^{n+1}|^2\,d\Omega = -\frac{1}{2}\int_{\Omega^0}\frac{\phi^n\rho_{\mathrm{f}}J(\underline{y}_{\mathrm{s}}^n)-\phi^{n-1}\rho_{\mathrm{f}}J(\underline{y}_{\mathrm{s}}^{n-1})}{\Delta t}|\tilde{\underline{v}}_{\mathrm{f}}^{n+1}|^2\,d\Omega = -\frac{\rho_{\mathrm{f}}}{2\Delta t}\left(\|\tilde{\underline{v}}_{\mathrm{f}}^{n+1}\|^2_{\phi^n,\Omega_{\mathrm{f}}^{n+1}} - \|\tilde{\underline{v}}_{\mathrm{f}}^{n+1}\|^2_{\phi^{n-1},\Omega_{\mathrm{f}}^{n}}\right). \quad (16)$$

Gathering (14), (15) and (16), we get

$$\frac{\rho_{\mathrm{f}}}{\Delta t}\left(\tilde{\underline{v}}_{\mathrm{f}}^{n+1},\tilde{\underline{v}}_{\mathrm{f}}^{n+1}\right)_{\phi^n,\Omega_{\mathrm{f}}^{n+1}}-\frac{\rho_{\mathrm{f}}}{\Delta t}\left(\underline{v}_{\mathrm{f}}^{n}\cdot\tilde{\underline{v}}_{\mathrm{f}}^{n+1}\right)_{\phi^{n-1},\Omega_{\mathrm{f}}^{n}}+\int_{\Omega_{\mathrm{f}}^{n}}\underline{\nabla}_{\underline{\mathrm{x}}}\cdot\left(\rho_{\mathrm{f}}\phi^{n-1}\tilde{\underline{v}}_{\mathrm{f}}^{n+1}\otimes(\underline{v}_{\mathrm{f}}^{n}-\underline{v}_{\mathrm{s}}^{n-\frac{1}{2}})\right)\cdot\tilde{\underline{v}}_{\mathrm{f}}^{n+1}\,d\Omega$$
$$=\frac{\rho_{\mathrm{f}}}{2\Delta t}\left(\|\tilde{\underline{v}}_{\mathrm{f}}^{n+1}\|^2_{\phi^n,\Omega_{\mathrm{f}}^{n+1}}-\|\underline{v}_{\mathrm{f}}^{n}\|^2_{\phi^{n-1},\Omega_{\mathrm{f}}^{n}}+\|\tilde{\underline{v}}_{\mathrm{f}}^{n+1}-\underline{v}_{\mathrm{f}}^{n}\|^2_{\phi^{n-1},\Omega_{\mathrm{f}}^{n}}\right)+\mathcal{T}_1. \quad (17)$$

Then, substituting this result in (13a) and summing with (13b) and (13c) while applying the identity $(a-b,a)=\frac{1}{2}a^2-\frac{1}{2}b^2+\frac{1}{2}(a-b)^2$ to $(\underline{v}_{\mathrm{f}}^{n+1}-\tilde{\underline{v}}_{\mathrm{f}}^{n+1},\underline{v}_{\mathrm{f}}^{n+1})_{\phi^n,\Omega^{n+1}}$, we get (using $\Delta t\,\underline{v}_{\mathrm{s}}^{n+\frac{1}{2}}=\underline{y}_{\mathrm{s}}^{n+1}-\underline{y}_{\mathrm{s}}^{n}$)

$$\frac{\mathcal{K}_{\mathrm{f}}^{n+1}-\mathcal{K}_{\mathrm{f}}^{n}}{\Delta t}+\frac{\mathcal{K}_{\mathrm{s}}^{n+1}-\mathcal{K}_{\mathrm{s}}^{n}}{\Delta t}+\int_{\Omega^0}\left(\frac{\partial\Psi}{\partial\underline{\underline{e}}}\Big|^{n+\frac{1}{2}\sharp}+\frac{\partial\Psi^{\mathrm{damp}}}{\partial\dot{\underline{\underline{e}}}}\Big|^{n+\frac{1}{2}\sharp}\right):d_{\underline{y}}\underline{\underline{e}}^{n+\frac{1}{2}\sharp}\cdot\underline{v}_{\mathrm{s}}^{n+\frac{1}{2}}\,d\Omega$$
$$-\int_{\Omega_{\mathrm{f}}^{n+1}}\phi^n p^{n+1}\underline{\nabla}_{\underline{\mathrm{x}}}\cdot\left(\underline{v}_{\mathrm{f}}^{n+1}-\underline{v}_{\mathrm{s}}^{n+\frac{1}{2}}\right)d\Omega-\int_{\Omega_{\mathrm{f}}^{n+1}}p^{n+1}(\underline{\nabla}_{\underline{\mathrm{x}}}\phi^n)\cdot(\underline{v}_{\mathrm{f}}^{n+1}-\underline{v}_{\mathrm{s}}^{n+\frac{1}{2}})\,d\Omega$$
$$+\frac{\rho_{\mathrm{f}}}{2\Delta t}\left[\left\|\tilde{\underline{v}}_{\mathrm{f}}^{n+1}-\underline{v}_{\mathrm{f}}^{n}\right\|^2_{\phi^{n-1},\Omega_{\mathrm{f}}^{n}}+\left\|\underline{v}_{\mathrm{f}}^{n+1}-\tilde{\underline{v}}_{\mathrm{f}}^{n+1}\right\|^2_{\phi^n,\Omega_{\mathrm{f}}^{n+1}}\right]\underbrace{-2\mu\left(\underline{\underline{\varepsilon}}(\tilde{\underline{v}}_{\mathrm{f}}^{n+1})\cdot\underline{n},(\tilde{\underline{v}}_{\mathrm{f}}^{n+1}-\underline{v}_{\mathrm{s}}^{n+\frac{1}{2}})\right)_{\phi^n,\Gamma_{N\mathrm{nos}}^{n+1}}}_{\mathcal{T}_2}$$
$$\underbrace{+\frac{\gamma\mu}{h}\left[\left(\underline{v}_{\mathrm{s}}^{n+\frac{1}{2}}-\tilde{\underline{v}}_{\mathrm{f}}^{n+1},\underline{v}_{\mathrm{s}}^{n+\frac{1}{2}}\right)_{\phi^n,\Gamma_{N\mathrm{nos}}^{n+1}}+\left(\tilde{\underline{v}}_{\mathrm{f}}^{n+1}-\underline{v}_{\mathrm{s}}^{n-\frac{1}{2}},\tilde{\underline{v}}_{\mathrm{f}}^{n+1}\right)_{\phi^n,\Gamma_{N\mathrm{nos}}^{n+1}}\right]}_{\mathcal{T}_3}$$
$$=\left(\underline{t}^{n+1},\underline{v}_{\mathrm{f}}^{n+1}\right)_{\phi^n,\Gamma_N^{n+1}}+\left(\underline{t}_0^{n+1},\underline{v}_{\mathrm{s}}^{n+\frac{1}{2}}\right)_{1-\phi^n,\Gamma_N^0}-\mathcal{T}_1$$
$$-2\mu\left\|\underline{\varepsilon}(\tilde{\underline{v}}_{\mathrm{f}}^{n+1})\right\|^2_{\phi^n,\Omega_{\mathrm{f}}^{n+1}}-\int_{\Omega_{\mathrm{f}}^{n+1}}(\underline{v}_{\mathrm{f}}^{n+1}-\underline{v}_{\mathrm{s}}^{n+\frac{1}{2}})\cdot|\phi^n|^2\,\underline{\underline{D}}_{\mathrm{f}}\cdot(\underline{v}_{\mathrm{f}}^{n+1}-\underline{v}_{\mathrm{s}}^{n+\frac{1}{2}})\,d\Omega. \quad (18)$$

We used here the following identity that comes from (6) evaluated with $\tilde{\underline{v}}_{\mathrm{f}}^{*}=\underline{v}_{\mathrm{s}}^{n+\frac{1}{2}}$

$$\bar{\mathcal{R}}_{\mathrm{f}}^{d}(\underline{v}_{\mathrm{s}}^{n+\frac{1}{2}})-\mathcal{R}_p(\underline{v}_{\mathrm{s}}^{n+\frac{1}{2}})$$
$$=2\mu\left(\underline{\underline{\varepsilon}}(\tilde{\underline{v}}_{\mathrm{f}}^{n+1})\cdot\underline{n},\underline{v}_{\mathrm{s}}^{n+\frac{1}{2}}\right)_{\phi^n,\Gamma_{N\mathrm{nos}}^{n+1}}-\frac{\gamma\mu}{h}\left(\tilde{\underline{v}}_{\mathrm{f}}^{n+1}-\underline{v}_{\mathrm{s}}^{n-\frac{1}{2}},\underline{v}_{\mathrm{s}}^{n+\frac{1}{2}}\right)_{\phi^n,\Gamma_{N\mathrm{nos}}^{n+1}}.$$

Considering now

$$\mathcal{T}_3=\frac{\gamma\mu}{h}\left[(\underline{v}_{\mathrm{s}}^{n+\frac{1}{2}}-\tilde{\underline{v}}_{\mathrm{f}}^{n+1},\underline{v}_{\mathrm{s}}^{n+\frac{1}{2}})_{\phi^n,\Gamma_{N\mathrm{nos}}^{n+1}}+(\tilde{\underline{v}}_{\mathrm{f}}^{n+1}-\underline{v}_{\mathrm{s}}^{n-\frac{1}{2}},\tilde{\underline{v}}_{\mathrm{f}}^{n+1})_{\phi^n,\Gamma_{N\mathrm{nos}}^{n+1}}\right]$$
$$=\frac{\gamma\mu}{h}\Big[(\underline{v}_{\mathrm{s}}^{n+\frac{1}{2}}-\tilde{\underline{v}}_{\mathrm{f}}^{n+1},\underline{v}_{\mathrm{s}}^{n+\frac{1}{2}}-\tilde{\underline{v}}_{\mathrm{f}}^{n+1})_{\phi^n,\Gamma_{N\mathrm{nos}}^{n+1}}+(\underline{v}_{\mathrm{s}}^{n+\frac{1}{2}}-\tilde{\underline{v}}_{\mathrm{f}}^{n+1},\tilde{\underline{v}}_{\mathrm{f}}^{n+1})_{\phi^n,\Gamma_{N\mathrm{nos}}^{n+1}}$$
$$+(\tilde{\underline{v}}_{\mathrm{f}}^{n+1}-\underline{v}_{\mathrm{s}}^{n-\frac{1}{2}},\tilde{\underline{v}}_{\mathrm{f}}^{n+1})_{\phi^n,\Gamma_{N\mathrm{nos}}^{n+1}}\Big]$$
$$=\frac{\gamma\mu}{h}\|\tilde{\underline{v}}_{\mathrm{f}}^{n+1}-\underline{v}_{\mathrm{s}}^{n+\frac{1}{2}}\|^2_{\phi^n,\Gamma_{N\mathrm{nos}}^{n+1}}+\frac{\gamma\mu}{h}(\underline{v}_{\mathrm{s}}^{n+\frac{1}{2}}-\underline{v}_{\mathrm{s}}^{n-\frac{1}{2}},\tilde{\underline{v}}_{\mathrm{f}}^{n+1})_{\phi^n,\Gamma_{N\mathrm{nos}}^{n+1}},$$

we have that

$$(\underline{v}_{\mathrm{s}}^{n+\frac{1}{2}}-\underline{v}_{\mathrm{s}}^{n-\frac{1}{2}},\tilde{\underline{v}}_{\mathrm{f}}^{n+1})_{\phi^n,\Gamma_{N\mathrm{nos}}^{n+1}}=(\underline{v}_{\mathrm{s}}^{n+\frac{1}{2}}-\underline{v}_{\mathrm{s}}^{n-\frac{1}{2}},\tilde{\underline{v}}_{\mathrm{f}}^{n+1}-\underline{v}_{\mathrm{s}}^{n+\frac{1}{2}})_{\phi^n,\Gamma_{N\mathrm{nos}}^{n+1}}+(\underline{v}_{\mathrm{s}}^{n+\frac{1}{2}}-\underline{v}_{\mathrm{s}}^{n-\frac{1}{2}},\underline{v}_{\mathrm{s}}^{n+\frac{1}{2}})_{\phi^n,\Gamma_{N\mathrm{nos}}^{n+1}}.$$

Using $2(a,b) \leq \|a\|^2 + \|b\|^2$ with the first term, and $2(a-b,a) = \|a\|^2 - \|b\|^2 + \|a-b\|^2$ with the second one, we obtain

$$(\underline{v}_{\mathrm{s}}^{n+\frac{1}{2}} - \underline{v}_{\mathrm{s}}^{n-\frac{1}{2}}, \tilde{\underline{v}}_{\mathrm{f}}^{n+1})_{\phi^n,\Gamma_{N\mathrm{nos}}^{n+1}} \geq -\frac{1}{2}\|\underline{v}_{\mathrm{s}}^{n+\frac{1}{2}} - \underline{v}_{\mathrm{s}}^{n-\frac{1}{2}}\|^2_{\phi^n,\Gamma_{N\mathrm{nos}}^{n+1}} - \frac{1}{2}\|\tilde{\underline{v}}_{\mathrm{f}}^{n+1} - \underline{v}_{\mathrm{s}}^{n+\frac{1}{2}}\|^2_{\phi^n,\Gamma_{N\mathrm{nos}}^{n+1}}$$
$$+ \frac{1}{2}\|\underline{v}_{\mathrm{s}}^{n+\frac{1}{2}} - \underline{v}_{\mathrm{s}}^{n-\frac{1}{2}}\|^2_{\phi^n,\Gamma_{N\mathrm{nos}}^{n+1}} + \frac{1}{2}\|\underline{v}_{\mathrm{s}}^{n+\frac{1}{2}}\|^2_{\phi^n,\Gamma_{N\mathrm{nos}}^{n+1}} - \frac{1}{2}\|\underline{v}_{\mathrm{s}}^{n-\frac{1}{2}}\|^2_{\phi^n,\Gamma_{N\mathrm{nos}}^{n+1}},$$

hence,

$$\mathcal{T}_3 \geq \frac{\gamma\mu}{2h}\|\tilde{\underline{v}}_{\mathrm{f}}^{n+1} - \underline{v}_{\mathrm{s}}^{n+\frac{1}{2}}\|^2_{\phi^n,\Gamma_{N\mathrm{nos}}^{n+1}} + \frac{\gamma\mu}{2h}\|\underline{v}_{\mathrm{s}}^{n+\frac{1}{2}}\|^2_{\phi^n,\Gamma_{N\mathrm{nos}}^{n+1}} - \frac{\gamma\mu}{2h}\|\underline{v}_{\mathrm{s}}^{n-\frac{1}{2}}\|^2_{\phi^n,\Gamma_{N\mathrm{nos}}^{n+1}}. \tag{19}$$

For the term $\mathcal{T}_2$, we use Young's inequality $(a,b) \leq \frac{1}{2L}\|a\|^2 + \frac{L}{2}\|b\|^2$, with L homogeneous to a length here, to get

$$-\mathcal{T}_2 \leq \mu\left[L\|\underline{\underline{\varepsilon}}(\tilde{\underline{v}}_{\mathrm{f}}^{n+1})\cdot\underline{n}\|^2_{\phi^n,\Gamma_{N\mathrm{nos}}^{n+1}} + \frac{1}{L}\|\tilde{\underline{v}}_{\mathrm{f}}^{n+1} - \underline{v}_{\mathrm{s}}^{n+\frac{1}{2}}\|^2_{\phi^n,\Gamma_{N\mathrm{nos}}^{n+1}}\right],$$

and the inverse inequality (11) then gives

$$\mathcal{T}_2 \geq -\mu\frac{C_{ie}L}{h}\|\underline{\underline{\varepsilon}}(\tilde{\underline{v}}_{\mathrm{f}}^{n+1})\|^2_{\phi^n,\Omega_{\mathrm{f}}^{n+1}} - \frac{\mu}{L}\|\tilde{\underline{v}}_{\mathrm{f}}^{n+1} - \underline{v}_{\mathrm{s}}^{n+\frac{1}{2}}\|^2_{\phi^n,\Gamma_{N\mathrm{nos}}^{n+1}}. \tag{20}$$

Using the bounds (19) and (20) in (18), we obtain

$$\frac{\mathcal{K}_{\mathrm{f}}^{n+1} - \mathcal{K}_{\mathrm{f}}^{n}}{\Delta t} + \frac{\mathcal{K}_{\mathrm{s}}^{n+1} - \mathcal{K}_{\mathrm{s}}^{n}}{\Delta t} + \int_{\Omega^0}\left(\frac{\partial\Psi}{\partial\underline{\underline{e}}}\Big|^{n+\frac{1}{2}\sharp} + \frac{\partial\Psi^{\mathrm{damp}}}{\partial\dot{\underline{\underline{e}}}}\Big|^{n+\frac{1}{2}\sharp}\right) : d_{\underline{t}}\underline{\underline{e}}^{n+\frac{1}{2}\sharp}\cdot\underline{v}_{\mathrm{s}}^{n+\frac{1}{2}}\,d\Omega$$
$$\underbrace{-\int_{\Omega_{\mathrm{f}}^{n+1}} p^{n+1}(\underline{\nabla}_{\underline{\mathrm{x}}}\phi^n)\cdot(\underline{v}_{\mathrm{f}}^{n+1} - \underline{v}_{\mathrm{s}}^{n+\frac{1}{2}})\,d\Omega - \int_{\Omega_{\mathrm{f}}^{n+1}} p^{n+1}\phi^n\underline{\nabla}_{\underline{\mathrm{x}}}\cdot(\underline{v}_{\mathrm{f}}^{n+1} - \underline{v}_{\mathrm{s}}^{n+\frac{1}{2}})\,d\Omega}_{\mathcal{T}_4}$$
$$+\frac{\rho_{\mathrm{f}}}{2\Delta t}\left\|\tilde{\underline{v}}_{\mathrm{f}}^{n+1} - \underline{v}_{\mathrm{f}}^{n}\right\|^2_{\phi^{n-1},\Omega_{\mathrm{f}}^{n}} + \frac{\rho_{\mathrm{f}}}{2\Delta t}\left\|\underline{v}_{\mathrm{f}}^{n+1} - \tilde{\underline{v}}_{\mathrm{f}}^{n+1}\right\|^2_{\phi^n,\Omega_{\mathrm{f}}^{n+1}} + \frac{\gamma\mu}{2h}\|\underline{v}_{\mathrm{s}}^{n+\frac{1}{2}}\|^2_{\phi^n,\Gamma_{N\mathrm{nos}}^{n+1}} - \frac{\gamma\mu}{2h}\|\underline{v}_{\mathrm{s}}^{n-\frac{1}{2}}\|^2_{\phi^n,\Gamma_{N\mathrm{nos}}^{n+1}}$$
$$+\mu\left(2 - \frac{C_{ie}L}{h}\right)\left\|\underline{\underline{\varepsilon}}(\tilde{\underline{v}}_{\mathrm{f}}^{n+1})\right\|^2_{\phi^n,\Omega_{\mathrm{f}}^{n+1}} + \mu\left(\frac{\gamma}{2h} - \frac{1}{L}\right)\|\tilde{\underline{v}}_{\mathrm{f}}^{n+1} - \underline{v}_{\mathrm{s}}^{n+\frac{1}{2}}\|^2_{\phi^n,\Gamma_{N\mathrm{nos}}^{n+1}}$$
$$\leq (\underline{t}^{n+1}, \underline{v}_{\mathrm{f}}^{n+1})_{\phi^n,\Gamma_N^{n+1}} + (\underline{t}_0^{n+1}, \underline{v}_{\mathrm{s}}^{n+\frac{1}{2}})_{1-\phi^n,\Gamma_N^0} - \mathcal{T}_1$$
$$- \int_{\Omega_{\mathrm{f}}^{n+1}}(\underline{v}_{\mathrm{f}}^{n+1} - \underline{v}_{\mathrm{s}}^{n+\frac{1}{2}})\cdot|\phi^n|^2\,\underline{\underline{D}}_{\mathrm{f}}\cdot(\underline{v}_{\mathrm{f}}^{n+1} - \underline{v}_{\mathrm{s}}^{n+\frac{1}{2}})\,d\Omega.$$

Now, using $\underline{\nabla}\cdot(\phi\underline{v}_{\mathrm{f}}) = \underline{\nabla}\,\phi\cdot\underline{v}_{\mathrm{f}} + \phi\underline{\nabla}\cdot\underline{v}_{\mathrm{f}}$, and (7a) evaluated with $\dfrac{p^{n+1}}{\rho_{\mathrm{f}}}$ – again, assuming this is allowed by the spatial discretization, see Section 3.3 – we have

$$\begin{aligned}
\mathcal{T}_4 &= -\int_{\Omega_{\mathrm{f}}^{n+1}} p^{n+1}(\underline{\nabla}_{\underline{\mathrm{x}}}\phi^n)\cdot(\underline{v}_{\mathrm{f}}^{n+1} - \underline{v}_{\mathrm{s}}^{n+\frac{1}{2}})\,d\Omega - \int_{\Omega_{\mathrm{f}}^{n+1}} p^{n+1}\phi^n\underline{\nabla}_{\underline{\mathrm{x}}}\cdot(\underline{v}_{\mathrm{f}}^{n+1} - \underline{v}_{\mathrm{s}}^{n+\frac{1}{2}})\,d\Omega \\
&= -\int_{\Omega_{\mathrm{f}}^{n+1}} p^{n+1}\underline{\nabla}_{\underline{\mathrm{x}}}\cdot(\phi^n(\underline{v}_{\mathrm{f}}^{n+1} - \underline{v}_{\mathrm{s}}^{n+\frac{1}{2}}))\,d\Omega \\
&= \int_{\Omega^0}\frac{p^{n+1}}{\rho_{\mathrm{f}}}\frac{m^{n+1} - m^n}{\Delta t}\,d\Omega \\
&= \int_{\Omega^0}\frac{\partial\Psi}{\partial m}\Big|^{n+\frac{1}{2}\sharp}\frac{m^{n+1} - m^n}{\Delta t}\,d\Omega.
\end{aligned} \tag{21}$$

Furthermore, thanks to (9) we have

$$\begin{aligned}\frac{\partial\Psi}{\partial\underline{e}}\Big|^{n+\frac{1}{2}\sharp} : d_{\underline{y}}\underline{\underline{e}}^{n+\frac{1}{2}\sharp}\cdot\underline{v}_{\rm s}^{n+\frac{1}{2}} + \frac{\partial\Psi}{\partial m}\Big|^{n+\frac{1}{2}\sharp}\frac{m^{n+1}-m^n}{\Delta t}\\ = \frac{\partial\Psi}{\partial\underline{e}}\Big|^{n+\frac{1}{2}\sharp} : \frac{\underline{\underline{e}}^{n+1}-\underline{\underline{e}}^n}{\Delta t} + \frac{\partial\Psi}{\partial m}\Big|^{n+\frac{1}{2}\sharp}\frac{m^{n+1}-m^n}{\Delta t}\\ = \frac{\Psi^{\rm n+1}-\Psi^{\rm n}}{\Delta t}.\end{aligned}$$

Finally, we are led to

$$\begin{aligned}&\frac{\mathcal{E}^{n+1}-\mathcal{E}^n}{\Delta t} + \frac{\gamma\mu}{2h}\|\underline{v}_{\rm s}^{n+\frac{1}{2}}\|^2_{\phi^n,\Gamma^{n+1}_{N\rm nos}} - \frac{\gamma\mu}{2h}\|\underline{v}_{\rm s}^{n-\frac{1}{2}}\|^2_{\phi^n,\Gamma^{n+1}_{N\rm nos}}\\ &\quad\le \left(\underline{t}^{n+1},\underline{v}_{\rm f}^{n+1}\right)_{\phi^n,\Gamma_N^{n+1}} + \left(\underline{t}_0^{n+1},\underline{v}_{\rm s}^{n+\frac{1}{2}}\right)_{1-\phi^n,\Gamma_N^0} - \int_{\Omega^0}\frac{\partial\Psi^{\rm damp}}{\partial\dot{\underline{e}}}\Big|^{n+\frac{1}{2}\sharp} : d_{\underline{y}}\underline{\underline{e}}^{n+\frac{1}{2}\sharp}\cdot\underline{v}_{\rm s}^{n+\frac{1}{2}}\,d\Omega\\ &\qquad - \int_{\Omega_{\rm f}^{n+1}}(\underline{v}_{\rm f}^{n+1}-\underline{v}_{\rm s}^{n+\frac{1}{2}})\cdot|\phi^n|^2\,\underline{\underline{D}}_{\rm f}\cdot(\underline{v}_{\rm f}^{n+1}-\underline{v}_{\rm s}^{n+\frac{1}{2}})\,d\Omega - \mathcal{T}_1\\ &\qquad - \frac{\rho_{\rm f}}{2\Delta t}\left\|\underline{\tilde{v}}_{\rm f}^{n+1}-\underline{v}_{\rm f}^n\right\|^2_{\phi^{n-1},\Omega_{\rm f}^n} - \frac{\rho_{\rm f}}{2\Delta t}\left\|\underline{v}_{\rm f}^{n+1}-\underline{\tilde{v}}_{\rm f}^{n+1}\right\|^2_{\phi^n,\Omega_{\rm f}^{n+1}}\\ &\quad - \mu\left(2-\frac{C_{ie}L}{h}\right)\left\|\underline{\underline{\varepsilon}}(\underline{\tilde{v}}_{\rm f}^{n+1})\right\|^2_{\phi^n,\Omega_{\rm f}^{n+1}} - \mu\left(\frac{\gamma}{2h}-\frac{1}{L}\right)\|\underline{\tilde{v}}_{\rm f}^{n+1}-\underline{v}_{\rm s}^{n+\frac{1}{2}}\|^2_{\phi^n,\Gamma^{n+1}_{N\rm nos}}, \quad (22)\end{aligned}$$

Therefore, we can have (12) provided we can find L such that $2-\dfrac{C_{ie}L}{h}\ge 0$ and $\dfrac{\gamma}{2h}-\dfrac{1}{L}>0$, i.e. when $\gamma > C_{ie}$. ■

Remark 4
Proposition 2 ensures the energy stability of our scheme provided $\gamma\mu\Delta t = O(h)$. This CFL-like condition and the interface term $\frac{\gamma\mu}{2h}\|\underline{v}_{\rm s}^{n+\frac{1}{2}}\|^2_{\phi^n,\Gamma_{N\rm nos}}$, that could be incorporated to the numerical energy if $\Gamma_{N\rm nos}$ was fixed, already appeared in the Robin based fluid-structure interaction splitting scheme of [1].

Remark 5
All the physical dissipation terms already seen in the continuous energy balance (5) are present in this discrete balance. In addition, as in [1], the terms $\left\|\underline{\tilde{v}}_{\rm f}^{n+1}-\underline{v}_{\rm f}^n\right\|^2_{\phi^{n-1},\Omega_{\rm f}^n}$, $\left\|\underline{v}_{\rm f}^{n+1}-\underline{\tilde{v}}_{\rm f}^{n+1}\right\|^2_{\phi^n,\Omega_{\rm f}^{n+1}}$ and $\|\underline{\tilde{v}}_{\rm f}^{n+1}-\underline{v}_{\rm s}^{n+\frac{1}{2}}\|^2_{\phi^n,\Gamma^{n+1}_{N\rm nos}}$ bring numerical dissipation.

Remark 6
In line with Remark 1, let us mention that this stability analysis can easily be reduced to a fluid-structure interaction problem in the ALE formalism. Nevertheless, one noticeable difference is that (16) – a crucial ingredient of the stability analysis that rests here on (7a) and the definition of ϕ – would then require a "geometric conservation law" (GCL), see e.g. Proposition 4.7.1 in [37], or (9.53) in [20]. Indeed, this type of condition is classically used to ensure stability at the discrete level with moving domains [16, 17, 20, 24, 38, 40].

3.3 Consistency considerations pertaining to spatial discretization

In this section, we provide some insight on consistency perturbations that may arise in the above energy estimate due to spatial discretization. First of all, since the porosity is computed

explicitly at Step 0 of our algorithm, it is natural to compute it exactly as $\phi^n = \frac{m^n/\rho_\mathrm{f}+\phi_0}{J(\underline{y}_\mathrm{s}^n)}$ at the quadrature points, and store these values for use in the next steps. Then, in order for (21) to hold, we recall that the discrete spaces for the pressure and the mass need to coincide, a reasonable choice that we will make. However, in this case we need to adapt the pressure law at Step 2a into

$$p^{n+1} \hat{=} \pi_m\left(\rho_\mathrm{f} \frac{\partial \Psi}{\partial m}\Big|^{n+\frac{1}{2}\sharp}\right), \tag{23}$$

where π_m denotes a projection operator onto the discrete space chosen for the fluid mass. In our case we will consider L^2-projection. Then, in our above stability analysis, the only modification induced pertains to (16), for which we now have by testing (7a) at time step $n-1$ with $q_h^* = \pi_m(|\underline{\tilde{v}}_\mathrm{f}^{n+1}|^2)$

$$\begin{aligned}
&\frac{1}{2}\int_{\Omega_\mathrm{f}^n} |\underline{\tilde{v}}_\mathrm{f}^{n+1}|^2 \underline{\nabla}_{\underline{\mathrm{x}}}\cdot(\rho_\mathrm{f}\phi^{n-1}\,(\underline{v}_\mathrm{f}^n - \underline{v}_\mathrm{s}^{n-\frac{1}{2}}))\,d\Omega \\
&\qquad = \frac{1}{2}\int_{\Omega_\mathrm{f}^n} \pi_m(|\underline{\tilde{v}}_\mathrm{f}^{n+1}|^2)\underline{\nabla}_{\underline{\mathrm{x}}}\cdot(\rho_\mathrm{f}\phi^{n-1}\,(\underline{v}_\mathrm{f}^n - \underline{v}_\mathrm{s}^{n-\frac{1}{2}}))\,d\Omega + \mathcal{S}_1 \\
&\qquad = -\frac{1}{2}\int_{\Omega^0} \frac{m^n - m^{n-1}}{\Delta t}\pi_m(|\underline{\tilde{v}}_\mathrm{f}^{n+1}|^2)\,d\Omega + \mathcal{S}_1 \\
&\qquad = -\frac{1}{2}\int_{\Omega^0} \frac{\phi^n\rho_\mathrm{f}J(\underline{y}_\mathrm{s}^n) - \phi^{n-1}\rho_\mathrm{f}J(\underline{y}_\mathrm{s}^{n-1})}{\Delta t}\pi_m(|\underline{\tilde{v}}_\mathrm{f}^{n+1}|^2)\,d\Omega + \mathcal{S}_1 \\
&\qquad = -\frac{\rho_\mathrm{f}}{2\Delta t}\left(\|(\pi_m(|\underline{\tilde{v}}_\mathrm{f}^{n+1}|^2))^{\frac{1}{2}}\|^2_{\phi^n,\Omega_\mathrm{f}^{n+1}} - \|(\pi_m(|\underline{\tilde{v}}_\mathrm{f}^{n+1}|^2))^{\frac{1}{2}}\|^2_{\phi^{n-1},\Omega_\mathrm{f}^n}\right) + \mathcal{S}_1 \\
&\qquad = -\frac{\rho_\mathrm{f}}{2\Delta t}\left(\|\underline{\tilde{v}}_\mathrm{f}^{n+1}\|^2_{\phi^n,\Omega_\mathrm{f}^{n+1}} - \|\underline{\tilde{v}}_\mathrm{f}^{n+1}\|^2_{\phi^{n-1},\Omega_\mathrm{f}^n}\right) + \mathcal{S}_1 + \mathcal{S}_2,
\end{aligned}$$

with the following consistency perturbations induced in (16), i.e. our specific version of the GCL,

$$\begin{cases}
\mathcal{S}_1 = \dfrac{1}{2}\displaystyle\int_{\Omega_\mathrm{f}^n}\big(|\underline{\tilde{v}}_\mathrm{f}^{n+1}|^2 - \pi_m(|\underline{\tilde{v}}_\mathrm{f}^{n+1}|^2)\big)\underline{\nabla}_{\underline{\mathrm{x}}}\cdot(\rho_\mathrm{f}\phi^{n-1}\,(\underline{v}_\mathrm{f}^n - \underline{v}_\mathrm{s}^{n-\frac{1}{2}}))\,d\Omega \\
\mathcal{S}_2 = \dfrac{\rho_\mathrm{f}}{2\Delta t}\Big(\|\underline{\tilde{v}}_\mathrm{f}^{n+1}\|^2_{\phi^n,\Omega_\mathrm{f}^{n+1}} - \|\underline{\tilde{v}}_\mathrm{f}^{n+1}\|^2_{\phi^{n-1},\Omega_\mathrm{f}^n} \\
\qquad\qquad - \|(\pi_m(|\underline{\tilde{v}}_\mathrm{f}^{n+1}|^2))^{\frac{1}{2}}\|^2_{\phi^n,\Omega_\mathrm{f}^{n+1}} + \|(\pi_m(|\underline{\tilde{v}}_\mathrm{f}^{n+1}|^2))^{\frac{1}{2}}\|^2_{\phi^{n-1},\Omega_\mathrm{f}^n}\Big)
\end{cases}$$

Therefore, the final energy balance (22) is modified into

$$\begin{aligned}
&\frac{\mathcal{E}^{n+1}-\mathcal{E}^n}{\Delta t} + \frac{\gamma\mu}{2h}\|\underline{v}_\mathrm{s}^{n+\frac{1}{2}}\|^2_{\phi^n,\Gamma_{N\mathrm{nos}}^{n+1}} - \frac{\gamma\mu}{2h}\|\underline{v}_\mathrm{s}^{n-\frac{1}{2}}\|^2_{\phi^n,\Gamma_{N\mathrm{nos}}^{n+1}} \\
&\quad \le \left(\underline{t}^{n+1},\underline{v}_\mathrm{f}^{n+1}\right)_{\phi^n,\Gamma_N^{n+1}} + \left(\underline{t}_0^{n+1},\underline{v}_\mathrm{s}^{n+\frac{1}{2}}\right)_{1-\phi^n,\Gamma_N^0} - \int_{\Omega^0}\frac{\partial\Psi^{\mathrm{damp}}}{\partial\underline{\dot{e}}}\Big|^{n+\frac{1}{2}\sharp} : d_{\underline{y}}\underline{e}^{n+\frac{1}{2}\sharp}\cdot\underline{v}_\mathrm{s}^{n+\frac{1}{2}}\,d\Omega \\
&\qquad - \int_{\Omega_\mathrm{f}^{n+1}}(\underline{v}_\mathrm{f}^{n+1} - \underline{v}_\mathrm{s}^{n+\frac{1}{2}})\cdot|\phi^n|^2\,\underline{\underline{D}}_\mathrm{f}\cdot(\underline{v}_\mathrm{f}^{n+1} - \underline{v}_\mathrm{s}^{n+\frac{1}{2}})\,d\Omega - \mathcal{T}_1 - \mathcal{S}_1 - \mathcal{S}_2 \\
&\qquad + \frac{\rho_\mathrm{f}}{2\Delta t}\left\|\underline{\tilde{v}}_\mathrm{f}^{n+1} - \underline{v}_\mathrm{f}^n\right\|^2_{\phi^{n-1},\Omega_\mathrm{f}^n} + \frac{\rho_\mathrm{f}}{2\Delta t}\left\|\underline{v}_\mathrm{f}^{n+1} - \underline{\tilde{v}}_\mathrm{f}^{n+1}\right\|^2_{\phi^n,\Omega_\mathrm{f}^{n+1}} \\
&\qquad - \mu\left(2 - \frac{C_{ie}L}{h}\right)\left\|\underline{\underline{\varepsilon}}(\underline{\tilde{v}}_\mathrm{f}^{n+1})\right\|^2_{\phi^n,\Omega_\mathrm{f}^{n+1}} - \mu\left(\frac{\gamma}{2h} - \frac{1}{L}\right)\|\underline{\tilde{v}}_\mathrm{f}^{n+1} - \underline{v}_\mathrm{s}^{n+\frac{1}{2}}\|^2_{\phi^n,\Gamma_{N\mathrm{nos}}^{n+1}}.
\end{aligned} \tag{24}$$

Remark 7 (Pressure discretization)
When the free energy Ψ is quadratic in m – a rather common assumption – the pressure and fluid mass are linearly related by the pressure law, and therefore assuming that the corresponding discrete spaces are identical we can drop the projection in (23). In addition, it should be pointed out that specific numerical issues – namely, numerical locking and pressure instabilities – are likely to arise when the solid constituent is considered as nearly incompressible – i.e. with a large bulk modulus associated with J_s in $\Psi_\mathrm{s}(\underline{\underline{e}}, J_\mathrm{s})$ – due to the similarity of (7) with a Stokes problem, but this topic lies beyond the scope of the present article.

4 Numerical illustrations

In this section, we present various numerical results to illustrate the behavior of the poroelastic model under large deformations, simulated with our proposed method, namely, two test problems inspired from [9] – see also [41] – and the detailed numerical monitoring of the energy balance considered in the above stability analysis. The free energy considered in these examples is given by

$$\Psi = \Psi^{\mathrm{skel}} + \Psi^{\mathrm{bulk}} + \Psi^{\mathrm{por}},$$

where Ψ^{skel} is potential of Ciarlet-Geymonat type, i.e.

$$\Psi^{\mathrm{skel}} = \kappa_1(I_1 I_3^{-\frac{1}{3}} - 3) + \kappa_2(I_2 I_3^{-\frac{2}{3}} - 3) + \kappa(\sqrt{I_3} - 1 - \log(\sqrt{I_3})),$$

with the classical invariants

$$I_1 = \mathrm{tr}(\underline{\underline{C}}), \qquad I_2 = \frac{1}{2}\left((\mathrm{tr}\,\underline{\underline{C}})^2 - \mathrm{tr}(\underline{\underline{C}}^2)\right), \qquad I_3 = \det(\underline{\underline{C}}).$$

The term

$$\Psi^{\mathrm{bulk}}(J_\mathrm{s}) = \kappa_\mathrm{s}\left(\frac{J_\mathrm{s}}{1-\phi_0} - 1 - \log(\frac{J_\mathrm{s}}{1-\phi_0})\right)$$

governs the compressibility of the solid constituent, and the last term

$$\Psi^{\mathrm{por}} = -\eta_{\mathrm{por}} \ln\big(\frac{m}{\rho_\mathrm{f}} + \phi_0\big)$$

aims at preventing the porosity ϕ from taking negative values, see [10]. The parameter values common to the three test problems are $\kappa = \kappa_1 = 2\,10^3$, $\kappa_2 = 33$, $\rho_\mathrm{s} = \rho_\mathrm{f} = 10^3$, $\mu = 0.035$, $\phi_0 = 0.1$ and $\gamma = 20$ (all SI), while Table 1 gives the parameter values that differ. The same 2D square geometry is considered in all test problems, albeit with different dimensions as specified in the table. The mesh is obtained by a regular splitting of the domain into 72 triangular elements, as shown in Fig. 1. As discretization spaces we use continuous-$P1$ elements for the solid displacement and for the fluid mass, as well as for the pressure. For the fluid velocities, due to the Stokes-like nature of Step 2a we use continuous-$P1$ with an additional internal "bubble" degree of freedom.

Remark 8 (Calibration of stabilization constant)
Regarding the choice of the stabilization constant γ, the mathematical analysis of Proposition 2 has shown that it should be conditioned by the lower bound given by C_{ie}, the constant in the inverse inequality (11). For the latter constant, a rough estimate obtained by assuming linear shape functions and constant fluid fraction would be 2 in 2D (3 in 3D). In practice, we have chosen $\gamma = 20$ to be conservative – see also Remark 3 – and after numerically checking that in this case the impact of the penalization term in the overall energy balance remains small.

Parameter	$\|\Omega^0\|$	Δt	κ_{s}	η_{d}	η_{por}	$\underline{\underline{D}}_{\mathrm{f}}$
Swelling	10^{-4}	10^{-3}	$2\,10^{3}$	0	0	$10^{7}\underline{\underline{I}}$
Drainage	10^{-6}	$2\,10^{-6}$	$2\,10^{5}$	68	1.5	$4\,10^{5}\underline{\underline{I}}$
Energy	10^{-4}	10^{-4}	$2\,10^{3}$	0	0	$10^{7}\underline{\underline{I}}$

Table 1: **Parameters with different values among test problems** (SI units).

4.1 Implementation considerations

We implemented our proposed method in FreeFem++ [26], for the two-dimensional version of the poromechanical model.

Three Newton algorithms are implemented in the code, namely,

1. for the solution of the fluid-pressure problem (7);
2. for the solution of the solid problem (8);
3. for coupling these two sub-steps within the implicit step.

We used the same convergence criteria for these three iteration loops, i.e. tolerance parameters for the absolute and relative – with respect to initialization step – values of the residuals, set to 10^{-7} and 10^{-13}, respectively.

The FreeFem++ environment is very powerful, in particular for prototyping purposes, but does not allow as much control as an in-house finite element software on the numerical operators to be implemented. For this reason, we resorted to several simplifications in this numerical study, namely:

- for $\left.\dfrac{\partial \Psi}{\partial \underline{\underline{e}}}\right|^{n+\frac{1}{2}\sharp}$ we used the simpler rule

$$\left.\frac{\partial \Psi}{\partial \underline{\underline{e}}}\right|^{n+\frac{1}{2}\sharp} \hat{=} \frac{\partial \Psi}{\partial \underline{\underline{e}}}(\underline{\underline{e}}^{n+\frac{1}{2}\sharp}, m^{n+1}),$$

  as already considered and assessed in [25], instead of the approach of [22] considered in (9b);

- in addition, the convective term in (6) – namely, the third term – was computed on the domain Ω^{n+1} instead of Ω^n, which leads us to changing $\mathcal{S}_1$ into

$$\mathcal{S}_1' = \frac{1}{2}\int_{\Omega_{\mathrm{f}}^{n+1}} |\tilde{\underline{v}}_{\mathrm{f}}^{n+1}|^2 \underline{\nabla}_{\underline{\mathrm{x}}} \cdot (\rho_{\mathrm{f}}\phi^{n-1}\,(\underline{v}_{\mathrm{f}}^{n} - \underline{v}_{\mathrm{s}}^{n-\frac{1}{2}}))\,d\Omega \\ - \frac{1}{2}\int_{\Omega_{\mathrm{f}}^{n}} \pi_m(|\tilde{\underline{v}}_{\mathrm{f}}^{n+1}|^2) \underline{\nabla}_{\underline{\mathrm{x}}} \cdot (\rho_{\mathrm{f}}\phi^{n-1}\,(\underline{v}_{\mathrm{f}}^{n} - \underline{v}_{\mathrm{s}}^{n-\frac{1}{2}}))\,d\Omega;$$

- finally, the computation of ϕ at Step 0. is performed weakly by L^2 projection in the finite element space, instead of exactly at quadrature points as specified. This introduces an extra consistency perturbation to be added to $\mathcal{S}_1$ and $\mathcal{S}_2$, viz.

$$\mathcal{S}_3 = \frac{1}{2}\int_{\Omega^0} \left(\frac{\phi^n \rho_{\mathrm{f}} J(\underline{y}_{\mathrm{s}}^{n}) - \phi^{n-1}\rho_{\mathrm{f}} J(\underline{y}_{\mathrm{s}}^{n-1})}{\Delta t} - \frac{m^n - m^{n-1}}{\Delta t} \right) \pi_m(|\tilde{\underline{v}}_{\mathrm{f}}^{n+1}|^2)\,d\Omega.$$

Nevertheless, we provide below a numerical assessment of the energy balance in order to check that these simplifications do not significantly affect this balance. In what follows, we introduce the following notation

$$\mathcal{S}_4 = \frac{\gamma\mu}{2h}\|\underline{v}_{\mathrm{s}}^{n+\frac{1}{2}}\|^2_{\phi^n,\Gamma_{N\mathrm{nos}}^{n+1}} - \frac{\gamma\mu}{2h}\|\underline{v}_{\mathrm{s}}^{n-\frac{1}{2}}\|^2_{\phi^n,\Gamma_{N\mathrm{nos}}^{n+1}}.$$

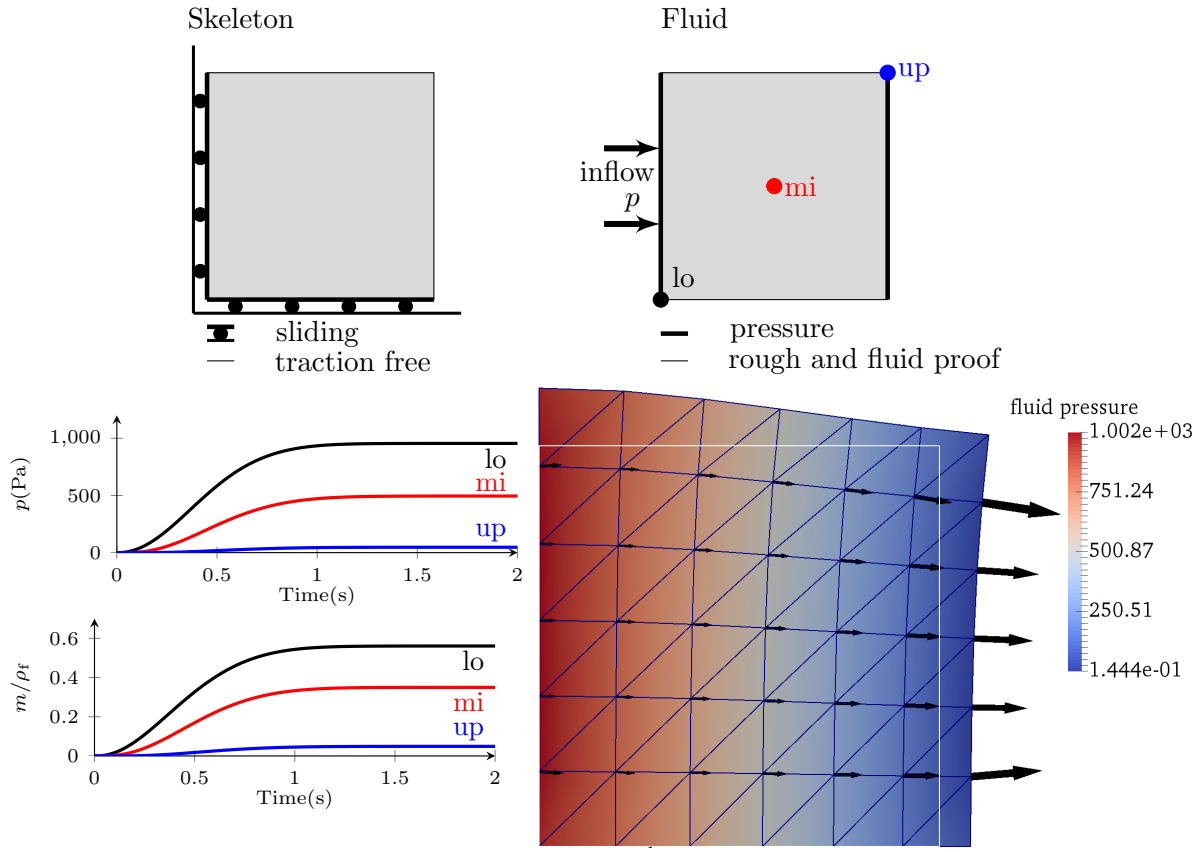

Figure 1: **Swelling under porous flow.** Top row: geometry and boundary conditions – Bottom row: (left) fluid pressure and mass at three points shown on top-right; (right) fluid velocity and pressure at steady state on deformed configuration, with initial configuration contour in white

4.2 Swelling test under porous flow

In the swelling test, no external force is applied to the system, and a gradual pressure increase is prescribed on the inlet side, see Fig. 1, in the form $p_{\mathrm{ext}} = 10^3(1 - \exp -t^2/0.25)$ as a Neumann boundary condition applied on the fluid only, while maintaining $p_{\mathrm{ext}} = 0$ on the outlet side (on the right of the sample). The top and bottom sides are assumed to be of no-sliding type ($\underline{v}_{\mathrm{f}} = \underline{v}_{\mathrm{s}}$), and normal displacements are prevented for the solid on the left and bottom sides. We have no volume-distributed fluid source nor sink. As expected, the system is gradually filled with fluid until a stationary state is reached, in which the fluid pressure is in equilibrium with elastic forces. The simulations results presented in Fig. 1 are consistent with those given in [9].

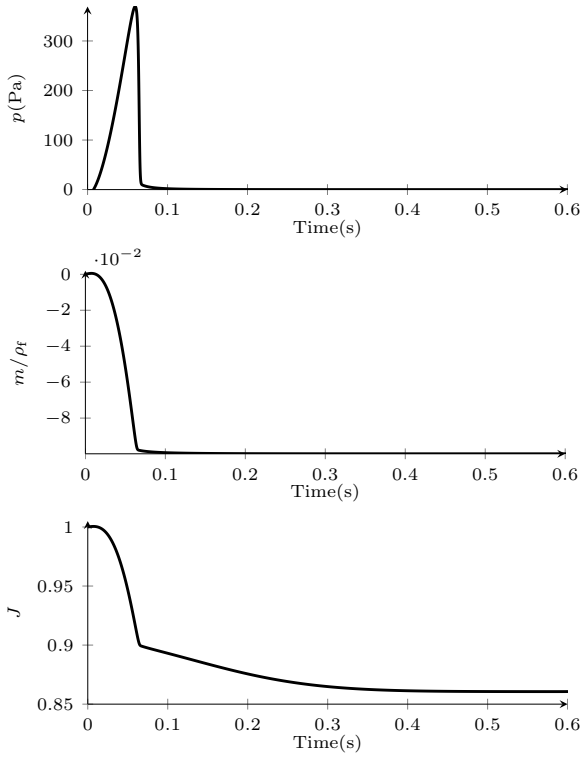

Figure 2: **Drainage test.** Pressure, fluid mass and jacobian of deformation in time

4.3 Drainage test

In the drainage test, geometry and solid essential boundary conditions are the same as in the swelling test. An external pressure $p_{\text{ext}} = 10^4(1 - \exp -t^2/0.04)$ is applied on all the sides of the square. All sides are of no-sliding type, and a volume-distributed sink linearly related to the pressure ($\theta = -\rho_{\text{f}}\beta(p - p_{\text{sink}})$, with $p_{\text{sink}} = 0$ and $\beta = 0.01$) allows the fluid to escape the material. As shown in Fig. 2, in a first phase, the fluid is drained out of the system nearly completely, until m/ρ_{f} approaches -0.1 (i.e. $\phi \approx 0$). Then, only the solid phase remains, and the material behaves like a standard solid, that compresses according to its bulk modulus κ_{s}. Solutions are here homogeneous in space, and we can verify that the solutions satisfy the following identity that comes from (7a)

$$\frac{m^{n+1} - m^n}{\rho_{\text{f}}\Delta t} = -J^n\beta p^n.$$

This illustrates how the penalization term Ψ^{por} used in the energy is effective to prevent ϕ from reaching negative values.

Remark 9
In the end of this simulation, m is stable and the denominator of (9b) vanishes. In an in-house finite element software, a test could be performed at quadrature points in order to replace, when it is not well defined, the finite difference definition of p (9b) by its asymptotic expression. As FreeFem++ does not allow this, we used in this simulation for the pressure law the mid-point rule

$$\frac{p^{n+1}}{\rho_{\text{f}}} = \frac{1}{2}\pi_m\left[\frac{\partial\Psi}{\partial m}(J^n, m^{n+1}) + \frac{\partial\Psi}{\partial m}(J^n, m^n)\right].$$

4.4 Energy balance monitoring

We consider here a test case that satisfies the assumptions of the stability analysis, with no external loading, and no energy sources, but only an initial deformation prescribed on the skeleton (of about 20%). Geometry and boundary conditions are the same as in the drainage test, but the fluid remains in the skeleton as there is no volume-distributed fluid source nor sink. The monitoring of the energy increment gives an illustration of Proposition 2 and of the various perturbations induced in the energy balance by spatial discretization, see Fig. 3. We observe that the departures from exact energy stability – namely, when the energy rate is positive – are very limited, and appear to be primarily explained by the perturbation $\mathcal{S}_3$ induced in the GCL due to computing ϕ by projection instead of exact expression at quadrature points. Of course, this perturbation could be easily removed in an in-house finite element software.

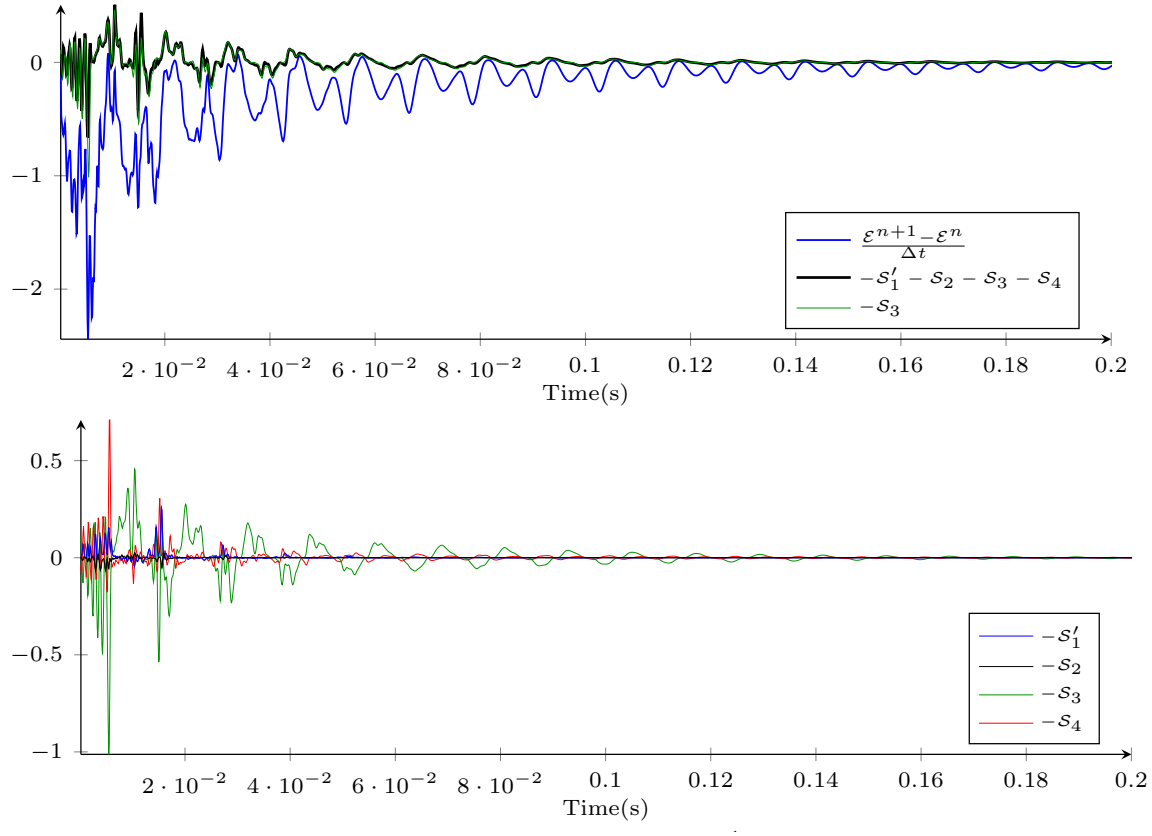

Figure 3: **Energy balance monitoring in a homogeneous test case.** Top: bound of the energy increment by the consistency term $-\mathcal{S}_1' - \mathcal{S}_2 - \mathcal{S}_3 - \mathcal{S}_4$ in time, according to (24), and $-\mathcal{S}_3$ alone – Bottom: plot of the separate contributions $-\mathcal{S}_1'$, $-\mathcal{S}_2$, $-\mathcal{S}_3$ and $-\mathcal{S}_4$; note that $\mathcal{S}_3$, and then $\mathcal{S}_4$, are an order of magnitude larger than $\mathcal{S}_1$ and $\mathcal{S}_2$

5 Concluding remarks

We have proposed an effective partitioned time scheme adapted to the poromechanics formulation of [10], and established a discrete energy estimate for this time scheme. This energy estimate is consistent with the continuous energy balance, up to some numerical dissipation effects, and some perturbations that have been carefully identified and numerically assessed. Among these perturbations, our assessment reveals that the major effect – albeit quite limited

quantitatively – lies in a departure from a GCL type property that can be easily treated by evaluating the fluid fraction quantity at the Gauss quadrature points, when this is possible in the finite element software.

In addition, we have provided some numerical illustrations of our numerical strategy by reproducing some test cases proposed in [9], with typical features of large strains and rapid flows as enabled by our general poromechanical formulation, and also a singular transition related to total drainage in the second example.

Further work will focus on spatial discretization issues, and in particular on the treatment of numerical locking – and associated pressure instabilities – phenomena that arise when the solid behavior approaches incompressibility.

Acknowledgement: The authors are grateful to Miguel Angel Fernández (Inria) for some insightful discussions on partitioned methods with Robin coupling conditions.

References

[1] M. Astorino, F. Chouly, and M.A. Fernández. Robin based semi-implicit coupling in fluid-structure interaction: stability analysis and numerics. *SIAM J. Sci. Comput.*, 31(6):4041–4065, 2009.

[2] M. Astorino, J.F. Gerbeau, O. Pantz, and K.F. Traoré. Fluid-structure interaction and multi-body contact: Application to aortic valves. *Computer Methods in Applied Mechanics and Engineering*, 198(45-46):3603–3612, 2009.

[3] S. Badia, F. Nobile, and C. Vergara. Fluid–structure partitioned procedures based on Robin transmission conditions. *Journal of Computational Physics*, 227(14):7027–7051, 2008.

[4] S. Badia, A. Quaini, and A. Quarteroni. Modular vs. non-modular preconditioners for fluid-structure systems with large added-mass effect. *Computer Methods in Applied Mechanics and Engineering*, 197(49-50):4216–4232, 2008.

[5] S. Badia, A. Quaini, and A. Quarteroni. Coupling Biot and Navier-Stokes equations for modelling fluid-poroelastic media interaction. *Journal Of Computational Physics*, 228(21):7986–8014, 2009.

[6] M.A. Biot. Theory of finite deformations of porous solids. *Indiana University Mathematics Journal*, 21(7):597–620, 1972.

[7] E. Burman and M.A Fernández. Stabilization of explicit coupling in fluid-structure interaction involving fluid incompressibility. *Computer Methods In Applied Mechanics And Engineering*, 2009.

[8] P. Causin, J.F. Gerbeau, and F. Nobile. Added-mass effect in the design of partitioned algorithms for fluid-structure problems. *Comput Method Appl M*, 194(42-44):4506–4527, 2005.

[9] D. Chapelle, J.F. Gerbeau, J. Sainte-Marie, and I.E. Vignon-Clementel. A poroelastic model valid in large strains with applications to perfusion in cardiac modeling. *Computational Mechanics*, 46(1):91–101, 2009.

[10] D. Chapelle and P. Moireau. General coupling of porous flows and hyperelastic formulations-From thermodynamics principles to energy balance and compatible time schemes. *European Journal of Mechanics - B/Fluids*, 46:82–96, 2014.

[11] A.J. Chorin. A numerical method for solving incompressible viscous flow problems. *J. Comput. Phys.*, 2(1):12–26, 1967.

[12] P.G. Ciarlet. *Mathematical Elasticity, Volume I: Three-Dimensional Elasticity.* North-Holland, 1988.

[13] O. Coussy. *Poromechanics.* John Wiley and Sons, 2004.

[14] R. de Boer. *Trends in Continuum Mechanics of Porous Media.* Springer, 2005.

[15] J. Donea, S. Giuliani, and J.P. Halleux. An arbitrary Lagrangian-Eulerian finite element method for transient dynamic fluid-structure interactions. *Comp. Meth. Appl. Mech. Eng.*, pages 689—723, 1982.

[16] C. Farhat, P. Geuzaine, and C. Grandmont. The Discrete Geometric Conservation Law and the Nonlinear Stability of ALE Schemes for the Solution of Flow Problems on Moving Grids. *J Comput Phys*, 174(2):669–694, 2001.

[17] C. Farhat, M. Lesoinne, and P. Le Tallec. Load and motion transfer algorithms for fluid/structure interaction problems with non-matching discrete interfaces: Momentum and energy conservation, optimal discretization and application to aeroelasticity. *Computer Methods in Applied Mechanics and Engineering*, 157(1–2):95–114, 1998.

[18] C.A. Felippa, K.C. Park, and C. Farhat. Partitioned analysis of coupled mechanical systems. *Computer Methods in Applied Mechanics and Engineering*, 190(24-25):3247–3270, 2001.

[19] M.A. Fernández, J.F. Gerbeau, and C. Grandmont. A projection semi-implicit scheme for the coupling of an elastic structure with an incompressible fluid. *International Journal for Numerical Methods in Engineering*, 69(4):794–821, January 2007.

[20] L. Formaggia, A. Quarteroni, and A. Veneziani. *Cardiovascular Mathematics: Modeling and Simulation of the Circulatory System*, volume 1. Springer Science & Business Media, 2010.

[21] J.F. Gerbeau and M. Vidrascu. A Quasi-Newton Algorithm Based on a Reduced Model for Fluid-Structure Interaction Problems in Blood Flows. *ESAIM: M2AN*, 37(4):631–647, 2003.

[22] O. Gonzalez. Exact energy and momentum conserving algorithms for general models in nonlinear elasticity. *Computer Methods in Applied Mechanics and Engineering*, 190(13-14):1763–1783, 2000.

[23] J.L. Guermond, P. Minev, and J. Shen. An overview of projection methods for incompressible flows. *Comput Method Appl M*, 195(44-47):6011–6045, September 2006.

[24] H. Guillard and C. Farhat. On the significance of the geometric conservation law for flow computations on moving meshes. *Computer Methods in Applied Mechanics and Engineering*, 190(11):1467–1482, 2000.

[25] P. Hauret and P. Le Tallec. Energy-controlling time integration methods for nonlinear elastodynamics and low-velocity impact. *Comput Method Appl M*, 195(37-40):4890–4916, 2006.

[26] F. Hecht. New development in FreeFem++. *J. Numer. Math.*, 20(3-4):251–265, 2012.

[27] M. Heil, A.L. Hazel, and J. Boyle. Solvers for large-displacement fluid-structure interaction problems: Segregated versus monolithic approaches. *Computational Mechanics*, 43(1):91–101, 2008.

[28] U. Küttler, M. Gee, C. Förster, A. Comerford, and W.A. Wall. Coupling strategies for biomedical fluid–structure interaction problems. *International Journal for Numerical Methods in Biomedical Engineering*, 26(3-4):305–321, 2010.

[29] U. Küttler and W.A. Wall. Fixed-point fluid–structure interaction solvers with dynamic relaxation. *Computational Mechanics*, 43(1):61–72, 2008.

[30] L. Lanoye, J. Vierendeels, P. Segers, and P. Verdonck. Vascular fluid-structure-interaction using fluent and abaqus software. *Journal of Biomechanics*, 39:S440, 2006.

[31] P. Le Tallec. Numerical methods for nonlinear three-dimensional elasticity. In P.G. Ciarlet and J.L. Lions, editors, *Handbook of Numerical Analysis, Vol. III*. Elsevier, 1994.

[32] P. Le Tallec and P. Hauret. Energy conservation in fluid structure interactions. In O. Pironneau Y. Kuznetsov, P. Neittanmaki, editor, *Numerical Methods for Scientific Computing / Variational Problems and Applications – CIMNE Barcelona*, 2003.

[33] P. Le Tallec and J. Mouro. Fluid structure interaction with large structural displacements. *Computer Methods in Applied Mechanics and Engineering*, 190(24-25):3039–3067, 2001.

[34] B. Markert, Y. Heider, and W. Ehlers. Comparison of monolithic and splitting solution schemes for dynamic porous media problems. *Int. J. Numer. Meth. Engng.*, 82(11):1341–1383, 2010.

[35] H.G. Matthies and J. Steindorf. Partitioned but strongly coupled iteration schemes for nonlinear fluid-structure interaction. *Computers and Structures*, 80:1991–1999, 2002.

[36] J. Nitsche. Über ein Variationsprinzip zur Lösung von Dirichlet-Problemen bei Verwendung von Teilräumen, die keinen Randbedingungen unterworfen sind. *Abh. Math. Sem. Univ. Hamburg*, 36:9–15, 1971.

[37] F. Nobile. *Numerical approximation of fluid-structure interaction problems with application to haemodynamics*. PhD thesis, EPFL, 2001.

[38] F. Nobile and L. Formaggia. A Stability Analysis for the Arbitrary Lagrangian-Eulerian Formulation with Finite Elements. *East-West Journal of Numerical Mathematics*, 7(2):105–131, 1999.

[39] R. Temam. Une méthode d'approximation de la solution des équations de Navier-Stokes. *Bull. Soc. Math.*, France 96:115–152, 1968.

[40] P.D. Thomas and C.K. Lombard. Geometric conservation law and its application to flow computations on moving grids. *AIAA Journal*, 17(10):1030–1037, 1979.

[41] A.T. Vuong, L. Yoshihara, and W.A. Wall. A general approach for modeling interacting flow through porous media under finite deformations. *Computer Methods In Applied Mechanics And Engineering*, 283:1240–1259, 2015.

Chapter 4

Total convergence analysis of a monolithic scheme for linear poromechanics

4.1 Introduction

In Chapter 3, we established an effective and energy-preserving time discretization of (1.3). The purpose of this chapter is to study spatial discretization aspects of our poromechanical formulation, in order to guarantee numerical stability. To that purpose, we establish in Section 4.2 a linearization of (1.3) and we perform its theoretical and numerical convergence study.

It is known that the discretization of a Stokes problem involves mixed finite elements, that velocity and pressure must be approximated separately, and that the couple of spaces must be compatible in the sense of an *inf-sup condition*, see (Ladyzhenskaya and Silverman, 1969; Babuška, 1973; Brezzi, 1974). Numerically, the violation of this condition often leads to strong node-to-node spatial oscillations in the pressure field. Our poromechanical model involves a Stokes-like fluid sub-problem, coupled with a solid matrix. It is natural to thoroughly investigate how this problem translates in our framework, and to perform both a theoretical convergence analysis to see how numerical oscillations arise, and numerical tests to illustrate them. Our approach is inspired from (Le Tallec and Mani, 2000) which establishes the total convergence of a linearized fluid structure interaction problem, using an energy conservative scheme.

4.2 A linear porous flows and elastic coupling formulation - the continuous problem

4.2.1 Linearization of the weak formulation for convergence analysis

We consider the poromechanical formulation introduced in Section 1.4 with a total stress tensor given by

$$\underline{\underline{\Sigma}} = \phi\underline{\underline{\Sigma}}_{\text{vis}} + \frac{\partial\Psi(\underline{\underline{e}}, m)}{\partial\underline{\underline{e}}}\Big|_m,$$

with $\Psi(\underline{\underline{e}}, m)$ the Helmholtz free energy of the mixture. Due to fluid incompressibility, $\Psi(\underline{\underline{e}}, m) = \Psi_{\text{s}}(\underline{\underline{e}}, J_{\text{s}})$ with Ψ_{s} the solid free energy – meaning that the fluid cannot store any energy – hence, we also have

$$\underline{\underline{\Sigma}} = \phi\underline{\underline{\Sigma}}_{\text{vis}} + \frac{\partial\Psi_{\text{s}}(\underline{\underline{e}}, J_{\text{s}})}{\partial\underline{\underline{e}}}\Big|_{J_{\text{s}}} - pJ\underline{\underline{C}}^{-1},$$

see (Chapelle and Moireau, 2014). Recalling (1.1), this gives for the solid contribution

$$\underline{\underline{\Sigma}}_{\rm s} = \frac{\partial \Psi(\underline{\underline{e}}, m)}{\partial \underline{\underline{e}}}\Big|_m + \phi p J \underline{\underline{C}}^{-1} = \frac{\partial \Psi_{\rm s}(\underline{\underline{e}}, J_{\rm s})}{\partial \underline{\underline{e}}}\Big|_{J_{\rm s}} - (1-\phi) p J \underline{\underline{C}}^{-1}.$$

In addition, we have

$$p = \rho_{\rm f} \frac{\partial \Psi(\underline{\underline{e}}, m)}{\partial m}\Big|_{\underline{\underline{e}}} = -\frac{\partial \Psi_{\rm s}(\underline{\underline{e}}, J_{\rm s})}{\partial J_{\rm s}}\Big|_{\underline{\underline{e}}}. \tag{4.1}$$

We consider a linearization of (1.3) around the solution at rest : $(\bar{\underline{y}}_{\rm s}, \bar{\underline{v}}_{\rm s}, \bar{\underline{v}}_{\rm f}, \bar{m}) \equiv 0$ (then $p \equiv 0$). Then ϕ will vary around $\phi_0 = \bar{\phi} \neq 0$, and the Green-Lagrange strain tensor $\underline{\underline{e}}$ reduces to its linear expression $\underline{\underline{\varepsilon}}$. As in (Chapelle and Moireau, 2014), we construct the free energy functional as follows

$$\Psi_{\rm s} = \Psi^{\rm skel}(\underline{\underline{\varepsilon}}) + \Psi^{\rm bulk}(J_{\rm s}), \tag{4.2}$$

with

$$\Psi^{\rm bulk}(J_{\rm s}) = \frac{\kappa_{\rm s}}{2}\left(\frac{J_{\rm s}}{1-\phi_0} - 1\right)^2,$$

and $\Psi^{\rm skel}$ a quadratic form of $\underline{\underline{\varepsilon}}$. Furthermore, we assume the coercivity of $\Psi^{\rm skel}$, that is, there exists a $\lambda > 0$ such that $\Psi^{\rm skel}(\underline{\underline{\varepsilon}}) \geq \lambda \|\underline{\underline{\varepsilon}}\|^2_{L^2(\Omega)}$, and we also assume that sufficient boundary conditions are imposed on the structure to prevent any rigid body transformations. Therefore the Korn inequality gives the equivalence between the norm defined by $\Psi^{\rm skel}$ and the H^1 norm on Ω. Let us notice that if we add the assumption of isotropy, it is known that $\Psi^{\rm skel}$ can be written as the Saint-Venant-Kirchhoff constitutive law.

In our linear frame, $J - 1$ reduces to $\operatorname{tr} \underline{\underline{\varepsilon}}(\underline{y}_{\rm s})$, hence $\Psi^{\rm bulk}$ turns into

$$\Psi^{\rm bulk}(J_{\rm s}) = \frac{\kappa_{\rm s}}{2(1-\phi_0)^2}\left(\operatorname{tr} \underline{\underline{\varepsilon}}(\underline{y}_{\rm s}) - \frac{m}{\rho_{\rm f}}\right)^2,$$

and (4.1) gives the following relation between p, m and $\underline{y}_{\rm s}$,

$$p = \frac{\kappa_{\rm s}}{(1-\phi_0)^2}\left(\frac{m}{\rho_{\rm f}} - \operatorname{tr} \underline{\underline{\varepsilon}}(\underline{y}_{\rm s})\right) \quad \text{or equivalently} \quad \frac{m}{\rho_{\rm f}} = \frac{(1-\phi_0)^2}{\kappa_{\rm s}} p + \operatorname{div}(\underline{y}_{\rm s}),$$

with which $\Psi^{\rm bulk}$ rewrites

$$\Psi^{\rm bulk} = \frac{(1-\phi_0)^2}{2\kappa_{\rm s}} p^2. \tag{4.3}$$

Now we define the tensor $\underline{\underline{\sigma}}^{\rm skel} = \frac{\partial \Psi^{\rm skel}}{\partial \underline{\underline{\varepsilon}}}$, independent of m and p in order to have

$$\frac{\partial \Psi}{\partial \underline{\underline{\varepsilon}}}\Big|_m = \underline{\underline{\sigma}}^{\rm skel} + \frac{\kappa_{\rm s}}{(1-\phi_0)^2}\left(\operatorname{tr} \underline{\underline{\varepsilon}}(\underline{y}_{\rm s}) - \frac{m}{\rho_{\rm f}}\right)\underline{\underline{\mathbb{1}}} = \underline{\underline{\sigma}}^{\rm skel} - p\underline{\underline{\mathbb{1}}},$$

and $\underline{\underline{\Sigma}}_{\rm s}$ reduces to

$$\underline{\underline{\sigma}}_{\rm s} = \underline{\underline{\sigma}}^{\rm skel} - (1-\phi_0) p \underline{\underline{\mathbb{1}}}. \tag{4.4}$$

We assume that the fluid viscosity tensor is given by $\underline{\underline{\sigma}}_{\rm vis} = 2\mu \underline{\underline{\varepsilon}}$. When we keep only first order terms, and we express m as a function of p, (1.3) becomes – Ω_t, resp. a borders Γ_t, reduces to

Ω^0 that we will denote by Ω, resp. Γ, J to 1, and ALE terms disappear –

$$\begin{cases} \displaystyle\int_\Omega \rho_{s0}(1-\phi_0)\partial_t \underline{v}_s \cdot \underline{v}_s^*\, d\Omega + \int_\Omega \underline{\underline{\sigma}}_s : \underline{\underline{\varepsilon}}(\underline{v}_s^*)\, d\Omega - \int_\Omega (\underline{v}_f - \underline{v}_s)\cdot \phi_0^2 \underline{\underline{k}}_f^{-1}\cdot \underline{v}_s^*\, d\Omega \\ \qquad + \displaystyle\int_\Omega p \underline{\nabla}_{\underline{x}}\phi_0 \cdot \underline{v}_s^* d\Omega = \int_\Omega \rho_{s0}(1-\phi_0)\underline{f}\cdot \underline{v}_s^*\, d\Omega + \int_{\Gamma_N^0} (1-\phi_0)\underline{t}_0 \cdot \underline{v}_s^*\, dS \\ \qquad + \displaystyle\int_{\Gamma_{N\mathrm{nof}}\bigcup\Gamma_{N\mathrm{nos}}} \underline{t}_0\cdot \underline{v}_s^*\, dS - \int_{\Gamma_{N\mathrm{nof}}} \phi_0(\pi_\tau \underline{t}_0)\cdot \underline{v}_s^* dS - \mathcal{R}_f^{\mathrm{c,lin}}(\underline{v}_s^*) \quad (4.5a) \\ \displaystyle\int_\Omega \rho_f \phi_0 \partial_t \underline{v}_f \cdot \underline{v}_f^*\, d\Omega - \int_\Omega \theta \underline{v}_f \cdot \underline{v}_f^* d\Omega + \int_\Omega \left(-p\,\mathrm{div}(\phi_0 \underline{v}_f^*) + \phi_0\, \underline{\underline{\sigma}}_{\mathrm{vis}}(\underline{v}_f) : \underline{\underline{\varepsilon}}(\underline{v}_f^*)\right) d\Omega \\ \qquad + \displaystyle\int_\Omega (\underline{v}_f - \underline{v}_s)\cdot \phi_0^2 \underline{\underline{k}}_f^{-1}\cdot \underline{v}_f^*\, d\Omega = \int_\Omega \rho_f \phi_0\, \underline{f}\cdot \underline{v}_f^*\, d\Omega + \int_{\Gamma_N \bigcup \Gamma_{N\mathrm{nof}}} \phi_0\, \underline{t}_0 \cdot \underline{v}_f^*\, dS \quad (4.5b) \\ \displaystyle\int_\Omega \left(\frac{(1-\phi_0)^2}{\kappa_s}\partial_t p + \mathrm{tr}\,\underline{\underline{\varepsilon}}(\underline{v}_s)\right) p^*\, d\Omega + \int_\Omega \mathrm{div}(\phi_0\,(\underline{v}_f - \underline{v}_s))\, p^*\, d\Omega = \int_\Omega \frac{\theta}{\rho_f} p^* d\Omega, \quad (4.5c) \end{cases}$$

with

$$\begin{aligned} \mathcal{R}_f^{\mathrm{c,lin}}(\underline{v}_s^*) &= \int_\Omega \rho_f\phi_0 \partial_t \underline{v}_f \cdot \underline{v}_s^*\, d\Omega - \int_\Omega \theta \underline{v}_f\cdot \underline{v}_s^* d\Omega + \int_\Omega \left(-p\,\mathrm{div}(\phi_0 \underline{v}_f^*) + \phi_0\, \underline{\underline{\sigma}}_{\mathrm{vis}}(\underline{v}_f) : \underline{\underline{\varepsilon}}(\underline{v}_s^*)\right) d\Omega \\ &+ \int_\Omega (\underline{v}_f - \underline{v}_s)\cdot \phi_0^2 \underline{\underline{k}}_f^{-1}\cdot \underline{v}_s^*\, d\Omega - \int_\Omega \rho_f\phi_0\, \underline{f}\cdot \underline{v}_s^*\, d\Omega - \int_{\Gamma_N} \phi_0\, \underline{t}_0\cdot \underline{v}_s^*\, dS - \int_{\Gamma_{N\mathrm{nof}}} \phi_0(\pi_\tau \underline{t}_0)\cdot \underline{v}_s^*\, dS. \end{aligned} \quad (4.6)$$

Remark 5
The corresponding strong formulation reads

$$\begin{cases} \rho_f\phi_0\partial_t \underline{v}_f - \mathrm{div}(\phi_0 \underline{\underline{\sigma}}_{\mathrm{vis}}(\underline{v}_f)) + \phi_0 \underline{\nabla}\, p + \phi_0^2 \underline{\underline{k}}_f^{-1}\cdot(\underline{v}_f - \underline{v}_s) = \rho_f\phi_0 \underline{f} + \theta \underline{v}_f, \text{ in } \Omega \\ \qquad \rho_f\left(\dfrac{(1-\phi_0)^2}{\kappa_s}\partial_t p + \mathrm{div}(\underline{v}_s)\right) + \mathrm{div}\big(\rho_f\phi_0(\underline{v}_f - \underline{v}_s)\big) = \theta, \qquad \text{in } \Omega \\ \qquad\qquad \underline{v}_f = \underline{v}_s, \qquad \text{on } \Gamma_{N\mathrm{nos}} \end{cases}$$

$$\begin{cases} \rho_{s0}(1-\phi_0)\partial_t \underline{v}_s - \mathrm{div}\,\underline{\underline{\sigma}}_s + p\underline{\nabla}\,\phi_0 - \phi_0^2 \underline{\underline{k}}_f^{-1}\cdot(\underline{v}_f - \underline{v}_s) = \rho_{s0}(1-\phi_0)\underline{f} \quad \text{in } \Omega \\ \qquad\qquad \underline{v}_s = \partial_t \underline{y}_s \qquad \text{in } \Omega \\ \qquad\qquad (\underline{\underline{\sigma}}^s(\underline{y}_s) + \underline{\underline{\sigma}}_f(\underline{v}_f, p))\underline{n} = \underline{t}_0 \quad \text{on } \Gamma_{N\mathrm{nos}}. \end{cases}$$

Remark 6 (Existence and uniqueness of a solution)
Existence and uniqueness of a solution of the continuous problem were established in a fluid-structure interaction linear (Du et al., 2003; Boulakia, 2005) and non linear frame (Grandmont and Maday, 2000). It would be interesting to propose an adequate treatment of the fluid portion ϕ_0 and of the volume friction term in order to translate these results to our frame.

4.2.2 Nitsche's linear weak formulation

We define

$$Q = L^2(\Omega),$$

and for any $(\underline{w}_D)$ in $W = H^1(\Omega)^3$,

$$W(\underline{w}_D) = \{\underline{v}^* \in W \;\Big|\; \underline{v}^*|_{\Gamma_D} = \underline{w}_D\},$$

We also introduce the state vector as

$$X = \left[\underline{v}_{\rm f}, \underline{v}_{\rm s}, \underline{y}_{\rm s}, p\right] \text{ that belongs to } V = W(\underline{v}_{\rm f}^{\rm pr}) \times W \times W(\underline{y}_{\rm s}^{\rm pr}) \times Q$$

and its corresponding test functions vector

$$X^* = \left[\underline{v}_{\rm f}^*, \underline{v}_{\rm s}^*, \underline{y}_{\rm s}^*, p^*\right] \text{ that belongs to } V^0 = W(0) \times W \times W(0) \times Q.$$

We consider Ω_h (with borders $\Gamma_{N{\rm nos},h}$, $\Gamma_{N{\rm nof},h}$, $\Gamma_{D,h}$ and $\Gamma_{N,h}$) a discretization of Ω of refinement h –typically, the maximum diameter of all the elements in the mesh. We use a finite element strategy and we assume that the solid displacement and the solid velocity are discretized in the same space $W_h^{\rm s}$, the fluid velocity is chosen in $W_h^{\rm f}$ and the pressure in Q_h. For any $\underline{w}_{{\rm f},D}$ in $W_h^{\rm f}$ and any $\underline{w}_{{\rm s},D}$ in $W_h^{\rm s}$ we define

$$W_h^{\rm f}(\underline{w}_{{\rm f},D}) = \{\underline{v}^* \in W_h^{\rm f} \;\Big|\; \underline{v}^*|_{\Gamma_{D,h}} = \underline{w}_{{\rm f},D}\},$$
$$W_h^{\rm s}(\underline{w}_{{\rm s},D}) = \{\underline{v}^* \in W_h^{\rm s} \;\Big|\; \underline{v}^*|_{\Gamma_{D,h}} = \underline{w}_{{\rm s},D}\}.$$

Then the finite element spaces associated with V and V^0 are

$$V_h = W_h^{\rm f}(\underline{v}_{{\rm f},h}^{\rm pr}) \times W_h^{\rm s} \times W_h^{\rm s}(\underline{y}_{{\rm s},h}^{\rm pr}) \times Q_h,$$
$$V_h^0 = W_h^{\rm f}(0) \times W_h^{\rm s} \times W_h^{\rm s}(0) \times Q_h,$$

for $(\underline{v}_{{\rm f},h}^{\rm pr}, \underline{y}_{{\rm s},h}^{\rm pr})$ in $W_h^{\rm f} \times W_h^{\rm s}$.

We will use the elasticity and weighted L^2-scalar product notations

$$(\underline{y}, \underline{y}^*)_{\rm skel} = \int_\Omega \underline{\underline{\sigma}}^{\rm skel}(\underline{y}) : \underline{\underline{\varepsilon}}(\underline{y}^*)\, d\Omega, \quad \text{and} \quad (a,b)_{\zeta,\Omega} = \int_\Omega \zeta\, ab\, d\Omega.$$

As in the splitting time-scheme of Chapter 3, fluid and solid constituents are implicitly and weakly coupled on $\Gamma_{N{\rm nos}}$ through $\underline{v}_{\rm f} = \underline{v}_{\rm s}$ with Robin coupling conditions derived from Nitsche's interface method (Nitsche, 1971; Burman and Fernández, 2007). Unlike in (4.5b), this condition is weakly imposed in the fluid resolution, so the fluid test function $\underline{v}_{\rm f}^*$ has no reason to vanish on $\Gamma_{N{\rm nos}}$. Therefore, the integration by part that leads to (4.5b) involves the new term $\left((\underline{\underline{\sigma}}_{\rm vis}(\underline{v}_{\rm f}) - p)\cdot\underline{n}, \underline{v}_{\rm f}^*\right)_{\phi_0,\Gamma_{N{\rm nos}}}$ in the fluid equation right hand side (RHS). Furthermore, we use that $\mathcal{R}_{\rm f}^{\rm c,lin}(\underline{v}_{\rm s}^*) = \left((\underline{\underline{\sigma}}_{\rm vis}(\underline{v}_{\rm f}) - p)\cdot\underline{n}, \underline{v}_{\rm s}^*\right)_{\phi_0,\Gamma_{N{\rm nos}}}$.

We can derive the following equation, satisfied by the solution of (4.5), $X = (\underline{v}_{\rm f}, \underline{v}_{\rm s}, \underline{y}_{\rm s}, p)$ in V, for any $X^* = (\underline{v}_{\rm f}^*, \underline{v}_{\rm s}^*, \underline{y}_{\rm s}^*, p^*)$ in V^0

$$\begin{aligned}
&\rho_{\rm f}\left(\partial_t \underline{v}_{\rm f}, \underline{v}_{\rm f}^*\right)_{\phi_0,\Omega} + \left(\underline{\underline{\sigma}}_{\rm vis}(\underline{v}_{\rm f}), \underline{\underline{\varepsilon}}(\underline{v}_{\rm f}^*)\right)_{\phi_0,\Omega} + \rho_{\rm s0}\left(\partial_t \underline{v}_{\rm s}, \underline{v}_{\rm s}^*\right)_{(1-\phi_0),\Omega} + \left(\partial_t \underline{y}_{\rm s} - \underline{v}_{\rm s}, \underline{y}_{\rm s}^*\right)_{\rm skel} \\
&\quad - \left((\underline{\underline{\sigma}}_{\rm vis}(\underline{v}_{\rm f}) - p)\cdot\underline{n}, \underline{v}_{\rm f}^* - \underline{v}_{\rm s}^*\right)_{\phi_0,\Gamma_{N{\rm nos}}} - \left((\underline{\underline{\sigma}}_{\rm vis}(\underline{v}_{\rm f}^*) + p^*)\cdot\underline{n}, \underline{v}_{\rm f} - \underline{v}_{\rm s}\right)_{\phi_0,\Gamma_{N{\rm nos}}} \\
&\quad + \frac{\gamma\mu}{h}\left(\underline{v}_{\rm f} - \underline{v}_{\rm s}, \underline{v}_{\rm f}^* - \underline{v}_{\rm s}^*\right)_{\phi_0,\Gamma_{N{\rm nos}}} + \left(\underline{v}_{\rm f} - \underline{v}_{\rm s}, \underline{v}_{\rm f}^* - \underline{v}_{\rm s}^*\right)_{\phi_0^2\underline{\underline{k}}_{\rm f}^{-1},\Omega} \\
&\quad + (p^*, {\rm div}(\phi_0(\underline{v}_{\rm f} - \underline{v}_{\rm s})))_\Omega - (p, {\rm div}(\phi_0(\underline{v}_{\rm f}^* - \underline{v}_{\rm s}^*)))_\Omega \\
&\quad + \left(\underline{\underline{\sigma}}_{\rm s}, \underline{\underline{\varepsilon}}(\underline{v}_{\rm s}^*)\right)_\Omega - (p, {\rm div}(\underline{v}_{\rm s}^*))_{\phi_0,\Omega} + \frac{1}{\kappa_{\rm s}}\left(\partial_t p, p^*\right)_{(1-\phi_0)^2,\Omega} + (p^*, {\rm div}\,\underline{v}_{\rm s})_\Omega \\
&= \int_\Omega \rho_{s0}(1-\phi_0)\underline{f}\cdot\underline{v}_{\rm s}^*\, d\Omega + \int_{\Gamma_N^0}(1-\phi_0)\underline{t}_0\cdot\underline{v}_{\rm s}^*\, dS + \int_{\Gamma_{N{\rm nof}}\bigcup\Gamma_{N{\rm nos}}}\underline{t}_0\cdot\underline{v}_{\rm s}^*\, dS - \int_{\Gamma_{N{\rm nof}}}\phi_0(\pi_\tau\underline{t}_0)\cdot\underline{v}_{\rm s}^* dS \\
&\quad + \int_\Omega \theta\underline{v}_{\rm f}\cdot\underline{v}_{\rm f}^* d\Omega + \int_\Omega \rho_{\rm f}\phi_0\,\underline{f}\cdot\underline{v}_{\rm f}^*\, d\Omega + \int_{\Gamma_N\bigcup\Gamma_{N{\rm nof}}}\phi_0\,\underline{t}_0\cdot\underline{v}_{\rm f}^*\, dS + \int_\Omega \frac{\theta}{\rho_{\rm f}}p^* d\Omega,
\end{aligned}$$

where the fourth and sixth terms of the left hand side (LHS) are both consistent, and are here respectively to impose weakly the solid velocity, and to bring some symmetry. We now use the relation

$$\left(\underline{\underline{\sigma}}_{\rm s}, \underline{\underline{\varepsilon}}(\underline{v}_{\rm s}^*)\right)_\Omega - (p\,{\rm div}(\underline{v}_{\rm s}^*))_{\phi_0,\Omega} = \left(\underline{y}_{\rm s}, \underline{v}_{\rm s}^*\right)_{\rm skel} - (p, {\rm div}(\underline{v}_{\rm s}^*))_\Omega$$

to get that the solution X in V of (4.5) satisfies, for any X^* in V^0

$$\begin{aligned}
&\rho_{\rm f}\left(\partial_t \underline{v}_{\rm f}, \underline{v}_{\rm f}^*\right)_{\phi_0,\Omega} + \frac{1}{\kappa_{\rm s}}\left(\partial_t p, p^*\right)_{(1-\phi_0)^2,\Omega} + \rho_{\rm s}\left(\partial_t \underline{v}_{\rm s}, \underline{v}_{\rm s}^*\right)_{1-\phi_0,\Omega} + \left(\partial_t \underline{y}_{\rm s}, \underline{y}_{\rm s}^*\right)_{\rm skel} + M(X, X^*) \\
&= \int_\Omega \rho_{s0}(1-\phi_0)\underline{f}\cdot\underline{v}_{\rm s}^*\, d\Omega + \int_{\Gamma_N^0}(1-\phi_0)\underline{t}_0\cdot\underline{v}_{\rm s}^*\, dS + \int_{\Gamma_{N{\rm nof}}\bigcup\Gamma_{N{\rm nos}}} \underline{t}_0\cdot\underline{v}_{\rm s}^*\, dS - \int_{\Gamma_{N{\rm nof}}}\phi_0(\pi_\tau\underline{t}_0)\cdot\underline{v}_{\rm s}^* dS \\
&\qquad + \int_\Omega \theta\underline{v}_{\rm f}\cdot\underline{v}_{\rm f}^* d\Omega + \int_\Omega \rho_{\rm f}\phi_0\,\underline{f}\cdot\underline{v}_{\rm f}^*\, d\Omega + \int_{\Gamma_N\bigcup\Gamma_{N{\rm nof}}}\phi_0\,\underline{t}_0\cdot\underline{v}_{\rm f}^*\, dS + \int_\Omega \theta p^* d\Omega, \quad (4.7)
\end{aligned}$$

where we introduced the bilinear form

$$\begin{aligned}
M(X, X^*) = {}& 2\mu\left(\underline{\underline{\varepsilon}}(\underline{v}_{\rm f}), \underline{\underline{\varepsilon}}(\underline{v}_{\rm f}^*)\right)_{\phi_0,\Omega} + \left(\underline{y}_{\rm s}, \underline{v}_{\rm s}^*\right)_{\rm skel} - \left(\underline{v}_{\rm s}, \underline{y}_{\rm s}^*\right)_{\rm skel} \\
&- (p, {\rm div}(\phi_0\underline{v}_{\rm f}^* + (1-\phi_0)\underline{v}_{\rm s}^*)))_\Omega + (p^*, {\rm div}(\phi_0\underline{v}_{\rm f} + (1-\phi_0)\underline{v}_{\rm s})))_\Omega \\
&- \left(\underline{\underline{\sigma}}_{\rm f}(\underline{v}_{\rm f}, p)\underline{n}, \underline{v}_{\rm f}^* - \underline{v}_{\rm s}^*\right)_{\phi_0,\Gamma_{N{\rm nos}}} - \left(\underline{v}_{\rm f} - \underline{v}_{\rm s}, \underline{\underline{\sigma}}_{\rm f}(\underline{v}_{\rm f}^*, -p^*)\underline{n}\right)_{\phi_0,\Gamma_{N{\rm nos}}} \\
&+ \frac{\gamma\mu}{h}\left(\underline{v}_{\rm f} - \underline{v}_{\rm s}, \underline{v}_{\rm f}^* - \underline{v}_{\rm s}^*\right)_{\phi_0,\Gamma_{N{\rm nos}}} + \left(\underline{v}_{\rm f} - \underline{v}_{\rm s}, \underline{v}_{\rm f}^* - \underline{v}_{\rm s}^*\right)_{\phi_0^2\underline{\underline{k}}_{\rm f}^{-1},\Omega}. \quad (4.8)
\end{aligned}$$

Remark 7
Note that $-\left(\underline{\underline{\sigma}}_{\rm f}(\underline{v}_{\rm f}, p)\underline{n}, \underline{v}_{\rm f}^* - \underline{v}_{\rm s}^*\right)_{\phi_0,\Gamma_{N{\rm nos}}}$ involves the trace of p and $\underline{\underline{\varepsilon}}(\underline{v}_{\rm f})$ on $\Gamma_{N{\rm nos}}$, which is not properly defined in the spaces considered. Nevertheless, when $(\underline{v}_{\rm f}, \underline{v}_{\rm s}, \underline{y}_{\rm s}, p)$ is the continuous solution, this term can be defined by duality as the residual of the fluid equation.

4.2.3 Time continuous energy balance

For the sake of simplicity in this section, we will assume that $\underline{t}_0 = 0$ on $\Gamma_{N{\rm nos}}$, $\Gamma_{N{\rm nof}}$ and Γ_N, $\underline{f} = \underline{0}$, $\theta = 0$, $\underline{y}_{\rm s}^{\rm pr} = \underline{0}$ and $\underline{v}_{\rm f}^{\rm pr} = \underline{0}$. For any X, we define the following energy norm

$$\|X\|_{\mathcal{E}}^2 = \frac{\rho_{\rm f}}{2}\|\underline{v}_{\rm f}\|_{\phi_0,\Omega}^2 + \frac{\rho_{\rm s}}{2}\|\underline{v}_{\rm s}\|_{(1-\phi_0),\Omega}^2 + \frac{1}{2}\|\underline{y}_{\rm s}\|_{\rm skel}^2 + \frac{1}{2\kappa_{\rm s}}\|p\|_{(1-\phi_0)^2,\Omega}^2$$

where the first two terms are the fluid and solid kinetic energy, and the last two correspond to the total Helmholtz free energy $\int_\Omega \Psi\, d\Omega$.

Let us recall the trace inequality and, for discrete functions, the trace inverse inequality (see Lemma 1 in Chapter 3).

Lemma 1 (Trace inequality)
There exists a constant C_{tr} depending only on Ω (a Lipschitz domain) and Γ_{Nnos} such that

$$\|\underline{v}\|_{H^{\frac{1}{2}}(\Gamma_{Nnos})}^2 \le C_{tr}\|\underline{v}\|_{H^1(\Omega)}^2, \quad \forall \underline{v} \in H^1(\Omega)^3. \quad (4.9)$$

Lemma 2 (Trace inverse inequality)
If h is the typical maximal diameter of all the finite elements in the mesh, there exists a constant C_{ie} that depends on Ω, Γ_{Nnos} and the type of shape functions, such that

$$\|\underline{\underline{\varepsilon}}(\underline{v}_h)\cdot\underline{n}\|_{L^2(\Gamma_{Nnos})}^2 \le \frac{C_{ie}}{h}\|\underline{\underline{\varepsilon}}(\underline{v}_h)\|_{L^2(\Omega)}^2, \quad \forall \underline{v}_h \in W_h^{\rm f}. \quad (4.10)$$

Note that (4.7) comes down to a Cauchy problem, so existence and uniqueness of the solution in the finite dimensional space V_h is guaranteed. Let X_h in V_h be the semi-discrete solution of (4.7), for any X^* in V_h^0. The energy of X_h becomes $\mathcal{E}_h = \|X_h\|_{\mathcal{E}}^2$. Now, the evaluation of (4.7) with the test functions $X^* = X_h$ gives:

$$\partial_t \mathcal{E}_h + 2\mu \|\underline{\underline{\varepsilon}}(\underline{v}_{\mathrm{f},h})\|_{\phi_0,\Omega}^2 + \|\underline{v}_{\mathrm{f},h} - \underline{v}_{\mathrm{s},h}\|_{\phi_0^2 \underline{\underline{k}}_{\mathrm{f}}^{-1},\Omega}^2 + \frac{\gamma\mu}{h}\|\underline{v}_{\mathrm{f},h} - \underline{v}_{\mathrm{s},h}\|_{\phi_0,\Gamma_{N\mathrm{nos}}}^2 - 4\mu \left(\underline{\underline{\varepsilon}}(\underline{v}_{\mathrm{f},h})\underline{n}, \underline{v}_{\mathrm{f},h} - \underline{v}_{\mathrm{s},h}\right)_{\phi_0,\Gamma_{N\mathrm{nos}}} = 0.$$

Then, we use Young's inequality $(a,b) \leq \frac{1}{2L}\|a\|^2 + \frac{L}{2}\|b\|^2$, with L homogeneous to a length here, and the inverse inequality (4.10), to get

$$\begin{aligned} 4\mu \left(\underline{\underline{\varepsilon}}(\underline{v}_{\mathrm{f},h})\underline{n}, \underline{v}_{\mathrm{f},h} - \underline{v}_{\mathrm{s},h}\right)_{\phi_0,\Gamma_{N\mathrm{nos}}} &\leq 2\mu \left[L\|\underline{\underline{\varepsilon}}(\underline{v}_{\mathrm{f},h})\cdot\underline{n}\|_{\phi_0,\Gamma_{N\mathrm{nos}}}^2 + \frac{1}{L}\|\underline{v}_{\mathrm{f},h} - \underline{v}_{\mathrm{s},h}\|_{\phi_0,\Gamma_{N\mathrm{nos}}}^2 \right] \\ &\leq 2\mu \frac{C_{ie}L}{h}\|\underline{\underline{\varepsilon}}(\underline{v}_{\mathrm{f},h})\|_{\phi_0,\Omega}^2 + 2\frac{\mu}{L}\|\underline{v}_{\mathrm{f},h} - \underline{v}_{\mathrm{s},h}\|_{\phi_0,\Gamma_{N\mathrm{nos}}}^2. \end{aligned} \tag{4.11}$$

We end up with the following energy balance

$$\partial_t \mathcal{E}_h + 2\mu\left(1 - \frac{C_{ie}L}{h}\right)\|\underline{\underline{\varepsilon}}(\underline{v}_{\mathrm{f},h})\|_{\phi_0,\Omega}^2 + \mu\left(\frac{\gamma}{h} - \frac{2}{L}\right)\|\underline{v}_{\mathrm{f},h} - \underline{v}_{\mathrm{s},h}\|_{\phi_0,\Gamma_{N\mathrm{nos}}}^2 + \|\underline{v}_{\mathrm{f},h} - \underline{v}_{\mathrm{s},h}\|_{\phi_0^2\underline{\underline{k}}_{\mathrm{f}}^{-1},\Omega}^2 \leq 0$$

which ensures the stability of semi-discrete solution X_h provided that $\gamma \geq 2C_{ie}$.

4.3 The fully discrete problem

4.3.1 Time scheme

We consider in (4.7) a first-order backward Euler method in the fluid, for both $\underline{v}_{\mathrm{f}}$ and p, to keep it as close as possible to the splitting scheme of Chapter 3 (otherwise $p^{n+\frac{1}{2}}$ would have been a natural choice to avoid numerical dissipation), and a midpoint scheme for the solid. Using the notations $a^{n+\frac{1}{2}} \doteq \frac{a^{n+1}+a^n}{2}$ and $D_\tau a^{n+\frac{1}{2}} \doteq \frac{a^{n+1}-a^n}{\Delta t}$, we look for $(\underline{v}_{\mathrm{f},h}^n, \underline{v}_{\mathrm{s},h}^n, \underline{y}_{\mathrm{s},h}^n, p_h^n)_{n\geq 0}$ in $V_h^{\mathbb{N}}$ such that, for any n in $\mathbb{N}$ and $(\underline{v}_{\mathrm{f}}^*, \underline{v}_{\mathrm{s}}^*, \underline{y}_{\mathrm{s}}^*, p^*)$ in V_h^0,

$$\begin{aligned} &\rho_{\mathrm{f}}\left(D_\tau \underline{v}_{\mathrm{f},h}^{n+\frac{1}{2}}, \underline{v}_{\mathrm{f}}^*\right)_{\phi_0,\Omega} + \rho_{\mathrm{s}}\left(D_\tau \underline{v}_{\mathrm{s},h}^{n+\frac{1}{2}}, \underline{v}_{\mathrm{s}}^*\right)_{1-\phi_0,\Omega} + \frac{1}{\kappa_{\mathrm{s}}}\left(D_\tau p_h^{n+\frac{1}{2}}, p^*\right)_{(1-\phi_0)^2,\Omega} \\ &\quad + \left(D_\tau \underline{y}_{\mathrm{s},h}^{n+\frac{1}{2}}, \underline{y}_{\mathrm{s}}^*\right)_{\mathrm{skel}} + M((\underline{v}_{\mathrm{f},h}^{n+1}, \underline{v}_{\mathrm{s},h}^{n+\frac{1}{2}}, \underline{y}_{\mathrm{s},h}^{n+\frac{1}{2}}, p_h^{n+1}), (\underline{v}_{\mathrm{f}}^*, \underline{v}_{\mathrm{s}}^*, \underline{y}_{\mathrm{s}}^*, p^*)) \\ &= \int_\Omega \rho_{s0}(1-\phi_0)\underline{f}^{n+1}\cdot\underline{v}_{\mathrm{s}}^*\, d\Omega + \int_{\Gamma_N^0}(1-\phi_0)\underline{t}_0^{n+1}\cdot\underline{v}_{\mathrm{s}}^*\, dS + \int_{\Gamma_{N\mathrm{nof}}\bigcup\Gamma_{N\mathrm{nos}}} \underline{t}_0^{n+1}\cdot\underline{v}_{\mathrm{s}}^*\, dS - \int_{\Gamma_{N\mathrm{nof}}} \phi_0(\pi_\tau \underline{t}_0^{n+1})\cdot\underline{v}_{\mathrm{s}}^* dS \\ &\quad + \int_\Omega \theta^n \underline{v}_{\mathrm{f},h}^{n+1}\cdot\underline{v}_{\mathrm{f}}^* d\Omega + \int_\Omega \rho_{\mathrm{f}}\phi_0\, \underline{f}^{n+1}\cdot\underline{v}_{\mathrm{f}}^*\, d\Omega + \int_{\Gamma_N\bigcup\Gamma_{N\mathrm{nof}}} \phi_0\, \underline{t}_0^{n+1}\cdot\underline{v}_{\mathrm{f}}^*\, dS + \int_\Omega \theta^n p^* d\Omega, \end{aligned} \tag{4.12}$$

with adequate initial conditions.

4.3.2 Stability analysis in energy norm

In this section again, and for the rest of the document, we will assume that $\underline{t}_0 = 0$ on $\Gamma_{N\mathrm{nos}}$, $\Gamma_{N\mathrm{nof}}$ and Γ_N, $\underline{f} = \underline{0}$, $\theta = 0$, $\underline{y}_{\mathrm{s}}^{\mathrm{pr}} = \underline{0}$ and $\underline{v}_{\mathrm{f}}^{\mathrm{pr}} = \underline{0}$ (as a consequence, $V = V^0$). The evaluation of (4.12) with admissible test functions

$$\underline{v}_{\mathrm{f}}^* = \underline{v}_{\mathrm{f},h}^{n+1}, \quad \underline{v}_{\mathrm{s}}^* = \underline{v}_{\mathrm{s},h}^{n+\frac{1}{2}}, \quad \underline{y}_{\mathrm{s}}^* = \underline{y}_{\mathrm{s},h}^{n+\frac{1}{2}}, \quad \text{and} \quad p^* = p_h^{n+1}$$

gives

$$0 = \rho_{\mathrm{f}} \left(D_\tau \underline{v}_{\mathrm{f},h}^{n+\frac{1}{2}}, \underline{v}_{\mathrm{f},h}^{n+1} \right)_{\phi_0,\Omega} + \frac{1}{\kappa_{\mathrm{s}}} \left(D_\tau p_h^{n+\frac{1}{2}}, p_h^{n+1} \right)_{(1-\phi_0)^2,\Omega} + \left(D_\tau \underline{y}_{\mathrm{s},h}^{n+\frac{1}{2}}, \underline{y}_{\mathrm{s},h}^{n+\frac{1}{2}} \right)_{\mathrm{skel}}$$
$$+ \rho_{\mathrm{s}} \left(D_\tau \underline{v}_{\mathrm{s},h}^{n+\frac{1}{2}}, \underline{v}_{\mathrm{s},h}^{n+\frac{1}{2}} \right)_{1-\phi_0,\Omega} + 2\mu \left(\underline{\underline{\varepsilon}}(\underline{v}_{\mathrm{f},h}^{n+1}), \underline{\underline{\varepsilon}}(\underline{v}_{\mathrm{f},h}^{n+1}) \right)_{\phi_0,\Omega} - 4\mu \left(\underline{\underline{\varepsilon}}(\underline{v}_{\mathrm{f},h}^{n+1})\underline{n}, \underline{v}_{\mathrm{f},h}^{n+1} - \underline{v}_{\mathrm{s},h}^{n+\frac{1}{2}} \right)_{\phi_0,\Gamma_{N\mathrm{nos}}}$$
$$+ \frac{\gamma\mu}{h} \left(\underline{v}_{\mathrm{f},h}^{n+1} - \underline{v}_{\mathrm{s},h}^{n+\frac{1}{2}}, \underline{v}_{\mathrm{f},h}^{n+1} - \underline{v}_{\mathrm{s},h}^{n+\frac{1}{2}} \right)_{\phi_0,\Gamma_{N\mathrm{nos}}} + \left(\underline{v}_{\mathrm{f},h}^{n+1} - \underline{v}_{\mathrm{s},h}^{n+\frac{1}{2}}, \underline{v}_{\mathrm{f},h}^{n+1} - \underline{v}_{\mathrm{s},h}^{n+\frac{1}{2}} \right)_{\phi_0^2 \underline{\underline{k}}_{\mathrm{f}}^{-1},\Omega}.$$

We introduce the state vector $X_h^n = \left[\underline{v}_{\mathrm{f},h}^n, \underline{v}_{\mathrm{s},h}^n, \underline{y}_{\mathrm{s},h}^n, p_h^n \right]$ and its energy $\mathcal{E}_h^n = \|X_h^n\|_{\mathcal{E}}^2$ at iteration n. Then, we apply twice the identity $\langle a-b, a \rangle = \frac{1}{2}||a||^2 - \frac{1}{2}||b||^2 + \frac{1}{2}||a-b||^2$ to $\underline{v}_{\mathrm{f}}$ and to p, to get

$$\frac{\mathcal{E}_h^{n+1} - \mathcal{E}_h^n}{\Delta t} + \frac{\rho_{\mathrm{f}}}{2\Delta t} \|\underline{v}_{\mathrm{f},h}^{n+1} - \underline{v}_{\mathrm{f},h}^n\|_{\phi_0,\Omega}^2 + \frac{1}{2\kappa_{\mathrm{s}}\Delta t} \|p_h^{n+1} - p_h^n\|_{(1-\phi_0)^2,\Omega}^2 + 2\mu \|\underline{\underline{\varepsilon}}(\underline{v}_{\mathrm{f},h}^{n+1})\|_{\phi_0,\Omega}^2$$
$$+ \|\underline{v}_{\mathrm{s},h}^{n+\frac{1}{2}} - \underline{v}_{\mathrm{f},h}^{n+1}\|_{\phi_0^2 \underline{\underline{k}}_{\mathrm{f}}^{-1},\Omega}^2 + \frac{\gamma\mu}{h} \|\underline{v}_{\mathrm{s},h}^{n+\frac{1}{2}} - \underline{v}_{\mathrm{f},h}^{n+1}\|_{\phi_0,\Gamma_{N\mathrm{nos}}}^2 \underbrace{- 4\mu (\underline{\underline{\varepsilon}}(\underline{v}_{\mathrm{f},h}^{n+1})\underline{n}, \underline{v}_{\mathrm{f},h}^{n+1} - \underline{v}_{\mathrm{s},h}^{n+\frac{1}{2}})_{\phi_0,\Gamma_{N\mathrm{nos}}}}_{\mathcal{T}_1} = 0, \tag{4.13}$$

using that

$$\underline{\underline{\sigma}}^{\mathrm{skel}} \left(\frac{\underline{y}_{\mathrm{s},h}^{n+1} - \underline{y}_{\mathrm{s},h}^n}{\Delta t} \right) : \underline{\underline{\varepsilon}} \left(\frac{\underline{y}_{\mathrm{s},h}^{n+1} + \underline{y}_{\mathrm{s},h}^n}{2} \right) + \frac{(1-\phi_0)^2}{\kappa_{\mathrm{s}}} \frac{p_h^{n+1} - p_h^n}{\Delta t} p_h^{n+1}$$
$$= \frac{\underline{\underline{\sigma}}^{\mathrm{skel}}(\underline{y}_{\mathrm{s},h}^{n+1}) : \underline{\underline{\varepsilon}}(\underline{y}_{\mathrm{s},h}^{n+1}) - \underline{\underline{\sigma}}^{\mathrm{skel}}(\underline{y}_{\mathrm{s},h}^n) : \underline{\underline{\varepsilon}}(\underline{y}_{\mathrm{s},h}^n)}{2\Delta t} + \frac{(1-\phi_0)^2}{2\kappa_{\mathrm{s}}\Delta t} \left[(p_h^{n+1})^2 - (p_h^n)^2 + (p_h^{n+1} - p_h^n)^2 \right]$$
$$= \frac{\Psi(\underline{\underline{\varepsilon}}(\underline{y}_{\mathrm{s},h}^{n+1}), p_h^{n+1}) - \Psi(\underline{\underline{\varepsilon}}(\underline{y}_{\mathrm{s},h}^n), p_h^n)}{\Delta t} + \frac{(1-\phi_0)^2}{2\kappa_{\mathrm{s}}\Delta t} (p_h^{n+1} - p_h^n)^2.$$

In (4.13), the increment of $\mathcal{E}_h^n$ is followed by two terms of numerical dissipation, two terms of physical dissipation, and the dissipative term in $\frac{\gamma\mu}{h}$ that comes from Nitsche's method. We apply the bound (4.11) to $\underline{v}_{\mathrm{f},h}^{n+1}$ and $\underline{v}_{\mathrm{s},h}^{n+\frac{1}{2}}$ to control the remaining term $\mathcal{T}_1$, and to get that for any length L,

$$\frac{\mathcal{E}_h^{n+1} - \mathcal{E}_h^n}{\Delta t} + 2\mu(1 - \frac{C_{ie}L}{h}) \|\underline{\underline{\varepsilon}}(\underline{v}_{\mathrm{f},h}^{n+1})\|_{\phi_0,\Omega}^2 + \mu(\frac{\gamma}{h} - \frac{2}{L}) \|\underline{v}_{\mathrm{f},h}^{n+1} - \underline{v}_{\mathrm{s},h}^{n+\frac{1}{2}}\|_{\phi_0,\Gamma_{N\mathrm{nos}}}^2$$
$$+ \frac{\rho_{\mathrm{f}}}{2\Delta t} \|\underline{v}_{\mathrm{f},h}^{n+1} - \underline{v}_{\mathrm{f},h}^n\|_{\phi_0,\Omega}^2 + \frac{1}{2\kappa_{\mathrm{s}}\Delta t} \|p_h^{n+1} - p_h^n\|_{(1-\phi_0)^2,\Omega}^2 + \|\underline{v}_{\mathrm{s},h}^{n+\frac{1}{2}} - \underline{v}_{\mathrm{f},h}^{n+1}\|_{\phi_0^2 \underline{\underline{k}}_{\mathrm{f}}^{-1},\Omega}^2 \leq 0.$$

Therefore, the energy stability of the scheme is ensured provided that we can find L such that $1 \geq \frac{C_{ie}L}{h}$ and $\frac{\gamma}{h} \geq \frac{2}{L}$, i.e. when $\gamma \geq 2C_{ie}$. We note here that the numerical perturbation that appears in Chapter 3 (because of the splitting and the non-linearities) and the CFL-like condition it introduces, do not intervene anymore.

4.3.3 Inf-sup property on the static problem

In order to establish the total convergence of our scheme, we will resort to the projection P associated with the bilinear form M, see Section 4.3.4. The purpose of this section is to establish for M an inf-sup condition that will provide a control of $P - I$, with I the identity.

We introduce the following discrete norm, associated with the stabilisation,

$$\|X\|_h^2 \hat{=} \|\underline{v}_\mathrm{f}\|_{H^1(\Omega)}^2 + \|\underline{v}_\mathrm{s}\|_{H^1(\Omega)}^2 + \|\underline{y}_\mathrm{s}\|_{H^1(\Omega)}^2 + \|p\|_{L^2(\Omega)}^2 + \frac{\gamma\mu}{h}\|\underline{v}_\mathrm{f} - \underline{v}_\mathrm{s}\|_{L^2(\Gamma_{N\mathrm{nos}})}^2 + \|\underline{v}_\mathrm{f} - \underline{v}_\mathrm{s}\|_{L^2(\Omega)}^2.$$

For physical reasons, ϕ_0 is bounded by 0 and 1, and in what follows we will make the two following assumptions,

$$\inf_\Omega \phi_0 > 0 \quad \text{and} \quad \sup_\Omega \phi_0 < 1$$

and

$$\exists(\alpha_1, \alpha_2) \in (\mathbb{R}^+)^2 \mid \forall(\underline{\mathrm{x}}, \underline{\omega}) \in \Omega \times \mathbb{R}^3, \alpha_1 \underline{\omega}^2 \leq \underline{\omega} \cdot \underline{\underline{k}}_\mathrm{f}(\underline{\mathrm{x}}) \cdot \underline{\omega} \leq \alpha_2 \underline{\omega}^2,$$

in order to ensure the equivalence between norms $\|\cdot\|_{\phi_0,\Omega}$, $\|\cdot\|_{(1-\phi_0),\Omega}$, $\|\cdot\|_{(1-\phi_0)^2,\Omega}$, $\|\cdot\|_{\phi_0^2 \underline{\underline{k}}_\mathrm{f}^{-1},\Omega}$, $\|\cdot\|_{L^2(\Omega)}$.

Our objective in this section is to establish a stability (inf-sup) property for M defined by (4.8) for $\|\cdot\|_h$.

We begin with establishing a lemma, that we will use in the following proof to construct virtual fluid and solid velocity fields.

Let $\mathcal{V}_h$ and $\mathcal{Q}_h$ be finite dimensional subspaces of Hilbert spaces $\mathcal{V}$ and $\mathcal{Q}$ with scalar products $(\cdot,\cdot)_\mathcal{V}$ and $(\cdot,\cdot)_\mathcal{Q}$. Let $a(\cdot,\cdot)$ and $b(\cdot,\cdot)$ be continuous linear forms on $\mathcal{V} \times \mathcal{V}$ and $\mathcal{V} \times \mathcal{Q}$, and f and g linear forms on $\mathcal{V}$ and $\mathcal{Q}$. We look for (v_h, p_h) in $\mathcal{V}_h \times \mathcal{Q}_h$ solution of

$$\begin{cases} a(v_h, v^*) + b(v^*, p_h) = f(v^*), & \forall v^* \in \mathcal{V}_h, \\ b(v_h, p^*) = g(p^*), & \forall p^* \in \mathcal{Q}_h. \end{cases} \tag{4.14}$$

We can introduce operators A_h from $\mathcal{V}_h$ to $\mathcal{V}_h'$ and B_h from $\mathcal{V}_h$ to $\mathcal{Q}_h'$. B denotes the continuous operator from $\mathcal{V}$ to $\mathcal{Q}'$.

Lemma 3
Let us suppose that $\mathrm{Ker}\, B^t = \{0\}$, *and that* $a(\cdot,\cdot)$ *is elliptic on* $\mathcal{V}$, *that is, there exists* $\alpha_0 > 0$ *such that*

$$a(v, v) \geq \alpha_0 \|v\|_\mathcal{V}^2, \quad \forall v \in \mathcal{V}.$$

If, moreover, b *satisfies an inf-sup property, that is, there exists* $k_0 > 0$ *independent of* h *such that*

$$\inf_{p \in \mathcal{Q}_h} \sup_{v \in \mathcal{V}_h} \frac{b(v,p)}{\|v\|_\mathcal{V} \|p\|_\mathcal{Q}} \geq k_0, \tag{4.15}$$

then, the system (4.14) *has a unique solution* (u_h, p_h). *In addition. one has the bound*

$$\begin{cases} \|v_h\|_\mathcal{V} \leq \dfrac{1}{\alpha_0}\|f\|_{\mathcal{V}'} + \left(\dfrac{\|a\|}{\alpha_0} + 1\right)\dfrac{1}{k_0}\|g\|_{\mathcal{Q}'} \\ \|p_h\|_\mathcal{Q} \leq \dfrac{1}{k_0}\left(\dfrac{\|a\|}{\alpha_0} + 1\right)\|f\|_{\mathcal{V}'} + \dfrac{\|a\|}{k_0^2}\left(\dfrac{\|a\|}{\alpha_0} + 1\right)\|g\|_{\mathcal{Q}'}. \end{cases} \tag{4.16}$$

Proof. The inf-sup condition (4.15) ensures that $\mathrm{Ker}\, B_h^t = \{0\}$, then Proposition 2.2, §II.2 in (Brezzi and Fortin, 2012) ensures that $g \in \mathrm{Im}\, B_h$. The ellipticity of a on $\mathcal{V}_h$ inherits from the one on $\mathcal{V}$, and the application of Theorem 1.1, §II.1 in (Brezzi and Fortin, 2012) on the discrete problem gives the results. ■

Remark 8
In the case of a Stokes problem, $a(\cdot,\cdot)$ is elliptic and it is known that $\mathrm{Ker}\, B^t = \mathrm{Ker}(-\mathrm{grad}) = \{0\}$ when a Dirichlet condition is applied on a non-empty portion of the boundary, so the issue is in checking (4.15), with $b(v,q) = \int_\Omega q\, \mathrm{div}\, v\, d\Omega$.

Proposition 4 (Inf-sup property on M)
Let us make the following assumptions:

- *there exists λ_{f} such that*

$$\inf_{p\in Q_h}\sup_{\underline{v}_{\mathrm{f}}\in W_h^{\mathrm{f}}}\frac{(p,\mathrm{div}(\phi_0\underline{v}_{\mathrm{f}}))_\Omega}{\|p\|_{L^2(\Omega)}\|\underline{v}_{\mathrm{f}}\|_{H^1(\Omega)}}\geq\lambda_{\mathrm{f}}>0, \tag{4.17}$$

- *there exists λ_{s} such that*

$$\inf_{p\in Q_h}\sup_{\underline{v}_{\mathrm{s}}\in W_h^{\mathrm{s}}}\frac{(p,\mathrm{div}((1-\phi_0)\underline{v}_{\mathrm{s}}))_\Omega}{\|p\|_{L^2(\Omega)}\|\underline{v}_{\mathrm{s}}\|_{H^1(\Omega)}}\geq\lambda_{\mathrm{s}}>0, \tag{4.18}$$

- *W_h^{f} and W_h^{s} have identical traces on Γ_{Nnos}, that is*

$$\left\{\underline{v}_{\mathrm{f}}|_{\Gamma_{Nnos}},\underline{v}_{\mathrm{f}}\in W_h^{\mathrm{f}}\right\}=\left\{\underline{v}_{\mathrm{s}}|_{\Gamma_{Nnos}},\underline{v}_{\mathrm{s}}\in W_h^{\mathrm{s}}\right\}, \tag{4.19}$$

- *the Robin coefficient satisfies*

$$\gamma>2C_{ie}. \tag{4.20}$$

Then the operator M defined by (4.8) satisfies an inf-sup property for $\|\cdot\|_h$: there exists $\beta>0$ independent of h such that

$$\inf_{X\in V_h}\sup_{X^*\in V_h}\frac{M(X,X^*)}{\|X\|_h\|X^*\|_h}\geq\beta,$$

or, equivalently

$$\forall X\in V_h,\exists X^*\in V_h\quad|\quad\|X^*\|_h\leq\|X\|_h\quad\textit{and}\quad M(X,X^*)\geq\beta\|X\|_h^2.$$

Remark 9
When ϕ_0 is homogeneous in space, the condition (4.17) takes the following form

$$\exists\lambda_{\mathrm{f}}>0\mid\inf_{p\in Q_h}\sup_{\underline{v}_{\mathrm{f}}\in W_h^{\mathrm{f}}}\frac{(p,\mathrm{div}\,\underline{v}_{\mathrm{f}})_\Omega}{\|p\|_{L^2(\Omega)}\|\underline{v}_{\mathrm{f}}\|_{H^1(\Omega)}}\geq\lambda_{\mathrm{f}}>0. \tag{4.21}$$

In the numerical resolution, the condition (4.21) is easier to verify than (4.17) because it doesn't involve ϕ_0, and comes down to a well known condition on $W_h^{\mathrm{f}}\times Q_h$ for variables $\underline{v}_{\mathrm{f}}$ and p. In practice, we will see (see Section 4.4) that the condition (4.21) plays a prominent role in the stability of numerical scheme especially when the solid constituent approaches incompressibility ($\kappa_{\mathrm{s}}\to\infty$). In addition, perturbations induced by spatial variations of ϕ_0 in the condition (4.17), or by violations of conditions (4.18) or (4.19) are generally of secondary importance.

Proof. Let $X_h=\left[\underline{v}_{\mathrm{f},h},\underline{v}_{\mathrm{s},h},\underline{y}_{\mathrm{s},h},p_h\right]$ in V_h, we will build an $\bar{X}_h$ in V_h and a $\beta>0$ that satisfies the above condition in several steps, in order to control the different terms that appear in $\|\cdot\|_h$.

1. We define $X_h^1=\left[0,0,-\underline{v}_{\mathrm{s},h},0\right]$, then $M(X_h,X_h^1)\geq\alpha_1\|\underline{v}_{\mathrm{s},h}\|^2_{H^1(\Omega)}$, with $\alpha_1>0$.

2. We pick $X_h^2 = X_h$. The energy bound derived in Section 4.2.3 gives for any length L

$$\begin{aligned} M(X_h, X_h^2) &= 2\mu\|\underline{\underline{\varepsilon}}(\underline{v}_{\mathrm{f},h})\|^2_{\phi_0, L^2(\Omega)} + \frac{\gamma\mu}{h}\|\underline{v}_{\mathrm{f},h} - \underline{v}_{\mathrm{s},h}\|^2_{\phi_0, L^2(\Gamma_{N\mathrm{nos}})} + \|\underline{v}_{\mathrm{f},h} - \underline{v}_{\mathrm{s},h}\|^2_{\phi_0^2\underline{\underline{k}}_{\mathrm{f}}^{-1}, L^2(\Omega)} \\ &\quad - 4\mu(\underline{\underline{\varepsilon}}(\underline{v}_{\mathrm{f},h})\underline{n}, \underline{v}_{\mathrm{f},h} - \underline{v}_{\mathrm{s},h})_{\phi_0, L^2(\Gamma_{N\mathrm{nos}})} \\ &\geq 2\mu\left(1 - \frac{C_{ie}L}{h}\right)\|\underline{\underline{\varepsilon}}(\underline{v}_{\mathrm{f},h})\|^2_{\phi_0, L^2(\Omega)} + \mu\left(\frac{\gamma}{h} - \frac{2}{L}\right)\|\underline{v}_{\mathrm{f},h} - \underline{v}_{\mathrm{s},h}\|^2_{\phi_0, L^2(\Gamma_{N\mathrm{nos}})} \\ &\quad + \|\underline{v}_{\mathrm{f},h} - \underline{v}_{\mathrm{s},h}\|^2_{\phi_0^2\underline{\underline{k}}_{\mathrm{f}}^{-1}, L^2(\Omega)}. \end{aligned}$$

Thanks to the assumption on γ, and norm equivalences, we build $\alpha_2 > 0$ such that

$$M(X_h, X_h^2) \geq \alpha_2\left(\|\underline{v}_{\mathrm{f},h}\|^2_{H^1(\Omega)} + \frac{\gamma\mu}{h}\|\underline{v}_{\mathrm{f},h} - \underline{v}_{\mathrm{s},h}\|^2_{L^2(\Gamma_{N\mathrm{nos}})} + \|\underline{v}_{\mathrm{f},h} - \underline{v}_{\mathrm{s},h}\|^2_{L^2(\Omega)}\right).$$

3. Thanks to (4.19), we define $\mathcal{L}(\underline{y}_{\mathrm{s},h})$ a lifting of $\underline{y}_{\mathrm{s},h}|_{\Gamma_{N\mathrm{nos}}}$ in W_h^{f} satisfying

$$\|\mathcal{L}(\underline{y}_{\mathrm{s},h})\|_{H^1(\Omega)} \leq C\|\underline{y}_{\mathrm{s},h}\|_{H^{\frac{1}{2}}(\Gamma_{N\mathrm{nos}})}.$$

According to Remark 8 and thanks to (4.17), Lemma 3 ensures the existence of $(\underline{w}_h^3, p_h^3)$ in $W_h^{\mathrm{f}} \times Q_h$ such that for any $(\underline{w}^*, p^*)$ in $W_h^{\mathrm{f}} \times Q_h$

$$\left\{\begin{aligned} \left(\underline{\underline{\varepsilon}}(\underline{w}_h^3), \underline{\underline{\varepsilon}}(\underline{w}^*)\right)_\Omega + \left(p_h^3, \mathrm{div}(\phi_0\underline{w}^*)\right)_\Omega &= 0, \\ \left(p^*, \mathrm{div}(\phi_0\underline{w}_h^3)\right)_\Omega &= -\left(p^*, \mathrm{div}\left[(1-\phi_0)\underline{y}_{\mathrm{s},h} + \phi_0\mathcal{L}(\underline{y}_{\mathrm{s},h})\right]\right)_\Omega, \\ \underline{w}_h^3|_{\Gamma_{N\mathrm{nos}}} &= 0, \end{aligned}\right. \tag{4.22}$$

and for C and C' independent of h, see (4.16) and (4.9),

$$\|\underline{w}_h^3\|_{H^1(\Omega)} \leq C'(\|\underline{y}_{\mathrm{s},h}\|_{H^1(\Omega)} + \|\mathcal{L}(\underline{y}_{\mathrm{s},h})\|_{H^1(\Omega)}) \leq C\|\underline{y}_{\mathrm{s},h}\|_{H^1(\Omega)}.$$

Now let us construct $X_h^3 = \left[\underline{v}_{\mathrm{f},h}^3, \underline{y}_{\mathrm{s},h}, 0, 0\right]$, with $\underline{v}_{\mathrm{f},h}^3 = \mathcal{L}(\underline{y}_{\mathrm{s},h}) + \underline{w}_h^3$; then we have

$$\|\underline{v}_{\mathrm{f},h}^3\|_{H^1(\Omega)} \leq C\|\underline{y}_{\mathrm{s},h}\|_{H^1(\Omega)}.$$

The purpose of this construction is to get $\underline{v}_{\mathrm{f},h}^3$ such that $\left(p, \mathrm{div}(\phi_0\underline{v}_{\mathrm{f},h}^3 + (1-\phi_0)\underline{y}_{\mathrm{s},h})\right)_\Omega = 0$ and $\underline{v}_{\mathrm{f},h}^3 = \underline{y}_{\mathrm{s},h}$ on $\Gamma_{N\mathrm{nos}}$, which finally allows to write that, for any (η_1, η_2, η_3) in $(\mathbb{R}^+)^3$

$$\begin{aligned} M(X_h, X_h^3) &= 2\mu\left(\underline{\underline{\varepsilon}}(\underline{v}_{\mathrm{f},h}) : \underline{\underline{\varepsilon}}(\underline{v}_{\mathrm{f},h}^3)\right)_{\phi_0,\Omega} + \left(\underline{y}_{\mathrm{s},h}, \underline{y}_{\mathrm{s},h}\right)_{\mathrm{skel}} - 2\mu\left(\underline{\underline{\varepsilon}}(\underline{v}_{\mathrm{f},h}^3)\cdot\underline{n}, \underline{v}_{\mathrm{f},h} - \underline{v}_{\mathrm{s},h}\right)_{\phi_0,\Gamma_{N\mathrm{nos}}} \\ &\quad + \left(\underline{v}_{\mathrm{f},h} - \underline{v}_{\mathrm{s},h}, \underline{v}_{\mathrm{f},h}^3 - \underline{y}_{\mathrm{s},h}\right)_{\phi_0^2\underline{\underline{k}}_{\mathrm{f}}^{-1},\Omega}. \end{aligned}$$

Using Young inequality we have

$$\begin{aligned} M(X_h, X_h^3) &\geq -\mu\left(\eta_1\|\underline{\underline{\varepsilon}}(\underline{v}_{\mathrm{f},h}^3)\|^2_{\phi_0,\Omega} + \frac{1}{\eta_1}\|\underline{\underline{\varepsilon}}(\underline{v}_{\mathrm{f},h})\|^2_{\phi_0,\Omega}\right) + C\|\underline{y}_{\mathrm{s},h}\|^2_{H^1(\Omega)} \\ &\quad - \mu\left(\eta_2\|\underline{\underline{\varepsilon}}(\underline{v}_{\mathrm{f},h}^3)\|^2_{\phi_0,\Gamma_{N\mathrm{nos}}} + \frac{1}{\eta_2}\|\underline{v}_{\mathrm{f},h} - \underline{v}_{\mathrm{s},h}\|^2_{\phi_0,\Gamma_{N\mathrm{nos}}}\right) \\ &\quad - \left(\frac{1}{2\eta_3}\|\underline{v}_{\mathrm{f},h} - \underline{v}_{\mathrm{s},h}\|^2_{\phi_0^2\underline{\underline{k}}_{\mathrm{f}}^{-1},\Omega} + \eta_3\|\underline{y}_{\mathrm{s},h}\|^2_{H^1(\Omega)}\right). \end{aligned}$$

And the trace inverse inequality finally gives

$$M(X_h, X_h^3) \geq \left[C - \left(\mu\eta_1 + \mu\eta_2 \frac{C_{ie}}{h} + \eta_3\right)\right] \|\underline{y}_{\mathrm{s},h}\|^2_{H^1(\Omega)} - \frac{\mu}{\eta_1}\|\underline{\underline{\varepsilon}}(\underline{v}_{\mathrm{f},h})\|^2_{\phi_0,\Omega} - \frac{\mu}{\eta_2}\|\underline{v}_{\mathrm{f},h} - \underline{v}_{\mathrm{s},h}\|^2_{\phi_0,\Gamma_{N\mathrm{nos}}} - \frac{1}{2\eta_3}\|\underline{v}_{\mathrm{f},h} - \underline{v}_{\mathrm{s},h}\|^2_{\phi_0^2\underline{\underline{k}}_{\mathrm{f}}^{-1},\Omega}.$$

Choosing for example

$$\eta_1 = \frac{C}{4}\left(\mu + \frac{C_{ie}}{\gamma}\right)^{-1},\ \eta_2 = \frac{h\eta_1}{\gamma\mu},\ \eta_3 = \frac{C}{4}, \text{ and defining } \alpha_3 = \frac{C}{2} \text{ and } \beta_3 = \max\left(\frac{\mu}{\eta_1}, \frac{2}{C}\right)$$

–α_3 and β_3 are obviously independent of h –, we end up with

$$M(X_h, X_h^3) \geq \alpha_3\|\underline{y}_{\mathrm{s},h}\|^2_{H^1(\Omega)} - \beta_3\left(\|\underline{v}_{\mathrm{f},h}\|^2_{H^1(\Omega)} + \frac{\gamma\mu}{h}\|\underline{v}_{\mathrm{f},h} - \underline{v}_{\mathrm{s},h}\|^2_{L^2(\Gamma_{N\mathrm{nos}})} + \|\underline{v}_{\mathrm{f},h} - \underline{v}_{\mathrm{s},h}\|^2_{L^2(\Omega)}\right). \quad (4.23)$$

In addition, there exists $\gamma_3 > 0$ such that

$$\|X_h^3\|_h = \|\underline{v}_{\mathrm{f},h}^3\|^2_{H^1(\Omega)} + \|\underline{y}_{\mathrm{s},h}\|^2_{H^1(\Omega)} + \|\underline{v}_{\mathrm{f},h}^3 - \underline{y}_{\mathrm{s},h}\|^2_{L^2(\Omega)}$$
$$\leq \|\underline{v}_{\mathrm{f},h}^3\|^2_{H^1(\Omega)} + \|\underline{y}_{\mathrm{s},h}\|^2_{H^1(\Omega)} + \|\underline{v}_{\mathrm{f},h}^3\|^2_{L^2(\Omega)} + \|\underline{y}_{\mathrm{s},h}\|^2_{L^2(\Omega)} \leq \gamma_3\|\underline{y}_{\mathrm{s},h}\|^2_{H^1(\Omega)} \leq \gamma_3\|X_h\|_h.$$

4. As a consequence of (4.17), we can construct $\underline{v}_{\mathrm{f},h}^4$ such that for a positive λ,

$$\begin{cases} \|\underline{v}_{\mathrm{f},h}^4\|_{H^1(\Omega)} \leq \|p_h\|_{L^2(\Omega)}, \\ -\left(p_h, \mathrm{div}(\phi_0\underline{v}_{\mathrm{f},h}^4)\right)_\Omega \geq \lambda\|p_h\|^2_{L^2(\Omega)}. \end{cases} \quad (4.24)$$

Once again, (4.19) allows to introduce $\mathcal{L}(\underline{v}_{\mathrm{f},h}^4)$ a lifting of $\underline{v}_{\mathrm{f},h}^4|_{\Gamma_{N\mathrm{nos}}}$ in W_h^{s} such that

$$\|\mathcal{L}(\underline{v}_{\mathrm{f},h}^4)\|_{H^1(\Omega)} \leq C\|\underline{v}_{\mathrm{f},h}^4\|_{H^{\frac{1}{2}}(\Gamma_{N\mathrm{nos}})}.$$

According to Remark 8 and thanks to (4.18), Lemma 3 ensures the existence of $(\underline{w}_h^4, p_h^4)$ in $W_h^{\mathrm{s}} \times Q_h$ such that for any $(\underline{w}^*, p^*)$ in $W_h^{\mathrm{s}} \times Q_h$,

$$\begin{cases} \left(\underline{\underline{\varepsilon}}(\underline{w}_h^4), \underline{\underline{\varepsilon}}(\underline{w}^*)\right)_\Omega + \left(p_h^4, \mathrm{div}((1-\phi_0)\underline{w}^*)\right)_\Omega = 0, \\ \left(p^*, \mathrm{div}((1-\phi_0)\underline{w}_h^4)\right)_\Omega = -\left(p^*, \mathrm{div}\left[(1-\phi_0)\mathcal{L}(\underline{v}_{\mathrm{f},h}^4)\right]\right)_\Omega, \\ \underline{w}_h^4|_{\Gamma_{N\mathrm{nos}}} = 0, \end{cases}$$

and for C, C' and C'' independent of h, see (4.16) and (4.9),

$$\|\underline{w}_h^4\|_{H^1(\Omega)} \leq C''\|\mathcal{L}(\underline{v}_{\mathrm{f},h}^4)\|_{H^1(\Omega)} \leq C'\|\underline{v}_{\mathrm{f},h}^4\|_{H^1(\Omega)}.$$

Finally, we build $X_h^4 = \left[\underline{v}_{\mathrm{f},h}^4, \underline{v}_{\mathrm{s},h}^4, 0, 0\right]$ with $\underline{v}_{\mathrm{s},h}^4 = \mathcal{L}(\underline{v}_{\mathrm{f},h}^4) + \underline{w}_h^4$; then

$$\|\underline{v}_{\mathrm{s},h}^4\|_{H^1(\Omega)} \leq \|\underline{w}_h^4\|_{H^1(\Omega)} + \|\mathcal{L}(\underline{v}_{\mathrm{f},h}^4)\|_{H^1(\Omega)} \leq C\|\underline{v}_{\mathrm{f},h}^4\|_{H^1(\Omega)} \leq C\|p_h\|_{L^2(\Omega)}.$$

This construction gives a control on p_h through the divergence term, neutralizing the $\underline{v}_{\mathrm{s},h}^4$ contribution. It also imposes $\underline{v}_{\mathrm{f},h}^4 = \underline{v}_{\mathrm{s},h}^4$ on $\Gamma_{N\mathrm{nos}}$, and finally allows to write that, for any $(\eta_1, \eta_2, \eta_3, \eta_4)$ in $(\mathbb{R}^+)^4$,

$$M(X_h, X_h^4) = 2\mu\left(\underline{\underline{\varepsilon}}(\underline{v}_{\mathrm{f},h}) : \underline{\underline{\varepsilon}}(\underline{v}_{\mathrm{f},h}^4)\right)_{\phi_0,\Omega} + \left(\underline{y}_{\mathrm{s},h}, \underline{v}_{\mathrm{s},h}^4\right)_{\mathrm{skel}} - \left(\underline{\underline{\sigma}}_{\mathrm{vis}}(\underline{v}_{\mathrm{f},h}^4)\cdot\underline{n}, \underline{v}_{\mathrm{f},h} - \underline{v}_{\mathrm{s},h}\right)_{\phi_0,\Gamma_{N\mathrm{nos}}}$$
$$+ \left(\underline{v}_{\mathrm{f},h} - \underline{v}_{\mathrm{s},h}, \underline{v}_{\mathrm{f},h}^4 - \underline{v}_{\mathrm{s},h}^4\right)_{\phi_0^2\underline{\underline{k}}_{\mathrm{f}}^{-1},\Omega} - \left(p_h, \mathrm{div}(\phi_0\underline{v}_{\mathrm{f},h}^4)\right)_\Omega.$$

Young and trace inverse inequalities now give

$$M(X_h, X_h^4) \geq -\left(\eta_1 C\|\underline{v}_{\mathrm{f},h}\|^2_{H^1(\Omega)} + \frac{C}{\eta_1}\|p_h\|^2_{L^2(\Omega)}\right) - \left(\eta_2 C\|\underline{y}_{\mathrm{s},h}\|^2_{H^1(\Omega)} + \frac{1}{\eta_2}C\|p_h\|^2_{L^2(\Omega)}\right)$$
$$- \left(\eta_3 \frac{C_{ie}}{h}\|p_h\|^2_{L^2(\Omega)} + \frac{1}{\eta_3}C\|\underline{v}_{\mathrm{f},h} - \underline{v}_{\mathrm{s},h}\|^2_{L^2(\Gamma_{N\mathrm{nos}})}\right)$$
$$- \left(\frac{C}{\eta_4}\|p_h\|^2_{L^2(\Omega)} + \eta_4 C\|\underline{v}_{\mathrm{f},h} - \underline{v}_{\mathrm{s},h}\|^2_{L^2(\Omega)}\right) + \lambda\|p_h\|^2_{L^2(\Omega)}.$$

We apply it to

$$\eta_1 = \eta_2 = \eta_4 = \frac{5C}{\lambda},\ \eta_3 = \frac{h\lambda}{5C_{ie}},\ \text{ and we define } \alpha_4 = \frac{\lambda}{5} \text{ and } \beta_4 = \max\left(\eta_1 C, \frac{5C_{ie}C}{\gamma\mu\lambda}\right),$$

α_4 and β_4 don't depend on h and we end up with

$$M(X_h, X_h^4) \geq \alpha_4\|p_h\|_{L^2(\Omega)}$$
$$- \beta_4\left(\|\underline{v}_{\mathrm{f},h}\|^2_{H^1(\Omega)} + \|\underline{y}_{\mathrm{s},h}\|^2_{H^1(\Omega)} + \frac{\gamma\mu}{h}\|\underline{v}_{\mathrm{f},h} - \underline{v}_{\mathrm{s},h}\|^2_{L^2(\Gamma_{N\mathrm{nos}})} + \|\underline{v}_{\mathrm{f},h} - \underline{v}_{\mathrm{s},h}\|^2_{L^2(\Omega)}\right).$$

We also have the following bound

$$\|X_h^4\|_h = \|\underline{v}^4_{\mathrm{f},h}\|^2_{H^1(\Omega)} + \|\underline{v}^4_{\mathrm{s},h}\|^2_{H^1(\Omega)} + \|\underline{v}^4_{\mathrm{f},h} - \underline{v}^4_{\mathrm{s},h}\|^2_{L^2(\Omega)}$$
$$\leq \|\underline{v}^4_{\mathrm{f},h}\|^2_{H^1(\Omega)} + \|\underline{v}^4_{\mathrm{s},h}\|^2_{H^1(\Omega)} + \|\underline{v}^4_{\mathrm{f},h}\|^2_{H^1(\Omega)} + \|\underline{v}^4_{\mathrm{s},h}\|^2_{H^1(\Omega)} \leq \gamma_4\|p_h\|^2_{L^2(\Omega)} \leq \gamma_4\|X_h\|^2_h.$$

Now, let us define the following positive coefficients, that don't depend on h,

$$\delta_3 = \frac{\alpha_2}{\alpha_3 + 2\beta_3},\ \delta_4 = \frac{\alpha_3\delta_3}{2\beta_4},\ \text{ and } \beta = \min\left(\frac{\alpha_2}{2}, \alpha_1, \frac{\delta_3\alpha_3}{2}, \delta_4\alpha_4\right)$$

and let us introduce $\bar{X_h} = X_h^1 + X_h^2 + \delta_3 X_h^3 + \delta_4 X_h^4$. By construction, we end up with

$$\begin{aligned}
M(X_h, \bar{X_h}) \geq\ & \alpha_1\|\underline{v}_{\mathrm{s},h}\|^2_{H^1(\Omega)} + \alpha_2\left(\|\underline{v}_{\mathrm{f},h}\|^2_{H^1(\Omega)} + \frac{\gamma\mu}{h}\|\underline{v}_{\mathrm{f},h} - \underline{v}_{\mathrm{s},h}\|^2_{L^2(\Gamma_{N\mathrm{nos}})} + \|\underline{v}_{\mathrm{f},h} - \underline{v}_{\mathrm{s},h}\|^2_{L^2(\Omega)}\right) \\
& + \delta_3\alpha_3\|\underline{y}_{\mathrm{s},h}\|^2_{H^1(\Omega)} - \delta_3\beta_3\left(\|\underline{v}_{\mathrm{f},h}\|^2_{H^1(\Omega)} + \frac{\gamma\mu}{h}\|\underline{v}_{\mathrm{f},h} - \underline{v}_{\mathrm{s},h}\|^2_{L^2(\Gamma_{N\mathrm{nos}})}\right. \\
& \left. + \|\underline{v}_{\mathrm{f},h} - \underline{v}_{\mathrm{s},h}\|^2_{L^2(\Omega)}\right) + \delta_4\alpha_4\|p_h\|_{L^2(\Omega)} - \delta_4\beta_4\left(\|\underline{v}_{\mathrm{f},h}\|^2_{H^1(\Omega)}\right. \\
& \left. + \|\underline{y}_{\mathrm{s},h}\|^2_{H^1(\Omega)} + \frac{\gamma\mu}{h}\|\underline{v}_{\mathrm{f},h} - \underline{v}_{\mathrm{s},h}\|^2_{L^2(\Gamma_{N\mathrm{nos}})} + \|\underline{v}_{\mathrm{f},h} - \underline{v}_{\mathrm{s},h}\|^2_{L^2(\Omega)}\right) \\
\geq\ & (\alpha_2 - \delta_3\beta_3 - \delta_4\beta_4)\left(\|\underline{v}_{\mathrm{f},h}\|^2_{H^1(\Omega)} + \frac{\gamma\mu}{h}\|\underline{v}_{\mathrm{f},h} - \underline{v}_{\mathrm{s},h}\|^2_{L^2(\Gamma_{N\mathrm{nos}})} + \|\underline{v}_{\mathrm{f},h} - \underline{v}_{\mathrm{s},h}\|^2_{L^2(\Omega)}\right) \\
& + \alpha_1\|\underline{v}_{\mathrm{s},h}\|^2_{H^1(\Omega)} + (\delta_3\alpha_3 - \delta_4\beta_4)\|\underline{y}_{\mathrm{s},h}\|^2_{H^1(\Omega)} + \delta_4\alpha_4\|p_h\|^2_{L^2(\Omega)} \\
\geq\ & \beta\|X_h\|^2_h,
\end{aligned}$$

and

$$\|\bar{X_h}\|_h \leq (2 + \delta_3\gamma_3 + \delta_4\gamma_4)\|X_h\|_h.$$

We conclude the proof with the following two inequalities

$$\left\|\frac{\bar{X_h}}{2 + \delta_3\gamma_3 + \delta_4\gamma_4}\right\|_h \leq \|X_h\|_h \quad \text{and} \quad M\left(X_h, \frac{\bar{X_h}}{2 + \delta_3\gamma_3 + \delta_4\gamma_4}\right) \geq \frac{\beta}{2 + \delta_3\gamma_3 + \delta_4\gamma_4}\|X_h\|^2_h.$$

■

4.3.4 Convergence in time and space of the fully discretized scheme solution

We introduce a new state function space with more regularity $V^+ = (H^2(\Omega)^3)^3 \times H^1(\Omega)$, and denote as follows the two natural norms over V and V^+:

$$\|X\|_V^2 = \|\underline{v}_{\rm f}\|_{H^1(\Omega)}^2 + \|\underline{v}_{\rm s}\|_{H^1(\Omega)}^2 + \|\underline{y}_{\rm s}\|_{H^1(\Omega)}^2 + \|p\|_{L^2(\Omega)}^2,$$
$$\|X\|_{V^+}^2 = \|\underline{v}_{\rm f}\|_{H^2(\Omega)}^2 + \|\underline{v}_{\rm s}\|_{H^2(\Omega)}^2 + \|\underline{y}_{\rm s}\|_{H^2(\Omega)}^2 + \|p\|_{H^1(\Omega)}^2.$$

We also introduce $V^- = (L^2(\Omega)^3)^2 \times H^1(\Omega)^3 \times L^2(\Omega)$, whose natural norm is equivalent to $\|\cdot\|_{\mathcal{E}}$.

We denote that under the assumptions of Proposition 4, existence and uniqueness of a solution X_h^{n+1} to the discrete problem (4.12) results from the invertibility of the total operator – both dynamical terms and static form M. It stems from the positivity of M – see the proof of Proposition 4 – and from the following argument. For X_h in its kernel, we have

$$\begin{aligned} 0 &= \rho_{\rm f} \left(\frac{1}{\Delta t} \underline{v}_{{\rm f},h}^{n+1}, \underline{v}_{{\rm f},h}^{n+1} \right)_{\phi_0,\Omega} + \rho_{\rm s} \left(\frac{1}{\Delta t} \underline{v}_{{\rm s},h}^{n+1}, \underline{v}_{{\rm s},h}^{n+1} \right)_{1-\phi_0,\Omega} + \frac{1}{\kappa_{\rm s}} \left(\frac{1}{\Delta t} p_h^{n+1}, p_h^{n+1} \right)_{(1-\phi_0)^2,\Omega} \\ &\quad + \left(\frac{1}{\Delta t} \underline{y}_{{\rm s},h}^{n+1}, \underline{y}_{{\rm s},h}^{n+1} \right)_{\rm skel} + M((\underline{v}_{{\rm f},h}^{n+1}, \underline{v}_{{\rm s},h}^{n+1}, \underline{y}_{{\rm s},h}^{n+1}, p_h^{n+1}), (\underline{v}_{{\rm f},h}^{n+1}, \underline{v}_{{\rm s},h}^{n+1}, \underline{y}_{{\rm s},h}^{n+1}, p_h^{n+1})) \\ &\geq \frac{\rho_{\rm f}}{\Delta t} \left\| \underline{v}_{{\rm f},h}^{n+1} \right\|_{\phi_0,\Omega}^2 + \frac{\rho_{\rm s}}{\Delta t} \left\| \underline{v}_{{\rm s},h}^{n+1} \right\|_{1-\phi_0,\Omega}^2 + \frac{1}{\kappa_{\rm s} \Delta t} \left\| p_h^{n+1} \right\|_{(1-\phi_0)^2,\Omega}^2 + \frac{1}{\Delta t} \left\| \underline{y}_{{\rm s},h}^{n+1} \right\|_{\rm skel}^2, \end{aligned} \tag{4.25}$$

hence $X_h = 0$.

The continuous solution $X = (\underline{v}_{\rm f}, \underline{v}_{\rm s}, \underline{y}_{\rm s}, p)$ in V of (4.5) satisfies, for any $(\underline{v}_{\rm f}^*, \underline{v}_{\rm s}^*, \underline{y}_{\rm s}^*, p^*)$ in V, at any time t,

$$\begin{aligned} &\rho_{\rm f} \left(\partial_t \underline{v}_{\rm f}, \underline{v}_{\rm f}^* \right)_{\phi_0,\Omega} + \rho_{\rm s} \left(\partial_t \underline{v}_{\rm s}, \underline{v}_{\rm s}^* \right)_{1-\phi_0,\Omega} + \left(\partial_t \underline{y}_{\rm s}, \underline{y}_{\rm s}^* \right)_{\rm skel} + \frac{1}{\kappa_{\rm s}} \left(\partial_t p, p^* \right)_{(1-\phi_0)^2,\Omega} \\ &\qquad + M((\underline{v}_{\rm f}, \underline{v}_{\rm s}, \underline{y}_{\rm s}, p), (\underline{v}_{\rm f}^*, \underline{v}_{\rm s}^*, \underline{y}_{\rm s}^*, p^*)) = 0. \end{aligned} \tag{4.26}$$

The discrete solution $(X_h^n = (\underline{v}_{{\rm f},h}^n, p_h^n, \underline{y}_{{\rm s},h}^n, \underline{v}_{{\rm s},h}^n))_{n \geq 0}$ in $(V_h)^{\mathbb{N}}$ is such that for any $n \geq 0$, and any $(\underline{v}_{\rm f}^*, \underline{v}_{\rm s}^*, \underline{y}_{\rm s}^*, p^*)$ in V_h

$$\begin{aligned} &\rho_{\rm f} \left(D_\tau \underline{v}_{{\rm f},h}^{n+\frac{1}{2}}, \underline{v}_{\rm f}^* \right)_{\phi_0,\Omega} + \rho_{\rm s} \left(D_\tau \underline{v}_{{\rm s},h}^{n+\frac{1}{2}}, \underline{v}_{\rm s}^* \right)_{1-\phi_0,\Omega} + \left(D_\tau \underline{y}_{{\rm s},h}^{n+\frac{1}{2}}, \underline{y}_{\rm s}^* \right)_{\rm skel} \\ &\quad + \frac{1}{\kappa_{\rm s}} \left(D_\tau p_h^{n+\frac{1}{2}}, p^* \right)_{(1-\phi_0)^2,\Omega} + M((\underline{v}_{{\rm f},h}^{n+1}, \underline{v}_{{\rm s},h}^{n+\frac{1}{2}}, \underline{y}_{{\rm s},h}^{n+\frac{1}{2}}, p_h^{n+1}), (\underline{v}_{\rm f}^*, \underline{v}_{\rm s}^*, \underline{y}_{\rm s}^*, p^*)) = 0. \end{aligned} \tag{4.27}$$

The purpose of this section is to establish the following convergence result.

Proposition 5 (Total convergence)
Assuming that conditions (4.17), (4.18), (4.19) and (4.20) are satisfied, that the solution X of (4.5) belongs to $\mathcal{C}^1(0,T,V^+) \cap \mathcal{C}^2(0,T,V^-)$, with T the simulation time, and that $(X_h^n)_{n \geq 0}$ is the solution of (4.12). There exists a constant C depending only on $\|X\|_{L^\infty(0,T,V^+)}$, $\|\partial_t X\|_{L^\infty[0,T,V^+]}$ and $\|\partial_t^2 X\|_{L^\infty[0,T,\mathcal{E}]}$ such that, denoting

$$X_h^n - X(t^n) = \left[\underline{v}_{{\rm f},h}^n - \underline{v}_{\rm f}(t^n),\ p_h^n - p(t^n),\ \underline{v}_{{\rm s},h}^n - \underline{v}_{\rm s}(t^n),\ \underline{y}_{{\rm s},h}^n - \underline{y}_{\rm s}(t^n) \right],$$

we have

$$\|X_h^n - X(t^n)\|_{\mathcal{E}} \leq C(h + \Delta t).$$

Proof. Let us introduce the projection $P = \left[P_h^{\mathrm{f}}, P_h^{\mathrm{s}}, P_h^{\mathrm{y}}, P_h^{\mathrm{p}}\right]$ such that,

$$\forall X^* = (\underline{v}_{\mathrm{f}}^*, \underline{v}_{\mathrm{s}}^*, \underline{y}_{\mathrm{s}}^*, p^*) \in V_h, \quad M(PX, X^*) = M(X, X^*) \quad \text{i.e.}$$
$$M((P_h^{\mathrm{f}}\underline{v}_{\mathrm{f}}, P_h^{\mathrm{s}}\underline{v}_{\mathrm{s}}, P_h^{\mathrm{y}}\underline{y}_{\mathrm{s}}, P_h^{\mathrm{p}}p), (\underline{v}_{\mathrm{f}}^*, \underline{v}_{\mathrm{s}}^*, \underline{y}_{\mathrm{s}}^*, p^*)) = M((\underline{v}_{\mathrm{f}}, \underline{v}_{\mathrm{s}}, \underline{y}_{\mathrm{s}}, p), (\underline{v}_{\mathrm{f}}^*, \underline{v}_{\mathrm{s}}^*, \underline{y}_{\mathrm{s}}^*, p^*)). \quad (4.28)$$

We begin with establishing

Lemma 6
Under the hypothesis of Proposition 4, there exists a constant C independent of h such that, for any X in V^+ satisfying $X_1 = X_2$ on $\Gamma_{N\mathrm{nos}}$,

$$\|PX - X\|_{\mathcal{E}} \leq Ch\|X\|_{V^+}.$$

Remark 10
More generally, with shape functions of order $k > 1$ for PX we have that for any X in $V^k = (H^{k+1}(\Omega)^3)^3 \times H^k(\Omega)$ satisfying $X_1 = X_2$ on $\Gamma_{N\mathrm{nos}}$,

$$\|PX - X\|_{\mathcal{E}} \leq Ch^k\|X\|_{V^k},$$

with $\|\cdot\|_{V^k}$ the natural norm on V^k. To fix the ideas, we will restrict ourselves to the case $k = 1$.

Proof of Lemma 6. Under these assumptions, let us introduce the Clément (Clément, 1975) interpolation I_hX in V_h that satisfies

$$\begin{cases} \|X - I_hX\|_V \leq Ch\|X\|_{V^+}, \\ \|I_hX\|_V \leq C\|X\|_V, \\ (I_hX)_1 = (I_hX)_2 \quad \text{on } \Gamma_{N\mathrm{nos}}, \\ \|(I_hX - X)_4\|_{L^2(\Gamma_{N\mathrm{nos}})} \leq Ch^{1/2}\|X_4\|_{H^1(\Omega)}, \\ \|(I_hX - X)_1\|_{H^1(\Gamma_{N\mathrm{nos}})} \leq Ch^{1/2}\|X_1\|_{H^2(\Omega)}. \end{cases}$$

For $X^* \in V_h$, let us look at the terms of $M(X - I_hX, X^*)$ that are not controlled by $\|\cdot\|_h$. Thanks to the above properties and the Cauchy-Schwarz inequality,

$$\begin{aligned}(p - I_hp, (\underline{v}_{\mathrm{f}}^* - \underline{v}_{\mathrm{s}}^*) \cdot \underline{n})_{\Gamma_{N\mathrm{nos}}} &\leq h^{1/2}\|p - I_hp\|_{L^2(\Gamma_{N\mathrm{nos}})} \cdot \frac{1}{h^{1/2}}\|\underline{v}_{\mathrm{f}}^* - \underline{v}_{\mathrm{s}}^*\|_{L^2(\Gamma_{N\mathrm{nos}})} \\ &\leq Ch\|X\|_{V^+}\|X^*\|_h\end{aligned}$$

The same argument enables us to control $2\mu(\underline{\varepsilon}(\underline{v}_{\mathrm{f}} - I_h\underline{v}_{\mathrm{f}}) \cdot \underline{n}, \underline{v}_{\mathrm{f}}^* - \underline{v}_{\mathrm{s}}^*)_{\Gamma_{N\mathrm{nos}}}$, the Robin term vanishes since by construction $(X - I_hX)_1 = (X - I_hX)_2$ on $\Gamma_{N\mathrm{nos}}$, and all other terms are controlled with Cauchy-Schwarz. We end up with, for C independent of h,

$$M(X - I_hX, X^*) \leq Ch\|X\|_{V^+}\|X^*\|_h. \quad (4.29)$$

Now, Proposition 4 ensures the existence of X^* in V_h such that

$$\|X^*\|_h = 1 \text{ and } M(PX - I_hX, X^*) \geq \gamma\|PX - I_hX\|_h,$$

and we recall that by definition of P,

$$M(PX - I_hX, X^*) = M(X - I_hX, X^*),$$

therefore, using (4.29)

$$\gamma\|PX - I_hX\|_h \leq M(X - I_hX, X^*) \leq Ch\|X\|_{V^+}.$$

Finally, using that $\|\cdot\|_{\mathcal{E}} \leq \|\cdot\|_h$, and by construction of $I_h X$, the triangular inequality gives, with C independent of h,

$$\begin{aligned}\|PX - X\|_{\mathcal{E}} &\leq \|PX - I_h X\|_{\mathcal{E}} + \|I_h X - X\|_{\mathcal{E}} \\ &\leq Ch\|X\|_{V^+} + Ch\|X\|_{V^+}.\end{aligned}$$

■

Proof of Proposition 5. The inclusion $V_h \subset V$ enables us to choose discrete test functions in (4.26) and by construction of the projectors we get, for any $X^* = (\underline{v}_{\mathrm{f}}^*, \underline{v}_{\mathrm{s}}^*, \underline{y}_{\mathrm{s}}^*, p^*)$ in V_h

$$\begin{aligned}\rho_{\mathrm{f}} \left(\partial_t \underline{v}_{\mathrm{f}}, \underline{v}_{\mathrm{f}}^*\right)_{\phi_0,\Omega} + \rho_{\mathrm{s}} \left(\partial_t \underline{v}_{\mathrm{s}}, \underline{v}_{\mathrm{s}}^*\right)_{1-\phi_0,\Omega} + \left(\partial_t \underline{y}_{\mathrm{s}}, \underline{y}_{\mathrm{s}}^*\right)_{\mathrm{skel}} + \frac{1}{\kappa_{\mathrm{s}}} \left(\partial_t p, p^*\right)_{(1-\phi_0)^2,\Omega} \\ + M((P_h^{\mathrm{f}} \underline{v}_{\mathrm{f}}, P_h^{\mathrm{s}} \underline{v}_{\mathrm{s}}, P_h^{\mathrm{y}} \underline{y}_{\mathrm{s}}, P_h^{\mathrm{p}} p), (\underline{v}_{\mathrm{f}}^*, \underline{v}_{\mathrm{s}}^*, \underline{y}_{\mathrm{s}}^*, p^*)) = 0. \quad (4.30)\end{aligned}$$

We average the evaluations of (4.30) at time t^n and t^{n+1}, and gather consistency errors on the right hand side, to get that for any $X^* = (\underline{v}_{\mathrm{f}}^*, \underline{v}_{\mathrm{s}}^*, \underline{y}_{\mathrm{s}}^*, p^*)$ in V_h,

$$\begin{aligned}&\rho_{\mathrm{f}} \left((D_\tau P_h^{\mathrm{f}} \underline{v}_{\mathrm{f}})^n, \underline{v}_{\mathrm{f}}^*\right)_{\phi_0,\Omega} + \rho_{\mathrm{s}} \left((D_\tau P_h^{\mathrm{s}} \underline{v}_{\mathrm{s}})^{n+\frac{1}{2}}, \underline{v}_{\mathrm{s}}^*\right)_{1-\phi_0,\Omega} \\ &\qquad + \left((D_\tau P_h^{\mathrm{y}} \underline{y}_{\mathrm{s}})^{n+\frac{1}{2}}, \underline{y}_{\mathrm{s}}^*\right)_{\mathrm{skel}} + \frac{1}{\kappa_{\mathrm{s}}} \left((D_\tau P_h^{\mathrm{p}} p)^n, p^*\right)_{(1-\phi_0)^2,\Omega} \\ &\qquad + M(((P_h^{\mathrm{f}} \underline{v}_{\mathrm{f}})^{n+\frac{1}{2}}, (P_h^{\mathrm{s}} \underline{v}_{\mathrm{s}})^{n+\frac{1}{2}}, (P_h^{\mathrm{y}} \underline{y}_{\mathrm{s}})^{n+\frac{1}{2}}, (P_h^{\mathrm{p}} p)^{n+\frac{1}{2}}), (\underline{v}_{\mathrm{f}}^*, \underline{v}_{\mathrm{s}}^*, \underline{y}_{\mathrm{s}}^*, p^*)) \\ &= \rho_{\mathrm{f}} \left((D_\tau P_h^{\mathrm{f}} \underline{v}_{\mathrm{f}})^n - (\partial_t \underline{v}_{\mathrm{f}})^{n+\frac{1}{2}}, \underline{v}_{\mathrm{f}}^*\right)_{\phi_0,\Omega} + \rho_{\mathrm{s}} \left((D_\tau P_h^{\mathrm{s}} \underline{v}_{\mathrm{s}})^{n+\frac{1}{2}} - (\partial_t \underline{v}_{\mathrm{s}})^{n+\frac{1}{2}}, \underline{v}_{\mathrm{s}}^*\right)_{1-\phi_0,\Omega} \\ &+ \left((D_\tau P_h^{\mathrm{y}} \underline{y}_{\mathrm{s}})^{n+\frac{1}{2}} - (\partial_t \underline{y}_{\mathrm{s}})^{n+\frac{1}{2}}, \underline{y}_{\mathrm{s}}^*\right)_{\mathrm{skel}} + \frac{1}{\kappa_{\mathrm{s}}} \left((D_\tau P_h^{\mathrm{p}} p)^n - (\partial_t p)^{n+\frac{1}{2}}, p^*\right)_{(1-\phi_0)^2,\Omega}, \quad (4.31)\end{aligned}$$

where we defined for any function g continuous in time,

$$(D_\tau g)^{n+\frac{1}{2}} = \frac{g(t^{n+1}) - g(t^n)}{\Delta t}, (D_\tau g)^n = \frac{g(t^{n+1}) - g(t^{n-1})}{2\Delta t}, \quad \text{and} \quad (g)^{n+\frac{1}{2}} = \frac{g(t^{n+1}) + g(t^n)}{2}.$$

Now we introduce

$$\tilde{X}_h^n = X_h^n - (PX)^n \quad \text{with} \quad (PX)^n = \left[(P_h^{\mathrm{f}} \underline{v}_{\mathrm{f}})^{n-\frac{1}{2}}, P_h^{\mathrm{s}} \underline{v}_{\mathrm{s}}(t^n), P_h^{\mathrm{y}} \underline{y}_{\mathrm{s}}(t^n), (P_h^{\mathrm{p}} p)^{n-\frac{1}{2}}\right]$$

and we denote by $\mathcal{A}(\underline{v}_{\mathrm{f}}^*, \underline{v}_{\mathrm{s}}^*, \underline{y}_{\mathrm{s}}^*, p^*)$ the right hand side of (4.31) (the consistency terms). Then the subtraction (4.27) - (4.31) gives, for any $X^* = (\underline{v}_{\mathrm{f}}^*, \underline{v}_{\mathrm{s}}^*, \underline{y}_{\mathrm{s}}^*, p^*)$ in V_h,

$$\begin{aligned}\rho_{\mathrm{f}} \left(D_\tau \tilde{\underline{v}}_{\mathrm{f},h}^{n+\frac{1}{2}}, \underline{v}_{\mathrm{f}}^*\right)_{\phi_0,\Omega} + \rho_{\mathrm{s}} \left(D_\tau \tilde{\underline{v}}_{\mathrm{s},h}^{n+\frac{1}{2}}, \underline{v}_{\mathrm{s}}^*\right)_{1-\phi_0,\Omega} + \left(D_\tau \tilde{\underline{y}}_{\mathrm{s},h}^{n+\frac{1}{2}}, \underline{y}_{\mathrm{s}}^*\right)_{\mathrm{skel}} + \frac{1}{\kappa_{\mathrm{s}}} \left(D_\tau \tilde{p}_h^{n+\frac{1}{2}}, p^*\right)_{(1-\phi_0)^2,\Omega} \\ + M((\tilde{\underline{v}}_{\mathrm{f},h}^{n+1}, \tilde{\underline{v}}_{\mathrm{s},h}^{n+\frac{1}{2}}, \tilde{\underline{y}}_{\mathrm{s},h}^{n+\frac{1}{2}}, \tilde{p}_h^{n+1}), (\underline{v}_{\mathrm{f}}^*, \underline{v}_{\mathrm{s}}^*, \underline{y}_{\mathrm{s}}^*, p^*)) = \mathcal{A}(\underline{v}_{\mathrm{f}}^*, \underline{v}_{\mathrm{s}}^*, \underline{y}_{\mathrm{s}}^*, p^*). \quad (4.32)\end{aligned}$$

Following the steps of the energy stability analysis, we evaluate the previous equation with the following functions that are admissible:

$$\underline{v}_{\mathrm{f},h}^* = \tilde{\underline{v}}_{\mathrm{f},h}^{n+1}, \quad \underline{v}_{\mathrm{s},h}^* = \tilde{\underline{v}}_{\mathrm{s},h}^{n+\frac{1}{2}}, \text{ and } \underline{y}_{\mathrm{s},h}^* = \tilde{\underline{y}}_{\mathrm{s},h}^{n+\frac{1}{2}}, \quad p_h^* = \tilde{p}_h^{n+1}.$$

We introduce, for the evaluation of the right hand side of equation (4.32)

$$\mathcal{A} = \mathcal{A}(\tilde{\underline{v}}_{\mathrm{f},h}^{n+1}, \tilde{\underline{v}}_{\mathrm{s},h}^{n+\frac{1}{2}}, \tilde{\underline{y}}_{\mathrm{s},h}^{n+\frac{1}{2}}, \tilde{p}_h^{n+1})$$

and the energy of the error at iteration n

$$\tilde{\mathcal{E}}^n = \frac{\rho_{\mathrm{f}}}{2}\|\underline{\tilde{v}}^n_{\mathrm{f},h}\|^2_{\phi_0,\Omega} + \frac{\rho_s}{2}\|\underline{\tilde{v}}^n_{\mathrm{s},h}\|^2_{1-\phi_0,\Omega} + \frac{1}{2}\|\underline{\tilde{y}}^n_{\mathrm{s},h}\|^2_{\mathrm{skel}} + \frac{1}{2\kappa_{\mathrm{s}}}\|\tilde{p}^n_h\|^2_{(1-\phi_0)^2,\Omega}.$$

Then the same derivation as in Section 4.3.2 gives

$$\begin{aligned}\mathcal{A} = \frac{\tilde{\mathcal{E}}^{n+1}-\tilde{\mathcal{E}}^n}{\Delta t} + \frac{\rho_{\mathrm{f}}}{2\Delta t}\|\underline{\tilde{v}}^{n+1}_{\mathrm{f},h}-\underline{\tilde{v}}^n_{\mathrm{f},h}\|^2_{\phi_0,\Omega} + \frac{1}{2\kappa_{\mathrm{s}}\Delta t}\|\tilde{p}^{n+1}_h-\tilde{p}^n_h\|^2_{(1-\phi_0)^2,\Omega} + 2\mu\|\underline{\underline{\varepsilon}}(\underline{\tilde{v}}^{n+1}_{\mathrm{f},h})\|^2_{\phi_0,\Omega}\\ + \frac{\gamma\mu}{h}\|\underline{\tilde{v}}^{n+\frac12}_{\mathrm{s},h}-\underline{\tilde{v}}^{n+1}_{\mathrm{f},h}\|^2_{\phi_0,\Gamma_{N\mathrm{nos}}} + \|\underline{\tilde{v}}^{n+\frac12}_{\mathrm{s},h}-\underline{\tilde{v}}^{n+1}_{\mathrm{f},h}\|^2_{\phi_0^2\underline{\underline{k}}_{\mathrm{f}}^{-1},\Omega} \underbrace{- 4\mu(\underline{\underline{\varepsilon}}(\underline{\tilde{v}}^{n+1}_{\mathrm{f},h})\underline{n}, \underline{\tilde{v}}^{n+1}_{\mathrm{f},h}-\underline{\tilde{v}}^{n+\frac12}_{\mathrm{s},h})_{\phi_0,\Gamma_{N\mathrm{nos}}}}_{\mathcal{T}_1},\end{aligned} \tag{4.33}$$

with for any length L

$$\mathcal{T}_1 \le 2\mu\left[L\|\underline{\underline{\varepsilon}}(\underline{\tilde{v}}^{n+1}_{\mathrm{f},h})\underline{n}\|^2_{\phi_0,\Gamma_{N\mathrm{nos}}} + \frac{1}{L}\|\underline{\tilde{v}}^{n+1}_{\mathrm{f},h}-\underline{\tilde{v}}^{n+\frac12}_{\mathrm{s},h}\|^2_{\phi_0,\Gamma_{N\mathrm{nos}}}\right].$$

We use the trace inverse inequality to get that $\|\underline{\underline{\varepsilon}}(\underline{\tilde{v}}^{n+1}_{\mathrm{f},h})\underline{n}\|^2_{\phi_0,\Gamma_{N\mathrm{nos}}} \le \frac{C_{ie}}{h}\|\underline{\underline{\varepsilon}}(\underline{\tilde{v}}^{n+1}_{\mathrm{f},h})\|^2_{\Omega}$ and

$$\mathcal{T}_1 \le 2\mu\frac{C_{ie}L}{h}\|\underline{\underline{\varepsilon}}(\underline{\tilde{v}}^{n+1}_{\mathrm{f},h})\|^2_{\phi_0,\Omega} + \frac{2\mu}{L}\|\underline{\tilde{v}}^{n+1}_{\mathrm{f},h}-\underline{\tilde{v}}^{n+\frac12}_{\mathrm{s},h}\|^2_{\phi_0,\Gamma_{N\mathrm{nos}}},$$

so that (4.33) turns into

$$\frac{\tilde{\mathcal{E}}^{n+1}-\tilde{\mathcal{E}}^n}{\Delta t} \le 2\mu\left(\frac{C_{ie}L}{h}-1\right)\|\underline{\underline{\varepsilon}}(\underline{\tilde{v}}^{n+1}_{\mathrm{f},h})\|^2_{\phi_0,\Omega} + \mu\left(\frac{2}{L}-\frac{\gamma}{h}\right)\|\underline{\tilde{v}}^{n+1}_{\mathrm{f},h}-\underline{\tilde{v}}^{n+\frac12}_{\mathrm{s},h}\|^2_{\phi_0,\Gamma_{N\mathrm{nos}}} + \mathcal{A}.$$

Now we must control $\mathcal{A}$, which we decompose as follows:

$$\begin{cases}\mathcal{A}_1 = \rho_{\mathrm{f}}\left((D_\tau P^{\mathrm{f}}_h\underline{v}_{\mathrm{f}})^n - (\partial_t\underline{v}_{\mathrm{f}})^{n+\frac12}, \underline{\tilde{v}}^{n+1}_{\mathrm{f},h}\right)_{\phi_0,\Omega},\\ \mathcal{A}_2 = \rho_{\mathrm{s}}\left((D_\tau P^{\mathrm{s}}_h\underline{v}_{\mathrm{s}})^{n+\frac12} - (\partial_t\underline{v}_{\mathrm{s}})^{n+\frac12}, \underline{\tilde{v}}^{n+\frac12}_{\mathrm{s},h}\right)_{1-\phi_0,\Omega},\\ \mathcal{A}_3 = \left((D_\tau P^{\mathrm{y}}_h\underline{y}_{\mathrm{s}})^{n+\frac12} - (\partial_t\underline{y}_{\mathrm{s}})^{n+\frac12}, \underline{\tilde{y}}^{n+\frac12}_{\mathrm{s},h}\right)_{\mathrm{skel}},\\ \mathcal{A}_4 = \frac{1}{\kappa_{\mathrm{s}}}\left((D_\tau P^{\mathrm{p}}_h p)^n - (\partial_t p)^{n+\frac12}, \tilde{p}^{n+1}_h\right)_{(1-\phi_0)^2,\Omega}.\end{cases}$$

The linearity of P gives

$$(D_\tau P^{\mathrm{f}}_h\underline{v}_{\mathrm{f}})^n - (\partial_t\underline{v}_{\mathrm{f}})^{n+\frac12} = P^{\mathrm{f}}_h(D_\tau\underline{v}_{\mathrm{f}})^n - (D_\tau\underline{v}_{\mathrm{f}})^n + (D_\tau\underline{v}_{\mathrm{f}})^n - \partial_t\underline{v}_{\mathrm{f}}(t^n) + \partial_t\underline{v}_{\mathrm{f}}(t^n) - (\partial_t\underline{v}_{\mathrm{f}})^{n+\frac12}.$$

By assumption, $(D_\tau X)^n$ belongs to V^+ and has equal first and second component, so Lemma 6 gives

$$\begin{aligned}\|P^{\mathrm{f}}_h(D_\tau\underline{v}_{\mathrm{f}})^n - (D_\tau\underline{v}_{\mathrm{f}})^n\|_{\phi_0,\Omega} &\le \|P^{\mathrm{f}}_h(D_\tau X)^n - (D_\tau X)^n\|_{\mathcal{E}} \le Ch\|(D_\tau X)^n\|_{V^+}\\ &\le Ch\|\partial_t X\|_{L^\infty[0,T,V^+]}.\end{aligned}$$

Then, thanks to Taylor-Lagrange inequality,

$$\|(D_\tau\underline{v}_{\mathrm{f}})^n - \partial_t\underline{v}_{\mathrm{f}}(t^n)\|_{\phi_0,\Omega} \le C\|\partial_t^2 X\|_{L^\infty[0,T,\mathcal{E}]}\Delta t,$$

and $\underline{v}_{\mathrm{f}}$ being $\mathcal{C}^2$,

$$\|\partial_t \underline{v}_{\mathrm{f}}(t^n) - (\partial_t \underline{v}_{\mathrm{f}})^{n+\frac{1}{2}}\|_{\phi_0,\Omega} \leq C\|\partial_t^2 X\|_{L^\infty[0,T,\mathcal{E}]}\Delta t.$$

A final use of the Cauchy-Schwarz inequality gives

$$\mathcal{A}_1 \leq C_1(h+\Delta t)\|\tilde{\underline{v}}_{\mathrm{f},h}^{n+1}\|_{\phi_0,\Omega},$$

The same derivation gives the following bounds for $\mathcal{A}_2$, $\mathcal{A}_3$ and $\mathcal{A}_4$,

$$\mathcal{A}_2 \leq C_2(h+\Delta t)\|\tilde{\underline{v}}_{\mathrm{s},h}^{n+\frac{1}{2}}\|_{1-\phi_0,\Omega},$$

$$\mathcal{A}_3 \leq C_3(h+\Delta t)\|\tilde{\underline{y}}_{\mathrm{s},h}^{n+\frac{1}{2}}\|_{\mathrm{skel}},$$

$$\mathcal{A}_4 \leq C_4(h+\Delta t)\|\tilde{p}_h^{n+1}\|_{(1-\phi_0)^2,\Omega}.$$

We note that the C_i's depend on $\|\partial_t^2 X\|_{L^\infty[0,T,\mathcal{E}]}$ and $\|\partial_t X\|_{L^\infty[0,T,V^+]}$. We end up with, for $C'_A = \max_{1\leq i\leq 4} C_i$

$$\begin{aligned}\frac{\tilde{\mathcal{E}}^{n+1}-\tilde{\mathcal{E}}^n}{\Delta t} \leq\ & 2\mu\left(\frac{C_{ie}L}{h}-1\right)\|\underline{\varepsilon}(\tilde{\underline{v}}_{\mathrm{f},h}^{n+1})\|_{\phi_0,\Omega}^2 + \mu\left(\frac{2}{L}-\frac{\gamma}{h}\right)\left\|\tilde{\underline{v}}_{\mathrm{f},h}^{n+1}-\tilde{\underline{v}}_{\mathrm{s},h}^{n+\frac{1}{2}}\right\|_{\phi_0,\Gamma_{N\mathrm{nos}}}^2 \\ &+ C'_A(h+\Delta t)\left(\|\tilde{\underline{v}}_{\mathrm{f},h}^{n+1}\|_{\phi_0,\Omega} + \|\tilde{\underline{v}}_{\mathrm{s},h}^{n+\frac{1}{2}}\|_{1-\phi_0,\Omega} + \|\tilde{\underline{y}}_{\mathrm{s},h}^{n+\frac{1}{2}}\|_{\mathrm{skel}} + \|\tilde{p}_h^{n+1}\|_{(1-\phi_0)^2,\Omega}\right).\end{aligned}$$

Again, the assumption $\gamma > 2C_{ie}$ enables us to choose $L \in [2h/\gamma, h/C_{ie}]$ in order to have

$$\frac{\tilde{\mathcal{E}}^{n+1}-\tilde{\mathcal{E}}^n}{\Delta t} \leq C'_A(h+\Delta t)\left(\|\tilde{\underline{v}}_{\mathrm{f},h}^{n+1}\|_{\phi_0,\Omega} + \|\tilde{\underline{v}}_{\mathrm{s},h}^{n+\frac{1}{2}}\|_{1-\phi_0,\Omega} + \|\tilde{\underline{y}}_{\mathrm{s},h}^{n+\frac{1}{2}}\|_{\mathrm{skel}} + \|\tilde{p}_h^{n+1}\|_{(1-\phi_0)^2,\Omega}\right),$$

or, with the triangular inequality,

$$\tilde{\mathcal{E}}^{i+1} - \tilde{\mathcal{E}}^i \leq C'_A\Delta t(h+\Delta t)\left(\sqrt{\tilde{\mathcal{E}}^{i+1}} + \sqrt{\tilde{\mathcal{E}}^i}\right),$$

i.e.

$$\sqrt{\tilde{\mathcal{E}}^{i+1}} - \sqrt{\tilde{\mathcal{E}}^i} \leq C'_A\Delta t(h+\Delta t).$$

We sum those inequalities for i from 1 to $n+1$ to obtain

$$\sqrt{\tilde{\mathcal{E}}^{n+1}} \leq C'_A(n+1)\Delta t(h+\Delta t) + \sqrt{\tilde{\mathcal{E}}^0}.$$

This gives a L^2 convergence of $\tilde{\underline{v}}_{\mathrm{f},h}$, $\tilde{\underline{v}}_{\mathrm{s},h}$ and $\tilde{p}_h$ and a H^1 convergence of $\tilde{\underline{y}}_{\mathrm{s},h}$, in $(h,\Delta t)$, i.e.

$$\|X_h^n - (PX)^n\|_{\mathcal{E}} \leq C_A(h+\Delta t), \tag{4.34}$$

with C_A dependent only on $\|\partial_t^2 X\|_{L^\infty[0,T,\mathcal{E}]}$ and $\|\partial_t X\|_{L^\infty[0,T,V^+]}$. In addition, by definition of $(PX)^n$, and thanks to the continuity of P and the $\mathcal{C}^1$ nature of X, we have

$$\|(PX)^n - PX(t^n)\|_{\mathcal{E}} \leq C'\Delta t\|\partial_t X\|_{L^\infty[0,T,\mathcal{E}]}. \tag{4.35}$$

The triangular inequality and Lemma 6 conclude the argument:

$$\begin{aligned}\|X_h^n - X(t^n)\|_{\mathcal{E}} &\leq \|X_h^n - (PX)^n\|_{\mathcal{E}} + \|(PX)^n - PX(t^n)\|_{\mathcal{E}} + \|PX(t^n) - X(t^n)\|_{\mathcal{E}} \\ &\leq C_A(h+\Delta t) + C'\Delta t\|\partial_t X\|_{L^\infty[0,T,\mathcal{E}]} + Ch\|X\|_{L^\infty[0,T,V^+]}.\end{aligned}$$

■

Remark 11

The order of the time convergence is only 1 because of the specific choices we made on Section 4.3.1 – namely a first-order backward Euler in the fluid and midpoint scheme for the solid –, that aims at keeping a time scheme as close as possible to the splitting scheme of Chapter 3. Naturally, avoiding the shifting between fluid and solid discretizations (choosing for example a Crank–Nicolson method (Le Tallec and Hauret, 2002) for fluid) would give us a convergence in Δt^2.

4.4 Spatial convergence - numerical illustrations

In this section, we present various numerical results to illustrate the relevance of the above study and of Proposition 5 that ensures the total convergence of the numerical scheme (4.12) when conditions (4.17), (4.18), (4.19) and (4.20) are satisfied.

Remark 12 (Solid discretization and the condition (4.18))
We see in the proof of Proposition 4, and in the construction of X_4, that pressure is stabilized by $\underline{v}_{\rm f}$, therefore the inf-sup condition (4.17) plays a prominent role. In Section 4.4, solid velocity and displacement are in the same finite element space, and both the discrete unknowns for fluid pressure and solid velocity and displacement are in P_1. Despite the violation of (4.18), the numerical instabilities that we will observe when $W_h^{\rm f} \times W_h^{\rm s} \times Q_h$ is in $P_1 \times P_1 \times P_1$ will disappear in $P_1^b \times P_1 \times P_1$. Of course, attempts to bring stabilisation through the solid, in $P_1 \times P_1^b \times P_1$, were unsuccessful. In any case, the condition (4.19) is satisfied. This leads to the conclusion that when (4.19) and (4.20) are satisfied, (4.17) might be sufficient, and (4.18) not necessary.

The inf-sup condition (4.17) can be hard to impose in the numerical resolution, as it requires a non natural variable for the discretization of the fluid velocity. Therefore, it is natural to try to relax (4.17) into (4.21) and to study to what extent this simplification affects the numerical stability.

We propose here different situations to illustrate how numerical perturbations appear, and what is the relative importance of conditions (4.17), and (4.21).

First of all, let us notice that, compared with a classical Stokes mixed formulation, $\kappa_{\rm s}$ and the dynamical term in $\partial_t p$ adds a diagonal term on the mixed formulation matrix and therefore brings stability. For that reason, it is natural to look for numerical instabilities when this dynamical term is neutralised, that is, when $\kappa_{\rm s}$ grows and the solid constituent approaches incompressibility.

In Section 4.4.1, we illustrate the importance of (4.17) when ϕ_0 is spatially constant. In Section 4.4.2, we study the effect of spatial variations of ϕ_0 on spatial convergence of the scheme, for different discretization methods, and perform a numerical study of the relevance of (4.17) compared to (4.21). In Section 4.4.3, we extend our study to check that our conclusions remain relevant in the non-linear framework of Chapter 3.

We consider a linearization of the 2D swelling test case (Section 4.2 in Chapter 3) with a prescribed fluid velocity, presented in Figure 4.1, with parameters given in Table 4.1, and for $\Psi^{\rm skel}$ a Saint-Venant-Kirchhoff strain energy density of parameter $\lambda = \kappa - \frac{4(\kappa_1+\kappa_2)}{3}$ and $\mu = 2(\kappa_1 + \kappa_2)$.

Parameter	$\lvert\Omega\rvert$	Δt	γ	κ, κ_1	κ_2	$\rho_{\rm s}, \rho_{\rm f}$	μ	ϕ_0	$\underline{\underline{D}}_{\rm f}$	$\max(\underline{v}_{\rm f}^{\rm pr})$
Section 4.4.1	10^{-4}	10^{-3}	$2\,10^4, 2\,10^5$	$2\,10^3$	33	10^3	0.035	0.1	$10^7 \underline{\underline{I}}$	10^{-4}
Section 4.4.2	10^{-4}	10^{-3}	$2\,10^4, 2\,10^6$	$2\,10^3$	33	10^3	0.035	$\phi_0^{\rm nc}$	$10^7 \underline{\underline{I}}$	10^{-3}
Section 4.4.3	10^{-4}	10^{-3}	200	$2\,10^3$	33	10^3	0.035	0.1	$10^7 \underline{\underline{I}}$	0.05

Table 4.1 – **Parameter table.** All units are SI.

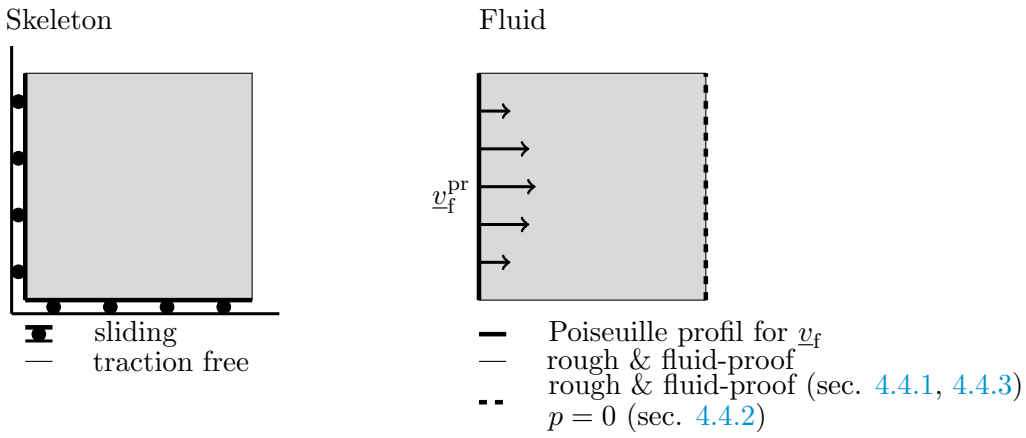

Figure 4.1 – Swelling test boundary conditions

4.4.1 Inf-sup compatible finite element spaces for fluid pressure and velocity

First, we assume that ϕ_0 is constant in space. Therefore, the inf-sup condition (4.17) reduces to the classical condition (4.21), widely studied in the context of the resolution of Stokes problems. It is well known that (4.21) is satisfied for example when $W_h^{\mathrm{f}} \times Q_h$ is in $P_1^b \times P_1$, but is violated in $P_1 \times P_1$.

The spatial step-length h will vary from 1/800 to 1/6400 and a reference configuration is obtained with $h = 1/7200$, 5 quadrature points are used, and κ_{s} will take the values $2e2$, $2e4$ and $2e8$. . The test case here is as follows (see Figure 4.1):

- $\underline{v}_{\mathrm{s}} \cdot \underline{n} = 0$ on the bottom and left faces
- Horizontal fluid velocity is imposed with a Poiseuille profil of amplitude 10^{-4} on the left face
- $\underline{v}_{\mathrm{s}} = \underline{v}_{\mathrm{f}}$ on the bottom, top and right faces.

Figure 4.3 illustrates the pressure instabilities that appear for a non inf-sup-compatible couple of finite element spaces.

We notice that these instabilities grow with γ. For smaller γ, they also appear, but disturb less the actual solution, and in that case the interface condition cannot be imposed with as much precision (see Figure 4.4).

Pressure perturbation is also more important when internal fluid-solid friction decreases because friction brings stability, or when the regularity of the solution of the problem decreases. More generally, for $\underline{v}_{\mathrm{f}}$ P_1, they often appear, their amplitude depends on the regularity of the actual solution, on the friction and on γ, and under certain circumstances, the perturbation they introduce may override the actual solution. The conclusion of this section is that choosing $\underline{v}_{\mathrm{f}}$ in P_1^b definitely brings more robustness and stability.

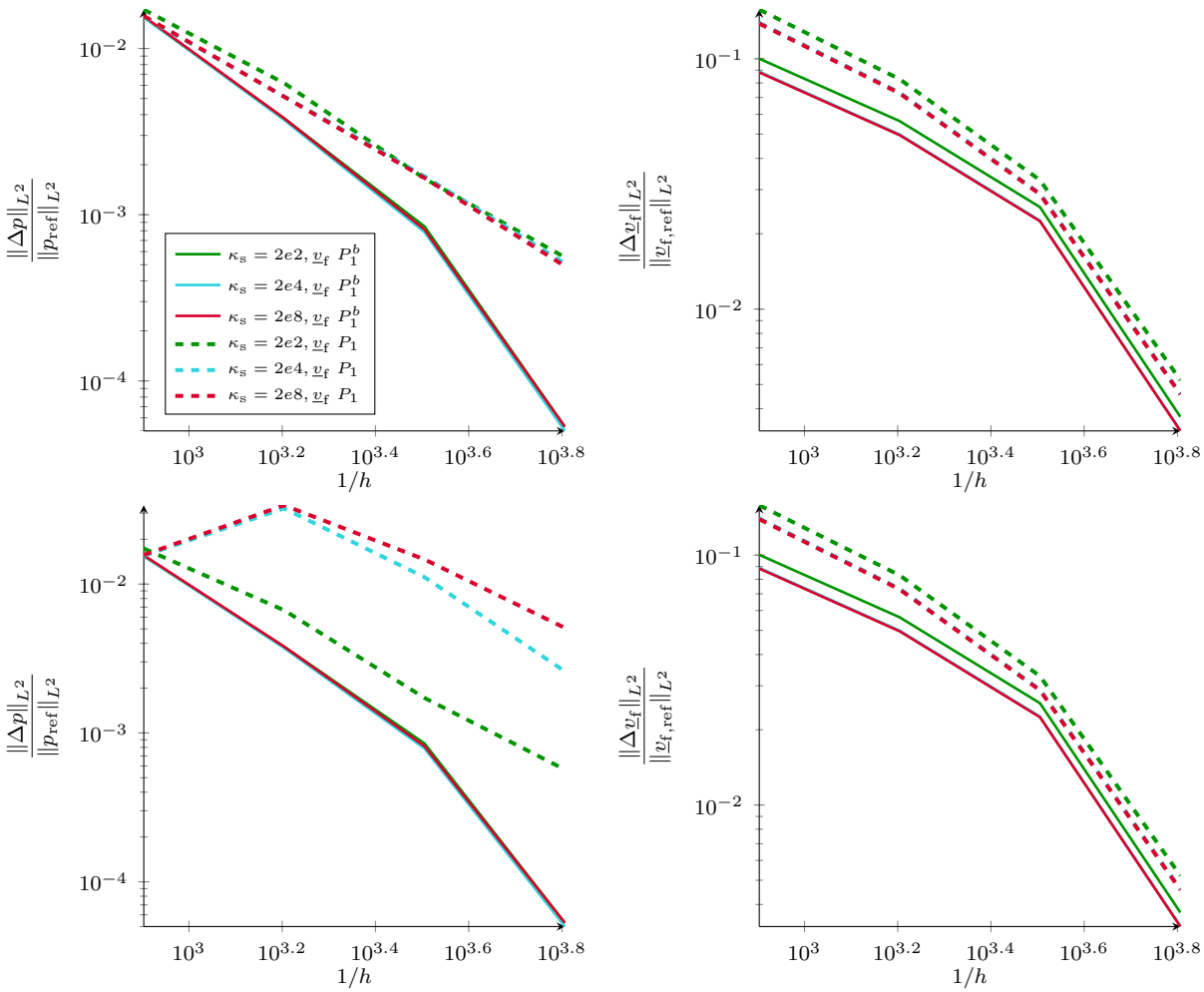

Figure 4.2 – **Spatial convergence graph, relevance of inf-sup compatible finite element spaces.** On the top, $\gamma = 2e4$, on the bottom, $\gamma = 2e5$. We compare the L^2 convergence of p and $\underline{v}_{\text{f}}$ for two finite element spaces choices for $\underline{v}_{\text{f}}$, and for increasing κ_{s}, at $t = 2$. Here, ϕ_0 is chosen constant in space. For higher values of κ_{s}, P_1^b discretization of $\underline{v}_{\text{f}}$, p converges in L^2 better than P_1.

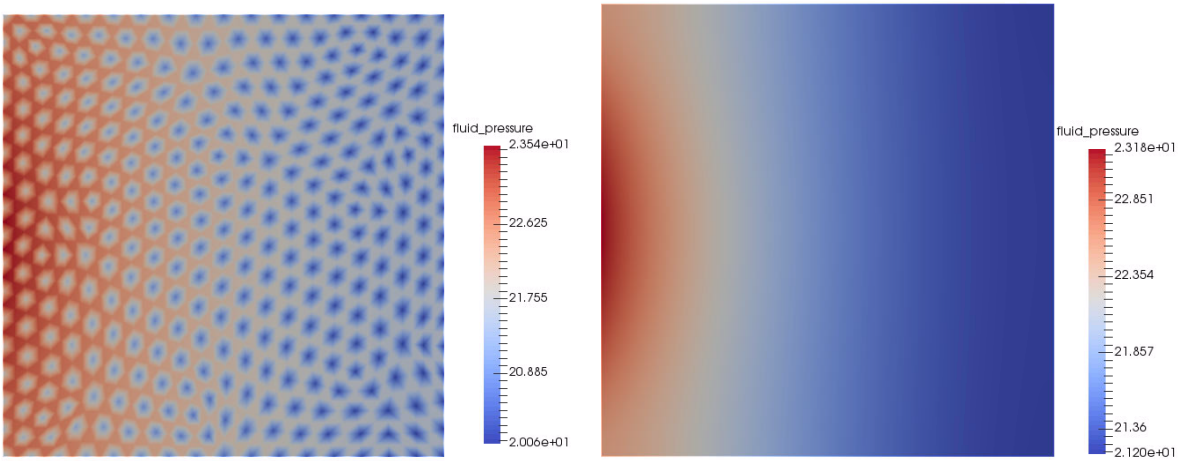

Figure 4.3 – **Pressure profil.** $\underline{v}_{\text{f}}$ is P_1 on the left and P_1^b on the right. Here, $1/h = 3200$, $\kappa_{\text{s}} = 2e8$ and $\gamma = 2e5$, pressure is disturbed when $W_h^{\text{f}} \times Q_h$ isn't inf-sup compatible.

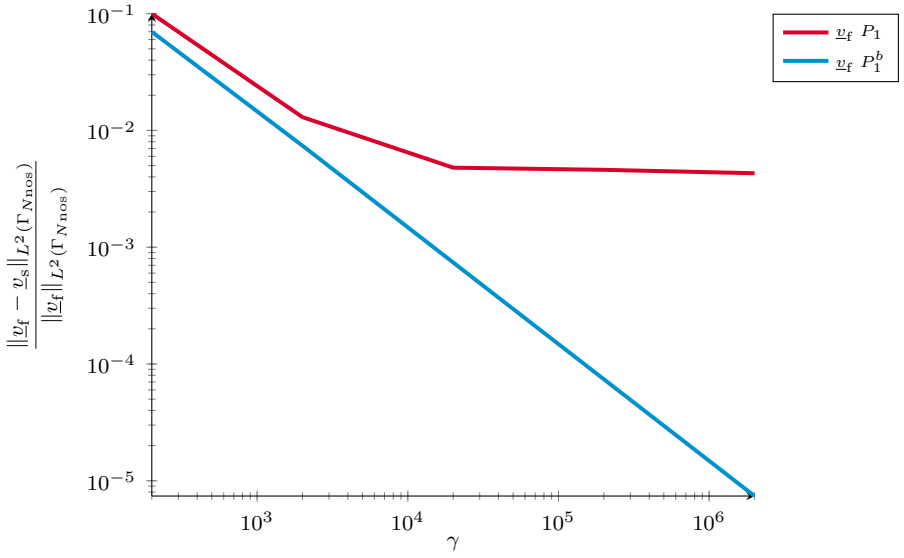

Figure 4.4 – γ **and the condition on** $\Gamma_{N\mathbf{nos}}$**.** When $W_h^\mathrm{f} \times Q_h$ isn't inf-sup compatible, the boundary condition $\underline{v}_\mathrm{f} = \underline{v}_\mathrm{s}$ on $\Gamma_{N\mathrm{nos}}$ cannot be imposed as precisely as when (4.21) is satisfied.

,

4.4.2 Discretization of a non-spatially-uniform ϕ

Then, we consider a non-spatially-uniform ϕ_0,

$$\phi_0 = \phi_0^{\mathrm{nc}}(x,y) = 0.5 + 0.4 \sin\left(\frac{10\pi x}{L}\right) \sin\left(\frac{10\pi \mathrm{y}}{L}\right),$$

and illustrate in Figure 4.5 the relevance of solving the fluid mixed problem with unknowns $(\underline{w}_\mathrm{f} = \phi_0 \underline{v}_\mathrm{f}, p)$ in $W_h^\mathrm{f} \times Q_h$, instead of $(\underline{v}_\mathrm{f}, p)$. We consider the same test as before, but with a Poiseuille amplitude of 10^{-3} on the left side and $p = 0$ on the right side ; for $\kappa_\mathrm{s} = 2e4$ (results are similar for $2e8$), with 5 quadrature points -which is common- and for $\gamma = 2e4$ (results are similar for $2e6$). We compare the spatial convergence curves of the following finite element choices:

- Choice 1: according to the above study, and in order to satisfy (4.17), unknowns are $(\underline{w}_\mathrm{f} = \phi \underline{v}_\mathrm{f}, p)$ in $P_1^b \times P_1$. Then, we get $\underline{v}_\mathrm{f}$ as a H^1 projection of $(\phi \underline{v}_\mathrm{f})/\phi$
- Choice 2: unknowns are $(\underline{v}_\mathrm{f}, p)$ in $P_1^b \times P_1$, and ϕ is calculated at the integration points
- Choice 3: unknowns are $(\underline{v}_\mathrm{f}, p)$ in $P_1^b \times P_1$, and ϕ is interpolated into P_1.

In the second and third methods, (4.17) is violated but (4.21) is satisfied. We see in Figure 4.5 that even if (4.17) gives better spatial convergences for fluid pressure and velocities, satisfying the relaxed conditions (4.21) gives converging algorithms and good numerical results. It's interesting to know as (4.17) is in most cases (especially in a non linear framework) much harder to impose at the discrete level than (4.21), as it requires to choose $\underline{w} = \phi \underline{v}_\mathrm{f}$ –as proposed in (Berger et al., 1999) – as discrete unknown for the fluid velocity, which is not as natural as $\underline{v}_\mathrm{f}$.

4.4.3 Extension to a non-linear framework

In this last section, we illustrate the relevance of this study for choosing adequate spatial discretization in a non linear framework. We perform simulation on the test case of Section 4.4.1,

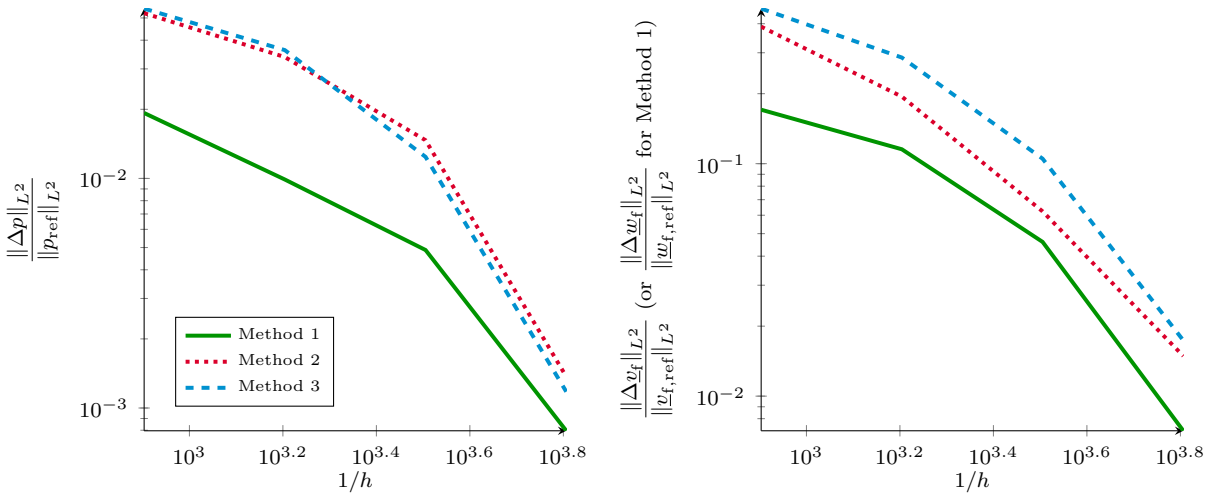

Figure 4.5 – **Spatial convergence graph, relevance of** (4.17) **vs** (4.21)**.** We compare the L^2 convergence of p and $\underline{v}_{\text{f}}$ (or $\underline{w}_{\text{f}}$ for Method 1), for Methods 1, 2 and 3, for $\kappa_{\text{s}} = 2e4$, at $t = 2$. All method are effective, but the first gives a better spatial convergence than the 2 others. In other words, ensuring (4.21) gives good results, (4.17) is even better. Each method is compared to its own reference solution (gotten with $1/h = 7200$).

using a splitting time scheme in the Arbitrary Lagrangian-Eulerian formalism. We consider a Saint-Venant-Kirchhoff law for the solid, and the free energy considered in the Section 4 of Chapter 3, with $\kappa_{\text{s}} = 2e5$, $1/h = 1600$, and parameters of Table 4.1. We compare the pressure that we obtained when discretizing $\underline{v}_{\text{f}}$ in P_1 and in P_1^b.

In order to satisfy (4.17), our discrete variables in the implicit fluid projection substep should be $(\phi \underline{v}_{\text{f}}, p, m)$. Nevertheless, the H^1 projection that enables us to go back from $(\phi \underline{v}_{\text{f}})$ to $\underline{v}_{\text{f}}$ (necessary for the explicit step) needs to reach ϕ at the integration points. The fluid portion ϕ varies in time and space, and its definition calls function that are defined on different meshes. Simulations are performed with FreeFem++ (Hecht, 2012), that present many advantages, but doesn't allow such manipulations. In the light of the relatively good results of the third method of Section 4.4.2, it is legitimate to relax (4.17) into (4.21), which is much easier to verify in the implementation. We illustrate in Figure 4.6 that the condition (4.21) is sufficient to prevent pressure perturbations.

4.5 Conclusion

To conclude, we began this chapter with deriving a linear problem (4.5) close to the poromechanical formulation (1.3). In this context, at the discrete level, a monolithic solver directly computes X_h^{n+1} in function of X_h^n. This simplified framework enabled us to establish conditions under which the convergence of our numerical scheme in $(h, \Delta t)$ is ensured, see conditions (4.17), (4.18), (4.19) and (4.20), and Proposition 5. Nevertheless, satisfying all of these criteria at the discrete level is generally very tedious. Therefore, we performed different numerical tests to illustrate the relative importance of these conditions. We verified that (4.18) is in practise not mandatory, and that (4.17) can be relaxed into (4.21) without affecting too much the stability properties. Therefore, we propose to choose discrete variables $(\underline{v}_{\text{f}}, \underline{v}_{\text{s}}, \underline{y}_{\text{s}}, p)$ in $P_1^b \times P_1 \times P_1 \times P_1$, as a good compromise between implementation difficulties and stability properties.

This choice allows to envision an adequate choice of spatial discretization for the non-linear case as revealed by our numerical tests. This paves the way for further implementation of the

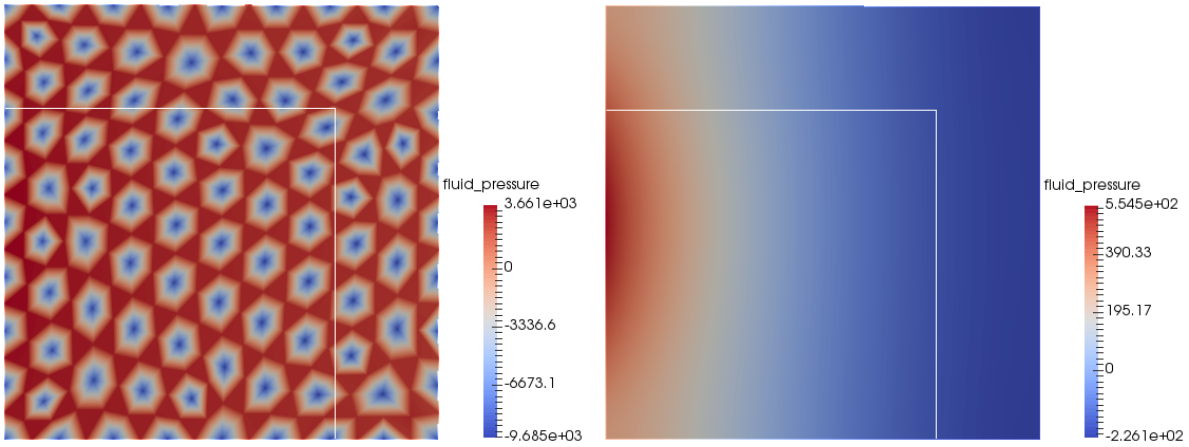

Figure 4.6 – **Pressure profil in non-linear, at $t = 1$, on the deformed configuration. In white is the reference configuration.** $\underline{v}_{\mathrm{f}}$ is P_1 on the left and P_1^b on the right. Pressure is disturbed when finite element spaces for $W_h^{\mathrm{f}} \times Q_h$ isn't inf-sup compatible, and satisfying (4.21) is enough to bring stability.

complete non-linear 3D poromechanical model of Chapter 3. We mention that 3D simulations of pressure wave propagation through porous cylinder were recently obtained in (Vuong et al., 2016).

Chapitre 5

Conclusions et perspectives

Plus de la moitié des pathologies cardiovasculaires sont la conséquence de troubles de la circulation dans le réseau de coronaires. Dans un contexte où de nombreux outils de modélisation cardiaque avaient été développés, cette thèse est née de la volonté de l'équipe MΞDISIM de faire un pas supplémentaire vers la prise en compte de la perfusion du tissu cardiaque par le réseau coronarien, jusqu'à présent généralement absente dans les modèles. Compte tenu de la finesse du réseau de capillaire en bout de chaîne, et des objectifs de modélisation, le myocarde perfusé peut être assimilé à un milieu poreux. Cela avait motivé l'élaboration d'une formulation de poromécanique générale, adaptée au contexte cardiaque (Chapelle and Moireau, 2014). Nous avons donc proposé dans cette thèse des outils mathématiques et numériques pour discrétiser cette formulation de poromécanique dans le but de l'intégrer aux modèles de coeur. Ce dernier chapitre présente les conclusions que l'on peut tirer de ces travaux, ainsi que les perspectives que l'on imagine pour leur faire suite. Il est organisé en fonction des trois chapitres de la thèse.

Chapitre 2

Conclusions

Nous avons commencé par rappeler les différents éléments des modèles cardiaques existants (Chapelle et al., 2012), en remplaçant le myocarde hyperélastique par un compartiment poreux (Chapelle and Moireau, 2014), pour prendre en compte sa perfusion par un réseau de coronaires s'intégrant au modèle de circulation sanguine au niveau de l'aorte. Cela nous permet d'introduire formellement un modèle 3D de coeur perfusé. S'inspirant de (Caruel et al., 2014), nous proposons ensuite une réduction dimensionnelle de modèle pour simuler en 0D un ventricule sphérique perfusé. Nous proposons une discrétisation temporelle de la formulation de poromécanique réduite compatible avec un bilan énergétique. Utilisant la librairie Matlab locale CardiacLab et après calibration, ce schéma nous permet de simuler des cycles cardiaques avec perfusion en 0D pour un coût de calcul très faible. Cette amélioration du modèle nous permet de modéliser la perfusion (pression et masse sanguine), jusqu'à présent inobservable dans les modèles, et de retrouver notamment le phénomène de flow impediment connu des physiologistes. C'est une étape majeure vers la modélisation des maladies coronariennes. Nous terminons par illustrer la pertinence de notre modèles dans un cadre d'applications cliniques, en reproduisant le mécanisme de vasodilatation et en étudiant des cas de sténoses.

Remarques et Perspectives

- Les temps de simulations restent élevés (une heure) car une quarantaine de cycles sont nécessaires avant d'atteindre un régime périodique. Cela est dû à l'état initial, trop loin

du cycle ciblé, qui n'est probablement pas calculé de manière optimale. Des progrès sur sa détermination permettraient facilement de réduire drastiquement les temps de calculs (un cycle prend de l'ordre d'une minute).

- De nombreuses applications cliniques sont envisagées, afin de modéliser toujours plus finement les maladies micro et macro-vasculaires coronariennes. Un enjeu demeure dans le couplage de ce modèles aux signaux accessibles sur des patients spécifiques, par acquisitions de données.
- Parmi les pistes d'améliorations du modèle on peut citer une meilleure modélisation de la circulation, notamment au niveau de l'aorte et le couplage de deux ventricule sphériques 0D pour un coeur complet.
- Ce modèle peut servir à la calibration de modèles plus complexes. L'enjeu est crucial en terme d'efficacité de calcul. Sa facilité de mise en oeuvre et son efficacité permettent également d'envisager de l'embarquer sur des systèmes de type smartphone, afin de le coupler à des capteurs et de l'acquisition de données, pour faire du suivi de patient.

Chapitre 3

Conclusions

Nous inspirant des méthodes développées en IFS, nous avons proposé pour la formulation de poromécanique un schéma en temps semi-implicite basé sur un couplage de Robin. La difficulté majeure ayant été le traitement de la fraction volumique fluide ϕ qui intervient dans tous les termes, et de sa dynamique. Nous avons établis un bilan d'énergie discret en grands déplacements et grandes déformations, garantissant la stabilité énergétique inconditionnelle du schéma. Grâce à un premier algorithme, implémenté en FreeFem++ (Hecht, 2012), basé sur ce schéma et ne se souciant pas des problématiques liées à la discrétisation spatiale, nous avons reproduit avec succès des simulations de gonflement et de drainage d'un milieu poreux carré en deux dimensions. Nous avons également obtenu une illustration numérique du bilan énergétique théorique obtenu.

Remarques et perspectives

- Il est important de souligner qu'en IFS, la raison d'être du couplage de Robin est d'introduire à l'interface fluide-structure une dissipation suffisante pour obtenir la stabilité énergétique théorique du schéma, indépendamment du ratio des masses volumiques fluide et solide, et sans avoir à considérer une discrétisation solide dissipative. Cependant, malgré l'absence de résultat de stabilité sous de telles hypothèses, le schéma de projection semi-implicite dont il est issu étant plus opérationnel (le couplage est imposé en dur), il est en pratique largement plus utilisé et a démontré d'excellentes propriétés numériques dans de nombreux cas. Dans notre cas, il est intéressant de souligner qu'un algorithme avec couplage en dur à l'interface (sans Robin), nous a également permis de reproduire exactement toutes les simulations de ce chapitre. Nous avons donc de bonnes raisons de penser que cette simplification, qui facilite considérablement la mise en oeuvre du schéma, ne menacera pas trop ses performances numériques. C'est d'ailleurs une simplification que nous avons commencé à utiliser lors de l'intégration de ce modèle de poromécanique à l'environnement HappyHeart.
- Notons que dans la Section 4, les erreurs de consistance introduites sont la conséquence de l'usage de FreeFem++ en particulier, mais que dans un code élément finis plus complet, la définition de ϕ aux points d'intégration ne représente aucune difficulté.

- D'après la Remarque 6, la transposition de notre analyse permet d'obtenir la stabilité énergétique inconditionnelle du schéma pour un problème d'IFS en formalisme ALE, en grands déplacements et grandes déformations. Notons alors que la conservation de la masse fluide doit être remplacée par une loi de conservation géométrique pour obtenir le résultat.

- Toujours en IFS, l'équation fluide de l'étape implicite peut être traité comme un problème de Poisson pour la pression, ce qui apporte un effet stabilisateur intéressant. Bien que cela semble difficile en gérant la dynamique de la masse fluide, il serait pertinent de voir si cela est transposable à notre contexte, pour simplifier l'algorithme.

- Conformément à la Remarque 5, l'inconvénient majeur du couplage de Robin est qu'il est consistent en $\gamma\Delta t/h$, ce qui impose typiquement de choisir Δt en $O(h^2)$. Des pistes sont à explorer pour améliorer cela : par extrapolation et correction, ou bien par une méthode Nitsche non-symétrique sans pénalisation (Burman and Fernández, 2014).

Chapitre 4

Conclusions

Nous avons linéarisé la formulation de poromécanique aux niveaux continu et discret, et avons établi un résultat garantissant dans ce cadre la convergence totale, sous conditions, de la solution discrète vers la solution continu. Cela nous a permis de mettre en évidence les rôles de l'incompressibilité solide et de la discrétisation spatiale dans l'apparition de perturbations numériques, que nous avons illustrés avec FreeFem++ (Hecht, 2012). Une étude de convergence spatiale nous a ensuite permis de déterminer un algorithme de discrétisation spatiale facile à mettre en oeuvre et gardant de bons résultats numériques lorsque le solide est incompressible. Enfin, un retour sur l'algorithme du Chapitre 3 accrédite dans un cadre non linéaire la méthode proposée.

Remarques et Perspectives

- De nouveau, la transcription au cadre non linéaire avec FreeFem++ ne permet pas de définir ϕ aux points d'intégration, ce qui oblige à l'interpoler dans $P1$. Cette limitation n'aura plus lieu d'être dès lors que l'algorithme sera implémenté dans un code éléments finis plus souple.

- Ce cadre linéaire serait propice à l'étude des questions d'existence et d'unicité de solutions pour le problème de poromécanique. Une source d'inspiration étant une fois de plus l'IFS : notamment (Du et al., 2003; Du et al., 2004) ; ou bien (Le Tallec and Mani, 2000) qui obtient ces résultats en linéaire grâce à des arguments de conservation d'énergie ; ou encore (Grandmont and Maday, 2000) (existence pour un fluide non linéaire et en ALE).

- Ces travaux, et les validations numériques des choix de discrétisation spatiale en configuration non-linéaire, ouvrent la voie vers l'implémentation du modèle complet de poromécanique non-linéaire du Chapitre 3. Notons que des simulations 3D de propagation d'onde de pression dans un cylindre poreux ont récemment été obtenues (Vuong et al., 2016).

Perspectives générales

Au delà des perspectives énoncées ci-dessus par chapitre, l'intégration d'un modèle de poromécanique pour modéliser le myocarde perfusé continue de présenter de nombreux défis. Par exemple, le couplage de ce flux poreux avec des modèles éventuellement multi-échelles représentant la circulation sanguine dans les artères et les veines coronariennes les plus larges posera la question d'où situer la frontière et de comment traiter les conditions de transmission (via le terme source volumique θ ou via les bords du modèle poreux). Encore, un effort reste à faire pour prendre en compte dans l'activité musculaire cardiaque l'indispensable approvisionnement en nutriments et en oxygène, via les coronaires. Enfin, afin de pouvoir mieux modéliser davantage de situations et de pathologies, les modèles doivent être validés, calibrés et couplés à des données cliniques.

Appendix A

Stability analysis of a Robin based semi-implicit coupling time scheme for non-linear fluid-structure interaction

As mentioned in this thesis, methods and results were first derived in a fluid-structure interaction (FSI) framework. This appendix presents what constituted a first step toward Chapter 3, that is a stability analysis of the Robin based semi-implicit time scheme (Astorino et al., 2009a) in a non-linear FSI framework. The scheme (Fernández et al., 2007) directly inspired (Astorino et al., 2009a). A stability and a convergence results of the first one were established (Fernández et al., 2007; Astorino and Grandmont, 2010) but only for a Leap-Frog time discretization scheme on the structure. The second introduces dissipation at the fluid-solid interface that allows the establishment of a stability result with a more natural conservative Newmark scheme on the structure (in a linear configuration in (Astorino et al., 2009a)), that will therefore remain valid for non-linear solid. In order to establish a stability result in non-linear and with a Newmark discretization, we propose here an adaptation of the Robin based version. Nevertheless, the first one is easier to implement, it is widely used and has shown very good numerical properties. Therefore, to facilitate the switching between both in analysis and implementation, we begin with permuting the explicit and implicit steps of the Robin based version to rewrite it in compliance with the explicit-implicit initial version.

A.1 Fluid-structure interaction strong formulation

Let us consider, for instance within a blood vessel, the coupling between a Navier-Stokes fluid on a domain Ω_f and a hyperelastic solid on Ω_s (see Figure A.1). They both interact on an interface $\Sigma = \Omega_\mathrm{f} \cap \Omega_\mathrm{s}$, where their velocity and stresses coincides. The solid is described in a Lagrangian frame by its displacement $\underline{y}_\mathrm{s} : \Omega_\mathrm{s} \times \mathbb{R}^+ \to \mathbb{R}^d$ ($d = 2,\ 3$), that governs the fluid domain displacements. The fluid is then represented in a ALE (Arbitrary Lagrangian Eulerian) formalism (see (Formaggia et al., 2010), Chapter 3): the current fluid domain $\Omega_\mathrm{f}(t) = \mathcal{A}(\Omega_\mathrm{f}, t)$ is given by the ALE mapping

$$\mathcal{A} = \mathcal{I}_{\Omega_\mathrm{f}} + \underline{y}_\mathrm{f}$$

where, in practise,

$$\underline{y}_\mathrm{f} = \mathrm{Ext}(\underline{y}_\mathrm{s}|_\Sigma) : \Omega_\mathrm{f} \times \mathbb{R}^+ \to \mathbb{R}^d$$

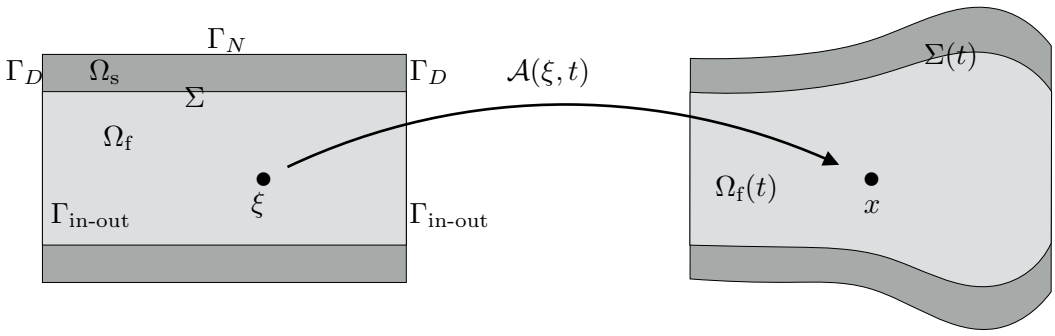

Figure A.1 – **Fluid-structure interaction modeling.** Blood wave propagation within a tube.

is the fluid domain displacement, with $\mathrm{Ext}(\cdot)$ a reasonable lifting operator from the reference interface Σ to the fluid reference domain Ω_f (e.g. a harmonic lifting). We denote by $\Sigma(t) = \partial\Omega_s(t) \cap \Omega_f(t)$ the current position of the fluid-solid interface, $\partial_t|_A$ the ALE time derivative, $\underline{\underline{\sigma}}_f(\underline{v}_f, p) = -p\underline{\underline{\mathbb{1}}} + 2\mu\underline{\underline{\varepsilon}}(\underline{v}_f)$ the fluid Cauchy stress tensor that derives from a Helmholtz free energy Ψ, μ the dynamic fluid viscosity, $\underline{\underline{\varepsilon}}(\underline{v}) = \frac{1}{2}(\underline{\nabla}\,\underline{v} + \underline{\nabla}\,\underline{v}^T)$ the linearised deformation tensor, $\underline{\underline{\Pi}}_s$ the first Piola-Kirchhoff solid stress tensor, $\underline{\underline{F}}^f = \underline{\nabla}\,\mathcal{A}$ the fluid domain deformation gradient, and $J^f = \det \underline{\underline{F}}^f$ the Jacobian; and finally respectively $\underline{n}_f$ and $\underline{n}_s$ the outgoing fluid and solid normals.

We denote $\partial\Omega_f = \Gamma_{in\text{-}out} \cup \Sigma$ and $\partial\Omega_s = \Gamma_D \cup \Gamma_N \cup \Sigma$ fluid and solid borders partitions (see Figure A.1), $\bar{p}$ a given pressure on $\Gamma_{in\text{-}out}$; ρ_f and ρ_s the fluid and solid densities,

The non-linear fluid-structure interaction problem considered writes as follow, (Astorino et al., 2009a): Find $\underline{v}_f : \Omega_f \times \mathbb{R}^+ \to \mathbb{R}^d$, the pressure $p : \Omega_f \times \mathbb{R}^+ \to \mathbb{R}$, the solid displacement $\underline{y}_s : \Omega_s \times \mathbb{R}^+ \to \mathbb{R}^d$ and the solid velocity $\underline{v}_s : \Omega_s \times \mathbb{R}^+ \to \mathbb{R}^d$ such that:

$$\left\{\begin{array}{rll} \rho_s \partial_t \underline{v}_s - \underline{\nabla} \cdot (\underline{\underline{\Pi}}_s(\underline{y}_s)) = \underline{f}, & \text{in} & \Omega_s, \\ \rho_f \partial_t \underline{v}_f|_{\mathcal{A}} + \rho_f \underline{\nabla} \cdot \big(\underline{v}_f \otimes (\underline{v}_f - \underline{w})\big) - \underline{\nabla} \cdot (\underline{\underline{\sigma}}_f(\underline{v}_f, p)) = 0, & \text{in} & \Omega_f(t), \\ \underline{\nabla} \cdot \underline{v}_f = 0, & \text{in} & \Omega_f(t), \end{array}\right. \tag{A.1}$$

With $\underline{v}_f(0) = \underline{v}_{f,0}$, $\underline{y}_s(0) = \underline{y}_{s,0}$, $\underline{v}_s(0) = \underline{v}_{s,0}$, and the following limit conditions

$$\left\{\begin{array}{rcll} \underline{y}_f & = & \mathrm{Ext}(\underline{y}_s|_\Sigma), \quad \underline{w} = \partial_t \underline{y}_f, & \text{in} \quad \Omega_f(t) = (I_{\Omega_f} + \underline{y}_f)(\Omega_f), \\ \partial_t \underline{y}_s & = & \underline{v}_s, & \text{in} \quad \Omega_s, \\ \underline{v}_f & = & \underline{v}_s, & \text{in} \quad \Sigma(t), \\ \underline{\underline{\Pi}}_s(\underline{y}_s)\underline{n}_s & = & -J^f \underline{\underline{\sigma}}_f(\underline{v}_f, p)(\underline{\underline{F}}^f)^{-T}\underline{n}_f, & \text{on} \quad \Sigma, \\ \underline{\underline{\sigma}}_f(\underline{v}_f, p)\underline{n}_f & = \underline{t} = & -\bar{p}\underline{n}_f, & \text{on} \quad \Gamma_{in\text{-}out}, \\ \underline{y}_s & = & \underline{y}_s^{pr}, & \text{on} \quad \Gamma_D, \\ \underline{\underline{\Pi}}_s(\underline{y}_s) & = & 0, & \text{on} \quad \Gamma_N. \end{array}\right. \tag{A.2}$$

We denote that a field defined on the fluid reference domain Ω_f is evaluated on the current domain $\Omega_f(t)$ by composing with $\mathcal{A}^{-1}(\cdot, t)$.

Remark 13 (FSI vs poromechanics strong form)
In order to enhance the similarities between these two problem, that motivated our approach, we propose here to write in red the terms of in the strong form of the poromechanical model (1.2) that are added to the non-linear FSI strong form in the ALE formalism (A.1) (where the

ALE velocity field $\underline{w}$ is replaced by the solid physical velocity $\underline{v}_{\rm s}$):

$$\left\{\begin{array}{rll}
\rho_{\rm s0}(1-\phi_0)\dfrac{{\rm d}\underline{v}_{\rm s}}{{\rm dt}} - \underline{\nabla}_{\underline{\xi}}\cdot(\underline{\underline{F}}\cdot\underline{\underline{\Sigma}}_s) + pJ\underline{\underline{F}}^{-T}\cdot\underline{\nabla}_{\underline{\xi}}\phi & & \\
\qquad -J\phi^2\underline{\underline{k}}_{\rm f}^{-1}\cdot(\underline{v}_{\rm f}-\underline{v}_{\rm s}) = \rho_{\rm s0}(1-\phi_0)\underline{f}, & \text{in } \Omega^0, & \text{(A.3a)} \\
\dfrac{1}{J}\dfrac{\rm d}{{\rm dt}}(\rho_{\rm f}J\phi\,\underline{v}_{\rm f}) + \underline{\nabla}_{\underline{x}}\cdot\big(\rho_{\rm f}\phi\,\underline{v}_{\rm f}\otimes\rho_{\rm f}(\underline{v}_{\rm f}-\underline{v}_{\rm s})\big) - \theta\underline{v}_{\rm f} & & \\
\qquad +\phi^2\underline{\underline{k}}_{\rm f}^{-1}\cdot(\underline{v}_{\rm f}-\underline{v}_{\rm s}) - \underline{\nabla}_{\underline{x}}\cdot(\phi\,\underline{\underline{\sigma}}_{\rm vis}) + \phi\underline{\nabla}_{\underline{x}}p = \rho_{\rm f}\phi\,\underline{f}, & \text{in } \Omega_t, & \text{(A.3b)} \\
\qquad \dfrac{1}{J}\dfrac{\rm d}{{\rm dt}}(J\rho_{\rm f}\phi) + \underline{\nabla}_{\underline{x}}\cdot\big(\rho_{\rm f}\phi(\underline{v}_{\rm f}-\underline{v}_{\rm s})\big) = \theta, & \text{in } \Omega_t. & \text{(A.3c)}
\end{array}\right.$$

A.2 Time-discrete partitioned coupling method

In the sequel we use the standard mid-point notation

$$g^{n+\frac{1}{2}} = \frac{g^n + g^{n+1}}{2},$$

except when otherwise specified for some specific variables that we then denote by $g^{n+\frac{1}{2}\sharp}$. For the solid part, we adopt a mid-point Newmark scheme given by

$$\begin{aligned}
\underline{y}_{\rm s}^{n+\frac{1}{2}} &= \frac{\underline{y}_{\rm s}^{n+1} + \underline{y}_{\rm s}^{n}}{2}, \\
\underline{v}_{\rm s}^{n+\frac{1}{2}} &= \frac{\underline{v}_{\rm s}^{n+1} + \underline{v}_{\rm s}^{n}}{2} = \frac{\underline{y}_{\rm s}^{n+1} - \underline{y}_{\rm s}^{n}}{\Delta t},
\end{aligned}$$

and

$$\underline{\underline{e}}^{n+\frac{1}{2}\sharp} = \underline{\underline{e}}(\underline{y}_{\rm s}^{n+\frac{1}{2}}), \quad \dot{\underline{\underline{e}}}^{n+\frac{1}{2}\sharp} = \frac{\underline{\underline{e}}^{n+1} - \underline{\underline{e}}^{n}}{\Delta t},$$

$$d_{\underline{y}}\underline{\underline{e}}^{n+\frac{1}{2}\sharp}\cdot\underline{v}^* = \frac{1}{2}\left(\underline{\underline{F}}(\underline{y}_{\rm s}^{n+\frac{1}{2}})^T\cdot\underline{\underline{\nabla}}_{\underline{\xi}}\underline{v}^* + \underline{\underline{\nabla}}_{\underline{\xi}}^T\underline{v}^*\cdot\underline{\underline{F}}(\underline{y}_{\rm s}^{n+\frac{1}{2}})\right),$$

Assuming a sufficiently regular mapping between the reference domain $\Omega_{\rm f}$ and the deformed configuration of time step n denoted by $\Omega_{\rm f}^n$, we define

$$\begin{aligned}
Q^n &= L^2(\Omega_{\rm f}^n), \\
V_{\rm f}^n &= H^1(\Omega_{\rm f}^n)^3, \\
V_{\rm s} &= H^1(\Omega_{\rm s})^3, \\
V_{\rm f}^n(\underline{\varphi}) &= \{\underline{v}^* \in V_{\rm f}^n \;\big|\; \underline{v}^*|_{\Sigma^n} = \underline{\varphi}|_{\Sigma^n}\}, \quad \forall\underline{\varphi} \in L^2(\Sigma^n)^3, \\
V_{\rm s}(\underline{\varphi}) &= \{\underline{v}^* \in V_{\rm s} \;\big|\; \underline{v}^*|_{\Gamma_D} = \underline{\varphi}|_{\Gamma_D}\}, \quad \forall\underline{\varphi} \in V_{\rm s}.
\end{aligned}$$

As in the continuous framework, we will use the same notation for functions defined in $\Omega_{\rm f}^0$ and $\Omega_{\rm f}^n$.

All the solution spaces considered here are implicitly assumed from now on to be discrete in space, typically using a finite element type strategy, but we do not dwell on space discretization in this paper. Nevertheless, we will denote by h the typical maximum diameter of all the finite elements in the mesh.

The partitioned method proposed in (Astorino et al., 2009a) writes as follow:

Given the solutions $(\underline{y}_{\rm s}^n, \underline{v}_{\rm s}^n)$ and $(\underline{v}_{\rm f}^n, p^n)$ up to time step n, perform the following steps:

- **Step 0.** Mesh update: $\Omega_{\mathrm{f}}^{n+1} = (I_{\Omega_{\mathrm{f}}^n} + \Delta t \underline{w}^{n+1})\Omega_{\mathrm{f}}^n$ with $\left\{ \begin{array}{r} \underline{w}^{n+1} = \mathrm{Ext}(\underline{v}_{\mathrm{s}}^n) \\ \underline{w}^{n+1}|_{\Gamma_{\text{in-out}}} = 0 \end{array} \right.$.

- **Step 1.** Explicit step: find $\underline{\tilde{v}}_{\mathrm{f}}^{n+1} \in V_{\mathrm{f}}^{n+1}$ such that $\forall \underline{\tilde{v}}_{\mathrm{f}}^* \in V_{\mathrm{f}}^{n+1}$

$$\begin{aligned} &\int_{\Omega_{\mathrm{f}}^{n+1}} \frac{\rho_{\mathrm{f}}}{\Delta t} \underline{\tilde{v}}_{\mathrm{f}}^{n+1} \cdot \underline{\tilde{v}}_{\mathrm{f}}^* \, d\Omega - \int_{\Omega_{\mathrm{f}}^n} \frac{\rho_{\mathrm{f}}}{\Delta t} \underline{v}_{\mathrm{f}}^n \cdot \underline{\tilde{v}}_{\mathrm{f}}^* \, d\Omega \\ &\quad + \int_{\Omega_{\mathrm{f}}^{n+1}} \underline{\nabla}_{\underline{\mathrm{x}}} \cdot \left(\rho_{\mathrm{f}} \underline{\tilde{v}}_{\mathrm{f}}^{n+1} \otimes (\underline{v}_{\mathrm{f}}^n - \underline{w}^{n+1}) \right) \cdot \underline{\tilde{v}}_{\mathrm{f}}^* \, d\Omega + 2\mu \int_{\Omega_{\mathrm{f}}^{n+1}} \underline{\underline{\varepsilon}}(\underline{\tilde{v}}_{\mathrm{f}}^{n+1}) : \underline{\underline{\varepsilon}}(\underline{\tilde{v}}_{\mathrm{f}}^*) \, d\Omega \\ &\quad + \frac{\gamma\mu}{h} \int_{\Sigma^{n+1}} (\underline{\tilde{v}}_{\mathrm{f}}^{n+1} - \underline{v}_{\mathrm{s}}^{n-\frac{1}{2}}) \cdot \underline{\tilde{v}}_{\mathrm{f}}^* \, dS = 2\mu \int_{\Sigma^{n+1}} \underline{\underline{\varepsilon}}(\underline{\tilde{v}}_{\mathrm{f}}^{n+1}) \cdot \underline{n}_{\mathrm{f}} \cdot \underline{\tilde{v}}_{\mathrm{f}}^* \, dS. \end{aligned} \tag{A.4a}$$

- **Step 2.** Implicit step (implicit coupling of two substeps, fluid and solid)

  - **Step 2a.** Fluid projection substep
    Find $(\underline{v}_{\mathrm{f}}^{n+1}, p^{n+1}) \in V_{\mathrm{f}}^{n+1}(\underline{v}_{\mathrm{s}}^{n+\frac{1}{2}}) \times Q^{n+1}$ such that $\forall (\underline{v}_{\mathrm{f}}^*, p^*) \in V_{\mathrm{f}}^{n+1}(0) \times Q^{n+1}$

$$\begin{aligned} &\int_{\Omega_{\mathrm{f}}^{n+1}} \frac{\rho_{\mathrm{f}}}{\Delta t} (\underline{v}_{\mathrm{f}}^{n+1} - \underline{\tilde{v}}_{\mathrm{f}}^{n+1}) \cdot \underline{v}_{\mathrm{f}}^* \, d\Omega - \int_{\Omega_{\mathrm{f}}^{n+1}} p^{n+1} \underline{\nabla}_{\underline{\mathrm{x}}} \cdot \underline{v}_{\mathrm{f}}^* \, d\Omega \\ &\qquad + \int_{\Omega_{\mathrm{f}}^{n+1}} p^* \underline{\nabla}_{\underline{\mathrm{x}}} \cdot \underline{v}_{\mathrm{f}}^{n+1} \, d\Omega = \int_{\Gamma_{\text{in-out}}^{n+1}} \underline{t}^{n+1} \cdot \underline{v}_{\mathrm{f}}^* \, d\Omega \end{aligned} \tag{A.4b}$$

  - **Step 2b.** Solid step
    Find $(\underline{y}_{\mathrm{s}}^{n+1}, \underline{v}_{\mathrm{s}}^{n+1}) \in V_{\mathrm{s}}(\underline{y}_{\mathrm{s}}^{\mathrm{pr}}(t^{n+1})) \times V^0(0)$ such that $\forall \underline{v}_{\mathrm{s}}^* \in V_{\mathrm{s}}(0)$

$$\left\{ \begin{array}{l} \displaystyle\int_{\Omega_{\mathrm{s}}} \frac{\rho_{\mathrm{s}}}{\Delta t} (\underline{v}_{\mathrm{s}}^{n+1} - \underline{v}_{\mathrm{s}}^n) \cdot \underline{v}_{\mathrm{s}}^* \, d\Omega + \int_{\Omega_{\mathrm{s}}} \left(\frac{\partial \Psi}{\partial \underline{\underline{e}}} \Big|^{n+\frac{1}{2}\sharp} + \frac{\partial \Psi^{\mathrm{damp}}}{\partial \underline{\dot{\underline{e}}}} \Big|^{n+\frac{1}{2}\sharp} \right) : d_{\underline{y}} \underline{\underline{e}}^{n+\frac{1}{2}\sharp} \cdot \underline{v}_{\mathrm{s}}^* \, d\Omega \\ \qquad \displaystyle + \frac{\gamma\mu}{h} \int_{\Sigma^{n+1}} (\underline{v}_{\mathrm{s}}^{n+\frac{1}{2}} - \underline{v}_{\mathrm{s}}^{n-\frac{1}{2}}) \cdot \underline{v}_{\mathrm{s}}^* \, dS = \int_{\Omega_{\mathrm{s}}} \rho_{\mathrm{s}} \underline{f}^{n+1} \cdot \underline{v}_{\mathrm{s}}^* \, d\Omega - \mathcal{R}_{\mathrm{f}}(\mathcal{L}^{n+1}(\underline{v}_{\mathrm{s}}^*)) \\ \qquad \displaystyle \underline{v}_{\mathrm{s}}^{n+\frac{1}{2}} = \frac{\underline{y}_{\mathrm{s}}^{n+1} - \underline{y}_{\mathrm{s}}^n}{\Delta t} \quad \text{in} \quad \Omega_{\mathrm{s}} \end{array} \right. \tag{A.4c}$$

Here, the lifting operator $\mathcal{L}^{n+1}$ satisfies that, for any $\underline{v}_{\mathrm{s}}^*$ in V_{s}, $\mathcal{L}^{n+1}(\underline{v}_{\mathrm{s}}^*) = \left\{ \begin{array}{ccc} \underline{v}_{\mathrm{s}}^* & \text{on} & \Sigma^{n+1} \\ 0 & \text{on} & \Gamma_{\text{in-out}}^{n+1} \end{array} \right.$ is a function of V_{f}^{n+1}, $\mathcal{R}_{\mathrm{f}}$ denotes the fluid discrete residual, such that for any $\underline{v}^*$ in V_{f}^{n+1}

$$\begin{aligned} \mathcal{R}_{\mathrm{f}}(\underline{v}^*) = &\int_{\Omega_{\mathrm{f}}^{n+1}} \frac{\rho_{\mathrm{f}}}{\Delta t} \underline{v}_{\mathrm{f}}^{n+1} \cdot \underline{v}^* \, d\Omega - \int_{\Omega_{\mathrm{f}}^n} \frac{\rho_{\mathrm{f}}}{\Delta t} \underline{v}_{\mathrm{f}}^n \cdot \underline{v}^* \, d\Omega + \int_{\Omega_{\mathrm{f}}^{n+1}} \underline{\nabla}_{\underline{\mathrm{x}}} \cdot \left(\rho_{\mathrm{f}} \underline{\tilde{v}}_{\mathrm{f}}^{n+1} \otimes (\underline{v}_{\mathrm{f}}^n - \underline{w}^{n+1}) \right) \cdot \underline{v}^* \, d\Omega \\ &- \int_{\Omega_{\mathrm{f}}^{n+1}} p^{n+1} \underline{\nabla}_{\underline{\mathrm{x}}} \cdot \underline{v}^* \, d\Omega + 2\mu \int_{\Omega_{\mathrm{f}}^{n+1}} \underline{\underline{\varepsilon}}(\underline{\tilde{v}}_{\mathrm{f}}^{n+1}) : \underline{\underline{\varepsilon}}(\underline{v}^*) \, d\Omega - \int_{\Gamma_{\text{in-out}}^{n+1}} \underline{t}^{n+1} \cdot \underline{v}^* \, dS, \end{aligned}$$

and we make the following discretization choice for $\frac{\partial \Psi}{\partial \underline{\underline{e}}} \Big|^{n+\frac{1}{2}\sharp}$ (see (Gonzalez, 2000))

$$\frac{\partial \Psi}{\partial \underline{\underline{e}}} \Big|^{n+\frac{1}{2}\sharp} \hat{=} \frac{\partial \Psi}{\partial \underline{\underline{e}}} (\underline{\underline{e}}^{n+\frac{1}{2}\sharp}) + \left(\frac{\Psi(\underline{\underline{e}}^{n+1}) - \Psi(\underline{\underline{e}}^n)}{\Delta t} - \frac{\partial \Psi}{\partial \underline{\underline{e}}} (\underline{\underline{e}}^{n+\frac{1}{2}\sharp}) : \underline{\dot{\underline{e}}}^{n+\frac{1}{2}} \right) \frac{\underline{\dot{\underline{e}}}^{n+\frac{1}{2}}}{\underline{\dot{\underline{e}}}^{n+\frac{1}{2}} : \underline{\dot{\underline{e}}}^{n+\frac{1}{2}}}. \tag{A.5}$$

In the sequel, we will choose $\Psi^{\mathrm{damp}} = \frac{\eta_{\mathrm{d}}}{2} \mathrm{tr}(\underline{\dot{\underline{e}}})^2$, with the discretization

$$\int_{\Omega_{\mathrm{s}}} \frac{\partial \Psi^{\mathrm{damp}}}{\partial \underline{\dot{\underline{e}}}} \Big|^{n+\frac{1}{2}\sharp} : d_{\underline{y}} \underline{\underline{e}}^{n+\frac{1}{2}\sharp} \cdot \underline{v}_{\mathrm{s}}^* \, d\Omega = \int_{\Omega_{\mathrm{s}}} \eta_{\mathrm{d}} \, d_{\underline{y}} \underline{\underline{e}}^{n+\frac{1}{2}\sharp} \cdot \underline{v}_{\mathrm{s}}^{n+\frac{1}{2}} : d_{\underline{y}} \underline{\underline{e}}^{n+\frac{1}{2}\sharp} \cdot \underline{v}_{\mathrm{s}}^* \, d\Omega.$$

A.3 Stability analysis

Our objective in this section is to establish the stability of the above nonlinear scheme, namely, a discrete energy balance similar to the one established in a linear framework in (Astorino et al., 2009a). We will then naturally assume that there exists a solution $(\underline{y}_{\rm s}^n, \underline{v}_{\rm s}^n, \underline{v}_{\rm f}^n, p^n)$ to the discrete equations (A.4) up to time step n.

Lemma 7
There exists a constant C_{ie} such that

$$\|\underline{\underline{\varepsilon}}(\underline{v}^*)\cdot\underline{n}_{\rm f}\|^2_{L^2(\Sigma^{n+1})} \leq \frac{C_{ie}}{h}\|\underline{\underline{\varepsilon}}(\underline{v}^*)\|^2_{L^2(\Omega_{\rm f}^{n+1})}, \quad \forall \underline{v}^* \in H^1(\Omega_{\rm f}^n)^3. \tag{A.6}$$

This inverse inequality is obtained by a standard scaling argument when noting that

$$\|\,\underline{\underline{\varepsilon}}(\underline{v}^*)\cdot\underline{n}_{\rm f}\|^2_{L^2(\Sigma^{n+1})} = \|\underline{\underline{\varepsilon}}(\underline{v}^*)\cdot\underline{n}_{\rm f})^2\|_{L^1(\Sigma^{n+1}}.$$

For the sake of simplicity in the stability analysis, we will assume that $\underline{f}=\underline{0}$ and $\underline{y}_{\rm s}^{\rm pr}=\underline{0}$. We then have the following result.

Proposition 8
Assuming that we have a Geometric Conservation Law

$$\int_{\Omega_{\rm f}^{n+1}}\rho_{\rm f}p^*d\Omega - \int_{\Omega_{\rm f}^{n}}\rho_{\rm f}p^*d\Omega + \int_{\Omega_{\rm f}^{n+1}}p^*\underline{\nabla}\cdot(\rho_{\rm f}(\underline{v}_{\rm f}^n-\underline{w}^{n+1}))d\Omega = 0, \text{ with } p^* = \frac{1}{2}|\tilde{\underline{v}}_{\rm f}^{n+1}|^2, \tag{A.7}$$

and that

$$\gamma \geq C_{ie}, \tag{A.8}$$

then, the time scheme (A.4) satisfies

$$\begin{aligned}\frac{\mathcal{E}^{n+1}-\mathcal{E}^n}{\Delta t} + \frac{\gamma\mu}{2h}\|\underline{v}_{\rm s}^{n+\frac{1}{2}}\|^2_{\Sigma^{n+1}} - \frac{\gamma\mu}{2h}\|\underline{v}_{\rm s}^{n-\frac{1}{2}}\|^2_{\Sigma^{n+1}} \\ \leq (\underline{t}^{n+1},\underline{v}_{\rm f}^{n+1})_{\Gamma^{n+1}_{in\text{-}out}} - \int_{\Omega_{\rm s}}\frac{\partial\Psi^{damp}}{\partial\dot{\underline{\underline{e}}}}\Big|^{n+\frac{1}{2}\sharp} : d_{\underline{y}}\underline{\underline{e}}^{n+\frac{1}{2}\sharp}\cdot\underline{v}_{\rm s}^{n+\frac{1}{2}}\,d\Omega \\ - \mathcal{T}_1 - \frac{\rho_{\rm f}}{2\Delta t}\left\|\tilde{\underline{v}}_{\rm f}^{n+1}-\underline{v}_{\rm f}^n\right\|^2_{\Omega_{\rm f}^n} - \frac{\rho_{\rm f}}{2\Delta t}\left\|\underline{v}_{\rm f}^{n+1}-\tilde{\underline{v}}_{\rm f}^{n+1}\right\|^2_{\Omega_{\rm f}^{n+1}} \\ - C\mu\left\|\underline{\underline{\varepsilon}}(\tilde{\underline{v}}_{\rm f}^{n+1})\right\|^2_{\Omega_{\rm f}^{n+1}} - C\frac{\mu}{L}\|\tilde{\underline{v}}_{\rm f}^{n+1}-\underline{v}_{\rm s}^{n+\frac{1}{2}}\|^2_{\Sigma^{n+1}},\end{aligned} \tag{A.9}$$

with C a positive dimensionless constant, L homogeneous to a length, $\mathcal{E}^n$ the total discrete energy at step n, i.e.

$$\mathcal{E}^n = \mathcal{K}_{\rm f}^n + \mathcal{K}_{\rm s}^n + \mathcal{W}^n = \frac{\rho_{\rm f}}{2}\|\underline{v}_{\rm f}^n\|^2_{\Omega_{\rm f}^n} + \frac{\rho_{\rm s}}{2}\|\underline{v}_{\rm s}^n\|^2_{\Omega_{\rm s}} + \int_{\Omega_{\rm s}}\Psi(\underline{\underline{e}}^n)\,d\Omega,$$

and $\mathcal{T}_1$ the discrete flux of outgoing fluid kinetic energy that crosses the domain borders

$$\mathcal{T}_1 = \frac{1}{2}\int_{\Gamma^{n+1}_{in\text{-}out}}\rho_{\rm f}|\tilde{\underline{v}}_{\rm f}^{n+1}|^2\underline{v}_{\rm f}^n\cdot\underline{n}_{\rm f}\,dS.$$

Proof. Respectively evaluating the equations (A.4a), (A.4b) and (A.4c) with the test functions

$$\tilde{\underline{v}}_{\rm f}^* = \tilde{\underline{v}}_{\rm f}^{n+1}, \quad \underline{v}_{\rm f}^* = \underline{v}_{\rm f}^{n+1} - \mathcal{L}^{n+1}(\underline{v}_{\rm s}^{n+\frac{1}{2}}), \quad \text{and} \quad \underline{v}_{\rm s}^* = \underline{v}_{\rm s}^{n+\frac{1}{2}},$$

we get, defining

$$\mathcal{R}_p(\underline{v}^*) = \int_{\Omega_{\mathrm{f}}^{n+1}} \rho_{\mathrm{f}} \frac{\underline{v}_{\mathrm{f}}^{n+1} - \tilde{\underline{v}}_{\mathrm{f}}^{n+1}}{\Delta t} \cdot \underline{v}^* \, d\Omega - \int_{\Omega_{\mathrm{f}}^{n+1}} p^{n+1} \underline{\nabla}_{\underline{\mathrm{x}}} \cdot \underline{v}^* \, d\Omega - \int_{\Gamma_{\text{in-out}}^{n+1}} \underline{t}^{n+1} \cdot \underline{v}^* \, dS$$

and using the weighted L^2-scalar product notation $(g,h)_\Omega = \int_\Omega gh \, d\Omega$,

$$\begin{aligned}
&\frac{\rho_{\mathrm{f}}}{\Delta t} \left(\tilde{\underline{v}}_{\mathrm{f}}^{n+1}, \tilde{\underline{v}}_{\mathrm{f}}^{n+1}\right)_{\Omega_{\mathrm{f}}^{n+1}} - \frac{\rho_{\mathrm{f}}}{\Delta t} \left(\underline{v}_{\mathrm{f}}^{n}, \tilde{\underline{v}}_{\mathrm{f}}^{n+1}\right)_{\Omega_{\mathrm{f}}^{n}} \\
&\qquad + \int_{\Omega_{\mathrm{f}}^{n+1}} \underline{\nabla}_{\underline{\mathrm{x}}} \cdot \left(\rho_{\mathrm{f}} \tilde{\underline{v}}_{\mathrm{f}}^{n+1} \otimes (\underline{v}_{\mathrm{f}}^{n} - \underline{w}^{n+1})\right) \cdot \tilde{\underline{v}}_{\mathrm{f}}^{n+1} \, d\Omega + 2\mu \|\underline{\varepsilon}(\tilde{\underline{v}}_{\mathrm{f}}^{n+1})\|_{\Omega_{\mathrm{f}}^{n+1}} \\
&\qquad\qquad + \frac{\gamma\mu}{h} \left(\tilde{\underline{v}}_{\mathrm{f}}^{n+1} - \underline{v}_{\mathrm{s}}^{n-\frac{1}{2}}, \tilde{\underline{v}}_{\mathrm{f}}^{n+1}\right)_{\Sigma^{n+1}} = 2\mu \left(\underline{\varepsilon}(\tilde{\underline{v}}_{\mathrm{f}}^{n+1}) \cdot \underline{n}_{\mathrm{f}}, \tilde{\underline{v}}_{\mathrm{f}}^{n+1}\right)_{\Sigma^{n+1}}, \quad \text{(A.10a)}
\end{aligned}$$

$$\begin{aligned}
&\frac{\rho_{\mathrm{f}}}{\Delta t} \left(\underline{v}_{\mathrm{f}}^{n+1} - \tilde{\underline{v}}_{\mathrm{f}}^{n+1}, \underline{v}_{\mathrm{f}}^{n+1}\right)_{\Omega_{\mathrm{f}}^{n+1}} - \int_{\Omega_{\mathrm{f}}^{n+1}} p^{n+1} \underline{\nabla}_{\underline{\mathrm{x}}} \cdot \underline{v}_{\mathrm{f}}^{n+1} \, d\Omega + \int_{\Omega_{\mathrm{f}}^{n+1}} p^{n+1} \underline{\nabla}_{\underline{\mathrm{x}}} \cdot \underline{v}_{\mathrm{f}}^{n+1} \, d\Omega \\
&\qquad\qquad = \left(\underline{t}^{n+1}, \underline{v}_{\mathrm{f}}^{n+1}\right)_{\Gamma_{\text{in-out}}^{n+1}} + \mathcal{R}_p(\mathcal{L}^{n+1}(\underline{v}_{\mathrm{s}}^{n+\frac{1}{2}})), \quad \text{(A.10b)}
\end{aligned}$$

$$\begin{aligned}
&\frac{\rho_{\mathrm{s}}}{2\Delta t} \|\underline{v}_{\mathrm{s}}^{n+1}\|_{\Omega_{\mathrm{s}}}^2 - \frac{\rho_{\mathrm{s}}}{2\Delta t} \|\underline{v}_{\mathrm{s}}^{n}\|_{\Omega_{\mathrm{s}}}^2 + \int_{\Omega_{\mathrm{s}}} \left(\frac{\partial \Psi}{\partial \underline{\underline{e}}}\Big|^{n+\frac{1}{2}\sharp} + \frac{\partial \Psi^{\mathrm{damp}}}{\partial \dot{\underline{\underline{e}}}}\Big|^{n+\frac{1}{2}\sharp} \right) : d_{\underline{y}} \underline{\underline{e}}^{n+\frac{1}{2}\sharp} \cdot \underline{v}_{\mathrm{s}}^{n+\frac{1}{2}} \, d\Omega \\
&\qquad + \frac{\gamma\mu}{h} \left(\underline{v}_{\mathrm{s}}^{n+\frac{1}{2}} - \underline{v}_{\mathrm{s}}^{n-\frac{1}{2}}, \underline{v}_{\mathrm{s}}^{n+\frac{1}{2}}\right)_{\Sigma^{n+1}} = -\mathcal{R}_{\mathrm{f}}(\mathcal{L}^{n+1}(\underline{v}_{\mathrm{s}}^{n+\frac{1}{2}})). \quad \text{(A.10c)}
\end{aligned}$$

For the first two terms of (A.10a), we use $2(a,b) = a^2 + b^2 - (a-b)^2$ to obtain

$$\begin{aligned}
&\frac{\rho_{\mathrm{f}}}{\Delta t} \left(\tilde{\underline{v}}_{\mathrm{f}}^{n+1}, \tilde{\underline{v}}_{\mathrm{f}}^{n+1}\right)_{\Omega_{\mathrm{f}}^{n+1}} - \frac{\rho_{\mathrm{f}}}{\Delta t} \left(\underline{v}_{\mathrm{f}}^{n}, \tilde{\underline{v}}_{\mathrm{f}}^{n+1}\right)_{\Omega_{\mathrm{f}}^{n}} \\
&\qquad = \frac{\rho_{\mathrm{f}}}{\Delta t} \left(\|\tilde{\underline{v}}_{\mathrm{f}}^{n+1}\|_{\Omega_{\mathrm{f}}^{n+1}}^2 - \frac{1}{2}\|\tilde{\underline{v}}_{\mathrm{f}}^{n+1}\|_{\Omega_{\mathrm{f}}^{n}}^2 - \frac{1}{2}\|\underline{v}_{\mathrm{f}}^{n}\|_{\Omega_{\mathrm{f}}^{n}}^2 + \frac{1}{2}\|\tilde{\underline{v}}_{\mathrm{f}}^{n+1} - \underline{v}_{\mathrm{f}}^{n}\|_{\Omega_{\mathrm{f}}^{n}}^2 \right). \quad \text{(A.11)}
\end{aligned}$$

Then, the next term in (A.10a) can be rewritten as in the proof of (Chapelle and Moireau, 2014, Theorem 7)

$$\begin{aligned}
&\int_{\Omega_{\mathrm{f}}^{n+1}} \underline{\nabla}_{\underline{\mathrm{x}}} \cdot (\rho_{\mathrm{f}} \tilde{\underline{v}}_{\mathrm{f}}^{n+1} \otimes (\underline{v}_{\mathrm{f}}^{n} - \underline{w}^{n+1})) \cdot \tilde{\underline{v}}_{\mathrm{f}}^{n+1} \, d\Omega \\
&\qquad = \int_{\Omega_{\mathrm{f}}^{n+1}} \frac{1}{2} |\tilde{\underline{v}}_{\mathrm{f}}^{n+1}|^2 \underline{\nabla}_{\underline{\mathrm{x}}} \cdot (\rho_{\mathrm{f}} (\underline{v}_{\mathrm{f}}^{n} - \underline{w}^{n+1})) \, d\Omega + \mathcal{T}_1, \quad \text{(A.12)}
\end{aligned}$$

because $\underline{w}^{n+1}$ satisfies $\underline{w}^{n+1} = \underline{v}_{\mathrm{f}}^{n}$ on Σ^{n+1} and $\underline{w}^{n+1} = 0$ on $\Gamma_{\text{in-out}}^{n+1}$; and the use of (A.7) gives

$$\frac{1}{2} \int_{\Omega_{\mathrm{f}}^{n+1}} |\tilde{\underline{v}}_{\mathrm{f}}^{n+1}|^2 \underline{\nabla}_{\underline{\mathrm{x}}} \cdot (\rho_{\mathrm{f}} (\underline{v}_{\mathrm{f}}^{n} - \underline{w}^{n+1})) \, d\Omega = -\frac{\rho_{\mathrm{f}}}{2\Delta t} \left(\|\tilde{\underline{v}}_{\mathrm{f}}^{n+1}\|_{\Omega_{\mathrm{f}}^{n+1}}^2 - \|\tilde{\underline{v}}_{\mathrm{f}}^{n+1}\|_{\Omega_{\mathrm{f}}^{n}}^2 \right). \quad \text{(A.13)}$$

Gathering (A.11), (A.12) and (A.13), we get

$$\begin{aligned}
&\frac{\rho_{\mathrm{f}}}{\Delta t} \left(\tilde{\underline{v}}_{\mathrm{f}}^{n+1}, \tilde{\underline{v}}_{\mathrm{f}}^{n+1}\right)_{\Omega_{\mathrm{f}}^{n+1}} - \frac{\rho_{\mathrm{f}}}{\Delta t} \left(\underline{v}_{\mathrm{f}}^{n} \cdot \tilde{\underline{v}}_{\mathrm{f}}^{n+1}\right)_{\Omega_{\mathrm{f}}^{n}} + \int_{\Omega_{\mathrm{f}}^{n+1}} \underline{\nabla}_{\underline{\mathrm{x}}} \cdot \left(\rho_{\mathrm{f}} \tilde{\underline{v}}_{\mathrm{f}}^{n+1} \otimes (\underline{v}_{\mathrm{f}}^{n} - \underline{w}^{n+1})\right) \cdot \tilde{\underline{v}}_{\mathrm{f}}^{n+1} \, d\Omega \\
&\qquad = \frac{\rho_{\mathrm{f}}}{2\Delta t} \left(\|\tilde{\underline{v}}_{\mathrm{f}}^{n+1}\|_{\Omega_{\mathrm{f}}^{n+1}}^2 - \|\underline{v}_{\mathrm{f}}^{n}\|_{\Omega_{\mathrm{f}}^{n}}^2 + \|\tilde{\underline{v}}_{\mathrm{f}}^{n+1} - \underline{v}_{\mathrm{f}}^{n}\|_{\Omega_{\mathrm{f}}^{n}}^2 \right) + \mathcal{T}_1. \quad \text{(A.14)}
\end{aligned}$$

Then, substituting this result in (A.10a) and summing with (A.10b) and (A.10c) while applying the identity $(a-b,a) = \frac{1}{2}a^2 - \frac{1}{2}b^2 + \frac{1}{2}(a-b)^2$ to $(\underline{v}_{\mathrm{f}}^{n+1} - \tilde{\underline{v}}_{\mathrm{f}}^{n+1}, \underline{v}_{\mathrm{f}}^{n+1})_{\Omega_{\mathrm{f}}^{n+1}}$, we get (using $\Delta t\, \underline{v}_{\mathrm{s}}^{n+\frac{1}{2}} = \underline{y}_{\mathrm{s}}^{n+1} - \underline{y}_{\mathrm{s}}^{n}$)

$$\begin{aligned}
&\frac{\mathcal{K}_{\mathrm{f}}^{n+1} - \mathcal{K}_{\mathrm{f}}^{n}}{\Delta t} + \frac{\mathcal{K}_{\mathrm{s}}^{n+1} - \mathcal{K}_{\mathrm{s}}^{n}}{\Delta t} + \int_{\Omega_{\mathrm{s}}} \left(\frac{\partial \Psi}{\partial \underline{\underline{e}}}\Big|^{n+\frac{1}{2}\sharp} + \frac{\partial \Psi^{\mathrm{damp}}}{\partial \dot{\underline{\underline{e}}}}\Big|^{n+\frac{1}{2}\sharp} \right) : d_{\underline{y}}\underline{\underline{e}}^{n+\frac{1}{2}\sharp} \cdot \underline{v}_{\mathrm{s}}^{n+\frac{1}{2}}\, d\Omega \\
&\quad + \frac{\rho_{\mathrm{f}}}{2\Delta t}\left[\|\tilde{\underline{v}}_{\mathrm{f}}^{n+1} - \underline{v}_{\mathrm{f}}^{n}\|_{\Omega_{\mathrm{f}}^{n}}^2 + \|\underline{v}_{\mathrm{f}}^{n+1} - \tilde{\underline{v}}_{\mathrm{f}}^{n+1}\|_{\Omega_{\mathrm{f}}^{n+1}}^2 \right] \underbrace{-2\mu \left(\underline{\underline{\varepsilon}}(\tilde{\underline{v}}_{\mathrm{f}}^{n+1}) \cdot \underline{n}_{\mathrm{f}}, (\tilde{\underline{v}}_{\mathrm{f}}^{n+1} - \underline{v}_{\mathrm{s}}^{n+\frac{1}{2}}) \right)_{\Sigma^{n+1}}}_{\mathcal{T}_2} \\
&\qquad \underbrace{+ \frac{\gamma\mu}{h}\left[\left(\underline{v}_{\mathrm{s}}^{n+\frac{1}{2}} - \tilde{\underline{v}}_{\mathrm{f}}^{n+1}, \underline{v}_{\mathrm{s}}^{n+\frac{1}{2}} \right)_{\Sigma^{n+1}} + \left(\tilde{\underline{v}}_{\mathrm{f}}^{n+1} - \underline{v}_{\mathrm{s}}^{n-\frac{1}{2}}, \tilde{\underline{v}}_{\mathrm{f}}^{n+1} \right)_{\Sigma^{n+1}} \right]}_{\mathcal{T}_3} \\
&\qquad\qquad = (\underline{t}^{n+1}, \underline{v}_{\mathrm{f}}^{n+1})_{\Gamma_{\mathrm{in\text{-}out}}^{n+1}} - \mathcal{T}_1 - 2\mu \left\| \underline{\underline{\varepsilon}}(\tilde{\underline{v}}_{\mathrm{f}}^{n+1}) \right\|_{\Omega_{\mathrm{f}}^{n+1}}^2 . \qquad \text{(A.15)}
\end{aligned}$$

We used here the following identity that comes from (A.4a) evaluated with $\tilde{\underline{v}}_{\mathrm{f}}^{*} = \mathcal{L}^{n+1}(\underline{v}_{\mathrm{s}}^{n+\frac{1}{2}})$ (where we remind that $\mathcal{L}^{n+1}(\underline{v}_{\mathrm{s}}^{n+\frac{1}{2}})|_{\Sigma^{n+1}} = \underline{v}_{\mathrm{s}}^{n+\frac{1}{2}}|_{\Sigma^{n+1}}$)

$$\begin{aligned}
&\mathcal{R}_{\mathrm{f}}(\mathcal{L}^{n+1}(\underline{v}_{\mathrm{s}}^{n+\frac{1}{2}})) - \mathcal{R}_{p}(\mathcal{L}^{n+1}(\underline{v}_{\mathrm{s}}^{n+\frac{1}{2}})) \\
&\qquad = 2\mu \left(\underline{\underline{\varepsilon}}(\tilde{\underline{v}}_{\mathrm{f}}^{n+1}) \cdot \underline{n}_{\mathrm{f}}, \underline{v}_{\mathrm{s}}^{n+\frac{1}{2}} \right)_{\Sigma^{n+1}} - \frac{\gamma\mu}{h} \left(\tilde{\underline{v}}_{\mathrm{f}}^{n+1} - \underline{v}_{\mathrm{s}}^{n-\frac{1}{2}}, \underline{v}_{\mathrm{s}}^{n+\frac{1}{2}} \right)_{\Sigma^{n+1}} .
\end{aligned}$$

Considering now

$$\begin{aligned}
\mathcal{T}_3 &= \frac{\gamma\mu}{h}\left[(\underline{v}_{\mathrm{s}}^{n+\frac{1}{2}} - \tilde{\underline{v}}_{\mathrm{f}}^{n+1}, \underline{v}_{\mathrm{s}}^{n+\frac{1}{2}})_{\Sigma^{n+1}} + (\tilde{\underline{v}}_{\mathrm{f}}^{n+1} - \underline{v}_{\mathrm{s}}^{n-\frac{1}{2}}, \tilde{\underline{v}}_{\mathrm{f}}^{n+1})_{\Sigma^{n+1}} \right] \\
&= \frac{\gamma\mu}{h}\Big[(\underline{v}_{\mathrm{s}}^{n+\frac{1}{2}} - \tilde{\underline{v}}_{\mathrm{f}}^{n+1}, \underline{v}_{\mathrm{s}}^{n+\frac{1}{2}} - \tilde{\underline{v}}_{\mathrm{f}}^{n+1})_{\Sigma^{n+1}} + (\underline{v}_{\mathrm{s}}^{n+\frac{1}{2}} - \tilde{\underline{v}}_{\mathrm{f}}^{n+1}, \tilde{\underline{v}}_{\mathrm{f}}^{n+1})_{\Sigma^{n+1}} \\
&\qquad + (\tilde{\underline{v}}_{\mathrm{f}}^{n+1} - \underline{v}_{\mathrm{s}}^{n-\frac{1}{2}}, \tilde{\underline{v}}_{\mathrm{f}}^{n+1})_{\Sigma^{n+1}} \Big] \\
&= \frac{\gamma\mu}{h} \|\tilde{\underline{v}}_{\mathrm{f}}^{n+1} - \underline{v}_{\mathrm{s}}^{n+\frac{1}{2}}\|_{\Sigma^{n+1}}^2 + \frac{\gamma\mu}{h} (\underline{v}_{\mathrm{s}}^{n+\frac{1}{2}} - \underline{v}_{\mathrm{s}}^{n-\frac{1}{2}}, \tilde{\underline{v}}_{\mathrm{f}}^{n+1})_{\Sigma^{n+1}},
\end{aligned}$$

we have that

$$(\underline{v}_{\mathrm{s}}^{n+\frac{1}{2}} - \underline{v}_{\mathrm{s}}^{n-\frac{1}{2}}, \tilde{\underline{v}}_{\mathrm{f}}^{n+1})_{\Sigma^{n+1}} = (\underline{v}_{\mathrm{s}}^{n+\frac{1}{2}} - \underline{v}_{\mathrm{s}}^{n-\frac{1}{2}}, \tilde{\underline{v}}_{\mathrm{f}}^{n+1} - \underline{v}_{\mathrm{s}}^{n+\frac{1}{2}})_{\Sigma^{n+1}} + (\underline{v}_{\mathrm{s}}^{n+\frac{1}{2}} - \underline{v}_{\mathrm{s}}^{n-\frac{1}{2}}, \underline{v}_{\mathrm{s}}^{n+\frac{1}{2}})_{\Sigma^{n+1}} .$$

Using $2(a,b) \leq \|a\|^2 + \|b\|^2$ with the first term, and $2(a-b,a) = \|a\|^2 - \|b\|^2 + \|a-b\|^2$ with the second one, we obtain

$$\begin{aligned}
(\underline{v}_{\mathrm{s}}^{n+\frac{1}{2}} - \underline{v}_{\mathrm{s}}^{n-\frac{1}{2}}, \tilde{\underline{v}}_{\mathrm{f}}^{n+1})_{\Sigma^{n+1}} \geq\ & -\frac{1}{2}\|\underline{v}_{\mathrm{s}}^{n+\frac{1}{2}} - \underline{v}_{\mathrm{s}}^{n-\frac{1}{2}}\|_{\Sigma^{n+1}}^2 - \frac{1}{2}\|\tilde{\underline{v}}_{\mathrm{f}}^{n+1} - \underline{v}_{\mathrm{s}}^{n+\frac{1}{2}}\|_{\Sigma^{n+1}}^2 \\
& + \frac{1}{2}\|\underline{v}_{\mathrm{s}}^{n+\frac{1}{2}} - \underline{v}_{\mathrm{s}}^{n-\frac{1}{2}}\|_{\Sigma^{n+1}}^2 + \frac{1}{2}\|\underline{v}_{\mathrm{s}}^{n+\frac{1}{2}}\|_{\Sigma^{n+1}}^2 - \frac{1}{2}\|\underline{v}_{\mathrm{s}}^{n-\frac{1}{2}}\|_{\Sigma^{n+1}}^2,
\end{aligned}$$

hence,

$$\mathcal{T}_3 \geq \frac{\gamma\mu}{2h}\|\tilde{\underline{v}}_{\mathrm{f}}^{n+1} - \underline{v}_{\mathrm{s}}^{n+\frac{1}{2}}\|_{\Sigma^{n+1}}^2 + \frac{\gamma\mu}{2h}\|\underline{v}_{\mathrm{s}}^{n+\frac{1}{2}}\|_{\Sigma^{n+1}}^2 - \frac{\gamma\mu}{2h}\|\underline{v}_{\mathrm{s}}^{n-\frac{1}{2}}\|_{\Sigma^{n+1}}^2 . \qquad \text{(A.16)}$$

For the term $\mathcal{T}_2$, we use Young's inequality $(a,b) \leq \frac{1}{2L}\|a\|^2 + \frac{L}{2}\|b\|^2$, with L homogeneous to a length here, to get

$$-\mathcal{T}_2 \leq \mu \left[L\|\underline{\underline{\varepsilon}}(\tilde{\underline{v}}_{\mathrm{f}}^{n+1}) \cdot \underline{n}_{\mathrm{f}}\|_{\Sigma^{n+1}}^2 + \frac{1}{L}\|\tilde{\underline{v}}_{\mathrm{f}}^{n+1} - \underline{v}_{\mathrm{s}}^{n+\frac{1}{2}}\|_{\Sigma^{n+1}}^2 \right],$$

and the inverse inequality (A.6) then gives

$$\mathcal{T}_2 \geq -\mu \frac{C_{ie} L}{h} \|\underline{\underline{\varepsilon}}(\tilde{\underline{v}}_{\mathrm{f}}^{n+1})\|_{\Omega_{\mathrm{f}}^{n+1}}^2 - \frac{\mu}{L} \|\tilde{\underline{v}}_{\mathrm{f}}^{n+1} - \underline{v}_{\mathrm{s}}^{n+\frac{1}{2}}\|_{\Sigma^{n+1}}^2. \tag{A.17}$$

Using the bounds (A.16) and (A.17) in (A.15), we obtain

$$\begin{aligned}
&\frac{\mathcal{K}_{\mathrm{f}}^{n+1} - \mathcal{K}_{\mathrm{f}}^{n}}{\Delta t} + \frac{\mathcal{K}_{\mathrm{s}}^{n+1} - \mathcal{K}_{\mathrm{s}}^{n}}{\Delta t} + \int_{\Omega_{\mathrm{s}}} \left(\frac{\partial \Psi}{\partial \underline{\underline{e}}} \Big|^{n+\frac{1}{2}\sharp} + \frac{\partial \Psi^{\mathrm{damp}}}{\partial \dot{\underline{\underline{e}}}} \Big|^{n+\frac{1}{2}\sharp} \right) : d_y \underline{\underline{e}}^{n+\frac{1}{2}\sharp} \cdot \underline{v}_{\mathrm{s}}^{n+\frac{1}{2}} \, d\Omega \\
&\quad + \frac{\rho_{\mathrm{f}}}{2\Delta t} \left\| \tilde{\underline{v}}_{\mathrm{f}}^{n+1} - \underline{v}_{\mathrm{f}}^{n} \right\|_{\Omega_{\mathrm{f}}^{n}}^2 + \frac{\rho_{\mathrm{f}}}{2\Delta t} \left\| \underline{v}_{\mathrm{f}}^{n+1} - \tilde{\underline{v}}_{\mathrm{f}}^{n+1} \right\|_{\Omega_{\mathrm{f}}^{n+1}}^2 + \frac{\gamma\mu}{2h} \|\underline{v}_{\mathrm{s}}^{n+\frac{1}{2}}\|_{\Sigma^{n+1}}^2 - \frac{\gamma\mu}{2h} \|\underline{v}_{\mathrm{s}}^{n-\frac{1}{2}}\|_{\Sigma^{n+1}}^2 \\
&\qquad + \mu \left(2 - \frac{C_{ie} L}{h} \right) \left\| \underline{\underline{\varepsilon}}(\tilde{\underline{v}}_{\mathrm{f}}^{n+1}) \right\|_{\Omega_{\mathrm{f}}^{n+1}}^2 + \mu \left(\frac{\gamma}{2h} - \frac{1}{L} \right) \|\tilde{\underline{v}}_{\mathrm{f}}^{n+1} - \underline{v}_{\mathrm{s}}^{n+\frac{1}{2}}\|_{\Sigma^{n+1}}^2 \\
&\qquad\qquad \leq (\underline{t}^{n+1}, \underline{v}_{\mathrm{f}}^{n+1})_{\Gamma_{\text{in-out}}^{n+1}} - \mathcal{T}_1.
\end{aligned}$$

Furthermore, thanks to (A.5) we have

$$\frac{\partial \Psi}{\partial \underline{\underline{e}}} \Big|^{n+\frac{1}{2}\sharp} : d_y \underline{\underline{e}}^{n+\frac{1}{2}\sharp} \cdot \underline{v}_{\mathrm{s}}^{n+\frac{1}{2}} = \frac{\partial \Psi}{\partial \underline{\underline{e}}} \Big|^{n+\frac{1}{2}\sharp} : \frac{\underline{\underline{e}}^{n+1} - \underline{\underline{e}}^{n}}{\Delta t} = \frac{\Psi^{\mathrm{n+1}} - \Psi^{\mathrm{n}}}{\Delta t}.$$

Finally, we are led to

$$\begin{aligned}
&\frac{\mathcal{E}^{n+1} - \mathcal{E}^{n}}{\Delta t} + \frac{\gamma\mu}{2h} \|\underline{v}_{\mathrm{s}}^{n+\frac{1}{2}}\|_{\Sigma^{n+1}}^2 - \frac{\gamma\mu}{2h} \|\underline{v}_{\mathrm{s}}^{n-\frac{1}{2}}\|_{\Sigma^{n+1}}^2 \\
&\qquad \leq (\underline{t}^{n+1}, \underline{v}_{\mathrm{f}}^{n+1})_{\Gamma_{\text{in-out}}^{n+1}} - \int_{\Omega_{\mathrm{s}}} \frac{\partial \Psi^{\mathrm{damp}}}{\partial \dot{\underline{\underline{e}}}} \Big|^{n+\frac{1}{2}\sharp} : d_y \underline{\underline{e}}^{n+\frac{1}{2}\sharp} \cdot \underline{v}_{\mathrm{s}}^{n+\frac{1}{2}} \, d\Omega \\
&\qquad\quad - \mathcal{T}_1 - \frac{\rho_{\mathrm{f}}}{2\Delta t} \left\| \tilde{\underline{v}}_{\mathrm{f}}^{n+1} - \underline{v}_{\mathrm{f}}^{n} \right\|_{\Omega_{\mathrm{f}}^{n}}^2 - \frac{\rho_{\mathrm{f}}}{2\Delta t} \left\| \underline{v}_{\mathrm{f}}^{n+1} - \tilde{\underline{v}}_{\mathrm{f}}^{n+1} \right\|_{\Omega_{\mathrm{f}}^{n+1}}^2 \\
&\qquad\quad - \mu \left(2 - \frac{C_{ie} L}{h} \right) \left\| \underline{\underline{\varepsilon}}(\tilde{\underline{v}}_{\mathrm{f}}^{n+1}) \right\|_{\Omega_{\mathrm{f}}^{n+1}}^2 - \mu \left(\frac{\gamma}{2h} - \frac{1}{L} \right) \|\tilde{\underline{v}}_{\mathrm{f}}^{n+1} - \underline{v}_{\mathrm{s}}^{n+\frac{1}{2}}\|_{\Sigma^{n+1}}^2,
\end{aligned} \tag{A.18}$$

Therefore, (A.8) ensure the existence of L such that $2 - \frac{C_{ie} L}{h} \geq 0$ and $\frac{\gamma}{2h} - \frac{1}{L} > 0$, and concludes the establishment of (A.9). ■

Remark 14
Proposition 8 ensures the energy stability of our scheme provided $\gamma\mu\Delta t = O(h)$. This CFL-like condition and the interface term $\frac{\gamma\mu}{2h} \|\underline{v}_{\mathrm{s}}^{n+\frac{1}{2}}\|_{\Sigma}^2$, that could be incorporated to the numerical energy if Σ was fixed, already appeared in the linear version of this stability analysis (Astorino et al., 2009a).

Remark 15
As in (Astorino et al., 2009a), in addition to the physical dissipation terms in this discrete balance, the terms $\left\| \tilde{\underline{v}}_{\mathrm{f}}^{n+1} - \underline{v}_{\mathrm{f}}^{n} \right\|_{\Omega_{\mathrm{f}}^{n}}^2$, $\left\| \underline{v}_{\mathrm{f}}^{n+1} - \tilde{\underline{v}}_{\mathrm{f}}^{n+1} \right\|_{\Omega_{\mathrm{f}}^{n+1}}^2$ and $\|\tilde{\underline{v}}_{\mathrm{f}}^{n+1} - \underline{v}_{\mathrm{s}}^{n+\frac{1}{2}}\|_{\Sigma^{n+1}}^2$ bring numerical dissipation.

Appendix B

Total convergence analysis of a monolithic scheme for linear fluid-structure interaction

In Appendix A, we present an effective and energy-preserving time discretization of (A.1). The purpose of this chapter is to study spatial discretization aspects of this fluid-structure interaction formulation, in order to guarantee numerical stability. To that purpose, we established in Section B.1 below a linearization of (A.1), and we perform its theoretical and numerical convergence study.

It is known that the discretization of a Stokes problem involves mixed finite elements, that velocity and pressure must be approximated separately, and that the couple of spaces must be compatible in the sense of an *inf-sup condition*, see (Ladyzhenskaya and Silverman, 1969; Babuška, 1973; Brezzi, 1974). Numerically, the violation of this condition often leads to strong node-to-node spatial oscillations in the pressure field. Our FSI model involves a Stokes-like fluid sub-problem, coupled with a solid matrix. It is natural to thoroughly investigate how this problem translates in our framework, and to perform both a theoretical convergence analysis to see how numerical oscillations arise and numerical tests to illustrate them. Our approach is inspired from (Le Tallec and Mani, 2000) which establishes the total convergence of a linearised fluid structure interaction problem, using an energy conservative scheme. A convergence analysis was also performed on the semi-implicit scheme of (Fernández et al., 2007) in (Astorino and Grandmont, 2010). Here, we perform it on a monolithic problem using a Robin interface coupling.

B.1 A linear flows and elastic coupling formulation - the continuous problem

B.1.1 Linearisation of the formulation for convergence analysis

We consider the FSI formulation introduced in Section A.1 with a solid stress tensor given by

$$\underline{\underline{\Sigma}} = \frac{\partial \Psi(\underline{\underline{e}})}{\partial \underline{\underline{e}}},$$

with Ψ the Helmholtz free energy of the solid quadratic in $\underline{\underline{\varepsilon}}$. Furthermore, we assume the coercivity of Ψ, that is, there exists a $\lambda > 0$ such that $\Psi(\underline{\underline{\varepsilon}}) \geq \lambda \|\underline{\underline{\varepsilon}}\|^2_{L^2(\Omega_s)}$, and we also assume that sufficient boundary conditions are imposed on the structure to prevent any rigid body

transformations. Therefore the Korn inequality gives the equivalence between the norm defined by Ψ and the H^1 norm on Ω_s. Let us notice that if we add the assumption of isotropy, it is known that Ψ can be written as the Saint-Venant-Kirchhoff constitutive law.

In our linear frame, $J-1$ reduces to $\operatorname{tr} \underline{\underline{\varepsilon}}(\underline{y}_s)$, and we define the reduced tensor $\underline{\underline{\sigma}}_s = \frac{\partial \Psi}{\partial \underline{\underline{\varepsilon}}}$. We assume that the fluid viscosity tensor is given by $\underline{\underline{\sigma}}_{vis} = 2\mu \underline{\underline{\varepsilon}}$. When we keep only first order terms, the weak formulation of FSI writes –$\Omega_f(t)$ and $\Omega_s(t)$ (resp. a borders $\Gamma(t)$) reduces to $\Omega_f(0)$ and $\Omega_s(0)$ that we will denote by Ω_f and Ω_s (resp. Γ), J to 1, and ALE terms disappear –

$$\begin{cases} \displaystyle\int_{\Omega_s} \rho_{s0} \partial_t \underline{v}_s \cdot \underline{v}_s^* \, d\Omega + \int_{\Omega_s} \underline{\underline{\sigma}}_s : \underline{\underline{\varepsilon}}(\underline{v}_s^*) \, d\Omega = \int_{\Omega_s} \rho_{s0} \underline{f} \cdot \underline{v}_s^* \, d\Omega - \mathcal{R}_f^{c,lin}(\mathcal{L}(\underline{v}_s^*)) & \text{(B.1a)} \\ \displaystyle\int_{\Omega_f} \rho_f \partial_t \underline{v}_f \cdot \underline{v}_f^* \, d\Omega + \int_{\Omega_f} \left(-p \operatorname{div} \underline{v}_f^* + \underline{\underline{\sigma}}_{vis}(\underline{v}_f) : \underline{\underline{\varepsilon}}(\underline{v}_f^*) \right) d\Omega + \int_{\Omega_f} p^* \operatorname{div} \underline{v}_f \, d\Omega & \\ \qquad = \displaystyle\int_{\Gamma_{in\text{-}out}} \underline{t}_0 \cdot \underline{v}_f^* \, dS & \text{(B.1b)} \end{cases}$$

with $\mathcal{L}$ a lifting operator from functions on Ω_s to functions on Ω_f, whose restrictions to Σ is the identity, and with the linear fluid residual

$$\mathcal{R}_f^{c,lin}(\underline{v}^*) = \int_{\Omega_f} \rho_f \partial_t \underline{v}_f \cdot \underline{v}^* \, d\Omega + \int_{\Omega_f} \left(-p \operatorname{div} \underline{v}_f^* + \underline{\underline{\sigma}}_{vis}(\underline{v}_f) : \underline{\underline{\varepsilon}}(\underline{v}^*) \right) d\Omega - \int_{\Gamma_{in\text{-}out}} \underline{t}_0 \cdot \underline{v}^* \, dS. \quad \text{(B.2)}$$

Remark 16
The corresponding strong formulation reads

$$\begin{cases} \rho_f \partial_t \underline{v}_f - \operatorname{div}(\underline{\underline{\sigma}}_{vis}(\underline{v}_f)) + \underline{\nabla} p = 0, & \text{in } \Omega_f \\ \operatorname{div} \underline{v}_f = 0, & \text{in } \Omega_f \\ \underline{v}_f = \underline{v}_s, & \text{on } \Sigma \end{cases}$$

$$\begin{cases} \rho_{s0} \partial_t \underline{v}_s - \operatorname{div} \underline{\underline{\sigma}}_s = \rho_{s0} \underline{f} & \text{in } \Omega_s \\ \underline{v}_s = \partial_t \underline{y}_s & \text{in } \Omega_s \\ (\underline{\underline{\sigma}}^s(\underline{y}_s) \underline{n}_s + \underline{\underline{\sigma}}_f(\underline{v}_f, p) \underline{n}_f) = 0 & \text{on } \Sigma. \end{cases}$$

Remark 17 (Existence and uniqueness of a solution)
Existence and uniqueness of a solution of the continuous problem were established (Grandmont and Maday, 2000; Du et al., 2003).

B.1.2 Nitsche's linear weak formulation

We define

$$\begin{aligned} Q &= L^2(\Omega_f), \\ W^f &= H^1(\Omega_f)^3, \\ W^s &= H^1(\Omega_s)^3, \\ W^f(\underline{\varphi}) &= \{ \underline{v}^* \in W^f \;\big|\; \underline{v}^*|_\Sigma = \underline{\varphi}|_\Sigma \}, \quad \forall \underline{\varphi} \in L^2(\Sigma)^3, \\ W^s(\underline{\varphi}) &= \{ \underline{v}^* \in W^s \;\big|\; \underline{v}^*|_{\Gamma_D} = \underline{\varphi}|_{\Gamma_D} \}, \quad \forall \underline{\varphi} \in W^s. \end{aligned}$$

We also introduce the state vector as

$$X = \left[\underline{v}_f, \underline{v}_s, \underline{y}_s, p \right] \text{ that belongs to } V = W^f(\underline{v}_f^{pr}) \times W^s \times W^s(\underline{y}_s^{pr}) \times Q$$

and its corresponding test functions vector

$$X^* = \left[\underline{v}_{\mathrm{f}}^*, \underline{v}_{\mathrm{s}}^*, \underline{y}_{\mathrm{s}}^*, p^*\right] \text{ that belongs to } V^0 = W^{\mathrm{f}}(0) \times W^{\mathrm{s}} \times W^{\mathrm{s}}(0) \times Q.$$

We consider $\Omega_{\mathrm{f},h}$, $\Omega_{\mathrm{s},h}$ (with borders Σ_h, $\Gamma_{D,h}$ and $\Gamma_{\text{in-out},h}$) discretizations of Ω_{f} and Ω_{s} of refinement h (typically, the maximum diameter of all the elements in the mesh). We use a finite element strategy and we assume that the solid displacement and the solid velocity are discretized in the same space W_h^{s}, the fluid velocity is chosen in W_h^{f} and the pressure in Q_h. For any $\underline{w}_{\mathrm{f},D}$ in $L^2(\Sigma_h)^3$ and any $\underline{w}_{\mathrm{s},D}$ in W_h^{s} we define

$$W_h^{\mathrm{f}}(\underline{w}_{\mathrm{f},D}) = \{\underline{v}^* \in W_h^{\mathrm{f}} \;\big|\; \underline{v}^*|_{\Sigma_h} = \underline{w}_{\mathrm{f},D}\},$$
$$W_h^{\mathrm{s}}(\underline{w}_{\mathrm{s},D}) = \{\underline{v}^* \in W_h^{\mathrm{s}} \;\big|\; \underline{v}^*|_{\Gamma_{D,h}} = \underline{w}_{\mathrm{s},D}\}.$$

Then the finite element spaces associated with V and V^0 are

$$V_h = W_h^{\mathrm{f}}(\underline{v}_{\mathrm{f},h}^{\mathrm{pr}}) \times W_h^{\mathrm{s}} \times W_h^{\mathrm{s}}(\underline{y}_{\mathrm{s},h}^{\mathrm{pr}}) \times Q_h,$$
$$V_h^0 = W_h^{\mathrm{f}}(0) \times W_h^{\mathrm{s}} \times W_h^{\mathrm{s}}(0) \times Q_h,$$

for $(\underline{v}_{\mathrm{f},h}^{\mathrm{pr}}, \underline{y}_{\mathrm{s},h}^{\mathrm{pr}})$ in $W_h^{\mathrm{f}} \times W_h^{\mathrm{s}}$.

We will use the elasticity and weighted L^2-scalar product notations

$$(\underline{y}, \underline{y}^*)_{\mathrm{skel}} = \int_{\Omega_{\mathrm{s}}} \underline{\underline{\sigma}}_{\mathrm{s}}(\underline{y}) : \underline{\underline{\varepsilon}}(\underline{y}^*)\, d\Omega, \quad \text{and} \quad (a,b)_{\Omega} = \int_{\Omega} ab\, d\Omega.$$

As in the splitting time-scheme of Section A.2, fluid and solid constituents are implicitly and weakly coupled on Σ through $\underline{v}_{\mathrm{f}} = \underline{v}_{\mathrm{s}}$ with Robin coupling conditions derived from Nitsche's interface method (Nitsche, 1971; Burman and Fernández, 2007). Unlike in (B.1b), this condition is weakly imposed in the fluid resolution, so the fluid test function $\underline{v}_{\mathrm{f}}^*$ has no reason to vanish on Σ. Therefore, the integration by part that leads to (B.1b) involves the new term $\left((\underline{\underline{\sigma}}_{\mathrm{vis}}(\underline{v}_{\mathrm{f}}) - p)\cdot \underline{n}_{\mathrm{f}}, \underline{v}_{\mathrm{f}}^*\right)_{\Sigma}$ in the fluid equation RHS. Furthermore, we use that $\mathcal{R}_{\mathrm{f}}^{\mathrm{c,lin}}(\mathcal{L}(\underline{v}_{\mathrm{s}}^*)) = \left((\underline{\underline{\sigma}}_{\mathrm{vis}}(\underline{v}_{\mathrm{f}}) - p)\cdot \underline{n}_{\mathrm{f}}, \underline{v}_{\mathrm{s}}^*\right)_{\Sigma}$.

We can derive the following equation, satisfied by the solution of (B.1), $X = (\underline{v}_{\mathrm{f}}, \underline{v}_{\mathrm{s}}, \underline{y}_{\mathrm{s}}, p)$ in V, for any $X^* = (\underline{v}_{\mathrm{f}}^*, \underline{v}_{\mathrm{s}}^*, \underline{y}_{\mathrm{s}}^*, p^*)$ in V^0

$$\begin{aligned}
&\rho_{\mathrm{f}}\left(\partial_t \underline{v}_{\mathrm{f}}, \underline{v}_{\mathrm{f}}^*\right)_{\Omega_{\mathrm{f}}} + \left(\underline{\underline{\sigma}}_{\mathrm{vis}}(\underline{v}_{\mathrm{f}}), \underline{\underline{\varepsilon}}(\underline{v}_{\mathrm{f}}^*)\right)_{\Omega_{\mathrm{f}}} + \rho_{\mathrm{s}0}\left(\partial_t \underline{v}_{\mathrm{s}}, \underline{v}_{\mathrm{s}}^*\right)_{\Omega_{\mathrm{s}}} + \left(\partial_t \underline{y}_{\mathrm{s}} - \underline{v}_{\mathrm{s}}, \underline{y}_{\mathrm{s}}^*\right)_{\mathrm{skel}} + \left(\underline{y}_{\mathrm{s}}, \underline{v}_{\mathrm{s}}^*\right)_{\mathrm{skel}} \\
&\qquad - \left((\underline{\underline{\sigma}}_{\mathrm{vis}}(\underline{v}_{\mathrm{f}}) - p)\cdot \underline{n}_{\mathrm{f}}, \underline{v}_{\mathrm{f}}^* - \underline{v}_{\mathrm{s}}^*\right)_{\Sigma} - \left((\underline{\underline{\sigma}}_{\mathrm{vis}}(\underline{v}_{\mathrm{f}}^*) + p^*)\cdot \underline{n}_{\mathrm{f}}, \underline{v}_{\mathrm{f}} - \underline{v}_{\mathrm{s}}\right)_{\Sigma} \\
&+ \frac{\gamma\mu}{h}\left(\underline{v}_{\mathrm{f}} - \underline{v}_{\mathrm{s}}, \underline{v}_{\mathrm{f}}^* - \underline{v}_{\mathrm{s}}^*\right)_{\Sigma} + \left(p^*, \operatorname{div} \underline{v}_{\mathrm{f}}\right)_{\Omega_{\mathrm{f}}} - \left(p, \operatorname{div} \underline{v}_{\mathrm{f}}^*\right)_{\Omega_{\mathrm{f}}} = \int_{\Omega_{\mathrm{s}}} \rho_{\mathrm{s}0} \underline{f}\cdot \underline{v}_{\mathrm{s}}^*\, d\Omega + \int_{\Gamma_{\text{in-out}}} \underline{t}_0 \cdot \underline{v}_{\mathrm{f}}^*\, dS,
\end{aligned}$$

where the fourth and seventh terms of the LHS are both consistent, and are here respectively to impose weakly the solid velocity, and to bring some symmetry. We get that the solution X in V of (B.1) satisfies, for any X^* in V^0

$$\begin{aligned}
&\rho_{\mathrm{f}}\left(\partial_t \underline{v}_{\mathrm{f}}, \underline{v}_{\mathrm{f}}^*\right)_{\Omega_{\mathrm{f}}} + \rho_{\mathrm{s}}\left(\partial_t \underline{v}_{\mathrm{s}}, \underline{v}_{\mathrm{s}}^*\right)_{\Omega_{\mathrm{s}}} + \left(\partial_t \underline{y}_{\mathrm{s}}, \underline{y}_{\mathrm{s}}^*\right)_{\mathrm{skel}} + M(X, X^*) \\
&\qquad = \int_{\Omega_{\mathrm{s}}} \rho_{\mathrm{s}0} \underline{f}\cdot \underline{v}_{\mathrm{s}}^*\, d\Omega + \int_{\Gamma_{\text{in-out}}} \underline{t}_0 \cdot \underline{v}_{\mathrm{f}}^*\, dS \quad \text{(B.3)}
\end{aligned}$$

where we introduced the bilinear form

$$M(X,X^*) = 2\mu\left(\underline{\underline{\varepsilon}}(\underline{v}_\mathrm{f}),\underline{\underline{\varepsilon}}(\underline{v}_\mathrm{f}^*)\right)_{\Omega_\mathrm{f}} + \left(\underline{y}_\mathrm{s},\underline{v}_\mathrm{s}^*\right)_\mathrm{skel} - \left(\underline{v}_\mathrm{s},\underline{y}_\mathrm{s}^*\right)_\mathrm{skel} + (p^*,\operatorname{div}\underline{v}_\mathrm{f})_{\Omega_\mathrm{f}} - (p,\operatorname{div}\underline{v}_\mathrm{f}^*)_{\Omega_\mathrm{f}}$$
$$- \left(\underline{\underline{\sigma}}_\mathrm{f}(\underline{v}_\mathrm{f},p)\underline{n}_\mathrm{f},\underline{v}_\mathrm{f}^*-\underline{v}_\mathrm{s}^*\right)_\Sigma - \left(\underline{v}_\mathrm{f}-\underline{v}_\mathrm{s},\underline{\underline{\sigma}}_\mathrm{f}(\underline{v}_\mathrm{f}^*,-p^*)\underline{n}_\mathrm{f}\right)_\Sigma + \frac{\gamma\mu}{h}\left(\underline{v}_\mathrm{f}-\underline{v}_\mathrm{s},\underline{v}_\mathrm{f}^*-\underline{v}_\mathrm{s}^*\right)_\Sigma . \quad \text{(B.4)}$$

Remark 18
Note that $-\left(\underline{\underline{\sigma}}_\mathrm{f}(\underline{v}_\mathrm{f},p)\underline{n}_\mathrm{f},\underline{v}_\mathrm{f}^*-\underline{v}_\mathrm{s}^*\right)_\Sigma$ involves the trace of p and $\underline{\underline{\varepsilon}}(\underline{v}_\mathrm{f})$ on Σ, which is not properly defined in the spaces considered. Nevertheless, when $(\underline{v}_\mathrm{f},\underline{v}_\mathrm{s},\underline{y}_\mathrm{s},p)$ is the continuous solution, this term can be defined by duality as the residual of the fluid equation.

B.1.3 Time continuous energy balance

For the sake of simplicity in this section, we will assume that $\underline{t}_0 = 0$ on $\Gamma_{\text{in-out}}$, $\underline{f} = \underline{0}$ and $\underline{y}_\mathrm{s}^{\mathrm{pr}} = \underline{0}$. For any X, we define the following energy norm

$$\|X\|_\mathcal{E}^2 = \frac{\rho_\mathrm{f}}{2}\|\underline{v}_\mathrm{f}\|_{\Omega_\mathrm{f}}^2 + \frac{\rho_\mathrm{s}}{2}\|\underline{v}_\mathrm{s}\|_{\Omega_\mathrm{s}}^2 + \frac{1}{2}\|\underline{y}_\mathrm{s}\|_\mathrm{skel}^2$$

where the first two terms are the fluid and solid kinetic energy, and the last corresponds to the Helmholtz free energy $\int_{\Omega_\mathrm{s}}\Psi\, d\Omega$.

Let us recall the trace inequality and, for discrete functions, the trace inverse inequality (see Lemma 1 in Section A.3).

Lemma 9 (Trace inequality)
There exists a constant C_{tr} depending only on Ω (a Lipschitz domain) and Σ such that

$$\|\underline{v}\|_{H^{\frac{1}{2}}(\Sigma)}^2 \le C_{tr}\|\underline{v}\|_{H^1(\Omega)}^2, \quad \forall \underline{v}\in H^1(\Omega)^3. \quad \text{(B.5)}$$

Lemma 10 (Trace inverse inequality)
If h is the typical maximal diameter of all the finite elements in the mesh, there exists a constant C_{ie} that depends on Ω, Σ and the type of shape functions, such that

$$\|\underline{\underline{\varepsilon}}(\underline{v}_h)\cdot\underline{n}_\mathrm{f}\|_{L^2(\Sigma)}^2 \le \frac{C_{ie}}{h}\|\underline{\underline{\varepsilon}}(\underline{v}_h)\|_{L^2(\Omega)}^2, \quad \forall \underline{v}_h\in W_h^\mathrm{f}. \quad \text{(B.6)}$$

Note that (B.3) comes down to a Cauchy problem, so existence and uniqueness of the solution in the finite dimensional space V_h is guaranteed. Let X_h in V_h be the semi-discrete solution of (B.3), for any X^* in V_h^0. The energy of X_h becomes $\mathcal{E}_h = \|X_h\|_\mathcal{E}^2$. Now, the evaluation of (B.3) with the test functions $X^* = X_h$ gives:

$$\partial_t\mathcal{E}_h + 2\mu\|\underline{\underline{\varepsilon}}(\underline{v}_{\mathrm{f},h})\|_{\Omega_\mathrm{f}}^2 + \frac{\gamma\mu}{h}\|\underline{v}_{\mathrm{f},h}-\underline{v}_{\mathrm{s},h}\|_\Sigma^2 - 4\mu\left(\underline{\underline{\varepsilon}}(\underline{v}_{\mathrm{f},h})\underline{n}_\mathrm{f},\underline{v}_{\mathrm{f},h}-\underline{v}_{\mathrm{s},h}\right)_\Sigma = 0.$$

Then, we use Young's inequality $(a,b)\le\frac{1}{2L}\|a\|^2+\frac{L}{2}\|b\|^2$, with L homogeneous to a length here, and the inverse inequality (B.6), to get

$$4\mu\left(\underline{\underline{\varepsilon}}(\underline{v}_{\mathrm{f},h})\underline{n}_\mathrm{f},\underline{v}_{\mathrm{f},h}-\underline{v}_{\mathrm{s},h}\right)_\Sigma \le 2\mu\left[L\|\underline{\underline{\varepsilon}}(\underline{v}_{\mathrm{f},h})\cdot\underline{n}_\mathrm{f}\|_\Sigma^2 + \frac{1}{L}\|\underline{v}_{\mathrm{f},h}-\underline{v}_{\mathrm{s},h}\|_\Sigma^2\right]$$
$$\le 2\mu\frac{C_{ie}L}{h}\|\underline{\underline{\varepsilon}}(\underline{v}_{\mathrm{f},h})\|_{\Omega_\mathrm{f}}^2 + 2\frac{\mu}{L}\|\underline{v}_{\mathrm{f},h}-\underline{v}_{\mathrm{s},h}\|_\Sigma^2. \quad \text{(B.7)}$$

We end up with the following energy balance

$$\partial_t\mathcal{E}_h + 2\mu\left(1-\frac{C_{ie}L}{h}\right)\|\underline{\underline{\varepsilon}}(\underline{v}_{\mathrm{f},h})\|_{\Omega_\mathrm{f}}^2 + \mu\left(\frac{\gamma}{h}-\frac{2}{L}\right)\|\underline{v}_{\mathrm{f},h}-\underline{v}_{\mathrm{s},h}\|_\Sigma^2 \le 0$$

which ensures the stability of semi-discrete solution X_h provided that $\gamma \ge 2C_{ie}$.

B.2 The fully discrete problem

B.2.1 Time scheme

We consider in (B.3) a first-order backward difference discretization in the fluid, for both $\underline{v}_{\mathrm{f}}$ and p, to keep it as close as possible to the splitting scheme of Section A.2 (otherwise $p^{n+\frac{1}{2}}$ would have been a natural choice to avoid numerical dissipation), and a midpoint scheme for the solid.

Using the notations $a^{n+\frac{1}{2}} \hat{=} \frac{a^{n+1}+a^n}{2}$ and $D_\tau a^{n+\frac{1}{2}} \hat{=} \frac{a^{n+1}-a^n}{\Delta t}$, we look for $(\underline{v}_{\mathrm{f},h}^n, \underline{v}_{\mathrm{s},h}^n, \underline{y}_{\mathrm{s},h}^n, p_h^n)_{n\geq 0}$ in $V_h^{\mathbb{N}}$ such that, for any n in $\mathbb{N}$ and $(\underline{v}_{\mathrm{f}}^*, \underline{v}_{\mathrm{s}}^*, \underline{y}_{\mathrm{s}}^*, p^*)$ in V_h^0,

$$\rho_{\mathrm{f}} \left(D_\tau \underline{v}_{\mathrm{f},h}^{n+\frac{1}{2}}, \underline{v}_{\mathrm{f}}^* \right)_{\Omega_{\mathrm{f}}} + \rho_{\mathrm{s}} \left(D_\tau \underline{v}_{\mathrm{s},h}^{n+\frac{1}{2}}, \underline{v}_{\mathrm{s}}^* \right)_{\Omega_{\mathrm{s}}} + \left(D_\tau \underline{y}_{\mathrm{s},h}^{n+\frac{1}{2}}, \underline{y}_{\mathrm{s}}^* \right)_{\mathrm{skel}}$$
$$+ M((\underline{v}_{\mathrm{f},h}^{n+1}, \underline{v}_{\mathrm{s},h}^{n+\frac{1}{2}}, \underline{y}_{\mathrm{s},h}^{n+\frac{1}{2}}, p_h^{n+1}), (\underline{v}_{\mathrm{f}}^*, \underline{v}_{\mathrm{s}}^*, \underline{y}_{\mathrm{s}}^*, p^*)) = \int_{\Omega_{\mathrm{s}}} \rho_{\mathrm{s}0} \underline{f}^{n+1} \cdot \underline{v}_{\mathrm{s}}^* \, d\Omega + \int_{\Gamma_{\text{in-out}}} \underline{t}_0^{n+1} \cdot \underline{v}_{\mathrm{f}}^* \, dS, \quad \text{(B.8)}$$

with adequate initial conditions.

B.2.2 Stability analysis in energy norm

In this section again, and for the rest of the document, we will assume that $\underline{t}_0 = 0$ on $\Gamma_{\text{in-out}}$, $\underline{f} = \underline{0}$ and $\underline{y}_{\mathrm{s}}^{\mathrm{pr}} = \underline{0}$ (as a consequence, $V = V^0$). The evaluation of (B.8) with admissible test functions

$$\underline{v}_{\mathrm{f}}^* = \underline{v}_{\mathrm{f},h}^{n+1}, \quad \underline{v}_{\mathrm{s}}^* = \underline{v}_{\mathrm{s},h}^{n+\frac{1}{2}}, \quad \underline{y}_{\mathrm{s}}^* = \underline{y}_{\mathrm{s},h}^{n+\frac{1}{2}}, \quad \text{and} \quad p^* = p_h^{n+1}$$

gives

$$\rho_{\mathrm{f}} \left(D_\tau \underline{v}_{\mathrm{f},h}^{n+\frac{1}{2}}, \underline{v}_{\mathrm{f},h}^{n+1} \right)_{\Omega_{\mathrm{f}}} + \rho_{\mathrm{s}} \left(D_\tau \underline{v}_{\mathrm{s},h}^{n+\frac{1}{2}}, \underline{v}_{\mathrm{s},h}^{n+\frac{1}{2}} \right)_{\Omega_{\mathrm{s}}} + \left(D_\tau \underline{y}_{\mathrm{s},h}^{n+\frac{1}{2}}, \underline{y}_{\mathrm{s},h}^{n+\frac{1}{2}} \right)_{\mathrm{skel}} + 2\mu \left(\underline{\underline{\varepsilon}}(\underline{v}_{\mathrm{f},h}^{n+1}), \underline{\underline{\varepsilon}}(\underline{v}_{\mathrm{f},h}^{n+1}) \right)_{\Omega_{\mathrm{f}}}$$
$$- 4\mu \left(\underline{\underline{\varepsilon}}(\underline{v}_{\mathrm{f},h}^{n+1}) \underline{n}_{\mathrm{f}}, \underline{v}_{\mathrm{f},h}^{n+1} - \underline{v}_{\mathrm{s},h}^{n+\frac{1}{2}} \right)_{\Sigma} + \frac{\gamma\mu}{h} \left(\underline{v}_{\mathrm{f},h}^{n+1} - \underline{v}_{\mathrm{s},h}^{n+\frac{1}{2}}, \underline{v}_{\mathrm{f},h}^{n+1} - \underline{v}_{\mathrm{s},h}^{n+\frac{1}{2}} \right)_{\Sigma} = 0.$$

We introduce the state vector $X_h^n = \left[\underline{v}_{\mathrm{f},h}^n, \underline{v}_{\mathrm{s},h}^n, \underline{y}_{\mathrm{s},h}^n, p_h^n \right]$ and its energy $\mathcal{E}_h^n = \|X_h^n\|_{\mathcal{E}}^2$ at iteration n. Then, we apply twice the identity $\langle a-b, a \rangle = \frac{1}{2}||a||^2 - \frac{1}{2}||b||^2 + \frac{1}{2}||a-b||^2$ to $\underline{v}_{\mathrm{f}}$ and to p, to get

$$\frac{\mathcal{E}_h^{n+1} - \mathcal{E}_h^n}{\Delta t} + \frac{\rho_{\mathrm{f}}}{2\Delta t} \|\underline{v}_{\mathrm{f},h}^{n+1} - \underline{v}_{\mathrm{f},h}^n\|_{\Omega_{\mathrm{f}}}^2 + 2\mu \|\underline{\underline{\varepsilon}}(\underline{v}_{\mathrm{f},h}^{n+1})\|_{\Omega_{\mathrm{f}}}^2$$
$$\underbrace{- 4\mu \left(\underline{\underline{\varepsilon}}(\underline{v}_{\mathrm{f},h}^{n+1}) \underline{n}_{\mathrm{f}}, \underline{v}_{\mathrm{f},h}^{n+1} - \underline{v}_{\mathrm{s},h}^{n+\frac{1}{2}} \right)_{\Sigma}}_{\mathcal{T}_1} + \frac{\gamma\mu}{h} \|\underline{v}_{\mathrm{s},h}^{n+\frac{1}{2}} - \underline{v}_{\mathrm{f},h}^{n+1}\|_{\Sigma}^2 = 0, \quad \text{(B.9)}$$

using that

$$\underline{\underline{\sigma}}_{\mathrm{s}} \left(\frac{\underline{y}_{\mathrm{s},h}^{n+1} - \underline{y}_{\mathrm{s},h}^n}{\Delta t} \right) : \underline{\underline{\varepsilon}} \left(\frac{\underline{y}_{\mathrm{s},h}^{n+1} + \underline{y}_{\mathrm{s},h}^n}{2} \right) = \frac{\Psi(\underline{\underline{\varepsilon}}(\underline{y}_{\mathrm{s},h}^{n+1})) - \Psi(\underline{\underline{\varepsilon}}(\underline{y}_{\mathrm{s},h}^n))}{\Delta t}.$$

In (B.9), the increment of $\mathcal{E}_h^n$ is followed by a term of numerical dissipation, a term of physical dissipation, and the dissipative term in $\frac{\gamma\mu}{h}$ that comes from Nitsche's method. We apply the bound (B.7) to $\underline{v}_{\mathrm{f},h}^{n+1}$ and $\underline{v}_{\mathrm{s},h}^{n+\frac{1}{2}}$ to control the remaining term $\mathcal{T}_1$, as that for any length L,

$$\frac{\mathcal{E}_h^{n+1} - \mathcal{E}_h^n}{\Delta t} + 2\mu(1 - \frac{C_{ie}L}{h}) \|\underline{\underline{\varepsilon}}(\underline{v}_{\mathrm{f},h}^{n+1})\|_{\Omega_{\mathrm{f}}}^2 + \mu(\frac{\gamma}{h} - \frac{2}{L}) \|\underline{v}_{\mathrm{f},h}^{n+1} - \underline{v}_{\mathrm{s},h}^{n+\frac{1}{2}}\|_{\Sigma}^2 + \frac{\rho_{\mathrm{f}}}{2\Delta t} \|\underline{v}_{\mathrm{f},h}^{n+1} - \underline{v}_{\mathrm{f},h}^n\|_{\Omega_{\mathrm{f}}}^2 \leq 0.$$

Therefore, the energy stability of the scheme is ensured provided that we can find L such that $1 \geq \frac{C_{ie}L}{h}$ and $\frac{\gamma}{h} \geq \frac{2}{L}$, i.e. when $\gamma \geq 2C_{ie}$.

B.2.3 Inf-sup property on the static problem

We introduce the following discrete norm, associated with the stabilisation,

$$\|X\|_h^2 \hat{=} \|\underline{v}_\mathrm{f}\|_{H^1(\Omega_\mathrm{f})}^2 + \|\underline{v}_\mathrm{s}\|_{H^1(\Omega_\mathrm{s})}^2 + \|\underline{y}_\mathrm{s}\|_{H^1(\Omega_\mathrm{s})}^2 + \|p\|_{L^2(\Omega_\mathrm{f})}^2 + \frac{\gamma\mu}{h}\|\underline{v}_\mathrm{f} - \underline{v}_\mathrm{s}\|_{L^2(\Sigma)}^2.$$

Our objective in this section is to establish a stability (inf-sup) property for M defined by (B.4) for $\|\cdot\|_h$.

We begin with establishing a lemma, that we will use in the following proof to construct virtual fluid and solid velocity fields.

Let $\mathcal{V}_h$ and $\mathcal{Q}_h$ be finite dimensional subspaces of Hilbert spaces $\mathcal{V}$ and $\mathcal{Q}$ with scalar products $(\cdot,\cdot)_\mathcal{V}$ and $(\cdot,\cdot)_\mathcal{Q}$. Let $a(\cdot,\cdot)$ and $b(\cdot,\cdot)$ be continuous linear forms on $\mathcal{V}\times\mathcal{V}$ and $\mathcal{V}\times\mathcal{Q}$, and f and g linear forms on $\mathcal{V}$ and $\mathcal{Q}$. We look for (v_h, p_h) in $\mathcal{V}_h \times \mathcal{Q}_h$ solution of

$$\begin{cases} a(v_h, v^*) + b(v^*, p_h) = f(v^*), & \forall v^* \in \mathcal{V}_h, \\ b(v_h, p^*) = g(p^*), & \forall p^* \in \mathcal{Q}_h. \end{cases} \tag{B.10}$$

We can introduce operators A_h from $\mathcal{V}_h$ to $\mathcal{V}_h'$ and B_h from $\mathcal{V}_h$ to $\mathcal{Q}_h'$. B denotes the continuous operator from $\mathcal{V}$ to $\mathcal{Q}'$.

Lemma 11
Let us suppose that $\operatorname{Ker} B^t = \{0\}$, *and that* $a(\cdot,\cdot)$ *is elliptic on* $\mathcal{V}$, *that is, there exists* $\alpha_0 > 0$ *such that*

$$a(v,v) \geq \alpha_0 \|v\|_\mathcal{V}^2, \quad \forall v \in \mathcal{V}.$$

If, moreover, b *satisfies an inf-sup property, that is, there exists* $k_0 > 0$ *independent of* h *such that*

$$\inf_{p\in\mathcal{Q}_h} \sup_{v\in\mathcal{V}_h} \frac{b(v,p)}{\|v\|_\mathcal{V}\|p\|_\mathcal{Q}} \geq k_0, \tag{B.11}$$

then, (B.10) *has a unique solution* (u_h, p_h). *In addition. one has the bound*

$$\begin{cases} \|v_h\|_\mathcal{V} \leq \dfrac{1}{\alpha_0}\|f\|_{\mathcal{V}'} + \left(\dfrac{\|a\|}{\alpha_0} + 1\right)\dfrac{1}{k_0}\|g\|_{\mathcal{Q}'} \\ \|p_h\|_\mathcal{Q} \leq \dfrac{1}{k_0}\left(\dfrac{\|a\|}{\alpha_0} + 1\right)\|f\|_{\mathcal{V}'} + \dfrac{\|a\|}{k_0^2}\left(\dfrac{\|a\|}{\alpha_0} + 1\right)\|g\|_{\mathcal{Q}'}. \end{cases} \tag{B.12}$$

Proof. The inf-sup condition (B.11) ensures that $\operatorname{Ker} B_h^t = \{0\}$, then Proposition 2.2, §II.2 in (Brezzi and Fortin, 2012) ensures that $g \in \operatorname{Im} B_h$. The ellipticity of a on $\mathcal{V}_h$ inherits from the one on $\mathcal{V}$, and the application of Theorem 1.1, §II.1 in (Brezzi and Fortin, 2012) on the discrete problem gives the results. ■

Remark 19
In the case of a Stokes problem, $a(\cdot,\cdot)$ is elliptic and it is known that $\operatorname{Ker} B^t = \operatorname{Ker}(-\mathrm{grad}) = \{0\}$ when a Dirichlet condition is applied on a non-empty portion of the boundary, so the issue is in checking (B.11), with $b(v,q) = \int_\Omega q \operatorname{div} v \, d\Omega$.

Proposition 12 (Inf-sup property on M)
Let us make the following assumptions:

- *there exists* λ_{f} *such that*

$$\inf_{p\in Q_h}\sup_{\underline{v}_{\mathrm{f}}\in W_h^{\mathrm{f}}}\frac{(p,\operatorname{div}\underline{v}_{\mathrm{f}})_{\Omega_{\mathrm{f}}}}{\|p\|_{L^2(\Omega_{\mathrm{f}})}\|\underline{v}_{\mathrm{f}}\|_{H^1(\Omega_{\mathrm{f}})}}\geq\lambda_{\mathrm{f}}>0, \tag{B.13}$$

- W_h^{f} *and* W_h^{s} *have identical traces on* Σ*, that is*

$$\left\{\underline{v}_{\mathrm{f}}|_\Sigma,\underline{v}_{\mathrm{f}}\in W_h^{\mathrm{f}}\right\}=\left\{\underline{v}_{\mathrm{s}}|_\Sigma,\underline{v}_{\mathrm{s}}\in W_h^{\mathrm{s}}\right\}, \tag{B.14}$$

- *the Robin coefficient satisfies*

$$\gamma>2C_{ie}. \tag{B.15}$$

Then the operator M *defined by* (B.4) *satisfies an inf-sup property for* $\|\cdot\|_h$*: there exists* $\beta>0$ *independent of* h *such that*

$$\inf_{X\in V_h}\sup_{X^*\in V_h}\frac{M(X,X^*)}{\|X\|_h\|X^*\|_h}\geq\beta,$$

or, equivalently

$$\forall X\in V_h,\exists X^*\in V_h\quad|\quad\|X^*\|_h\leq\|X\|_h\quad\textit{and}\quad M(X,X^*)\geq\beta\|X\|_h^2.$$

Remark 20
In the numerical resolution, condition (B.13) comes down to a well known condition on $W_h^{\mathrm{f}}\times Q_h$ for variables $\underline{v}_{\mathrm{f}}$ and p.

Proof. Let $X_h=\left[\underline{v}_{\mathrm{f},h},\underline{v}_{\mathrm{s},h},\underline{y}_{\mathrm{s},h},p_h\right]$ in V_h, we will build an $\bar{X}_h=\left[\underline{v}^*_{\mathrm{f},h},\underline{v}^*_{\mathrm{s},h},\underline{y}^*_{\mathrm{s},h},p^*\right]$ in V_h and a $\beta>0$ that satisfies the above condition in several steps, in order to control the different terms that appear in $\|\cdot\|_h$.

1. We define $X_h^1=\left[0,0,-\underline{v}_{\mathrm{s},h},0\right]$, then $M(X_h,X_h^1)\geq\alpha_1\|\underline{v}_{\mathrm{s},h}\|^2_{H^1(\Omega_{\mathrm{s}})}$, with $\alpha_1>0$.

2. We pick $X_h^2=X_h$. The energy bound derived in Section 4.2.3 gives for any length L

$$\begin{aligned}M(X_h,X_h^2)&=2\mu\|\underline{\varepsilon}(\underline{v}_{\mathrm{f},h})\|^2_{L^2(\Omega_{\mathrm{f}})}+\frac{\gamma\mu}{h}\|\underline{v}_{\mathrm{f},h}-\underline{v}_{\mathrm{s},h}\|^2_{L^2(\Sigma)}-4\mu\left(\underline{\varepsilon}(\underline{v}_{\mathrm{f},h})\underline{n}_{\mathrm{f}},\underline{v}_{\mathrm{f},h}-\underline{v}_{\mathrm{s},h}\right)_{L^2(\Sigma)}\\&\geq 2\mu\left(1-\frac{C_{ie}L}{h}\right)\|\underline{\varepsilon}(\underline{v}_{\mathrm{f},h})\|^2_{L^2(\Omega_{\mathrm{f}})}+\mu\left(\frac{\gamma}{h}-\frac{2}{L}\right)\|\underline{v}_{\mathrm{f},h}-\underline{v}_{\mathrm{s},h}\|^2_{L^2(\Sigma)}.\end{aligned}$$

   Thanks to the assumption on γ, and norm equivalences, we build $\alpha_2>0$ such that

$$M(X_h,X_h^2)\geq\alpha_2\left(\|\underline{v}_{\mathrm{f},h}\|^2_{H^1(\Omega_{\mathrm{f}})}+\frac{\gamma\mu}{h}\|\underline{v}_{\mathrm{f},h}-\underline{v}_{\mathrm{s},h}\|^2_{L^2(\Sigma)}\right).$$

3. Thanks to (B.14), we define $\mathcal{L}(\underline{y}_{\mathrm{s},h})$ a lifting of $\underline{y}_{\mathrm{s},h}|_\Sigma$ in W_h^{f} satisfying

$$\|\mathcal{L}(\underline{y}_{\mathrm{s},h})\|_{H^1(\Omega_{\mathrm{f}})}\leq C\|\underline{y}_{\mathrm{s},h}\|_{H^{\frac{1}{2}}(\Sigma)}.$$

   According to Remark 19 and thanks to (B.13), Lemma 11 ensures the existence of $(\underline{w}_h^3,p_h^3)$ in $W_h^{\mathrm{f}}\times Q_h$ such that for any $(\underline{w}^*,p^*)$ in $W_h^{\mathrm{f}}\times Q_h$

$$\begin{cases}\left(\underline{\varepsilon}(\underline{w}_h^3),\underline{\varepsilon}(\underline{w}^*)\right)_{\Omega_{\mathrm{f}}}+\left(p_h^3,\operatorname{div}\underline{w}^*\right)_{\Omega_{\mathrm{f}}}=0,\\ \left(p^*,\operatorname{div}\underline{w}_h^3\right)_{\Omega_{\mathrm{f}}}=-\left(p^*,\operatorname{div}\mathcal{L}(\underline{y}_{\mathrm{s},h})\right)_{\Omega_{\mathrm{f}}},\\ \underline{w}_h^3|_\Sigma=0,\end{cases} \tag{B.16}$$

and for C and C' independent of h, see (B.12) and (B.5),

$$\|\underline{w}_h^3\|_{H^1(\Omega_\mathrm{f})} \leq C'\|\mathcal{L}(\underline{y}_{\mathrm{s},h})\|_{H^1(\Omega_\mathrm{f})} \leq C\|\underline{y}_{\mathrm{s},h}\|_{H^1(\Omega_\mathrm{f})}.$$

Now let us construct $X_h^3 = \left[\underline{v}_{\mathrm{f},h}^3, \underline{y}_{\mathrm{s},h}, 0, 0\right]$, with $\underline{v}_{\mathrm{f},h}^3 = \mathcal{L}(\underline{y}_{\mathrm{s},h}) + \underline{w}_h^3$; then

$$\|\underline{v}_{\mathrm{f},h}^3\|_{H^1(\Omega_\mathrm{f})} \leq C\|\underline{y}_{\mathrm{s},h}\|_{H^1(\Omega_\mathrm{f})}.$$

The purpose of this construction is to get a $\underline{v}_{\mathrm{f},h}^3$ that satisfies $\left(p_h, \operatorname{div} \underline{v}_{\mathrm{f},h}^3\right)_{\Omega_\mathrm{f}} = 0$ and $\underline{v}_{\mathrm{f},h}^3 = \underline{y}_{\mathrm{s},h}$ on Σ, which finally allows to write that, for any (η_1, η_2, η_3) in $(\mathbb{R}^+)^3$

$$M(X_h, X_h^3) = 2\mu\left(\underline{\underline{\varepsilon}}(\underline{v}_{\mathrm{f},h}) : \underline{\underline{\varepsilon}}(\underline{v}_{\mathrm{f},h}^3)\right)_{\Omega_\mathrm{f}} + \left(\underline{y}_{\mathrm{s},h}, \underline{y}_{\mathrm{s},h}\right)_{\mathrm{skel}} - 2\mu\left(\underline{\underline{\varepsilon}}(\underline{v}_{\mathrm{f},h}^3)\cdot\underline{n}_\mathrm{f}, \underline{v}_{\mathrm{f},h} - \underline{v}_{\mathrm{s},h}\right)_\Sigma.$$

Using Young inequality we have

$$\begin{aligned} M(X_h, X_h^3) \geq -\mu\left(\eta_1\|\underline{\underline{\varepsilon}}(\underline{v}_{\mathrm{f},h}^3)\|_{\Omega_\mathrm{f}}^2 + \frac{1}{\eta_1}\|\underline{\underline{\varepsilon}}(\underline{v}_{\mathrm{f},h})\|_{\Omega_\mathrm{f}}^2\right) + C\|\underline{y}_{\mathrm{s},h}\|_{H^1(\Omega_\mathrm{s})}^2 \\ - \mu\left(\eta_2\|\underline{\underline{\varepsilon}}(\underline{v}_{\mathrm{f},h}^3)\|_\Sigma^2 + \frac{1}{\eta_2}\|\underline{v}_{\mathrm{f},h} - \underline{v}_{\mathrm{s},h}\|_\Sigma^2\right). \end{aligned}$$

And the trace inverse inequality gives

$$M(X_h, X_h^3) \geq \left[C - \left(\mu\eta_1 + \mu\eta_2\frac{C_{ie}}{h}\right)\right]\|\underline{y}_{\mathrm{s},h}\|_{H^1(\Omega_\mathrm{s})}^2 - \frac{\mu}{\eta_1}\|\underline{\underline{\varepsilon}}(\underline{v}_{\mathrm{f},h})\|_{\Omega_\mathrm{f}}^2 - \frac{\mu}{\eta_2}\|\underline{v}_{\mathrm{f},h} - \underline{v}_{\mathrm{s},h}\|_\Sigma^2.$$

Choosing for example

$$\eta_1 = \frac{C}{2}\left(\mu + \frac{C_{ie}}{\gamma}\right)^{-1},\ \eta_2 = \frac{h\eta_1}{\gamma\mu},\ \text{and defining } \alpha_3 = \frac{C}{2} \text{ and } \beta_3 = \frac{\mu}{\eta_1}$$

– α_3 and β_3 are obviously independent of h – we end up with

$$M(X_h, X_h^3) \geq \alpha_3\|\underline{y}_{\mathrm{s},h}\|_{H^1(\Omega_\mathrm{s})}^2 - \beta_3\left(\|\underline{v}_{\mathrm{f},h}\|_{H^1(\Omega_\mathrm{f})}^2 + \frac{\gamma\mu}{h}\|\underline{v}_{\mathrm{f},h} - \underline{v}_{\mathrm{s},h}\|_{L^2(\Sigma)}^2\right).$$

In addition, there exists $\gamma_3 > 0$ such that

$$\|X_h^3\|_h = \|\underline{v}_{\mathrm{f},h}^3\|_{H^1(\Omega_\mathrm{f})}^2 + \|\underline{y}_{\mathrm{s},h}\|_{H^1(\Omega_\mathrm{s})}^2 \leq \gamma_3\|\underline{y}_{\mathrm{s},h}\|_{H^1(\Omega_\mathrm{s})}^2 \leq \gamma_3\|X_h\|_h.$$

4. As a consequence of (B.13), we can construct $\underline{v}_{\mathrm{f},h}^4$ such that for a positive λ,

$$\begin{cases} \|\underline{v}_{\mathrm{f},h}^4\|_{H^1(\Omega_\mathrm{f})} \leq \|p_h\|_{L^2(\Omega_\mathrm{f})}, \\ -\left(p_h, \operatorname{div} \underline{v}_{\mathrm{f},h}^4\right)_{\Omega_\mathrm{f}} \geq \lambda\|p_h\|_{L^2(\Omega_\mathrm{f})}^2. \end{cases} \tag{B.17}$$

Once again, (B.14) allows to introduce $\underline{v}_{\mathrm{s},h}^4 = \mathcal{L}(\underline{v}_{\mathrm{f},h}^4)$ a lifting of $\underline{v}_{\mathrm{f},h}^4|_\Sigma$ in W_h^s such that

$$\|\mathcal{L}(\underline{v}_{\mathrm{f},h}^4)\|_{H^1(\Omega_\mathrm{f})} \leq C\|\underline{v}_{\mathrm{f},h}^4\|_{H^{\frac{1}{2}}(\Sigma)},$$

and we have, see (B.5), for C and C' independent of h

$$\|\underline{v}_{\mathrm{s},h}^4\|_{H^1(\Omega_\mathrm{s})} = \|\mathcal{L}(\underline{v}_{\mathrm{f},h}^4)\|_{H^1(\Omega_\mathrm{f})} \leq C'\|\underline{v}_{\mathrm{f},h}^4\|_{H^1(\Omega_\mathrm{f})} \leq C\|p_h\|_{L^2(\Omega_\mathrm{f})}.$$

Finally, we build $X_h^4 = \left[\underline{v}_{\mathrm{f},h}^4, \underline{v}_{\mathrm{s},h}^4, 0, 0\right]$. This construction gives a control on p_h through the divergence term. It also imposes $\underline{v}_{\mathrm{f},h}^4 = \underline{v}_{\mathrm{s},h}^4$ on Σ, and finally allows to write that, for any $(\eta_1, \eta_2, \eta_3, \eta_4)$ in $(\mathbb{R}^+)^4$,

$$M(X_h, X_h^4) = 2\mu \left(\underline{\underline{\varepsilon}}(\underline{v}_{\mathrm{f},h}) : \underline{\underline{\varepsilon}}(\underline{v}_{\mathrm{f},h}^4)\right)_{\Omega_\mathrm{f}} + \left(\underline{y}_{\mathrm{s},h}, \underline{v}_{\mathrm{s},h}^4\right)_{\mathrm{skel}} - \left(\underline{\underline{\sigma}}_{\mathrm{vis}}(\underline{v}_{\mathrm{f},h}^4) \cdot \underline{n}_\mathrm{f}, \underline{v}_{\mathrm{f},h} - \underline{v}_{\mathrm{s},h}\right)_\Sigma - \left(p_h, \operatorname{div} \underline{v}_{\mathrm{f},h}^4\right)_{\Omega_\mathrm{f}}$$

Young and trace inverse inequalities now give

$$M(X_h, X_h^4) \geq -\left(\eta_1 C \|\underline{v}_{\mathrm{f},h}\|_{H^1(\Omega_\mathrm{f})}^2 + \frac{C}{\eta_1}\|p_h\|_{L^2(\Omega_\mathrm{f})}^2\right) - \left(\eta_2 C \|\underline{y}_{\mathrm{s},h}\|_{H^1(\Omega_\mathrm{s})}^2 + \frac{1}{\eta_2} C \|p_h\|_{L^2(\Omega_\mathrm{f})}^2\right) - \left(\eta_3 \frac{C_{ie}}{h}\|p_h\|_{L^2(\Omega_\mathrm{f})}^2 + \frac{1}{\eta_3} C \|\underline{v}_{\mathrm{f},h} - \underline{v}_{\mathrm{s},h}\|_{L^2(\Sigma)}^2\right) + \lambda \|p_h\|_{L^2(\Omega_\mathrm{f})}^2.$$

We apply it to

$$\eta_1 = \eta_2 = \frac{4C}{\lambda},\ \eta_3 = \frac{h\lambda}{5C_{ie}},\ \text{ and we define } \alpha_4 = \frac{\lambda}{4} \text{ and } \beta_4 = \max\left(\eta_1 C, \frac{4C_{ie}C}{\gamma\mu\lambda}\right),$$

α_4 and β_4 don't depend on h and we end up with

$$M(X_h, X_h^4) \geq \alpha_4 \|p_h\|_{L^2(\Omega_\mathrm{f})} - \beta_4 \left(\|\underline{v}_{\mathrm{f},h}\|_{H^1(\Omega_\mathrm{f})}^2 + \|\underline{y}_{\mathrm{s},h}\|_{H^1(\Omega_\mathrm{s})}^2 + \frac{\gamma\mu}{h}\|\underline{v}_{\mathrm{f},h} - \underline{v}_{\mathrm{s},h}\|_{L^2(\Sigma)}^2\right).$$

We also have the following bound

$$\|X_h^4\|_h = \|\underline{v}_{\mathrm{f},h}^4\|_{H^1(\Omega_\mathrm{f})}^2 + \|\underline{v}_{\mathrm{s},h}^4\|_{H^1(\Omega_\mathrm{s})}^2 \leq \gamma_4 \|p_h\|_{L^2(\Omega_\mathrm{f})}^2 \leq \gamma_4 \|X_h\|_h^2.$$

Now, let us define the following positive coefficients, that don't depend on h,

$$\delta_3 = \frac{\alpha_2}{\alpha_3 + 2\beta_3},\ \delta_4 = \frac{\alpha_3\delta_3}{2\beta_4},\ \text{ and } \beta = \min\left(\frac{\alpha_2}{2}, \alpha_1, \frac{\delta_3\alpha_3}{2}, \delta_4\alpha_4\right)$$

and let us introduce $\bar{X_h} = X_h^1 + X_h^2 + \delta_3 X_h^3 + \delta_4 X_h^4$. By construction, we end up with

$$\begin{aligned}
M(X_h, \bar{X_h}) \geq\ & \alpha_1 \|\underline{v}_{\mathrm{s},h}\|_{H^1(\Omega_\mathrm{s})}^2 + \alpha_2 \left(\|\underline{v}_{\mathrm{f},h}\|_{H^1(\Omega_\mathrm{f})}^2 + \frac{\gamma\mu}{h}\|\underline{v}_{\mathrm{f},h} - \underline{v}_{\mathrm{s},h}\|_{L^2(\Sigma)}^2\right) \\
& + \delta_3\alpha_3 \|\underline{y}_{\mathrm{s},h}\|_{H^1(\Omega_\mathrm{s})}^2 - \delta_3\beta_3 \left(\|\underline{v}_{\mathrm{f},h}\|_{H^1(\Omega_\mathrm{f})}^2 + \frac{\gamma\mu}{h}\|\underline{v}_{\mathrm{f},h} - \underline{v}_{\mathrm{s},h}\|_{L^2(\Sigma)}^2\right) \\
& + \delta_4\alpha_4 \|p_h\|_{L^2(\Omega_\mathrm{f})} - \delta_4\beta_4 \left(\|\underline{v}_{\mathrm{f},h}\|_{H^1(\Omega_\mathrm{f})}^2 + \|\underline{y}_{\mathrm{s},h}\|_{H^1(\Omega_\mathrm{s})}^2 + \frac{\gamma\mu}{h}\|\underline{v}_{\mathrm{f},h} - \underline{v}_{\mathrm{s},h}\|_{L^2(\Sigma)}^2\right) \\
\geq\ & (\alpha_2 - \delta_3\beta_3 - \delta_4\beta_4) \left(\|\underline{v}_{\mathrm{f},h}\|_{H^1(\Omega_\mathrm{f})}^2 + \frac{\gamma\mu}{h}\|\underline{v}_{\mathrm{f},h} - \underline{v}_{\mathrm{s},h}\|_{L^2(\Sigma)}^2\right) \\
& + \alpha_1 \|\underline{v}_{\mathrm{s},h}\|_{H^1(\Omega_\mathrm{s})}^2 + (\delta_3\alpha_3 - \delta_4\beta_4)\|\underline{y}_{\mathrm{s},h}\|_{H^1(\Omega_\mathrm{s})}^2 + \delta_4\alpha_4 \|p_h\|_{L^2(\Omega_\mathrm{f})}^2 \\
\geq\ & \beta \|X_h\|_h^2,
\end{aligned}$$

and

$$\|\bar{X_h}\|_h \leq (2 + \delta_3\gamma_3 + \delta_4\gamma_4)\|X_h\|_h.$$

We conclude the proof with the following two inequalities

$$\left\|\frac{\bar{X_h}}{2 + \delta_3\gamma_3 + \delta_4\gamma_4}\right\|_h \leq \|X_h\|_h \quad \text{and} \quad M\left(X_h, \frac{\bar{X_h}}{2 + \delta_3\gamma_3 + \delta_4\gamma_4}\right) \geq \frac{\beta}{2 + \delta_3\gamma_3 + \delta_4\gamma_4}\|X_h\|_h^2.$$

■

B.2.4 Convergence in time and space of the fully discretized scheme solution

We introduce $V^+ = H^2(\Omega_\mathrm{f})^3 \times (H^2(\Omega_\mathrm{s})^3)^2 \times H^1(\Omega_\mathrm{f})$ a new state function space with more regularity, and denote as follows the two natural norms over V and V^+,

$$\|X\|_V^2 = \|\underline{v}_\mathrm{f}\|_{H^1(\Omega_\mathrm{f})}^2 + \|\underline{v}_\mathrm{s}\|_{H^1(\Omega_\mathrm{s})}^2 + \|\underline{y}_\mathrm{s}\|_{H^1(\Omega_\mathrm{s})}^2 + \|p\|_{L^2(\Omega_\mathrm{f})}^2,$$
$$\|X\|_{V^+}^2 = \|\underline{v}_\mathrm{f}\|_{H^2(\Omega_\mathrm{f})}^2 + \|\underline{v}_\mathrm{s}\|_{H^2(\Omega_\mathrm{s})}^2 + \|\underline{y}_\mathrm{s}\|_{H^2(\Omega_\mathrm{s})}^2 + \|p\|_{H^1(\Omega_\mathrm{f})}^2.$$

We also introduce $V^- = L^2(\Omega_\mathrm{f})^3 \times L^2(\Omega_\mathrm{s})^3 \times H^1(\Omega_\mathrm{s})^3 \times L^2(\Omega_\mathrm{f})$, whose natural norm is equivalent to $\|\cdot\|_\mathcal{E}$.

The continuous solution $X = (\underline{v}_\mathrm{f}, \underline{v}_\mathrm{s}, \underline{y}_\mathrm{s}, p)$ in V of (B.1) satisfies, for any $(\underline{v}_\mathrm{f}^*, \underline{v}_\mathrm{s}^*, \underline{y}_\mathrm{s}^*, p^*)$ in V, at any time t,

$$\rho_\mathrm{f} \left(\partial_t \underline{v}_\mathrm{f}, \underline{v}_\mathrm{f}^*\right)_{\Omega_\mathrm{f}} + \rho_\mathrm{s} \left(\partial_t \underline{v}_\mathrm{s}, \underline{v}_\mathrm{s}^*\right)_{\Omega_\mathrm{s}} + \left(\partial_t \underline{y}_\mathrm{s}, \underline{y}_\mathrm{s}^*\right)_\mathrm{skel} + M((\underline{v}_\mathrm{f}, \underline{v}_\mathrm{s}, \underline{y}_\mathrm{s}, p), (\underline{v}_\mathrm{f}^*, \underline{v}_\mathrm{s}^*, \underline{y}_\mathrm{s}^*, p^*)) = 0. \quad \text{(B.18)}$$

The discrete solution $(X_h^n = (\underline{v}_{\mathrm{f},h}^n, p_h^n, \underline{y}_{\mathrm{s},h}^n, \underline{v}_{\mathrm{s},h}^n))_{n\geq 0}$ in $(V_h)^\mathbb{N}$ is such that for any $n \geq 0$, and any $(\underline{v}_\mathrm{f}^*, \underline{v}_\mathrm{s}^*, \underline{y}_\mathrm{s}^*, p^*)$ in V_h

$$\rho_\mathrm{f} \left(D_\tau \underline{v}_{\mathrm{f},h}^{n+\frac{1}{2}}, \underline{v}_\mathrm{f}^*\right)_{\Omega_\mathrm{f}} + \rho_\mathrm{s} \left(D_\tau \underline{v}_{\mathrm{s},h}^{n+\frac{1}{2}}, \underline{v}_\mathrm{s}^*\right)_{\Omega_\mathrm{s}} + \left(D_\tau \underline{y}_{\mathrm{s},h}^{n+\frac{1}{2}}, \underline{y}_\mathrm{s}^*\right)_\mathrm{skel}$$
$$+ M((\underline{v}_{\mathrm{f},h}^{n+1}, \underline{v}_{\mathrm{s},h}^{n+\frac{1}{2}}, \underline{y}_{\mathrm{s},h}^{n+\frac{1}{2}}, p_h^{n+1}), (\underline{v}_\mathrm{f}^*, \underline{v}_\mathrm{s}^*, \underline{y}_\mathrm{s}^*, p^*)) = 0. \quad \text{(B.19)}$$

The purpose of this section is to establish the following convergence result.

Proposition 13 (Total convergence)
Assuming that conditions (B.13), (B.14) and (B.15) are satisfied, and that the solution X of (B.1) belongs to $\mathcal{C}^1(0,T,V^+) \cap \mathcal{C}^2(0,T,V^-)$, with T the duration of the simulation , then there exists a constant C depending only on $\|X\|_{L^\infty(0,T,V^+)}$, $\|\partial_t X\|_{L^\infty[0,T,V^+]}$ and $\|\partial_t^2 X\|_{L^\infty[0,T,\mathcal{E}]}$ such that

$$\|X_h^n - X(t^n)\|_\mathcal{E} \leq C(h + \Delta t),$$

where $(X_h^n)_{n\geq 0}$ is the solution of (B.8) and we remind that

$$X_h^n - X(t^n) = \left[\underline{v}_{\mathrm{f},h}^n - \underline{v}_\mathrm{f}(t^n),\ p_h^n - p(t^n),\ \underline{v}_{\mathrm{s},h}^n - \underline{v}_\mathrm{s}(t^n),\ \underline{y}_{\mathrm{s},h}^n - \underline{y}_\mathrm{s}(t^n)\right].$$

Proof. Let us introduce the projection $P = \left[P_h^\mathrm{f}, P_h^\mathrm{s}, P_h^\mathrm{y}, P_h^\mathrm{p}\right]$ such that,

$$\forall X^* = (\underline{v}_\mathrm{f}^*, \underline{v}_\mathrm{s}^*, \underline{y}_\mathrm{s}^*, p^*) \in V_h, \quad M(PX, X^*) = M(X, X^*) \quad \text{i.e.}$$
$$M((P_h^\mathrm{f}\underline{v}_\mathrm{f}, P_h^\mathrm{s}\underline{v}_\mathrm{s}, P_h^\mathrm{y}\underline{y}_\mathrm{s}, P_h^\mathrm{p}p), (\underline{v}_\mathrm{f}^*, \underline{v}_\mathrm{s}^*, \underline{y}_\mathrm{s}^*, p^*)) = M((\underline{v}_\mathrm{f}, \underline{v}_\mathrm{s}, \underline{y}_\mathrm{s}, p), (\underline{v}_\mathrm{f}^*, \underline{v}_\mathrm{s}^*, \underline{y}_\mathrm{s}^*, p^*)). \quad \text{(B.20)}$$

We begin with establishing

Lemma 14
Under the hypothesis of Proposition 12, there exists a constant C independent of h such that, for any X in V^+ satisfying $X_1 = X_2$ on Σ,

$$\|PX - X\|_\mathcal{E} \leq Ch\|X\|_{V^+}.$$

Remark 21
More generally, with shape functions of order $k > 1$ for PX we have that for any X in $V^k = H^{k+1}(\Omega_\mathrm{f})^3 \times (H^{k+1}(\Omega_\mathrm{s})^3)^2 \times H^k(\Omega_\mathrm{f})$ satisfying $X_1 = X_2$ on Σ,

$$\|PX - X\|_{\mathcal{E}} \leq Ch^k \|X\|_{V^k},$$

with $\|\cdot\|_{V^k}$ the natural norm on V^k. To fix the ideas, we will establish it here in the case $k = 1$.

Proof. Under these assumptions, let us introduce the Clément (Clément, 1975) interpolation $I_h X$ in V_h that satisfies

$$\begin{cases} \|X - I_h X\|_V \leq Ch\|X\|_{V^+}, \\ \|I_h X\|_V \leq C\|X\|_V, \\ (I_h X)_1 = (I_h X)_2 \quad \text{on } \Sigma, \\ \|(I_h X - X)_4\|_{L^2(\Sigma)} \leq Ch^{1/2}\|X_4\|_{H^1(\Omega_\mathrm{f})}, \\ \|(I_h X - X)_1\|_{H^1(\Sigma)} \leq Ch^{1/2}\|X_1\|_{H^2(\Omega_\mathrm{f})}. \end{cases}$$

For $X^* \in V_h$, let us look at the terms of $M(X - I_h X, X^*)$ that are not controlled by $\|\cdot\|_h$. Thanks to the above properties and the Cauchy-Schwarz inequality,

$$\begin{aligned} (p - I_h p, (\underline{v}_\mathrm{f}^* - \underline{v}_\mathrm{s}^*) \cdot \underline{n}_\mathrm{f})_\Sigma &\leq h^{1/2}\|p - I_h p\|_{L^2(\Sigma)} \cdot \frac{1}{h^{1/2}}\|\underline{v}_\mathrm{f}^* - \underline{v}_\mathrm{s}^*\|_{L^2(\Sigma)} \\ &\leq Ch\|X\|_{V^+}\|X^*\|_h \end{aligned}$$

The same argument enables us to control $2\mu(\underline{\underline{\varepsilon}}(\underline{v}_\mathrm{f} - I_h \underline{v}_\mathrm{f}) \cdot \underline{n}_\mathrm{f}, \underline{v}_\mathrm{f}^* - \underline{v}_\mathrm{s}^*)_\Sigma$, the Robin term vanishes because by construction $(X - I_h X)_1 = (X - I_h X)_2$ on Σ, and all other terms are controlled with Cauchy-Schwarz. We end up with, for C independent of h,

$$M(X - I_h X, X^*) \leq Ch\|X\|_{V^+}\|X^*\|_h. \tag{B.21}$$

Now, Proposition 12 ensures the existence of X^* in V_h such that

$$\|X^*\|_h = 1 \text{ and } M(PX - I_h X, X^*) \geq \gamma\|PX - I_h X\|_h,$$

and we recall that by definition of P,

$$M(PX - I_h X, X^*) = M(X - I_h X, X^*),$$

therefore, using (B.21)

$$\begin{aligned} \gamma\|PX - I_h X\|_h &\leq M(X - I_h X, X^*) \\ &\leq Ch\|X\|_{V^+}. \end{aligned}$$

Finally, using that $\|\cdot\|_{\mathcal{E}} \leq \|\cdot\|_h$, and by construction of $I_h X$, the triangular inequality gives, with C independent of h,

$$\begin{aligned} \|PX - X\|_{\mathcal{E}} &\leq \|PX - I_h X\|_{\mathcal{E}} + \|I_h X - X\|_{\mathcal{E}} \\ &\leq Ch\|X\|_{V^+} + Ch\|X\|_{V^+}. \end{aligned}$$

■

We can now proceed with the proof of Proposition 13. The inclusion $V_h \subset V$ enables us to choose discrete test functions in (B.18) and by construction of the projectors we get, for any $X^* = (\underline{v}_{\rm f}^*, \underline{v}_{\rm s}^*, \underline{y}_{\rm s}^*, p^*)$ in V_h

$$\rho_{\rm f}\left(\partial_t \underline{v}_{\rm f}, \underline{v}_{\rm f}^*\right)_{\Omega_{\rm f}} + \rho_{\rm s}\left(\partial_t \underline{v}_{\rm s}, \underline{v}_{\rm s}^*\right)_{\Omega_{\rm s}} + \left(\partial_t \underline{y}_{\rm s}, \underline{y}_{\rm s}^*\right)_{\rm skel} + M((P_h^{\rm f}\underline{v}_{\rm f}, P_h^{\rm s}\underline{v}_{\rm s}, P_h^{\rm y}\underline{y}_{\rm s}, P_h^{\rm p}p), (\underline{v}_{\rm f}^*, \underline{v}_{\rm s}^*, \underline{y}_{\rm s}^*, p^*)) = 0. \quad \text{(B.22)}$$

We average the evaluations of (B.22) at time t^n and t^{n+1}, and gather consistency errors on the right hand side, to get that for any $X^* = (\underline{v}_{\rm f}^*, \underline{v}_{\rm s}^*, \underline{y}_{\rm s}^*, p^*)$ in V_h,

$$\begin{aligned}
&\rho_{\rm f}\left((D_\tau P_h^{\rm f}\underline{v}_{\rm f})^n, \underline{v}_{\rm f}^*\right)_{\Omega_{\rm f}} + \rho_{\rm s}\left((D_\tau P_h^{\rm s}\underline{v}_{\rm s})^{n+\frac12}, \underline{v}_{\rm s}^*\right)_{\Omega_{\rm s}} + \left((D_\tau P_h^{\rm y}\underline{y}_{\rm s})^{n+\frac12}, \underline{y}_{\rm s}^*\right)_{\rm skel} \\
&\quad + M(((P_h^{\rm f}\underline{v}_{\rm f})^{n+\frac12}, (P_h^{\rm s}\underline{v}_{\rm s})^{n+\frac12}, (P_h^{\rm y}\underline{y}_{\rm s})^{n+\frac12}, (P_h^{\rm p}p)^{n+\frac12}), (\underline{v}_{\rm f}^*, \underline{v}_{\rm s}^*, \underline{y}_{\rm s}^*, p^*)) \\
&= \rho_{\rm f}\left((D_\tau P_h^{\rm f}\underline{v}_{\rm f})^n - (\partial_t \underline{v}_{\rm f})^{n+\frac12}, \underline{v}_{\rm f}^*\right)_{\Omega_{\rm f}} + \rho_{\rm s}\left((D_\tau P_h^{\rm s}\underline{v}_{\rm s})^{n+\frac12} - (\partial_t \underline{v}_{\rm s})^{n+\frac12}, \underline{v}_{\rm s}^*\right)_{\Omega_{\rm s}} \\
&\quad + \left((D_\tau P_h^{\rm y}\underline{y}_{\rm s})^{n+\frac12} - (\partial_t \underline{y}_{\rm s})^{n+\frac12}, \underline{y}_{\rm s}^*\right)_{\rm skel}, \quad \text{(B.23)}
\end{aligned}$$

where we defined for any function g continuous in time,

$$(D_\tau g)^{n+\frac12} = \frac{g(t^{n+1}) - g(t^n)}{\Delta t}, (D_\tau g)^n = \frac{g(t^{n+1}) - g(t^{n-1})}{2\Delta t}, \quad \text{and} \quad (g)^{n+\frac12} = \frac{g(t^{n+1}) + g(t^n)}{2}.$$

Now let us introduce

$$\tilde{X}_h^n = X_h^n - (PX)^n \quad \text{with} \quad (PX)^n = \left[(P_h^{\rm f}\underline{v}_{\rm f})^{n-\frac12}, P_h^{\rm s}\underline{v}_{\rm s}(t^n), P_h^{\rm y}\underline{y}_{\rm s}(t^n), (P_h^{\rm p}p)^{n-\frac12}\right]$$

and let us denote by $\mathcal{A}(\underline{v}_{\rm f}^*, \underline{v}_{\rm s}^*, \underline{y}_{\rm s}^*, p^*)$ the right hand side of (B.23) (the consistency terms). Then the subtraction (B.19) - (B.23) gives, for any $X^* = (\underline{v}_{\rm f}^*, \underline{v}_{\rm s}^*, \underline{y}_{\rm s}^*, p^*)$ in V_h,

$$\begin{aligned}
&\rho_{\rm f}\left(D_\tau \tilde{\underline{v}}_{{\rm f},h}^{n+\frac12}, \underline{v}_{\rm f}^*\right)_{\Omega_{\rm f}} + \rho_{\rm s}\left(D_\tau \tilde{\underline{v}}_{{\rm s},h}^{n+\frac12}, \underline{v}_{\rm s}^*\right)_{\Omega_{\rm s}} + \left(D_\tau \tilde{\underline{y}}_{{\rm s},h}^{n+\frac12}, \underline{y}_{\rm s}^*\right)_{\rm skel} \\
&\quad + M((\tilde{\underline{v}}_{{\rm f},h}^{n+1}, \tilde{\underline{v}}_{{\rm s},h}^{n+\frac12}, \tilde{\underline{y}}_{{\rm s},h}^{n+\frac12}, \tilde{p}_h^{n+1}), (\underline{v}_{\rm f}^*, \underline{v}_{\rm s}^*, \underline{y}_{\rm s}^*, p^*)) = \mathcal{A}(\underline{v}_{\rm f}^*, \underline{v}_{\rm s}^*, \underline{y}_{\rm s}^*, p^*). \quad \text{(B.24)}
\end{aligned}$$

Proceeding as in the energy stability analysis, we evaluate the previous equation with the following functions that are admissible:

$$\underline{v}_{{\rm f},h}^* = \tilde{\underline{v}}_{{\rm f},h}^{n+1}, \quad \underline{v}_{{\rm s},h}^* = \tilde{\underline{v}}_{{\rm s},h}^{n+\frac12}, \text{ and } \underline{y}_{{\rm s},h}^* = \tilde{\underline{y}}_{{\rm s},h}^{n+\frac12}, \quad p_h^* = \tilde{p}_h^{n+1}.$$

Let us introduce, for the evaluation of the right hand side of equation (B.24)

$$\mathcal{A} = \mathcal{A}(\tilde{\underline{v}}_{{\rm f},h}^{n+1}, \tilde{\underline{v}}_{{\rm s},h}^{n+\frac12}, \tilde{\underline{y}}_{{\rm s},h}^{n+\frac12}, \tilde{p}_h^{n+1})$$

and the energy of the error at iteration n

$$\tilde{\mathcal{E}}^n = \frac{\rho_{\rm f}}{2}\|\tilde{\underline{v}}_{{\rm f},h}^n\|_{\Omega_{\rm f}}^2 + \frac{\rho_s}{2}\|\tilde{\underline{v}}_{{\rm s},h}^n\|_{\Omega_{\rm s}}^2 + \frac12\|\tilde{\underline{y}}_{{\rm s},h}^n\|_{\rm skel}^2.$$

Then the same derivation as in Section B.2.2 gives

$$\begin{aligned}
\mathcal{A} = \frac{\tilde{\mathcal{E}}^{n+1} - \tilde{\mathcal{E}}^n}{\Delta t} + \frac{\rho_{\rm f}}{2\Delta t}\|\tilde{\underline{v}}_{{\rm f},h}^{n+1} - \tilde{\underline{v}}_{{\rm f},h}^n\|_{\Omega_{\rm f}}^2 + 2\mu\|\underline{\varepsilon}(\tilde{\underline{v}}_{{\rm f},h}^{n+1})\|_{\Omega_{\rm f}}^2 + \frac{\gamma\mu}{h}\|\tilde{\underline{v}}_{{\rm s},h}^{n+\frac12} - \tilde{\underline{v}}_{{\rm f},h}^{n+1}\|_\Sigma^2 \\
\underbrace{- 4\mu(\underline{\varepsilon}(\tilde{\underline{v}}_{{\rm f},h}^{n+1})\underline{n}_{\rm f}, \tilde{\underline{v}}_{{\rm f},h}^{n+1} - \tilde{\underline{v}}_{{\rm s},h}^{n+\frac12})_\Sigma}_{\mathcal{T}_1}, \quad \text{(B.25)}
\end{aligned}$$

with for any length L

$$\mathcal{T}_1 \leq 2\mu \left[L \|\underline{\underline{\varepsilon}}(\tilde{\underline{v}}_{\mathrm{f},h}^{n+1})\underline{n}_{\mathrm{f}}\|_{\Sigma}^2 + \frac{1}{L}\|\tilde{\underline{v}}_{\mathrm{f},h}^{n+1} - \tilde{\underline{v}}_{\mathrm{s},h}^{n+\frac{1}{2}}\|_{\Sigma}^2 \right].$$

We use the trace inverse inequality to get that $\|\underline{\underline{\varepsilon}}(\tilde{\underline{v}}_{\mathrm{f},h}^{n+1})\underline{n}_{\mathrm{f}}\|_{\Sigma}^2 \leq \frac{C_{ie}}{h}\|\underline{\underline{\varepsilon}}(\tilde{\underline{v}}_{\mathrm{f},h}^{n+1})\|_{\Omega}^2$ and

$$\mathcal{T}_1 \leq 2\mu \frac{C_{ie}L}{h}\|\underline{\underline{\varepsilon}}(\tilde{\underline{v}}_{\mathrm{f},h}^{n+1})\|_{\Omega_{\mathrm{f}}}^2 + \frac{2\mu}{L}\|\tilde{\underline{v}}_{\mathrm{f},h}^{n+1} - \tilde{\underline{v}}_{\mathrm{s},h}^{n+\frac{1}{2}}\|_{\Sigma}^2,$$

so that (B.25) turns into

$$\frac{\tilde{\mathcal{E}}^{n+1} - \tilde{\mathcal{E}}^{n}}{\Delta t} \leq 2\mu \left(\frac{C_{ie}L}{h} - 1 \right) \|\underline{\underline{\varepsilon}}(\tilde{\underline{v}}_{\mathrm{f},h}^{n+1})\|_{\Omega_{\mathrm{f}}}^2 + \mu \left(\frac{2}{L} - \frac{\gamma}{h} \right) \|\tilde{\underline{v}}_{\mathrm{f},h}^{n+1} - \tilde{\underline{v}}_{\mathrm{s},h}^{n+\frac{1}{2}}\|_{\Sigma}^2 + \mathcal{A}.$$

Now we must control $\mathcal{A}$, which we decompose as follows:

$$\begin{cases} \mathcal{A}_1 = \rho_{\mathrm{f}} \left((D_\tau P_h^{\mathrm{f}} \underline{v}_{\mathrm{f}})^n - (\partial_t \underline{v}_{\mathrm{f}})^{n+\frac{1}{2}}, \tilde{\underline{v}}_{\mathrm{f},h}^{n+1} \right)_{\Omega_{\mathrm{f}}}, \\ \mathcal{A}_2 = \rho_{\mathrm{s}} \left((D_\tau P_h^{\mathrm{s}} \underline{v}_{\mathrm{s}})^{n+\frac{1}{2}} - (\partial_t \underline{v}_{\mathrm{s}})^{n+\frac{1}{2}}, \tilde{\underline{v}}_{\mathrm{s},h}^{n+\frac{1}{2}} \right)_{\Omega_{\mathrm{s}}}, \\ \mathcal{A}_3 = \left((D_\tau P_h^{\mathrm{y}} \underline{y}_{\mathrm{s}})^{n+\frac{1}{2}} - (\partial_t \underline{y}_{\mathrm{s}})^{n+\frac{1}{2}}, \tilde{\underline{y}}_{\mathrm{s},h}^{n+\frac{1}{2}} \right)_{\mathrm{skel}}. \end{cases}$$

The linearity of P gives,

$$(D_\tau P_h^{\mathrm{f}} \underline{v}_{\mathrm{f}})^n - (\partial_t \underline{v}_{\mathrm{f}})^{n+\frac{1}{2}} = P_h^{\mathrm{f}}(D_\tau \underline{v}_{\mathrm{f}})^n - (D_\tau \underline{v}_{\mathrm{f}})^n + (D_\tau \underline{v}_{\mathrm{f}})^n - \partial_t \underline{v}_{\mathrm{f}}(t^n) + \partial_t \underline{v}_{\mathrm{f}}(t^n) - (\partial_t \underline{v}_{\mathrm{f}})^{n+\frac{1}{2}}.$$

By assumption, $(D_\tau X)^n$ belongs to V^+ and has equal first and second component, so Lemma 14 gives,

$$\begin{aligned} \|P_h^{\mathrm{f}}(D_\tau \underline{v}_{\mathrm{f}})^n - (D_\tau \underline{v}_{\mathrm{f}})^n\|_{\Omega_{\mathrm{f}}} &\leq \|P_h^{\mathrm{f}}(D_\tau X)^n - (D_\tau X)^n\|_{\mathcal{E}} \leq Ch\|(D_\tau X)^n\|_{V^+} \\ &\leq Ch\|\partial_t X\|_{L^\infty[0,T,V^+]}. \end{aligned}$$

Then, thanks to Taylor-Lagrange inequality,

$$\|(D_\tau \underline{v}_{\mathrm{f}})^n - \partial_t \underline{v}_{\mathrm{f}}(t^n)\|_{\Omega_{\mathrm{f}}} \leq C\|\partial_t^2 X\|_{L^\infty[0,T,\mathcal{E}]}\Delta t,$$

and the belonging of $\underline{v}_{\mathrm{f}}$ to $\mathcal{C}^2$ gives

$$\|\partial_t \underline{v}_{\mathrm{f}}(t^n) - (\partial_t \underline{v}_{\mathrm{f}})^{n+\frac{1}{2}}\|_{\Omega_{\mathrm{f}}} \leq C\|\partial_t^2 X\|_{L^\infty[0,T,\mathcal{E}]}\Delta t,$$

Finally, with Cauchy-Schwarz, we end up with

$$\mathcal{A}_1 \leq C_1(h + \Delta t)\|\tilde{\underline{v}}_{\mathrm{f},h}^{n+1}\|_{\Omega_{\mathrm{f}}},$$

The same derivation gives the following bounds for $\mathcal{A}_2$ and $\mathcal{A}_3$,

$$\begin{aligned} \mathcal{A}_2 &\leq C_2(h + \Delta t)\|\tilde{\underline{v}}_{\mathrm{s},h}^{n+\frac{1}{2}}\|_{\Omega_{\mathrm{s}}}, \\ \mathcal{A}_3 &\leq C_3(h + \Delta t)\|\tilde{\underline{y}}_{\mathrm{s},h}^{n+\frac{1}{2}}\|_{\mathrm{skel}}. \end{aligned}$$

Let us note that the C_i's depend on $\|\partial_t^2 X\|_{L^\infty[0,T,\mathcal{E}]}$ and $\|\partial_t X\|_{L^\infty[0,T,V^+]}$.

We end up with, for $C'_A = \max_{1\le i\le 4} C_i$

$$\frac{\tilde{\mathcal{E}}^{n+1}-\tilde{\mathcal{E}}^n}{\Delta t} \le 2\mu\left(\frac{C_{ie}L}{h}-1\right)\|\underline{\varepsilon}(\tilde{\underline{v}}_{\mathrm{f},h}^{n+1})\|^2_{\Omega_\mathrm{f}} + \mu\left(\frac{2}{L}-\frac{\gamma}{h}\right)\left\|\tilde{\underline{v}}_{\mathrm{f},h}^{n+1}-\tilde{\underline{v}}_{\mathrm{s},h}^{n+\frac{1}{2}}\right\|^2_{\Sigma} + C'_A(h+\Delta t)\left(\|\tilde{\underline{v}}_{\mathrm{f},h}^{n+1}\|_{\Omega_\mathrm{f}} + \|\tilde{\underline{v}}_{\mathrm{s},h}^{n+\frac{1}{2}}\|_{\Omega_\mathrm{s}} + \|\tilde{\underline{y}}_{\mathrm{s},h}^{n+\frac{1}{2}}\|_{\mathrm{skel}}\right).$$

Again, the assumption $\gamma > 2C_{ie}$ enables us to choose $L \in [2h/\gamma, h/C_{ie}]$ in order to have

$$\frac{\tilde{\mathcal{E}}^{n+1}-\tilde{\mathcal{E}}^n}{\Delta t} \le C'_A(h+\Delta t)\left(\|\tilde{\underline{v}}_{\mathrm{f},h}^{n+1}\|_{\Omega_\mathrm{f}} + \|\tilde{\underline{v}}_{\mathrm{s},h}^{n+\frac{1}{2}}\|_{\Omega_\mathrm{s}} + \|\tilde{\underline{y}}_{\mathrm{s},h}^{n+\frac{1}{2}}\|_{\mathrm{skel}}\right),$$

or, with the triangular inequality,

$$\tilde{\mathcal{E}}^{i+1}-\tilde{\mathcal{E}}^i \le C'_A\Delta t(h+\Delta t)\left(\sqrt{\tilde{\mathcal{E}}^{i+1}}+\sqrt{\tilde{\mathcal{E}}^i}\right),$$

i.e.

$$\sqrt{\tilde{\mathcal{E}}^{i+1}}-\sqrt{\tilde{\mathcal{E}}^i} \le C'_A\Delta t(h+\Delta t).$$

We sum those inequalities for i from 1 to $n+1$:

$$\sqrt{\tilde{\mathcal{E}}^{n+1}} \le C'_A(n+1)\Delta t(h+\Delta t)+\sqrt{\tilde{\mathcal{E}}^0}.$$

This gives a L^2 convergence of $\tilde{\underline{v}}_{\mathrm{f},h}$, $\tilde{\underline{v}}_{\mathrm{s},h}$ and $\tilde{p}_h$ and a H^1 convergence of $\tilde{\underline{y}}_{\mathrm{s},h}$, in $(h,\Delta t)$, i.e.

$$\|X_h^n-(PX)^n\|_{\mathcal{E}} \le C_A(h+\Delta t), \tag{B.26}$$

with C_A dependent only on $\|\partial_t^2 X\|_{L^\infty[0,T,\mathcal{E}]}$ and $\|\partial_t X\|_{L^\infty[0,T,V^+]}$. In addition, by definition of $(PX)^n$, and thanks to the continuity of P and the $\mathcal{C}^1$ nature of X, we have

$$\|(PX)^n-PX(t^n)\|_{\mathcal{E}} \le C'\Delta t\|\partial_t X\|_{L^\infty[0,T,\mathcal{E}]}. \tag{B.27}$$

The triangular inequality and Lemma 14 conclude the argument:

$$\begin{aligned}\|X_h^n-X(t^n)\|_{\mathcal{E}} &\le \|X_h^n-(PX)^n\|_{\mathcal{E}} + \|(PX)^n-PX(t^n)\|_{\mathcal{E}} + \|PX(t^n)-X(t^n)\|_{\mathcal{E}}\\ &\le C_A(h+\Delta t) + C'\Delta t\|\partial_t X\|_{L^\infty[0,T,\mathcal{E}]} + Ch\|X\|_{L^\infty[0,T,V^+]}.\end{aligned}$$

■

Remark 22
Order of time convergence is only 1 because of the specific choices we made on Section B.2.1, that aims at keeping a time scheme as close as possible to the splitting scheme of Section A.2. Naturally, avoiding the shifting between fluid and solid discretizations (choosing for example a midpoint scheme for fluid) would give us a convergence in Δt^2.

B.3 Conclusion

To conclude, we began this section with deriving a linear problem (B.1) close to the FSI formulation (A.1). In this context, at the discrete level, a monolithic solver directly computes X_h^{n+1} in function of X_h^n. This simplified framework enabled us to establish conditions under which the convergence of our numerical scheme in $(h,\Delta t)$ is ensured, see conditions (B.13), (B.14) and (B.15), and Proposition 13.

Annexe C

Résumé substantiel

Cette thèse est dédiée au développement de méthodes numériques pour la poromécanique, et à leur application dans un contexte de modélisation cardiaque. L'intérêt croissant des cliniciens pour la simulation numérique a stimulé la mise au point de modèles multi-physiques de plus en plus complets, notamment du coeur humain. Notre démarche est motivée par la prise en compte dans les modèles existants du réseau coronarien qui perfuse le myocarde, jusqu'à présent absent de la plupart des modèles, afin de mieux décrire les maladies vasculaires coronariennes. L'enjeu clinique est crucial alors qu'elles représentent à elles seules 20% des décès. Du point de vue de la modélisation, le réseau de coronaires introduit un couplage supplémentaire entre la circulation sanguine en sortie du coeur et le comportement mécanique du myocarde. Sa finesse, rendant impossible une modélisation détaillée, légitime une approche de type mixture consistant à modéliser le muscle cardiaque comme un milieu poreux, où coexistent en tout point les fibres musculaires et l'écoulement sanguin.

Nous appuyant sur des travaux existants, nous commençons par introduire formellement un modèle de coeur perfusé. La nouveauté consiste à remplacer les lois hyperélastiques représentant le muscle cardiaque par un milieux poreux, soumis à de grandes déformations, hébergeant un écoulement coronarien rapide interagissant avec la circulation sanguine. La difficulté de la mise en oeuvre de ce modèle réside dans les hypothèses de notre cadre de travail, et notamment la non-linéarité des équations.

Nous effectuons alors une réduction dimensionnelle de modèle permettant de reproduire en 0D, à moindre coût de calcul, un cycle cardiaque réaliste avec en plus des indicateurs déjà accessibles (volume, pression et débit dans l'aorte) la masse et la pression de perfusion dans les coronaires. Cela nous permet de reproduire des phénomènes physiologiques d'une grande importance pour des applications cliniques et auparavant invisibles dans les modèles, tels que la vasodilatation et certaines pathologies coronariennes.

L'implémentation et l'intégration du compartiment poreux pour représenter le myocarde perfusé dans les modèles 3D représente un défi technique d'un autre ordre. Nos travaux présentent donc ensuite l'analyse numérique d'une formulation de poromécanique valide dans un cadre général.

Nous inspirant de schémas en temps de type splitting établis en interaction fluide-structure pour modéliser les vaisseaux sanguins, nous proposons une discrétisation temporelle semi-implicite de notre système, valide en non-linéaire. Des arguments énergétiques nous permettent alors d'établir la stabilité inconditionnelle de ce schéma de couplage dans un cadre non-linéaire. La difficulté réside dans le traitement de la fraction volumique de fluide présente dans toutes les équations, des déplacements du maillage fluide, et dans la non-linéarité de notre système. Afin d'illustrer et valider notre démarche, l'environnement de calcul éléments finis FreeFem++ nous permet de reproduire des cas-tests classiques de gonflement et de drainage de milieux poreux

en 2D, puis de vérifier le bilan d'énergie satisfait au niveau discret.

Enfin, motivés par l'étude de la discrétisation spatiale de notre problème, nous établissons dans un cadre linéaire (petites déformations) un résultat de convergence totale (temps et espace) du schéma, sous conditions. Notre couplage fait intervenir un problème fluide en pression vitesse de type Navier-Stokes qui demande une attention particulière afin d'éviter tout verrouillage numérique et instabilités de pression. Nous proposons en particulier un traitement adéquat de la fraction volumique de fluide, ainsi qu'un choix d'espaces éléments finis pour les variables fluides et solides du problème couplé. Notre analyse nous permet ainsi de proposer une méthode de discrétisation spatiale facile d'implémentation, malgré la complexité du système, et présentant de bons résultats de stabilité. FreeFem++ nous permet à nouveau de valider notre démarche, par une étude de convergence spatiale, puis en illustrant les pathologies numériques associées à l'incompressibilité, et leur traitement efficace par les stratégies proposées, d'abord dans le cadre linéaire puis dans une situation générale (grandes déformations).

Bibliography

Aharinejad, S., Schreiner, W., and Neumann, F. (1998). Morphometry of human coronary arterial trees. *Anatomical Record*, 251(1):50–59. 15

Astorino, M., Chouly, F., and Fernández, M. (2009a). Robin based semi-implicit coupling in fluid-structure interaction: stability analysis and numerics. *Siam J. Sci. Comput.*, 31(6):4041–4065. 15, 19, 23, 26, 27, 107, 108, 109, 111, 114

Astorino, M., Gerbeau, J., Pantz, O., and Traoré, K. (2009b). Fluid–structure interaction and multi-body contact: application to aortic valves. *Computer Methods in Applied Mechanics and Engineering*, 198(45):3603–3612. 21

Astorino, M. and Grandmont, C. (2010). Convergence analysis of a projection semi-implicit coupling scheme for fluid–structure interaction problems. *Numerische Mathematik*, 116(4):721–767. 23, 27, 107, 115

Babuška, I. (1973). The finite element method with Lagrangian multipliers. *Numerische Mathematik*, 20(3):179–192. 23, 79, 115

Badia, S. and Codina, R. (2007). Convergence analysis of the FEM approximation of the first order projection method for incompressible flows with and without the inf-sup condition. *Numerische Mathematik*, 107(4):533–557. 23

Baffico, L., Grandmont, C., and Maury, B. (2010). Multiscale modeling of the respiratory tract. *Mathematical Models and Methods in Applied Sciences*, 20(01):59–93. 16

Bathe, K. and Rugonyi, S. (2001). On finite element analysis of fluid flows fully coupled with structural interactions. *Cmes*, 2(2):195–212. 21

Bech, G., De Bruyne, B., Pijls, N., de Muinck, E., Hoorntje, J., Escaned, J., Stella, P., Boersma, E., Bartunek, J., Koolen, J., et al. (2001). Fractional flow reserve to determine the appropriateness of angioplasty in moderate coronary stenosis a randomized trial. *Circulation*, 103(24):2928–2934. 47

Becker, R., Hansbo, P., and Stenberg, R. (2003). A finite element method for domain decomposition with non-matching grids. *ESAIM: Mathematical Modelling and Numerical Analysis*, 37(02):209–225. 23

Berger, L. (2015). *A Low Order Finite Element Method for Poroelasticity with Applications to Lung Modelling*. PhD thesis, University of Oxford. 16

Berger, L., Bordas, R., Burrowes, K., Grau, V., Tavener, S., and Kay, D. (2015). A poroelastic model coupled to a fluid network with applications in lung modelling. *International journal for numerical methods in biomedical engineering*. 16

Berger, L., Bordas, R., Kay, D., and Tavener, S. (1999). A stabilized finite element method for nonlinear poroelasticity. *Computer Methods in Applied Mechanics and Engineering*, 174(3-4):299–317. 99

Biot, M. (1941). General theory of three dimensional consolidation. *Journal of Applied Physics*, 12(2):155–164. 16

Biot, M. (1962). Mechanics of deformation and acoustic propagation in porous media. *Journal of applied physics*, 33(4):1482–1498. 16

Borja, R. (2006). On the mechanical energy and effective stress in saturated and unsaturated porous continua. *International Journal of Solids and Structures*, 43(6):1764–1786. 16

Boulakia, M. (2005). Existence of weak solutions for an interaction problem between an elastic structure and a compressible viscous fluid. *Comptes Rendus Mathematique*, 340(2):113–118. 81

Bowen, R. (1980). Incompressible porous media models by use of the theory of mixtures. *International Journal of Engineering Science*, 18(9):1129–1148. 16

Brezzi, F. (1974). On the existence, uniqueness and approximation of saddle-point problems arising from Lagrangian multipliers. *Revue française d'automatique, informatique, recherche opérationnelle. Analyse numérique*, 8(2):129–151. 23, 79, 115

Brezzi, F. and Fortin, M. (2012). *Mixed and Hybrid Finite Element Methods*, volume 15. Springer Science & Business Media. 86, 120

Brown, D., Popov, P., and Efendiev, Y. (2014). Effective equations for fluid-structure interaction with applications to poroelasticity. *Applicable Analysis*, 93(4):771–790. 16

Bryant, W., Hottman, W., and Trabant, P. (1975). Permeability of unconsolidated and consolidated marine sediments, Gulf of Mexico. *Marine Georesources & Geotechnology*, 1(1):1–14. 16

Burman, E. and Fernández, M. (2007). Stabilized explicit coupling for fluid–structure interaction using Nitsche's method. *Comptes Rendus Mathématique*, 345(8):467–472. 23, 82, 117

Burman, E. and Fernández, M. (2009). Stabilization of explicit coupling in fluid-structure interaction involving fluid incompressibility. *Computer Methods In Applied Mechanics And Engineering*. 23

Burman, E. and Fernández, M. (2014). Explicit strategies for incompressible fluid-structure interaction problems: Nitsche type mortaring versus Robin–Robin coupling. *International Journal for Numerical Methods in Engineering*, 97(10):739–758. 105

Caruel, M., Chabiniok, R., Moireau, P., Lecarpentier, Y., and Chapelle, D. (2014). Dimensional reductions of a cardiac model for effective validation and calibration. *Biomechanics and modeling in mechanobiology*, 13(4):897–914. 12, 25, 29, 35, 36, 38, 50, 103

Caruel, M., Moireau, P., and Chapelle, D. (2016). Stochastic modeling of chemical-mechanical coupling in striated muscles. to appear. 30, 31

Causin, P., Gerbeau, J., and Nobile, F. (2005). Added-mass effect in the design of partitioned algorithms for fluid–structure problems. *Computer methods in applied mechanics and engineering*, 194(42):4506–4527. 22

Chapelle, D. and Bathe, K. (2010). *The Finite Element Analysis of Shells - Fundamentals*. Springer Science & Business Media. 36

Chapelle, D., Gerbeau, J., Sainte-Marie, J., and Vignon-Clementel, I. (2009). A poroelastic model valid in large strains with applications to perfusion in cardiac modeling. *Computational Mechanics*, 46(1):91–101. 16, 34

Chapelle, D., Le Tallec, P., Moireau, P., and Sorine, M. (2012). Energy-preserving muscle tissue model: formulation and compatible discretizations. *International Journal for Multiscale Computational Engineering*, 10(2). 11, 29, 30, 40, 50, 103

Chapelle, D. and Moireau, P. (2014). General coupling of porous flows and hyperelastic formulations-From thermodynamics principles to energy balance and compatible time schemes. *European Journal of Mechanics - B/Fluids*, 46:82–96. 16, 17, 18, 20, 21, 25, 30, 31, 32, 33, 40, 80, 103, 112

Chilian, W., Layne, S., Klausner, E., Eastham, C., and Marcus, M. (1989). Redistribution of coronary microvascular resistance produced by dipyridamole. *American Journal of Physiology-Heart and Circulatory Physiology*, 256(2):H383–H390. 45

Chorin, A. (1968). Numerical solution of the Navier-Stokes equations. *Mathematics of computation*, 22(104):745–762. 22

Chorin, A. (1969). On the convergence of discrete approximations to the Navier-Stokes equations. *Mathematics of computation*, 23(106):341–353. 22

Cimrman, R. and Rohan, E. (2010). Two-scale modeling of tissue perfusion problem using homogenization of dual porous media. *International Journal for Multiscale Computational Engineering*, 8(1):81–102. 16

Clément, P. (1975). Approximation by finite element functions using local regularization. *Revue française d'automatique, informatique, recherche opérationnelle. Analyse numérique*, 9(2):77–84. 92, 125

Costa, K., Holmes, J., and Mcculloch, A. (2001). Modelling cardiac mechanical properties in three dimensions. *Philosophical Transactions of the Royal Society A: Mathematical, Physical and Engineering Sciences*, 359(1783):1233–1250. 11

Coussy, O. (2004). *Poromechanics*. John Wiley & Sons. 16

Coussy, O. (2011). *Mechanics and Physics of Porous Solids*. John Wiley & Sons. 16

Dautray, R. and Lions, J. (1988). *Analyse Mathematique et Calcul Numerique pour les Sciences et les Techniques. VO*. Masson, KTK Scientific Publishers. 21

Davies, J., Whinnett, Z., Francis, D., Manisty, C., Aguado-Sierra, J., Willson, K., Foale, R., Malik, I., Hughes, A., and Parker, K. (2006). Evidence of a dominant backward-propagating "suction" wave responsible for diastolic coronary filling in humans, attenuated in left ventricular hypertrophy. *Circulation*, 113(14):1768–1778. 14

De Boer, R. (2006). *Trends in Continuum Mechanics of Porous Media*, volume 18. Springer Science & Business Media. 16

Deheuvels, T. (2013). *Contributions à l'Etude d'Espaces de Fonctions et d'EDP dans une Classe de Domaines à Frontière Fractale Auto-Similaire*. PhD thesis, Université Rennes 1. 16

Du, Q., Gunzburger, M., Hou, L., and Lee, J. (2003). Analysis of a linear fluid-structure interaction problem. *Discrete and continuous dynamical systems*, 9(3):633–650. 23, 81, 105, 116

Du, Q., Gunzburger, M., Hou, L., and Lee, J. (2004). Semidiscrete finite element approximations of a linear fluid-structure interaction problem. *SIAM journal on numerical analysis*, 42(1):1–29. 105

Farhat, C., Van der Zee, K., and Geuzaine, P. (2006). Provably second-order time-accurate loosely-coupled solution algorithms for transient nonlinear computational aeroelasticity. *Computer methods in applied mechanics and engineering*, 195(17):1973–2001. 22

Fernández, M., Gerbeau, J., and Grandmont, C. (2007). A projection semi-implicit scheme for the coupling of an elastic structure with an incompressible fluid. *International Journal for Numerical Methods in Engineering*, 69(4):794–821. 15, 19, 22, 23, 26, 27, 107, 115

Fernández, M., Milisic, V., and Quarteroni, A. (2005). Analysis of a geometrical multiscale blood flow model based on the coupling of ODEs and hyperbolic PDEs. *Multiscale Modeling & Simulation*, 4(1):215–236. 16

Fernández, M. and Moubachir, M. (2005). A Newton method using exact jacobians for solving fluid–structure coupling. *Computers & Structures*, 83(2):127–142. 22

Figueroa, C., Vignon-Clementel, I., Jansen, K., Hughes, T., and Taylor, C. (2006). A coupled momentum method for modeling blood flow in three-dimensional deformable arteries. *Computer Methods in Applied Mechanics and Engineering*, 195(41-43):5685–5706. 15

Fischer, J., Samady, H., McPherson, J., Sarembock, I., Powers, E., Gimple, L., and Ragosta, M. (2002). Comparison between visual assessment and quantitative angiography versus fractional flow reserve for native coronary narrowings of moderate severity. *The American journal of cardiology*, 90(3):210–215. 47

Formaggia, L., Gerbeau, J., Nobile, F., and Quarteroni, A. (2001). On the coupling of 3D and 1D Navier–Stokes equations for flow problems in compliant vessels. *Computer Methods in Applied Mechanics and Engineering*, 191(6):561–582. 15

Formaggia, L., Lamponi, D., and Quarteroni, A. (2003). One-dimensional models for blood flow in arteries. *Journal of Engineering Mathematics*, 47(3/4):251–276. 15

Formaggia, L., Quarteroni, A., and Veneziani, A. (2010). *Cardiovascular Mathematics: Modeling and Simulation of the Circulatory System*, volume 1. Springer Science & Business Media. 107

Fung, Y. (2013). *Biomechanics: Mechanical Properties of Living Tissues*. Springer Science & Business Media. 16

Gerbeau, J. and Vidrascu, M. (2003). A quasi-Newton algorithm based on a reduced model for fluid-structure interaction problems in blood flows. *ESAIM: M2AN*, 37(4):631–647. 22

Go, A., Mozaffarian, D., Roger, V., Benjamin, E., Berry, J., Blaha, M., Dai, S., Ford, E., Fox, C., Franco, S., Fullerton, H., Gillespie, C., Hailpern, S., Heit, J., Howard, V., Huffman, M., Judd, S., Kissela, B., Kittner, S., Lackland, D., Lichtman, J., Lisabeth, L., Mackey, R., Magid, D., Marcus, G., Marelli, A., Matchar, D., McGuire, D., Mohler, E., Moy, C., Mussolino, M., Neumar, R., Nichol, G., Pandey, D., Paynter, N., Reeves, M., Sorlie, P.,

Stein, J., Towfighi, A., Turan, T., Virani, S., Wong, N., Woo, D., and Turner, M. (2014). *Heart Disease and Stroke Statistics–2014 Update*, volume 129. American Heart Association. 7

Gonzalez, O. (2000). Exact energy and momentum conserving algorithms for general models in nonlinear elasticity. *Computer Methods in Applied Mechanics and Engineering*, 190(13-14):1763–1783. 21, 40, 110

Gould, K., Kirkeeide, R., and Buchi, M. (1990). Coronary flow reserve as a physiologic measure of stenosis severity. *Journal of the American College of Cardiology*, 15(2):459–474. 45

Grandmont, C. and Maday, Y. (2000). Existence for an unsteady fluid-structure interaction problem. *ESAIM: Mathematical Modelling and Numerical Analysis*, 34(03):609–636. 23, 81, 105, 116

Guermond, J., Minev, P., and Shen, J. (2006). An overview of projection methods for incompressible flows. *Comput Method Appl M*, 195(44-47):6011–6045. 22

Guermond, J. and Quartapelle, L. (1998). On stability and convergence of projection methods based on pressure Poisson equation. *International Journal for Numerical Methods in Fluids*, 26(9):1039–1053. 23

Hansbo, P., Hermansson, J., and Svedberg, T. (2004). Nitsche's method combined with space–time finite elements for ale fluid–structure interaction problems. *Computer Methods in Applied Mechanics and Engineering*, 193(39):4195–4206. 23

Hecht, F. (2012). New development in FreeFem++. *J. Numer. Math.*, 20(3-4):251–265. 26, 100, 104, 105

Heil, M. (2004). An efficient solver for the fully coupled solution of large-displacement fluid-structure interaction problems. *Computer Methods in Applied Mechanics and Engineering*, 193(1-2):1–23. 21

Hornung, U. (2012). *Homogenization and Porous Media*, volume 6. Springer Science & Business Media. 16

Hunter, P. (1975). *Finite Element Analysis of Cardiac Muscle Mechanics.* PhD thesis, University of Oxford. 11

Huxley, A. (1957). Muscle structure and theories of contraction. *Prog. Biophys. Biophys. Chem*, 7:255–318. 11

Johnson, K., Sharma, P., and Oshinski, J. (2008). Coronary artery flow measurement using navigator echo gated phase contrast magnetic resonance velocity mapping at 3.0 t. *Journal of biomechanics*, 41(3):595–602. 16

Joly, P. and Semin, A. (2011). Mathematical and numerical modeling of wave propagation in fractal trees. *Comptes Rendus Mathématique*, 349(19):1047–1051. 16

Kajiya, F., Kajiya, M., Morimoto, T., Iwasaki, T., Inai, Y., Hirota, M., Kiyooka, T., Morizane, Y., Miyasaka, T., Mohri, S., et al. (2007). Physiomics of coronary perfusion and cardiac pumping. In *Cardiac perfusion and pumping engineering*, pages 1–15. World Scientific Publishing Co. 45

Kerckhoffs, R., Faris, O., Bovendeerd, P., Prinzen, F., Smits, K., McVeigh, E., and Arts, T. (2005). Electromechanics of paced left ventricle simulated by straightforward mathematical model: comparison with experiments. *American journal of physiology. Heart and circulatory physiology*, 289(5):H1889–H1897. 12

Ladyzhenskaya, O. and Silverman, R. (1969). *The Mathematical Theory of Viscous Incompressible Flow*, volume 76. Gordon and Breach New York. 23, 79, 115

Le Tallec, P., Gerbeau, J., Hauret, P., and Vidrascu, M. (2005). Fluid structure interaction problems in large deformation. *Comptes Rendus Mecanique*, 333(12):910–922. 21

Le Tallec, P. and Hauret, P. (2002). Energy conservation in fluid structure interactions. In Y. Kuznetsov, P. Neittanmaki, O. P., editor, *Numerical Methods for Scientific Computing / Variational Problems and Applications – CIMNE Barcelona*. 21, 26, 40, 43, 95

Le Tallec, P. and Mani, S. (2000). Numerical analysis of a linearised fluid-structure interaction problem. *Numerische Mathematik*, 87(2):317–354. 23, 27, 79, 105, 115

Le Tallec, P. and Mouro, J. (2001). Fluid structure interaction with large structural displacements. *Computer Methods in Applied Mechanics and Engineering*, 190(24-25):3039–3067. 22

Lee, J. and Smith, N. (2012). The multi-scale modelling of coronary blood flow. *Annals of biomedical engineering*, 40(11):2399–2413. 15

Liu, C. (2007). Cardiovascular diseases in China. *Biochemistry and Cell Biology*, 85(2):157–163. PMID: 17534394. 7

Loret, B. and Simões, F. (2005). A framework for deformation, generalized diffusion, mass transfer and growth in multi-species multi-phase biological tissues. *European Journal of Mechanics, A/Solids*, 24:757–781. 16

Mann, D., Zipes, D., Libby, P., and Bonow, R. (2014). *Braunwald's Heart Disease: a Textbook of Cardiovascular Medicine*. Elsevier Health Sciences. 46

Moireau, P. (2008). *Assimilation de Données par Filtrage pour les Systèmes Hyperboliques du Second Ordre. Applications à la Mécanique Cardiaque.* PhD thesis, Ecole Polytechnique. 10

Moireau, P., Xiao, N., Astorino, M., Figueroa, C., Chapelle, D., Taylor, C., and Gerbeau, J. (2012). External tissue support and fluid–structure simulation in blood flows. *Biomechanics and modeling in mechanobiology*, 11(1-2):1–18. 21

Mok, D. and Wall, W. (2001). Partitioned analysis schemes for the transient interaction of incompressible flows and nonlinear flexible structures. *Trends in computational structural mechanics, Barcelona*. 22

Mok, D., Wall, W., and Ramm, E. (2001). Accelerated iterative substructuring schemes for instationary fluid-structure interaction. *Computational Fluid and Solid Mechanics*, pages 1325–1328. 22

Morton, G., Chiribiri, A., Ishida, M., Hussain, S., Schuster, A., Indermuehle, A., Perera, D., Knuuti, J., Baker, S., Hedström, E., et al. (2012). Quantification of absolute myocardial perfusion in patients with coronary artery disease: comparison between cardiovascular magnetic resonance and positron emission tomography. *Journal of the American College of Cardiology*, 60(16):1546–1555. 48

Mynard, J. and Nithiarasu, P. (2008). A 1D arterial blood flow model incorporating ventricular pressure, aortic valve and regional coronary flow using the locally conservative Galerkin (LCG) method. *Communications in Numerical Methods in Engineering*, 24(5):367–417. 15

Nash, M. and Hunter, P. (2001). Computational mechanics of the heart. *Journal of Elasticity*, 61:113–141. 11

Nichols, M., Townsend, N., Scarborough, P., and Rayner, M. (2014). Cardiovascular disease in Europe. 2014: Epidemiological update. *European Heart Journal*, 35:2950–2959. 7, 15

Niederer, S. and Smith, N. (2009). The role of the Frank-Starling law in the transduction of cellular work to whole organ pump function: a computational modeling analysis. *PLoS computational biology*, 5(4):e1000371. 12

Nitsche, J. (1971). Über ein Variationsprinzip zur Lösung von Dirichlet-Problemen bei Verwendung von Teilräumen, die keinen Randbedingungen unterworfen sind. *Abh. Math. Sem. Univ. Hamburg*, 36:9–15. 82, 117

Ogden, R. and Holzapfel, G. (2006). *Mechanics of Biological Tissue*. Springer. 16

Peskin, C. (1977). Numerical analysis of blood flow in the heart. *Journal of Computational Physics*, 25(3):220–252. 11

Peskin, C. (1982). The fluid dynamics of heart valves: experimental, theoretical, and computational methods. *Annual review of fluid mechanics*, 14(1):235–259. 11

Pijls, N., van Schaardenburgh, P., Manoharan, G., Boersma, E., Bech, J., van't Veer, M., Bär, F., Hoorntje, J., Koolen, J., Wijns, W., et al. (2007). Percutaneous coronary intervention of functionally nonsignificant stenosis: 5-year follow-up of the defer study. *Journal of the American College of Cardiology*, 49(21):2105–2111. 47

Pijls, N., Van Son, J., Kirkeeide, R., De Bruyne, B., and Gould, K. (1993). Experimental basis of determining maximum coronary, myocardial, and collateral blood flow by pressure measurements for assessing functional stenosis severity before and after percutaneous transluminal coronary angioplasty. *Circulation*, 87(4):1354–1367. 47

Quarteroni, A. and Veneziani, A. (2003). Analysis of a geometrical multiscale model based on the coupling of ODE and PDE for blood flow simulations. *Multiscale Modeling & Simulation*, 1(2):173–195. 16

Sainte-Marie, J., Chapelle, D., Cimrman, R., and Sorine, M. (2006). Modeling and estimation of the cardiac electromechanical activity. *Computers and Structures*, 84(28):1743–1759. 11, 29, 33

Sapoval, B., Filoche, M., and Weibel, E. (2002). Smaller is better—but not too small: a physical scale for the design of the mammalian pulmonary acinus. *Proceedings of the National Academy of Sciences*, 99(16):10411–10416. 16

Spaan, J. (1985). Coronary diastolic pressure-flow relation and zero flow pressure explained on the basis of intramyocardial compliance. *Circulation Research*, 56(3):293–309. 44

Temam, R. (1968). Une méthode d'approximation de la solution des équations de Navier-Stokes. *Bull. Soc. Math.*, France 96:115–152. 22

Vignon-Clementel, I., Figueroa, C., Jansen, K., and Taylor, C. (2006). Outflow boundary conditions for three-dimensional finite element modeling of blood flow and pressure in arteries. *Computer methods in applied mechanics and engineering*, 195(29):3776–3796. 16

Vuong, A., Ager, C., and Wall, W. (2016). Two finite element approaches for Darcy and Darcy–Brinkman flow through deformable porous media—Mixed method vs. NURBS based (isogeometric) continuity. *Computer Methods in Applied Mechanics and Engineering*, 305:634–657. 101, 105

Vuong, A., Yoshihara, L., and Wall, W. (2015). A general approach for modeling interacting flow through porous media under finite deformations. *Computer Methods in Applied Mechanics and Engineering*, 283:1240–1259. 19

Watanabe, H., Sugiura, S., Kafuku, H., and Hisada, T. (2004). Multiphysics simulation of left ventricular filling dynamics using fluid-structure interaction finite element method. *Biophysical journal*, 87(3):2074–2085. 11

Westerhof, N., Boer, C., Lamberts, R., and Sipkema, P. (2006). Cross-talk between cardiac muscle and coronary vasculature. *Physiological Reviews*, 86(4):1263–1308. 14, 45

Xiong, G., Figueroa, C., Xiao, N., and Taylor, C. (2011). Simulation of blood flow in deformable vessels using subject-specific geometry and spatially varying wall properties. *International journal for numerical methods in biomedical engineering*, 27(7):1000–1016. 15

université PARIS-SACLAY

ÉCOLE DOCTORALE
Sciences mécaniques et énergétiques, matériaux et géosciences (SMEMAG)

Modélisation mécanique et méthodes numériques pour la poromécanique
Application à la perfusion du myocarde

Résumé : Cette thèse est dédiée au développement de méthodes numériques pour la poromécanique, et à leur application dans un contexte de modélisation cardiaque. Elle est motivée par la prise en compte, dans les modèles de coeur humain, du réseau coronarien qui perfuse le myocarde, afin de mieux décrire les maladies vasculaires coronariennes.
Nous appuyant sur des travaux existants, nous proposons un modèle de coeur perfusé, ainsi qu'une réduction 0D permettant de reproduire, à moindre coût de calcul, un cycle cardiaque réaliste avec masse et pression de perfusion. Le modèle mis au point nous permet de reproduire des phénomènes physiologiques auparavant inaccessibles dans les modèles, et d'une grande importance pour des applications cliniques, tels que la vasodilatation et les pathologies coronariennes.
L'intégration d'un compartiment poreux pour représenter le myocarde perfusé dans les modèles 3D représente un défi technique d'un autre ordre. Nous inspirant des schémas en temps de type splitting établis en interaction fluide-structure pour modéliser les vaisseaux sanguins, nous proposons une discrétisation semi-implicite d'une formulation générale de poromécanique, satisfaisant un bilan d'énergie au niveau discret. Afin d'illustrer et valider notre démarche, l'environnement de calcul élément finis FreeFem++ nous permet de reproduire des cas tests classiques de gonflement et de drainage de milieux poreux en 2D, puis de vérifier le bilan énergétique discret.
Enfin, motivés par l'étude de la discrétisation spatiale de notre problème, nous établissons dans un cadre linéaire un résultat de convergence totale du schéma sous conditions. Cela nous permet de proposer une méthode d'implémentation facile à mettre en oeuvre et présentant de bons résultats de stabilité. FreeFem++ nous permet à nouveau de valider nos résultats en illustrant les pathologies numériques associées à l'incompressibilité, et leur traitement efficace par les stratégies proposées, dans le cadre linéaire puis dans une situation générale.

Mots-clés : Poromécanique ; Analyse numérique ; Modélisation cardiaque ; Réduction dimensionnelle

Mechanical modeling and numerical methods for poromechanics
Application to myocardium perfusion

Abstract: This thesis is dedicated to the development of numerical methods for poromechanics, and to their application in a cardiac modeling context. It is motivated by the introduction into existing cardiac models of the coronary network that perfuses the myocardium, to better describe coronary vascular diseases.
Drawing our inspiration from existing works, we propose a perfused heart model, and a 0D reduction allowing the cost-effective reproduction of a realistic cardiac cycle with perfusion mass and pressure. The model derived illustrates physiological phenomena inaccessible in former models, and with great clinical application potential, such as vasodilatation and coronary diseases.
The integration of a porous compartment to represent the perfused myocardium within 3D models is more challenging. Relying on splitting time schemes established for fluid-structure interaction to model blood vessels, we propose a semi-implicit discretization of a general poromechanics formulation, satisfying a discrete energy balance. In order to illustrate and validate our approach, we reproduce in the finite element software FreeFem++ classical swelling and drainage 2D test cases, and we monitor the discrete energy balance.
Finally, motivated by the study of spatial discretization aspects of our problem, we establish in a linear framework a conditional total convergence result. This allows us to propose a computational method easy to implement and presenting good stability results. FreeFem++ enables us again to validate our results, illustrating numerical pathologies associated with incompressibility, and their efficient treatment with the proposed strategies, first in a linear framework and then in a general situation.

Keywords: Poromechanics ; Numerical analysis ; Cardiac modeling ; Dimensional reduction